



HAL
open science

Development and characterization of safety and versatile electrolytes for lithium and post lithium batteries

Hoang Phuong Khanh Ngo

► **To cite this version:**

Hoang Phuong Khanh Ngo. Development and characterization of safety and versatile electrolytes for lithium and post lithium batteries. Chemical and Process Engineering. Université Grenoble Alpes, 2019. English. NNT: 2019GREAI076 . tel-02475732

HAL Id: tel-02475732

<https://theses.hal.science/tel-02475732>

Submitted on 12 Feb 2020

HAL is a multi-disciplinary open access archive for the deposit and dissemination of scientific research documents, whether they are published or not. The documents may come from teaching and research institutions in France or abroad, or from public or private research centers.

L'archive ouverte pluridisciplinaire **HAL**, est destinée au dépôt et à la diffusion de documents scientifiques de niveau recherche, publiés ou non, émanant des établissements d'enseignement et de recherche français ou étrangers, des laboratoires publics ou privés.

THÈSE

Pour obtenir le grade de

DOCTEUR DE LA COMMUNAUTE UNIVERSITE GRENOBLE ALPES

Spécialité : 2MGE : Matériaux, Mécanique, Génie civil, Electrochimie

Arrêté ministériel : 25 mai 2016

Présentée par

Hoang Phuong Khanh NGO

Thèse dirigée par **Cristina IOJOIU** et
codirigée par **Patrick JUDEINSTEIN** et **Emilie PLANES**

préparée au sein du **Laboratoire d'Electrochimie et de Physico-
Chimie des Matériaux et des Interfaces (LEPMI)**
dans l'**École Doctorale I-MEP2 - Ingénierie - Matériaux,
Mécanique, Environnement, Energétique, Procédés, Production**

Développement et caractérisation des électrolytes plus sûrs et versatiles pour les batteries au lithium métallique ou post lithium

Thèse soutenue publiquement le **5 décembre 2019**,
devant le jury composé de :

Mme. Fannie ALLOIN
DR., LEPMI, Grenoble, Présidente

Mme. Meriem ANOUTI
Prof., PCM2E, Université de Tours, Rapporteur

M. Maurice MEDEBIELE
DR., ICBMS, Université de Lyon, Rapporteur

Mme. Katia ARAUJO DA SILVA
MdC., Université Clermont Auvergne, Examineur

Mme. Cristina IOJOIU
DR., LEPMI, Grenoble, Directeur de thèse

Mme. Emilie PLANES
MdC., LEPMI, Chambéry, Co-directeur de thèse

M. Patrick JUDEINSTEIN
DR., Université Paris-Saclay, Paris, Co-directeur de thèse



Acknowledgement

I appreciate my colleagues, my friend, my professors, and their help for contributing to this Ph.D. work.

First of all, I would like to send my appreciation to my supervisors Dr. Cristina IOJOIU, Dr. Patrick Judenstein, and Dr. Emilie Planes for their supports, their advice, and their help from the beginning to the end of this Ph.D. It is an honor for me to work with them in three years.

A big thank for Dr. Fannie Alloin, who's always supporting me even from my first days in France. Thanks a lot for your advice, your help, and the great moments sharing the 'electrochemical knowledge' together.

I had the great chance to work with many people in LEPMI during my Ph.D. time. My works may not finish without the warm help of Mme. Priscillia Soudant, Dr. Laure Cointeaux, Dr. Ly Nguyen, M. Vincent Martin. My sincere thanks for all of the colleagues, Ph.D. students, post-doctorates, inters, and my friends in Grenoble for your help and the wonderful moments worked in the laboratory or shared outside the laboratory.

Moreover, I'm grateful for the help of Mme. Anne-Laure Rollet (laboratory Phenix, Sorbonne University), M. Benoit Coasne (laboratory Liphy, Grenoble-Alpes University), and M. Fabrice Cousin (laboratory LLB, CEA Saclay). Thank you very much for your contribution in this thesis.

Last but not least, thank you to my lovely friends in Viet Nam. The long-distance talking times with you always make me feel better and stronger to pass through the difficulties and arrive at this final moment. Also for my dear lover, thank you for your advice and your unconditional love.

Finally, I would like to send my gratitude to the members of the committee for their time, and their corrections which help me to improve this manuscript.

This thesis is for you, my dear mom and dad.

Hoang Phuong Khanh NGO

Introduction

The demands for low-cost and safe energy have been gradually increasing, and promoting the development of electricity sources from nature, including solar, wind, or water. These renewable sources have been intermittently producing electricity, but the pressing challenge for future needs requires the development of electrical storage systems. In diverse technologies, rechargeable batteries are an essential energy conversion devices¹, which have been mainly using in the mobile electronic systems, hybrid electric vehicles, etc. Besides the advancements, the challenges have also put forward. To solve the world's energy needs, the safer, low-cost, and abundant elements-based future storable batteries have been attracting attention the recent years.

One of the most successful technologies is lithium batteries, especially Li-ion batteries (LIBs), which have been dominating the renewable energy for mobile devices.² These rechargeable batteries possess the lead technologies, such as high energy density, no memory effect, easy to design, present in various shapes and sizes, etc. The LIBs are also called as the 'rocking chair' batteries, where lithium exhibits in its ionic form and is inserted or deserted in the active materials. As with any technological system, the challenges prevent the sustainable development of LIBs are the security and the limit of raw resources of lithium metal.

Conventional electrolyte for LIBs is the solution of a dissolved lithium salt in organic solvents, which provides high ionic transport and conductivity. However, the damage issues of these batteries related to the flammability and toxicity of organic solvents cause the critical environmental disasters and low security for users. The pressing needs for safer LIBs promoted the studies of new electrolytes using ionic liquids (ILs) as solvents for dissolving lithium salt, or solid conducting polymers with high conductivity, good thermal stability, flexibility, and high security. Moreover, the exhausted future of an essential raw material i.e. lithium metal may interrupt the production of LIBs, or remarkably increase their price. As a reason, the alkali/alkali-earth metals are proposing as the most promising candidates for rechargeable technologies, including the batteries.

This work focuses on the high safety electrolytes i.e. design and characterization of polymer electrolytes, as well as the impact of cation nature i.e. alkali/alkaline-earth cations (lithium, sodium, potassium, cesium, magnesium, calcium, etc.) on the transport properties of IL and polymer-based electrolytes. The first study relates to the electrolytes consisted of a common IL i.e. 1-butyl-3-methyl imidazolium bis(trifluoromethanesulfonyl)imide, denoted as BMIm TFSI, and different alkali/alkaline-earth-based TFSI salts. These mixtures are prepared and characterized in terms of physical/ transport properties as a function of cation nature. Thus, the blend of polymer/salt, using poly(ethylene oxide) - PEO as polymer host and a dissolved inorganic salt, was reported in most of the studies of safer solid electrolytes for lithium batteries. Apart from the non-flammability, non-

volatility, flexibility, multi-functional, etc., the main issues of this system relating to the salt precipitation/aggregation, concentration gradient, low conductivity, insufficient cation transference number (t^+), capacity fading, etc. The single-ion polymer electrolytes (SIPES) have been proposed in recent years for improving the t^+ value and decreasing the growth of lithium dendrites during operation. In this work, two types of anions e.g. phenyl-oxoperfluoropentane sulfonate (p-SO₃), and phenyloxoperfluoropentane sulfonylimide (p-TFSI) are chemically bonded to the PEO backbone. Grafting these anions along the polymer chain helps to promote cation mobility in the polymer matrix and eliminate the problem of salt aggregation/ precipitation. From an application point of view, using these single-ion polymers may also improve the electrochemical stability of the electrode-electrolyte interface and the cyclability of battery. For the future storage technologies, the alkali-based single-ion polymers are investigated in terms of physical/conductive properties as a function of cation size. This manuscript presents the thematic studies including four chapters and an experimental annex.

Chapter 1 is a literature review of different types of electrolytes for lithium batteries including the advantages and challenges. The ionic liquid and polymer-based electrolytes for lithium and post lithium batteries are briefly recapped. Finally, the work aims are clarified.

Chapter 2 focuses on the physical and ionic transport properties of several systems based on the mixture of different alkali/alkaline-earth TFSI salts in a common ionic liquid BMIm TFSI. These binary systems are studied experimentally by the multi-technique approach to reach the thermodynamics (thermal properties), dynamics (viscosity, ionic conductivity, self-diffusion coefficients), and structural (IR spectroscopy) description of these systems.

Chapter 3 deals with the synthesis and characterization of two SIPES based on PEO as solid electrolytes for Li-metal polymer batteries. The thermal properties and conduction behavior of these new electrolytes are discussed as a function of polymer structure. The most conducting polymer films are performed in the symmetrical Li-metal cell, as well as in the full battery using LiFePO₄ (LFP) cathode.

In chapter 4, the impact of different alkali cations on thermal properties and conductivity behavior of the two SIPES performed in chapter 3 is investigated. These new materials are promising for electrolyte applications in the post lithium batteries.

This manuscript ends with an experimental annex where the protocols and techniques used in this work are described.

Table of contents

Chapter 1 Literature review	1
1. General context	2
1.1. Lithium metal batteries	3
1.2. Lithium-ion batteries: issues and challenges from electrolyte aspect	4
2. Ionic liquid electrolyte	7
2.1. Introduction.....	7
2.2. Physical and transport properties	9
2.3. Lithiated electrolytes based on IL.....	12
2.4. Ionic liquid doped alkali/alkaline-earth elements	15
3. Solid polymer electrolyte	18
3.1. Lithium salts	19
3.2. Poly(ethylene oxide) based electrolyte	19
3.3. Single-ion polymer electrolyte based on PEO	26
3.4. Application of SIPes in all-solid-state lithium metal batteries	31
4. Electrolyte approaches for future rechargeable batteries	33
5. The aim of this work	37
References	39
Chapter 2 Ionic liquid-based electrolytes	47
1. Introduction	49
2. Salt solubilization	49
3. Effect of salt concentration	51
3.1. BMIm TFSI and the binary system [Li][BMIm][TFSI]	51
3.2. The binary system [Cs][BMIm][TFSI]	64
3.3. Conclusions	71
4. Alkali/ alkaline-earth based BMIm TFSI	72
4.1. Thermal characteristics	72
4.2. Density and viscosity	74
4.3. Ionic conductivity	74
4.4. Self-diffusion coefficient	78
4.5. Cisoid and Transoid TFSI conformers	79
5. Conclusions	82
References	85
Chapter 3 Polymer-based electrolyte for Li-metal batteries	89
1. Cross-linked single-ion conducting polymer (SICP)	92

1.1. Syntheses of ionic block (ionomers)	92
1.1.1. Synthesis of Ip-SO ₃	95
1.1.2. Synthesis of I _x p-SO ₃ -db.....	97
1.1.3. Synthesis of Ip-TFSI	99
1.1.4. Synthesis of I ₁₀₀₀ p-TFSI-db.....	101
1.2. Characterization	102
1.2.1. Molar mass and cation exchange efficiency	102
1.2.2. Cross-linking degree and NCC dispersion	103
1.2.3. Thermal properties	107
1.2.4. Conductive and transport properties	111
1.2.5. Electrochemical stability	120
1.2.6. Lithium plating/stripping test	122
1.2.7. Cycling tests	126
1.3. Conclusions.....	134
2. Multi-block copolymer	135
2.1. Synthesis of Co _x p-SO ₃	136
2.1.1. Synthesis of FPES block.....	136
2.1.2. Synthesis of Co _x p-SO ₃	138
2.2. Characterization	140
2.2.1. Thermal properties	140
2.2.2. Conductivity	143
2.2.3. Electrochemical stabilization	144
2.2.4. Lithium transference number	145
2.2.5. Lithium dendritic growth test	146
2.2.6. Cycling tests	146
3. Conclusions	148
References	150
Chapter 4 Impact of alkali cations on conductivity behavior of polymer electrolytes	153
1. Introduction	155
2. Cross-linked ionomer	156
2.1. Thermal properties	157
2.2. Conductivity	160
3. Multi-block copolymer	164
3.1. Thermal properties	165
3.2. Conductivity	167
4. Conclusion	169

References	170
Conclusions and perspectives	171
Annex	180
A. Synthesis part	180
1. Synthesis process	180
2. Polymer film casting	185
3. Ionic liquid/ salts preparation	186
B Characterization techniques	187
1. Spectroscopy	187
2. Thermal and physical properties	189
3. Electrochemical properties	192

A decorative frame consisting of thin black lines forming an L-shape that surrounds the text. The lines are positioned to the left and below the text, with some segments extending further out to create a larger frame.

Chapter 1

Literature review

1. General context

The aspects of renewable sources, where energy is always available for consuming, have been widely studied for years. Energy storage is an economical and efficient solution that can satisfy the supply and demand of mobile electrical devices for modern life. Among the strategies, batteries appeared as a key of choice. Thanks to the advancement, these energy storable sources have been using for many criteria of technologies such as mobility, cyclability, performance, low-cost, etc., and applying in the large scale of applications such as e-communication, electronic devices, even transportation. In Fig. 1, different types of batteries with their volumetric and gravimetric energy density are compared.

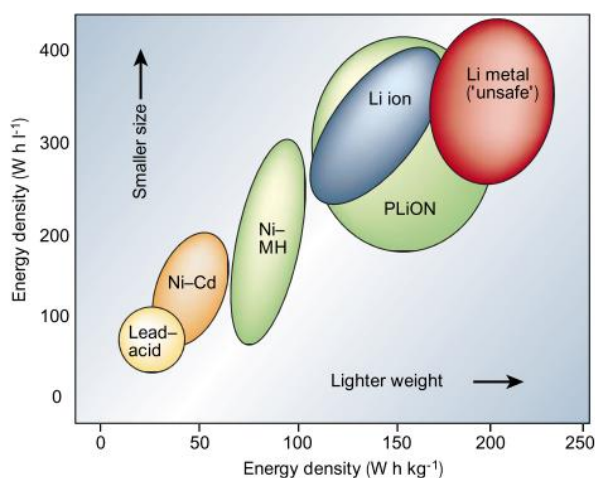


Fig. 1 Different battery technologies in terms of volumetric and gravimetric energy density.¹

The two terms of ‘primary’ and ‘secondary’ correspond to the definition of ‘non-rechargeable’ and ‘rechargeable’ batteries, respectively. Thus, the ongoing demands are requiring new recyclable technologies for economic and environmental reasons. The rechargeable batteries, which can charge and discharge multiple times in an external load, as opposed to the primary cells, have been advancing in recent years. A battery has one or many electrochemical units, and each of them consists of one positive, one negative electrode, separated by an electrolyte to allow the ionic transport. Since the first appearance, lithium batteries have been dominated the whole world’s interests due to its high energy density exhibited in a limited volume. This technology has been suitable for most of the personal mobile devices including smartphone, laptop, camera, electric vehicles, etc. Meanwhile, the safety aspect, which related to the flammability and toxicity of organic solvents content in conventional liquid electrolytes, prevents the development of lithium batteries.

1.1. Lithium metal batteries

Over the past decades, lithium metal became a promising candidate for energy technology releasing to the most electropositive potential of -3.04 V versus (*vs*) SHE (standard hydrogen electrode), as well as to the lightest weight of 6.94 g.mol⁻¹. These batteries offer high energy density in a lighter weight, with a long life-time, and design flexibility than other comparable technologies¹. Different types of lithium batteries, such as Li-ion, Li-S, or Li-air can reach approximately 250, 650, and even 950 Wh.kg⁻¹, respectively².

Back in the 1970s, the first primary battery using lithium metal as anode exhibited high capacity and variable discharge rate. The advances of numerous inorganic lithium salts dissolved in carbonate solvents provided a reversibly lithium plating/ stripping during operation. Later, the discovery of intercalation compounds promoted an obvious step forward for the battery aspect. However, as reported by Whittingham, using TiS₂ as cathode material and lithium metal as anode, separated by a liquid electrolyte, causing the formation of lithium dendrites during charge and discharge, allowing the cell's failure (see Fig. 2a).¹

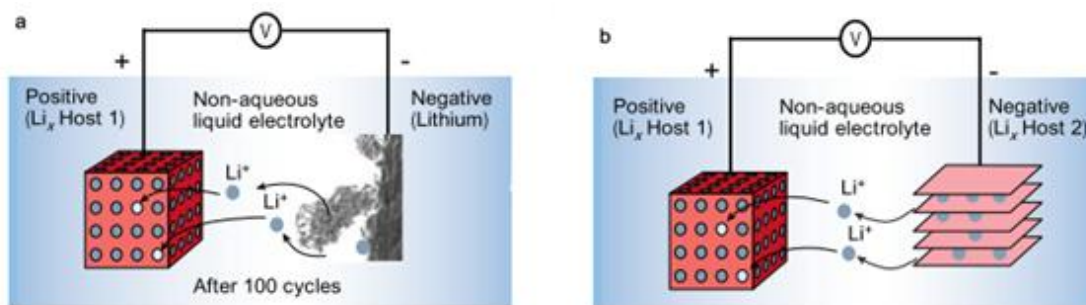


Fig. 2 Rechargeable li-metal battery with the demonstration of dendritic growth at the lithium metal surface (a) and li-ion battery (b).¹

Lithium metal is thermodynamically unstable in organic solvents and leads to the formation of an interphase electrode/electrolyte, called as 'solid electrolyte interphase' (SEI). The growth of this film consumes the anode, and causes the critical issues including low energy density, short cycle life, thermal runaway, risk of explosion hazards, cell's failure, etc.³ Thus, this film can also be penetrated by the growth of lithium dendrites (demonstrated in Fig. 3) and regrows by consuming more Li anode. The intimate relation between SEI and dendritic growth has been largely studied in the literature. To solve the issues, either the anode of Li-metal or the electrolytes were modified.⁴

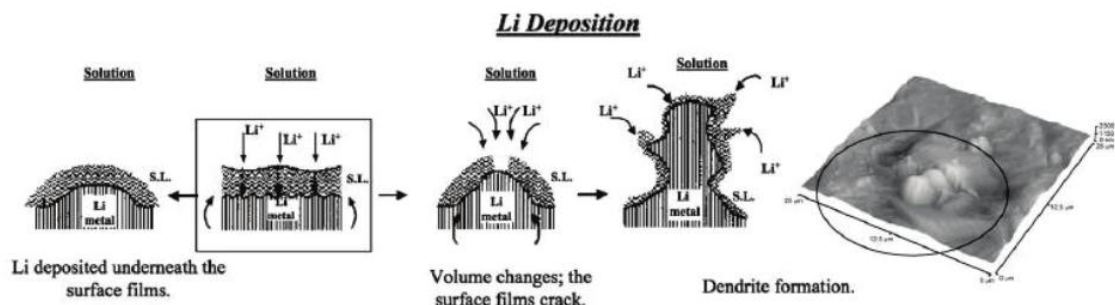


Fig. 3 The formation of lithium dendritic growth using an EC-DMC/LiPF₆ solution.⁵

In brief, the drawbacks of lithium metal batteries (LMBs) usually caused by the presence of unstable Li-metal in contact with the liquid-based electrolyte. Among many advancements for enhancing the safety issues of LMB, the appearance of lithium-ion batteries (LIBs) created an advanced step for energy storable devices.^{6,7} The inflammable organic solvents contained in conventional liquid electrolytes are the main reasons causing the critical damages such as chemical leakage, external heating, explosions, etc.. In this regard, the issues and challenges from electrolyte for LIBs and the new approaches using ionic liquid or conducting polymer-based electrolytes for future technologies will be mentioned in the next parts.

1.2. Lithium-ion batteries: issues and challenges from electrolyte aspect

Lithium-ion batteries (LIBs) have been the successful electrochemical power sources since their first commercialization in 1991 by Sony Inc.². In general, about 50 % of LIBs from the global battery market (in 2016) have been sold, in which 56 % were used for electric devices and mobile applications. Comparing to the other types of battery, LIBs provide high energy density, long lifetime, without the memory effects, low self-discharge, and existed in various shapes and sizes, as seen in Fig. 4.

Electrolyte does not determine the capacity (energy density or cyclability) but the safety, stability, and the current density of a system.⁸ The usable of electrode materials require high chemical stability of electrolyte since they are directly in contact with both electrodes. A basic electrolyte needs to be⁹:

- (i) chemically stable with the electrode materials during cell's operation,
- (ii) electrochemically stable with a large potential window,
- (iii) thermally stable: the melting and boiling points are higher than the operating temperature,
- (iv) high ionic conductivity, low cost, low toxicity, less impact from the synthesis process, and based on the abundant elements.

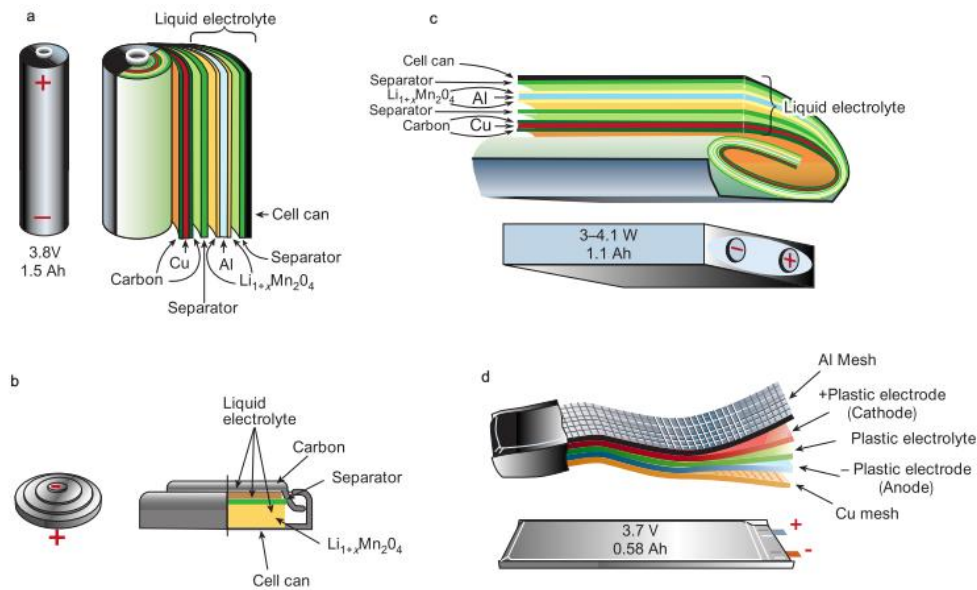


Fig. 4 The shapes, sizes and components of LIBs in cylindrical (a), coin (b), prismatic (c) and flat (d) form.¹

As seen in Fig. 5, during the discharge, Li^+ ions from the graphite anode migrate through the electrolyte and insert in the intercalation cathode material thus produces the energy. Otherwise, when the cell is charging, Li^+ ions from the positive electrode move through the electrolyte and remain in the opposite electrode. All along with these processes, electrons do not flow through the electrolyte but in the outer load. This technology helps to solve the growing of lithium dendritic during operation, which is the main issue of LMBs.

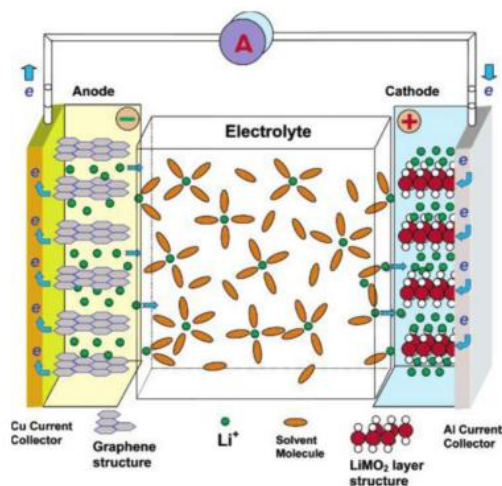


Fig. 5 Operation principle of rechargeable battery in discharge.

Electrolytes for LIBs are basically classified into 5 groups including the non-aqueous, aqueous, ionic liquid (IL), conducting polymer, and hybrid electrolyte, and most of the commercial LIBs are using the non-aqueous liquid electrolyte.

- **Liquid electrolytes**

Conventional non-aqueous liquid electrolyte is the mixture of lithium salt dissolved in organic solvents. In a LIB, the macro-porous separator impregnated with the electrolyte is sandwiched between two electrodes to prevent the short circuit and allow the migration of ions. This type of electrolyte offers many advantages due to the low-cost and high efficiency for ionic transport. The mixtures e.g. ethylene carbonate (EC), dimethyl carbonate (DMC), or ethyl methyl carbonate (EMC)/diethyl carbonate (DEC) ensures good ionic conductivity of the electrolyte, meanwhile the corrosion prevention of current collectors and the narrow electrochemical window causing by these solvents are still challenged.¹⁰ Commonly, the electrolyte consisted of lithium hexafluorophosphate (LiPF_6) in carbonate solvents is common in the commercial LIBs. Nevertheless, the demands of higher energy and safe electrolyte require new approaches for both lithium salts and organic solvents. Through which, the organic compounds contained high oxidation-potential fluorinated molecules become new nominees.

Although high ionic transfer in the liquid state, the safety issue of these electrolytes requires an improvement. The thermal runaway in LIB accompanies by a series of self-exothermic reactions, as described in Fig. 6 including the electrolyte oxidation, separator melt, SEI layer decomposition, electrodes breakdown, etc., and the flammability of organic solvents is an essential factor causing the critical damages.¹¹ The most common lithium salt used for conventional liquid electrolyte i.e. LiPF_6 is also unsafe due to its low thermal stability.

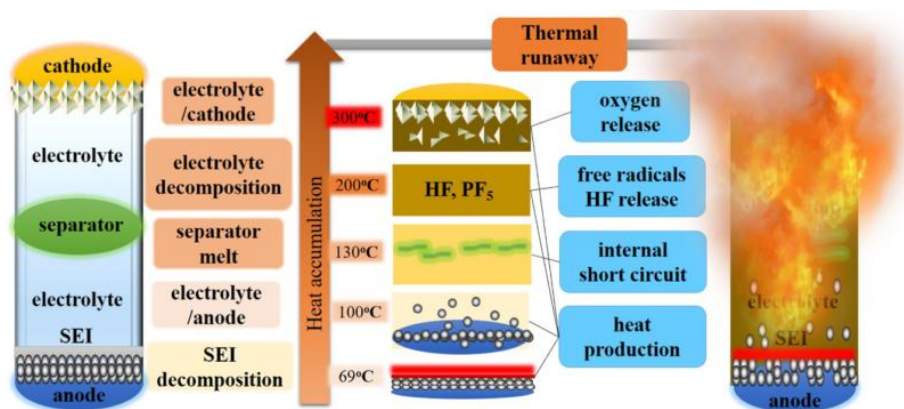


Fig. 6 The thermal runaway process in LIB.¹¹

For safer LIBs, the approaches of lithium salts and solvents aspects such as (i) using the stable lithium salts, (ii) adding the stabilizer additives, (iii) developing the non-flammable solvents, as well as (iv) using the polymer conducting materials have been widely carried out. Following, the advancements of non-flammable solvents such as using the ionic liquids for dissolving lithium salt or the polymer-based solid electrolytes will be further discussed.

2. Ionic liquid-based electrolytes

2.1. Introduction

The first ionic liquids (ILs) have been discovered by Paul Walden in 1914.¹² These molten salts (or molten oxides) compose of ions, that can be organic cations and organic/inorganic anions.¹³ During the 1990s, ILs having the melting point below 100 °C, usually called as ‘room temperature ionic liquids’ - RTILs, have been widely studied as green solvents for electrochemical applications.¹⁴ Various types of molten salt were investigated for energy storage due to the non-volatile, non-inflammable, and environmentally friendly characteristics, which were suitable for safer LIBs.¹⁵ ILs played the role of carbonate solvents in the liquid electrolyte for dissolving lithium salts and allowing the ions transfer between anode and cathode.¹⁶ They exhibit the liquid state in a wide range of temperatures, with negligible vapor pressure, and high thermal stability.¹⁷ The demand for high-security electrolyte makes ILs become one of the most promising solvents for future technology.¹⁸

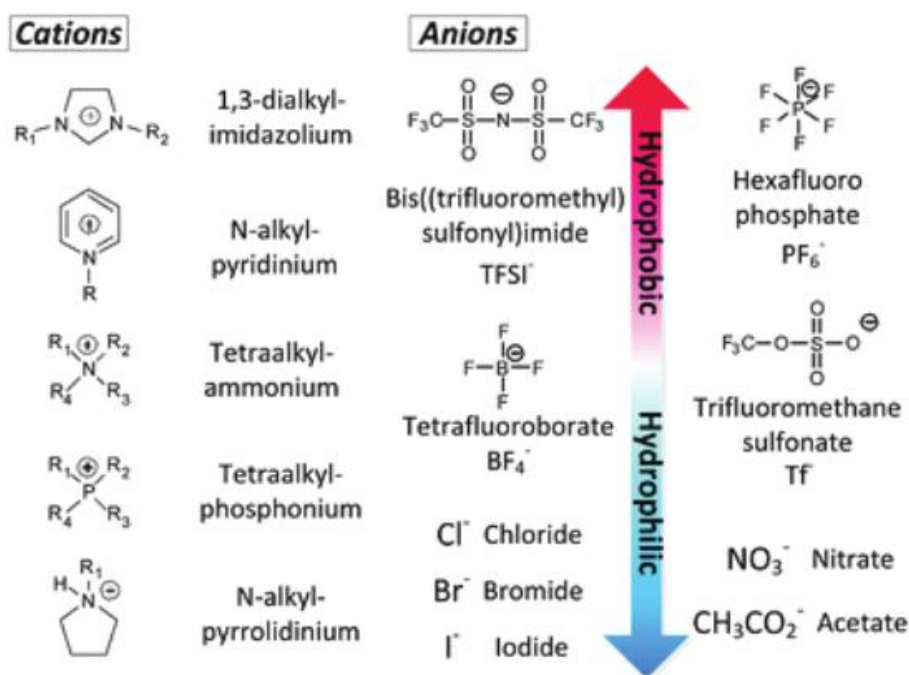


Fig. 7 Structure of several IL cations and anions commonly used in electrochemical.¹⁸

The common IL cations and anions used for electrochemical applications are presented in Fig. 7 including the organic cations e.g. imidazolium, pyridinium, alkylammonium, alkylphosphonium, alkylpyrrolidinium, etc., and a large choice from the inorganic anions e.g. the halides ([Cl⁻], [Br⁻], [I⁻]), [PF₆⁻], [NO₃⁻], [BF₄⁻], to the organic anions e.g. [TFSI⁻], [Tf⁻]. Based on the literature survey, the choice of IL anion/cation were explored in different systems, including Li-ion, Na-ion, Li-O₂ (air), Li-S, and Mg-ion batteries, etc.¹⁹ The physical/ electrochemical properties and therefore ionic

conductivity of IL-based electrolytes are very sensitive to the choice of cation and anion. In this regard, ILs' application usually depends on the system and its operated conditions.

Table 1 Several cation/anion combinations used for electrochemical application and their physical properties e.g. melting point (T_m), density (d), viscosity (η), conductivity (σ) at RT.²⁰

Cation 1-butyl-3-methyl imidazolium [BMIm⁺]

Anion	T_m (°C)	d (g.cm ⁻¹)	η (cP)	σ (S.cm ⁻¹)
BF ₄ ⁻	-82	1.17	233	0.17
PF ₆ ⁻	-8	1.36	312	0.14
CF ₃ SO ₃ ⁻	-40	1.21	73	0.32
CF ₃ SO ₂) ₂ N ⁻	-4	1.43	52	0.39

Anion bis(trifluoromethane)sulfonyl imide [TFSI⁻]

Cation	T_m (°C)	d (g.cm ⁻¹)	η (cP)	σ (S.cm ⁻¹)
1-methyl-3-methyl imidazolium	22	1.56	44	0.83
1-ethyl-3-methyl imidazolium	-3	1.52	34	0.88
1-ethyl-3-ethyl imidazolium	-4	1.43	52	0.39
1-isobutyl-3-methyl imidazolium	-30	1.43	83	0.26

The effect of cation/anion natures composed with 1-butyl-3-methyl imidazolium cation [BMIm⁺] or bis(trifluoromethane)sulfonyl imide anion [TFSI⁻] on physical properties of IL are presented in Table 1. A strong dependence of cation/anion nature influences the melting point, density, viscosity, and conductive properties of the neat ILs. As reported in the literature, ILs contained the organic cations, such as 1,3-dialkylimidazolium, tetraalkylammonium, phosphonium, trialkylsulfonium, with the soft anions i.e. (PF₆⁻), (BF₄⁻), (CF₃SO₃⁻), or [(CF₃SO₂)₂N⁻] were the promising candidates for electrochemical behaviors.^{21,22} The choice of IL displays an essential role for dissolving lithium salt, thermal stability, electrochemical behaviors, and the price of the resulted electrolytes. While the physical properties of the blends IL/salt have been investigated, the coordination shells and mechanism of conduction/ diffusion as a function of the coordinated cation were less reported. Investigating these behaviors is one of the main objectives of this work.

2.2. Physical and transport properties

Many factors can affect the properties of an IL including the combination of cation/anion nature, and its purity (the impurities content e.g. water or halides in IL).^{23,24} These properties were studied by a variety of techniques to measure thermal characteristics, viscosity, density, inter and intra molecular interaction (spectroscopy), ionic conductivity, self-diffusion coefficient, electrochemical stability, etc. Here, the essential physical and ionic transport properties of RTILs are discussed.

- **Thermal properties**

- a) *Degradation and melting temperature*

Most of RTIL used for energy storage has high thermal stabilities. The degradation temperatures (T_d) are usually higher than 400 °C, whatever the choice of cation/anion couple. However, the melting point (T_m) is dependent on IL structure, especially on the symmetry of cation, length of the alkyl chain, the charges distribution, as well as the anion nature.¹⁴

- b) *Glass transition temperature*

The glass transition temperature (T_g) is an important factor that assigns the mobility of the charge carriers. A low T_g induces high mobility of ions corresponding to high ionic conductivity. When the cation is asymmetric, the T_g value is rather low due to the increase of free volume.

- **Density**

Density of the RTILs is usually between 1 and 1.6 (g.cm⁻³).¹⁴ The length of alkyl chain and the anion/cation natures significantly influence IL density. The density also varies with the anion nature in an ascending order of $\text{BF}_4^- < \text{Cl}^- \approx \text{PF}_6^- < \text{CF}_3\text{SO}_3^- < (\text{CF}_3\text{SO}_2)_2\text{N}^-$, while the effect of cation is given by the order of pyrrolium > imidazolium > pyrrolidinium > quaternary ammonium.²⁵

- **Viscosity**

The biggest issue impeding diverse/various applications of ILs consists of the high viscosities, which prevent the mass transfer and ionic dissolution in IL. Viscosity of an IL is sensitive to the cation/anion natures, especially for the organic cations due to their large ionic size. A study of Bonhote et al.²¹ for the IL 1-alkyl-3methyl imidazolium TFSI, with the alkyl length of cation varied from methyl to butyl chain reported that viscosity decreased proportionally to the alkyl length. Thus, the anion gives also an effect on viscosity relating to the relative basicity and the possibility to form hydrogen bonds. The ILs based on small inorganic anions such as BF_4^- and PF_6^- are more viscous than the weakly basic TFSI⁻ anion, in which the charge delocalizes over the sulfoxide groups.²¹ Viscosity data are frequently presented as a function of temperature and are approximately fitted to the Vogel-Tammann-Fulcher (VTF) model.

- **Ionic conductivity**

Ionic conductivity is an essential factor for electrochemical applications. The conductivities of pure ILs are between 0.1 to 18 mS.cm⁻¹ at RT that are suitable for electrolyte behaviors. Moreover, the dissolution of salt in IL creates a ternary system which increasing the viscosity and reducing conductivity of the blend. The decrease of ionic conductivity is proportional to the salt concentration in IL. The evolution of conductivity with temperature follows a VTF model and shows an intimate correlation with the viscosity. For a given anion, conductivity of the organic cations vary in the order of 1-alkyl-3-methylimidazolium > N,N-dialkylpyrrolidinium > tetraalkylpyrrolidinium.²⁶ The study of M. Vranes et al.²⁷ about different physical properties of two ILs based TFSI i.e. 1-butyl-3-methylimidazolium [BMIm] and 1-butyl-3-methylpyrrolidinium [BMPyr] cations with [TFSI] anion, as a function of temperature showed that imidazolium-based IL exhibited lower density and viscosity than that of pyrrolidinium IL, and allowed higher ionic conductivity.

The ionicity of an IL is carried out by plotting the molar conductivity with the corresponded fluidity in the Walden plot. The diagrams of several imidazolium-based ILs are showed in Fig. 8.²⁸ The deviation from the reference line, which represents the data of a diluted solution of KCl, helps to determine a ‘good’ or ‘poor’ IL. In the ideal case of KCl, the ions are completely dissociated, and how far from this reference line, how low the ionic dissociation.

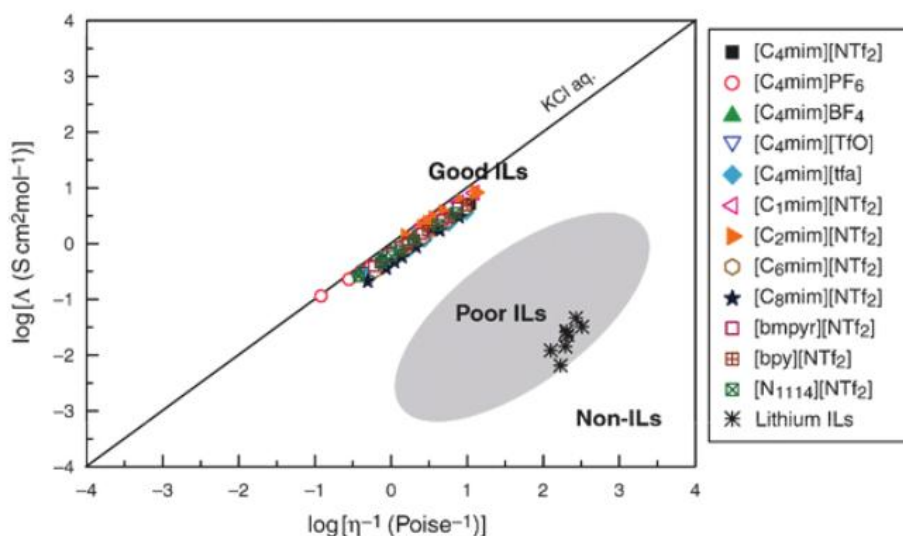


Fig. 8 Walden plot of several common RTILs represented the classification for ILs in term of ionicity.²⁸

- **Electrochemical stability window**

By definition, the electrochemical stability window is the range of potentials in which the electrolyte is neither reduced nor oxidized at the electrode surfaces. Most RTILs used for energy storages have wide electrochemical window, where the oxidation of anions occurs at high potential and the deposition of organic cations is found at lower voltage. Although the factors that can affect

the electrochemical stability of IL i.e. its purity, the tiny variation in anodic potential limit was found for several common anions, such as BF_4^- , PF_6^- , Tf^- , TFSI^- , etc.²⁵ Nevertheless, in the cathodic scan, the reduction potential was variable with the cation natures, for example: 1-alkyl-3-methylimidazolium cation was less stable in reduction than N,N-dialkylpyrrolidinium or tetraalkylpyrrolidinium cations.²⁹ The non-haloaluminate ILs usually show good electrochemical stability, usually in range of 4.5 to 6.0 V.

- **Cationic transference number**

Another factor of interest is the suitable ionic transport of IL-based electrolytes, especially the alkali cations for battery applications. In principle, the blend of x molar LiX salt dissolved in (1-x) molar of A^+X^- ionic liquid, forms a composition of $x\text{LiX} (1-x)\text{AX}$, and the Li transference number is calculated following this relation³⁰:

$$t_{\text{Li}} = \frac{x * u_{\text{Li}}}{x * u_{\text{Li}} + (1 - x) * u_{\text{A}} + u_{\text{X}}}$$

Where u_{Li} , u_{A^+} , u_{X^-} are the ionic mobility of Li^+ , cation A^+ , and anion X^- , respectively, t_{Li} is given by the ratio between lithium mobility and the mobility of total charge species in the blend. As a conclusion, Li transference number in ILs is lower than in organic solvents due to higher viscosity of IL.

- **Self - diffusion coefficient**

The fundamental characteristics including the degree of ionic association, diffusion coefficient, and ion-ion interaction have not been clarified in the literature. The ionic diffusion coefficient (D) presents the mass of a substance diffusing through a unit surface in a unit time. Diffusion process is depended on the molecular size of ions, its properties, temperature, and environmental pressure. In fact, two common methods, such as electrochemical and pulsed-gradient spin-echo nuclear magnetic resonance (PGF-NMR) were used to measure the diffusion coefficient of ILs. In most of the studies, the NMR was used as a noninvasive method, in which the self-diffusion coefficient of each charged species was measured separately.

However, the Coulombic attractive force in IL would associate the ions to form ion pairs or ion aggregates, and the equilibrium of attractive/repulsive interactions of ions, at a defined temperature, always kept the charged species in balance. Meanwhile, the NMR measurements can only detect a nucleus but cannot distinguish the ions and their associated forms. The D values obtained by NMR method are an average of self-diffusion coefficient of ions and their associated ions.³¹

The relationships between coefficient diffusion, viscosity, and ionic conductivity are investigated using the Nernst-Einstein equation. In 2006, the cationic transport number, $t^+ = D_{\text{cation}}/(D_{\text{cation}} + D_{\text{anion}})$, for the non-haloaluminate RTILs was found between 0.52 to 0.6 by Tokuda et al.³² This group also proved that the cations had higher diffusion coefficients than the anions at low temperature and approached at high temperature.

2.3. Lithiated electrolytes based on IL

Some RTILs can dissolved the lithium salts, which is an addition point for the green electrolytes of LIBs.¹⁴ Actually, for an overall IL study, the physical properties and conductivity behaviors of the neat ILs or the binary systems combined a dissolved salt in IL were observed as a function of temperature, salt concentration, IL cation/anion natures, or the operational conditions, etc.¹⁶ Moreover, some of them using the molecular dynamic (MD) simulation to further determine the solvated shells of coordinated cation i.e. Li^+ in IL. Here, a short literature review of the lithiated ILs for electrolyte aspect are reported.

The every first innovation in lithium batteries using imidazolium – TFSI ionic liquid with the LiTFSI salt as electrolyte has been reported in 1997.³³ After that, various studies using the binary system IL/lithium salt as electrolyte for LIBs showed good cycling stability. As investigated in the literature, the salt concentration dissolved in IL gives the direct impacts on IL physical, conductivity, and diffusivity properties, and changes the final performance of a battery. In fact, low salt concentration can be not sufficient for supplying the lithium ions in electrolyte, but higher concentration of salt caused a failure in conductivity related to higher viscosity obtained.

Followed J. Pitawala et al.³⁴, ionic conductivity of the binary system $[\text{Li}][\text{BMIm}][\text{TFSI}]$ decreases which increasing the salt concentration due to higher viscosity. These results fitted well to the VTF equation. The presence of salt augments the T_g and the T_g values increase with the amount of Li^+ doping. Thus, the solvation of Li^+ ion in TFSI-based IL was presented by J-C. Lassegues et al.³⁵ in 2006. In this work, the mixture of (1-x)1-ethyl-3-methylimidazolium bis(trifluoromethane) sulfonylimide $[\text{EMIm}][\text{TFSI}]$, and x LiTFSI were characterized by Raman spectroscopy at different concentration of Li^+ , below $x = 0.4$. They showed that intensity of the bands indicated the transoid conformers of TFSI⁻ (at 341 and 297 cm^{-1}) decreases with the evolution of x, and that the bidentates Li^+ coordinate with two oxygen atoms bounded to different sulfur atoms in the cisoid anion conformations at $x \sim 0.2$ to form $[\text{Li}(\text{TFSI})_2]^-$ complexes appear and increase.

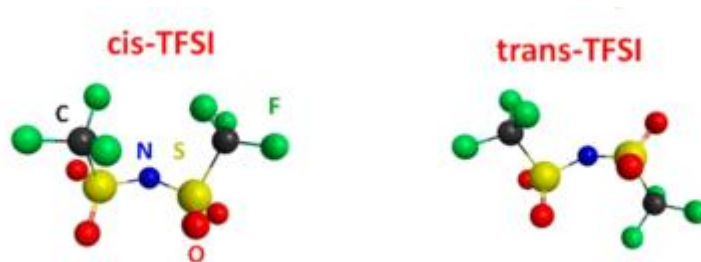


Fig. 9 A schematic of cisoid and transoid conformers of TFSI anions.³⁶

Later, S. Duluard et al.³⁷ studied the binary system $[\text{Li}][\text{BMIm}][\text{TFSI}]$ with the salt fraction $x < 0.2$, and showed that the transport properties decreased while increasing the value of x . In detail, all of the diffusion coefficients for Li^+ and IL cation/anion decreased significantly at high salt fraction (Fig. 10). Moreover, the lithium coordination numbers, determined from the Raman spectrum of the IL-based electrolytes, were about two anions for one Li^+ ion. The Li^+ was tetrahedrally coordinated to four oxygen atoms of different sulfur atoms of two anions and formed $[\text{Li}(\text{TFSI})_2]^-$ anionic cluster. While increasing the salt concentration may induct to the formation of bigger ionic cluster such as $[\text{Li}_m(\text{TFSI})_n]^{(n-m)-}$.

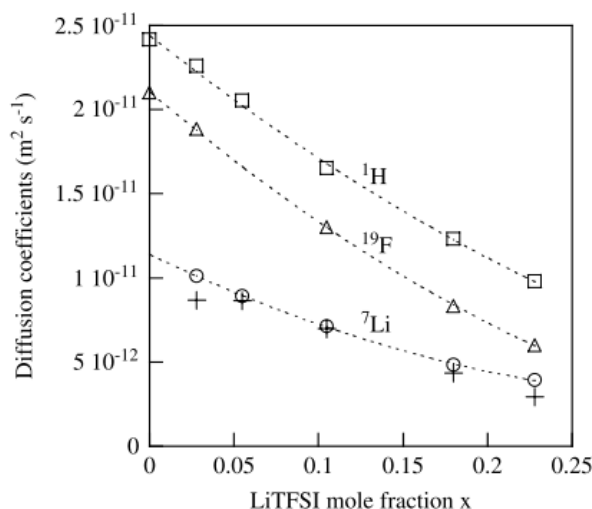


Fig. 10 The self-diffusion coefficient of proton, fluor, and lithium measured by PGSE-NMR for the blends of BMIm TFSI with LiTFSI as a function of salt concentration.³⁸

In 2010, A. Andriola et al.³⁹ studied the dissolution enthalpy of $[\text{Li}][\text{BMIm}][\text{TFSI}]$ system, using a ‘coffee-cup’ calorimeter, as described in Fig. 11. The salt LiTFSI was dissolved in IL using a magnetic stirring, and an isolated rubber on the top of the system. The temperature versus time was recorded at a constant pressure. They reported that the dissolution of LiTFSI in IL as solvent included three following processes: an endothermic breaking the attractions of LiTFSI salt, another endothermic breaking the attractions of IL ions and an exothermic related to the solvation process.

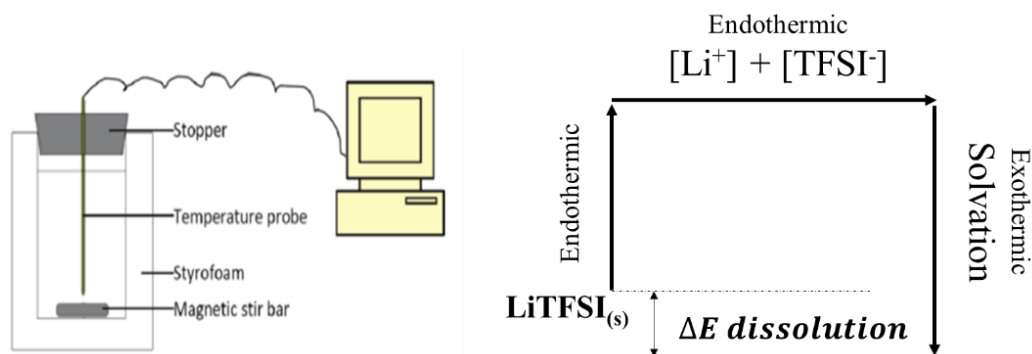


Fig. 11 Schematic view of a 'coffee-cup' calorimeter and the dissolution process of LiTFSI in BMIm TFSI.³⁹

As considered, the solute LiTFSI and solvent share the same anion and that the Li^+ ions are solvated by only the $[\text{TFSI}]^-$ anions. A value of $-18.07 \text{ kJ}\cdot\text{mol}^{-1}$ of dissolution enthalpy indicated that solvation enthalpy of Li^+ was higher than the crystal lattice enthalpy of LiTFSI meaning that each Li^+ ion can be solvated by multiple $[\text{TFSI}]^-$ anions to form the $[\text{Li}(\text{TFSI})_2]^-$, $[\text{Li}(\text{TFSI})_3]^{2-}$ or $[\text{Li}(\text{TFSI})_4]^{3-}$ complexes. At low concentration of salt, the anionic cluster $[\text{Li}(\text{TFSI})_2]^-$ seems to dominate in the blend IL/salt.

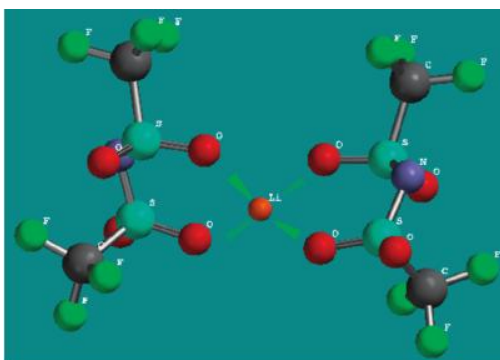


Fig. 12 Schematic structure of $[\text{Li}(\text{TFSI})_2]^-$ complexes where Li^+ is solvated by two different $[\text{TFSI}]^-$ anions.³⁹

By both experimental and MD simulations, J-C. Lassegues et al.⁴⁰ proved that not only in EMIm TFSI but also in the longer alkyl chain such as: BMIm TFSI and BMMIm TFSI doped LiTFSI, from low to medium Li^+ concentration (under $x = 0.2$), the presence of $[\text{Li}(\text{TFSI})_2]^-$ complexes is confirmed⁴⁰. At higher concentration, the formation of $[\text{Li}_m(\text{TFSI})_n]^{(n-m)-}$ aggregates with $n = 2m - 1$ were suggested. However, these aggregates provided the challenges to identify due to the limit of the IR and Raman spectroscopies.

The coordination of Li^+ with TFSI⁻, studied by H. Liu et al.⁴¹, showed that each Li^+ was coordinated with four oxygen atoms from different anions. At low molar fraction of lithium, the oxygen atoms from three TFSI⁻ ions (two monodentate and one bidentate) coordinated with Li^+ to form the $[\text{Li}(\text{TFSI})_3]^{2-}$ complexes. When increasing the concentration of lithium, about four anions were found around each Li^+ , which came from four monodentate TFSI⁻ anions. These rigid

structures limited the mobility of all charged species and led to the low diffusivity/conductivity of the combinations.

In brief, the coordination number of anions in the TFSI-based alkyl-imidazolium ILs changes with the lithium concentration. The Li^+ ion was coordinated with at least four oxygen atoms from different TFSI⁻ anions.³⁸ The aggregation of two lithium atoms with three anions was observed at low temperature and could be stable up to ten nanoseconds.⁴² Its presence increases the viscosity and results in a decrease of conductivity. However, the self-diffusion coefficients measured by PFG-NMR are not completely linked to the mobility of complexes but also the free ions and the aggregates, because this technique cannot distinguish the difference between them.

2.4. Ionic liquid doped alkali/alkaline-earth elements

While the blend of RTIL and a lithium salt are largely studied by both experimental techniques and MD simulation in the literature, the researches of IL doped with the alkali/alkaline-earth cations were rarely reported. Some of the studies investigated the complexes of Na^+ ion^{43,18}, and rarely for Mg^{2+} ion⁴⁴ in TFSI-based ILs. However, the understanding of the series of alkali/alkaline-earth metals such as potassium (K^+), Cesium (Cs^+), Calcium (Ca^{2+}) are still restricted. Besides the first appearance of Na-ion batteries (SIBs) in the 1970s, batteries based on the abundant elements will dominate the renewable energy aspect in the near future, and the approaches for lithium-based electrolytes can be applied to these new technologies. The recent studies about the effect of alkali/alkaline-earth cations on physical and transport properties of RTILs are resumed.

One among the promising candidates, against the use of lithium for battery applications, is its neighbor sodium. Having the very similar chemical properties, the Na-based ILs are expected to inherit all of the advances and characteristics of the Li-based ILs including the physical properties, conductive/diffusivity processes, solvation shell, ionic dissociation, performance, etc. A. Andriola et al.³⁹ studied the two systems $[\text{Li or Na}][\text{BMIm}][\text{TFSI}]$ with increasing the salt concentration, and showed that viscosity increased significantly with the amount of salt dissolved in IL. Moreover, the relative viscosity of Na-based IL was higher than Li composition, at the same temperature. They also noticed that conductivity of the lithiated ILs were higher than the Na-based IL, at over 0.1 mol/L as dissolved salt concentration, see Fig. 13.

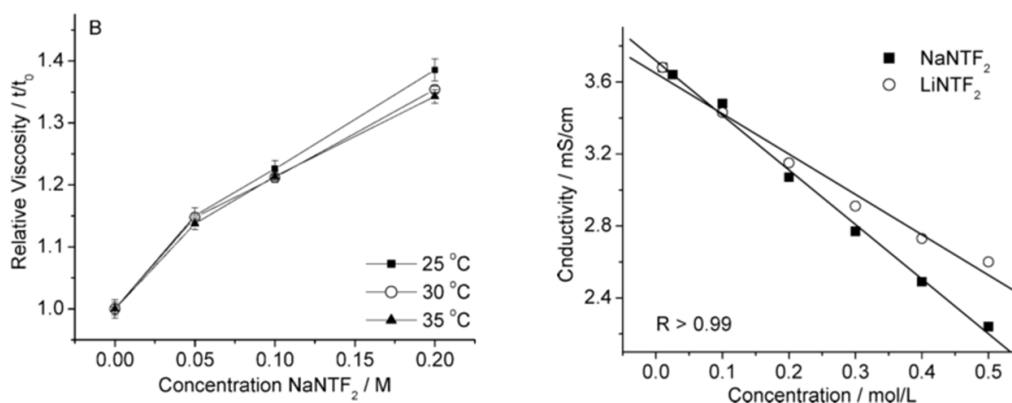


Fig. 13 Relative viscosity at various temperature and ionic conductivity versus NaTFSI concentration in a binary system of $[\text{Na}][\text{BMIm}][\text{TFSI}]$.³⁹

The issues of the blends of Li or Na coordinated in $\text{P}_{1224}\text{PF}_6$ and $\text{C}_3\text{mpyrFSI}$, reported by F. Chen et al.⁴⁵ were caused by the solubility of salt in IL, and the increase of viscosity with salt concentration resulting in the proportionally decrease of ionic conductivity. The alkali transference number increased while increasing the salt concentration. Comparing two alkali systems, the charged carriers in the lithiated ILs diffused faster than those of the Na-based ILs. The diffusion of alkali cations was less influenced by the salt concentration than the organic cations or anions of ILs.

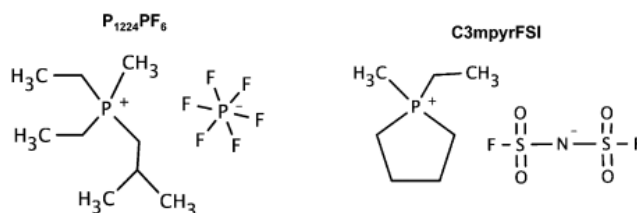


Fig. 14 Chemical structures of $\text{P}_{1224}\text{PF}_6$ and $\text{C}_3\text{mpyrFSI}$.⁴⁵

From an experimental point of view, the self-diffusion coefficient of ^{23}Na , which is an essential factor to determine the Na transference number in IL, was not measurable by PFG-NMR due to the limit of chemical shift and line width evolution with Na^+ concentration and temperature, followed H. Yoon et al.⁴⁶ The work of M. Hilder et al.⁴⁷ reported that transference number of Na^+ ion in the FSI-based ILs, determined by Bruce Vincent method, was around 0.3 to 0.4. Moreover, N. Wongittharom et al.⁴⁸ have successfully studied the mixture of various Na salts in Pyr TFSI using as electrolytes in a sodium metal battery with the NaFePO_4 cathode, operated at high temperature. Later the $[\text{Na}][\text{C}_3\text{C}_1\text{Pyr}][\text{FSA}]$ system studied by C. Ding et al.⁴⁹ showed the promising characteristics in terms of viscosity and ionic conductivity for electrolyte applications with about 60 % molar of sodium salt dissolved in IL.

The studies about the interaction/coordination between Na^+ ions and TFSI $^-$ anions proved that the coordination number of anions surrounded was about 2 or 3 and depending on the molar fraction of Na^+ , and the suggested complex structure was $[\text{Na}(\text{TFSI})_n]^{n-1}$.⁵⁰ Like lithium, each sodium atom

was surrounded by at less four oxygen atoms from different TFSI anions. However, the $[\text{Na}(\text{TFSI})_3]^{2-}$ complexes (Fig. 15) was found to dominate in the $\text{Na}_x\text{BIm}_{(1-x)}\text{TFSI}$ electrolyte, at $x < 0.2$.⁵¹

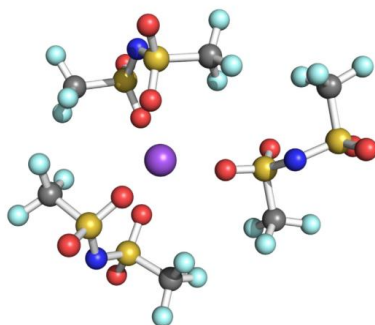


Fig. 15 The structure for $[\text{Na}(\text{TFSI})_3]^{2-}$ complexes from the DFT calculations. Atom's color code: sodium (violet), carbon (cyan), nitrogen (blue), oxygen (red), fluorine (cyan), and sulfur (yellow).⁵¹

Recently, J.M. Vincent-Luna et al.⁵² studied two alkali systems e.g. LiTFSI and NaTFSI in C_4PYR TFSI by MD simulation, and reported that the motion of mobile ions hid the conductive behavior, related to the formation of alkali clusters in IL. The Na^+ complexes were bulkier than the Li^+ one, inducing lower mobility. The MD atomistic scale and ab initio MD simulations, used to calculate the radial distribution functions (RDF) between different ion species, gave rather similar results of $g(r)$ for both Li^+ and Na^+ . The binding energies as a function of cluster were comparable for both alkali systems, and more stable for the Li^+ one.

In another point of view, the fast-growing technologies for magnesium-ion battery are requiring the new satisfying studies for IL-based electrolytes. The most outstanding is how to clarify the mechanism of conduction/diffusion of the multi-valences ions in IL. However, the coordination structures of Mg^{2+} in TFSI-based IL are complicated. Regarding the electrochemistry of magnesium in EMIm TFSI, Fuller et al.⁵³ pointed out that this metal was thermodynamically unstable in IL due to the irreversible Mg plating/stripping in electrolyte environment. The common anions such as BF_4^- or TFSI⁻ had strong coordination with the Mg^{2+} ion which prevent the oxidation/reduction of Mg^{2+}/Mg couple, followed G. Vardar et al.⁵⁴. From this point of view, the combinations of TFSI-based ILs with the Grignard reagents reported by G.T. Cheek et al.⁵⁵ could overcome this issue. However, the transport properties of Mg^{2+} in IL was restrained by a limit of studies in this aspect. Recently, G.A. Giffin et al.⁵⁶ observed the coordination spheres of TFSI anion with Li, Na, Mg (band at 740cm^{-1}) by Raman spectroscopy, and reported that Mg had three coordination spheres e.g. the contact ion pairs (bidentate coordination of one Mg^{2+} by one TFSI), bridging TFSI, and free TFSI. The number of coordination was about three to four TFSI per one Mg^{2+} , and exchanged rapidly between the neighbor complexes, whereas the Li and Na were surrounded by four TFSI⁻ at low concentration of salt, and by two TFSI⁻ while increasing the salt

content. The number of surrounded anions decreased when increasing the cation concentration. Fig. 16a presents a tetrahedral coordinated Mg^{2+} coordinated by two bidentate TFSI⁻ anions. Especially, the presence of a neighbor magnesium atom instantly increases the number of coordinated TFSI⁻ anions from five to seven (Fig. 16 c,d).

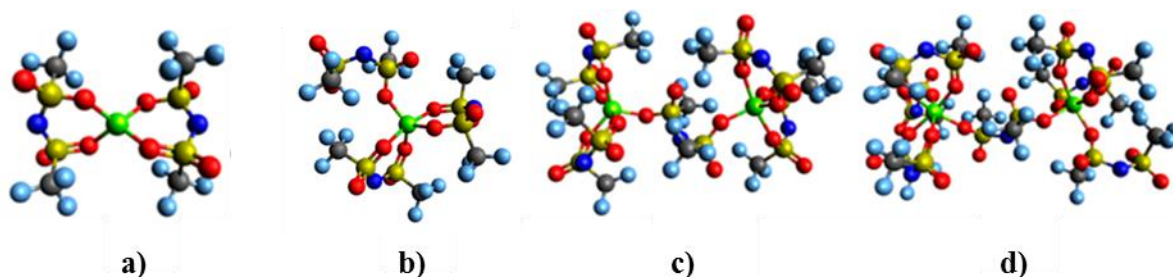


Fig. 16 Several suggest structures of coordinated Mg^{2+} ions in TFSI based IL. a) $Mg(TFSI)_2$; b) $[Mg(TFSI)_3]$; c) $[Mg_2(TFSI)_5]$; d) $[Mg_2(TFSI)_7]^{3-}$. Atom's color code: magnesium (green), carbon (grey), nitrogen (blue), hydrogen (white), oxygen (red), fluorine (green), and sulfur (yellow).⁵⁶

As a conclusion from this short bibliography, to better understand the effect of salt concentration and coordinated cation nature on IL properties, the additional studies are requiring. The interaction between different alkali/alkaline-earth metals and IL ions are further investigated. These electrolytes are expected to overcome the security issue of conventional liquid electrolytes using carbonate solvents, and to advance the future rechargeable batteries beyond lithium. However, besides the advantages in term of security, electrolyte leakage, and (or) internal short circuit during operation which are usually caused by the liquid electrolytes are still challenged. To enhance the safety of battery devices, the approaches using solid conducting polymer as electrolyte for lithium battery will be discussed in the following part.

3. Solid polymer electrolyte

The first polymer electrolytes (PEs) were discovered by Wright in 1973, and their applications in electrochemical technologies were developed after one decade.⁵⁷ PEs are the multi-functional films, which create the favorable conditions for ionic migration as electrolyte, and are used as separator to prevent the internal short circuit. Using the PEs helps to eliminate the leakage of electrolyte, which is a main reason causing the thermal instability of the batteries? Moreover, these solid films exhibit the excellent properties such as good mechanical strength, flexible, and easy to design in various shapes and sizes. Beside these impressive advantages, PEs also provide the possibility to use lithium metal, which is an ideal anode material for higher density capacity due to the lower reactivity of PE with lithium metal.⁵⁸ PE for lithium polymer batteries (LPBs) consists of a dissolved lithium salt in one or many polymer hosts e.g. poly(ethylene oxide) - PEO,

poly(vinylidene fluoride) –PVdF, poly(acrylonitrile) – PAN, poly(methyl methacrylate) – PMMA or poly(vinylidene fluoride-hexafluoro propylene) – PVdF-HFP, etc.⁵⁹

3.1. Lithium salts

The development of LIBs in the 1980s were limited to the choice of few anions including hexafluoroarsenate (AsF_6^-), perchlorate (ClO_4^-), hexafluorophosphate (PF_6^-), tetrafluoroborate (BF_4^-), and triflate (CF_3SO_3^-), (see Fig. 17). A good lithium salt for electrolyte should have high ionic dissolution and dissociation in solvents, high thermal and electrochemical stability, less toxic, less corrosive, and low-cost. The LiPF_6 and LiBF_4 are the most popular lithium salts for LIBs. The electrolytes of LiPF_6 or LiBF_4 dissolved in carbonate solvents can form the SEI on the graphite anode. Besides, the design of several anions was inspired to improve the thermal and conductivity properties of lithium salt. The large complex anions contained the sulfonyl groups were largely synthesized such as the CF_3SO_3^- (Tf)^{60,61}, or the bis(trifluoromethanesulfonyl)imide (TFSI)^{62,63} anions due to higher thermal/electrochemical properties, and less toxic. These anions have also the high delocalized charge distribution which can provide better stabilization comparing to the other anions.⁶²

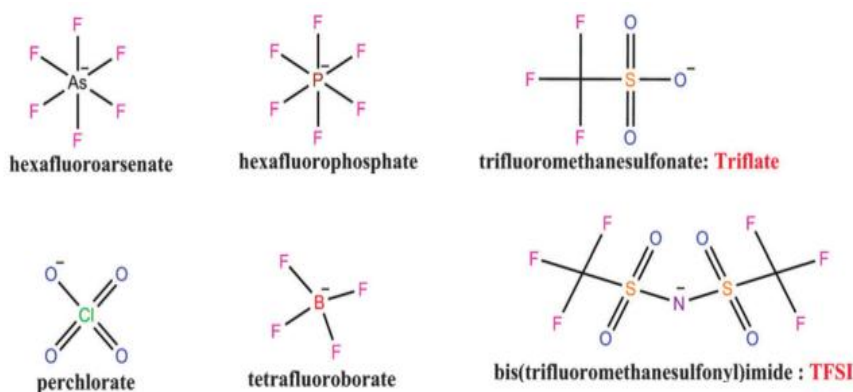


Fig. 17 Chemical structures of several simple anions for lithium salts.¹²

3.2. PEO-based electrolyte

3.2.1. Complexes of PEO and lithium salt

- Mechanism conduction of Li^+ in PEO

The PEO-based electrolytes are the most extensive studies for LPBs since the first complexes of PEO with the alkali metals were discovered in 1973.⁵⁷ Later, M. Armand et al.⁶⁴ proposed the use of the blends PEO/salt as solid electrolytes for lithium metal batteries, and published their first study on PEO-based electrolytes in 1987.⁶⁵ The PEO is a semi-crystalline polymer with the melting point at about 66°C, and the glass transition temperature of -60°C. The advantageously characteristics combine (i) the ability to dissolve a variety of lithium salts, (ii) an acceptable

stability versus the Li-metal, (iii) an electrochemical anodic stability up to roughly 3.9 V vs. Li⁺/Li. The ethylene oxide unit of PEO exhibits high donor number for Li⁺, hence produces the complexation and ionic dissociation, and promotes the ionic conduction inside the polymer matrix.⁶⁶

On the other hand, PEO-based PE drawback consists of (i) poor conductivities below the melting temperature, and (ii) poor mechanical strength above the melting of polymer (in the operating temperature range of LPBs). The low conductivity related to the Li⁺ conduction mechanism, and the semi-crystalline nature of PEO (PEO is crystallized to 75 – 80 % at RT)⁶⁷, but the conduction process occurs essentially in the amorphous phase via the segmental motion of the Li⁺ coordinating polymer chains.^{66,67,70} The schematic of Li⁺ motion in PEO matrix is presented in Fig. 18. The mechanism of Li⁺ conduction is a solvation/de-solvation process where Li⁺ is complexed by the ether oxygen atoms. The cation can jump between the neighboring coordinating sites in high molecular weight polymer by forming the non-labile bonds with the ether oxygen atoms.⁷¹

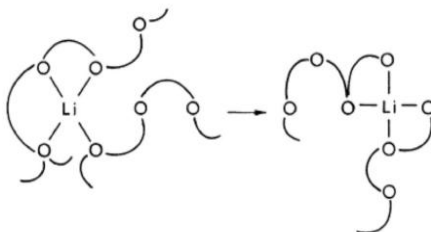


Fig. 18 Schema of Li⁺ motion in a polymer host⁷¹

The crystalline phase of PEO contributes to the mechanical strength, and is poorly conducting even in the most favorable cases, due to the high energy barrier for Li⁺ transport, and the required cooperative motion of Li⁺ between the preferred sites.^{72,73,74} Fig. 19 illustrates the morphologies of a semi-crystalline matrix and the Li⁺ conduction in amorphous and crystalline phases of PEO. The lithium conduction depends on chain mobility, high mobility results good ionic conductivity but poor mechanical properties.

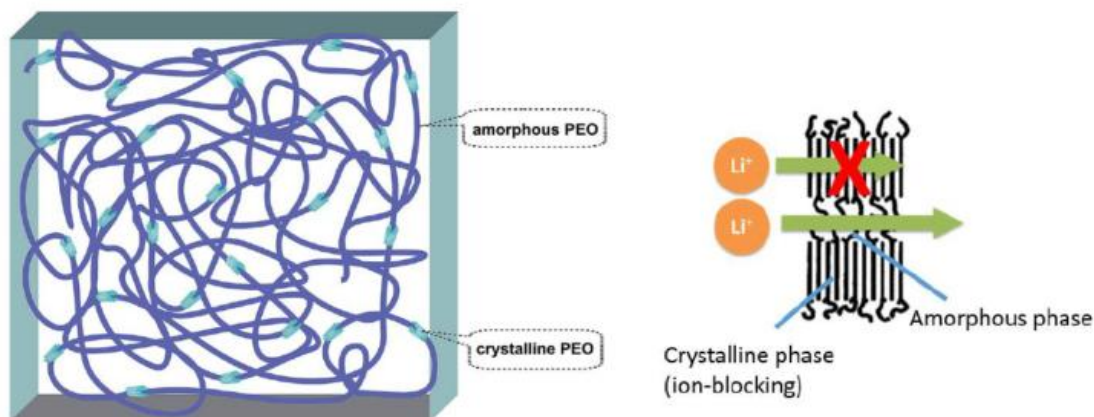


Fig. 19 Morphologies of semi-crystalline PEO and schematic representation of Li⁺ conduction in PEO.⁷⁵

- Anion nature and salt concentration

From the literature, various types of lithium salts have been investigated for LPBs, such as the LiPF₆, LiBF₄, LiClO₄, LiCF₃SO₃ (LiTf), LiTFSI, LiN(SO₂C₂F₅)₂ (LiBETI), etc.. Among these lithium salts, the LiTf or LiTFSI presented in most of studies for LPBs due to the high flexibility of sulfonyl groups, that helps to reduce the crystallinity of the PEO matrix (plasticizing effect). The low interaction between cation and anion due to the high-delocalized charge distribution of anion increases the dissociation and complexation of Li⁺ with the ether oxygen atoms. For example, ionic conductivity of the blend PEO/LiTFSI (EO/Li = 20) reported by M. Marzantowicz et al.⁷⁶ was about 10⁻³ S.cm⁻¹ at 80 °C, which was higher than the blend PEO/LiPF₆ (10⁻⁴ S.cm⁻¹)⁷⁷, and PEO/LiBETI (6.1 x 10⁻⁴ S.cm⁻¹)⁷⁸ at the same EO/Li ratio. Noted, the EO/Li ratio determined by the number of EO units per one Li⁺, which usually uses to represent the concentration of Li in PEO. However, low conductivity before the melting of polymer combines with the low cationic transport number (about 0.1 for TFSI⁷⁹ and 0.4 for Tf-based PEO⁸⁰) in different polyether networks restraint the application of these electrolytes.

In brief, many approaches have been proposed to improve the conductivity of PEO-based electrolytes, largely by decreasing the glass transition ability and preventing crystallization of the electrolyte to enhance the ionic conductivity at low temperatures, *e.g.* (i) by adding materials that can interact with the PEO and hinder the crystallization ability (nanoparticle charge, liquid or solid plasticizer, etc.)⁸¹, and (ii) by modification of the polymer matrix by copolymerization or by crosslinking. The common plasticizers such as succinonitrile, ether solution, carbonate, and even ionic liquids were added to reduce the crystallization of polymer and maintain the amorphous phases which products better ionic conductivity.⁸¹ The concentration of salt gives a significant impact on ionic conductivity of the PEO-based electrolytes by reducing the crystallinity of polymer. However, these effects are mostly dependent on the anion structure, its size, and its delocalization of the negative charge. The ion solvation occurs when the lattice energy of salt and the cohesive energy of polymer are overcompensated by the solvation energy of polymer-ion complexes, and the salts with low lattice energy are favorable for ion complexation. This energy depends on the interaction between lithium and anion (roughly scaling with the acidity of the conjugate acid of the anion), and the lithium salts contained large and soft anion, including electron withdrawing groups for extensive delocalization of electric charge such as LiTFSI, have been widely using.⁷²

- PEO with better conductivities at RT and mechanical properties

The low conductivity of linear PEO, below the melting point, is linked to the crystallinity, and the low segmental mobility of polymer chain. Many approaches have been developed to obtain the

amorphous polymer with low T_g (lower the T_g value, higher the mobility at a given temperature above the T_g). To realize that, the modified PEO have been synthesized, and different chemical architectures were reported during the last two decades. The main trend was to design the modified PEO with the introduction of different moieties that may disrupt the regularity of PEO segments, and decreased the ability to crystallize. The most common routes were the statistical copolymers, branched polymers (i.e. comb shape, stars shaped PEO, cross-linked PEO), block copolymers, etc. As a result, the mechanical strength of polymer electrolytes can be improved by cross-linking, or by adding the reinforced nano-fillers.

- Statistical copolymers

Since the linear PEO is very crystalline, even with the presence of lithium salt, the linear statistical copolymers have been prepared to disrupt the regularity of the repeating units, and get the amorphous polymer with higher conductivity at RT. In particular, the first report dealt with the including of short poly(dimethylsiloxane) fragment in linear PEO, poly(dimethylsiloxane-co-ethylene oxide). This material significantly improved the conductivities at low temperature due to the lowering of both crystalline fraction and T_g of the copolymers.⁸² This electrolyte reached $2.6 \times 10^{-4} \text{ S cm}^{-1}$ at RT.⁸³

- Cross-linking

Cross-linking is an effective way to limit the polymer chain rearrangement and suppress or significantly decrease the crystallinity degree of linear PEO. However, in a 3D network, the polymer segmental mobility decreases respecting to a linear polymer matrix, and resulting in a decrease of conductivity (a concomitant increase of mechanical properties). Nevertheless, the extent largely depends on the nature of the cross-linked chemical groups, as well as the cross-linked degree. Some examples of cross-linked PEO networks obtained by different approaches are cited below.

J. F. LeNest, and M. Mastragostino et al. designed a PEO network by the polycondensation of a 'di' or 'tri' functional monomers such as triisocyanate⁸⁴⁻⁸⁶, triphenylisocyanate⁸⁷, and polyether glycol. Next, Kim et al.⁸⁸ synthesized the phosphate-polyether networks using a crosslinking agent, i.e. phosphorus oxychloride (POCl_3), with poly(ethylene glycol)/poly(tetramethylene glycol) (PEG/PTMG) (70/30) copolymers. Another approach was to prepare the films forming macromonomers, as precursor for a 3D network, with moderate molecular weight bearing cross-linkable functions such as double or triple-bonds, that were then polymerized by different methods (i.e. UV irradiation, thermally, or with an external reactant)⁸⁹. The pre-polymers were either prepared by polycondensation of Jeffamines® with terephthalic acid⁹⁰ of polyethylene glycol⁹¹, or by ring-opening copolymerization of oxiranes⁹². As compared to the polymer electrolyte based on

linear PEO, the storage modulus (E') of cross-linked polymer electrolytes generally range between 1 and 10 MPa on the rubbery plateau (i.e. above the melting point), while PEO electrolytes generally started to creep upon melting. However, the higher the storage modulus, lower the conductivity since they are interrelated via chain segmental mobility.

The recent interesting approach reported by Thiam et al.⁹³ are illustrated in Fig. 20a. The macromonomer obtained by polycondensation of 3-chloro-2-chloromethyl-1-propene and polyethylene glycol (MW=1000 g/mol) included the regularly spaced pending C=C double bonds as the crosslinking functional groups. The polycondensate consisted in partially hydrogenating the double bonds to optimize the cross-linking degree of the resulting electrolytes, while maintaining a non EO unit to disrupt the regularity of linear PEO segments, and thereby affect crystallinity at low cross-linking density (Fig. 20 b,c). By hydrogenation of ca. 75 % of double bonds, an amorphous polymer electrolyte obtained with a conductivity of $5 \times 10^{-5} \text{ S cm}^{-1}$ at 20 °C, which is 10 times higher than that of linear polymer. However, at 60 °C the conductivity reached similar values to that of linear PEO-based electrolytes (Fig. 20b), with a storage modulus of about 1 MPa.

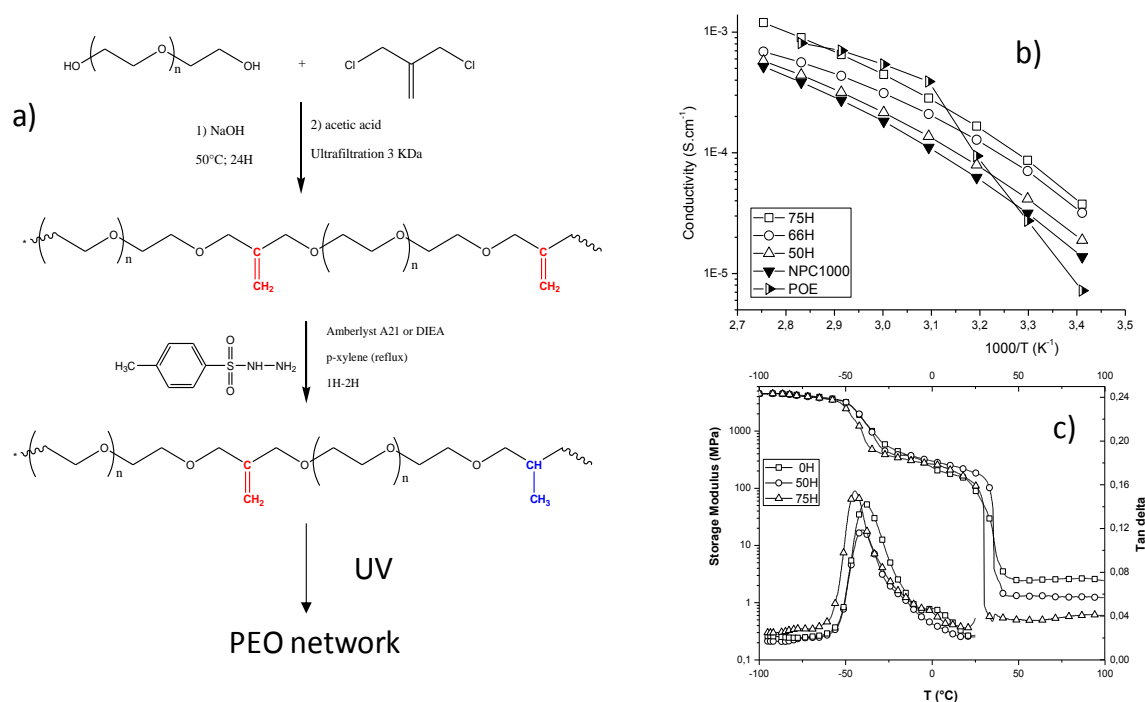


Fig. 20 (a) Synthesis of an amorphous PEO network in three steps including (i) synthesis of PC1000 by polycondensation of polyethylene glycol 1000 g mol⁻¹ with diethylether, 3-chloro-2-chloromethyl-1-propene; (ii) partial hydrogenation of double bonds (iii) crosslinking of the residual double bonds by UV irradiation; (b) Ionic conductivities of electrolytes based on the PEO networks (xH representing % double bonds hydrogenated), EO/Li=20; (c). Storage modulus and tan δ versus temperature of hydrogenated.⁹³

- Nano crystals cellulose reinforced polymer

Cellulose is the extracted product from the cell wall of green plants or marine animals. This semi-crystalline polymer are used due to the low-cost, non-toxic, and multi-function characteristics. The chemical structure in Fig. 21 shows that cellulose is a linear homo-polymer. The repeating units are linked by condensation of free OH functions, and continue throughout the macromolecular chain. Cellulose is colorless and insoluble in most of organic solvents and water. The pure cellulose extracted directly from nature often requires a treatments prior use. These whisker products, under various sizes such as cellulose microfibrils (MFC), microcrystalline cellulose (MCC), and nanocrystalline cellulose (NCC) are used for different purposes.

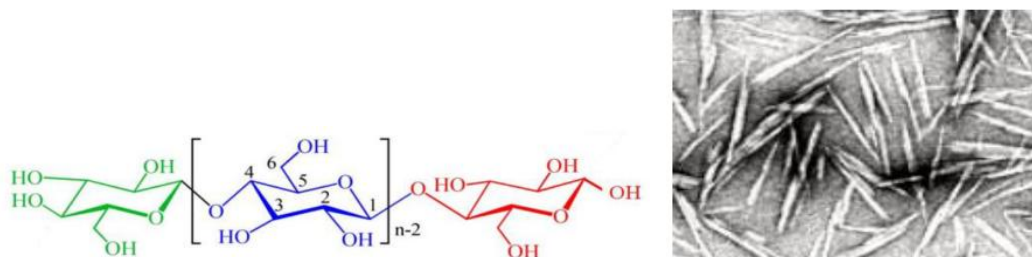


Fig. 21 Chemical structure and microscopy image of cellulose.

Recently, the demands of nano crystals fillers including cellulose, chitin, and starch as reinforcing agents in polymer matrixes has been advanced.^{94,95,96} The reinforced composite polymers displayed good mechanical properties even at low whiskers content due to the strong interactions of hydrogen bonds between the unit whiskers.⁹⁷ Many types of polymers reinforced with NCC were studied for all-solid-state battery, especially for the PEO-based electrolytes. The main advantage of whiskers is to maintain the polymer's mechanical properties (above the melting point) without a strong detrimental decrease of ionic conductivity at low whiskers content.⁹⁷

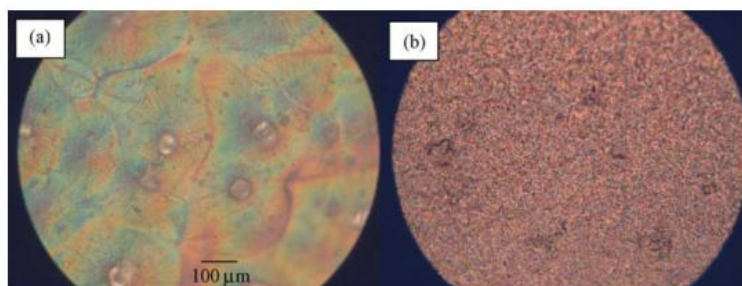


Fig. 22 Optical microscopy of unfilled PEO (a) and PEO reinforced 13.3 w.t.% whisker (b)⁹⁸

Later, the effects of low whiskers content of 6 wt.% in the blends of PEO/LiTFSI at different EO/Li ratio has been studied by M.A.S. Azizi Samir et al.⁹⁸. The report confirmed an independent role of whiskers on the phase transition temperatures, and the mobility of polymer matrix at low

concentration of salt. The crystallization phenomenon was dominated by the interactions between PEO and LiTFSI. However, the presence of 10 wt.% nano whiskers caused a significantly reduction of ionic conductivity for the blend PEO/LiTFSI (at EO/Li = 30) from about 10^{-3} to 3×10^{-4} S.cm⁻¹, at 90°C, which was explained by the interactions between cellulose and other components (PEO and LiTFSI), and the low dielectric constant of cellulosic charges. The impact of NCC on cross-linked PEO doped with LiTFSI was also investigated. The NCC content had no critical effect on the mechanism of conduction of Li⁺, and the cross-linking density dominated the decrease of conductivity. In brief, a homogenous dispersion of whiskers provided the high reinforced effect for the cross-linked matrix.

3.2.2. Complexes of PEO with several alkali/alkaline-earth metals

The complexes of alkali metals in PEO matrix have been firstly reported by D.E. Fenton et al.⁵⁷. These blends of PEO/alkali salt exhibit the promising RT conductivity of 10^{-5} S.cm⁻¹.⁹⁹ The ionic conduction/diffusion in polymer matrix depends on the solvation of cation by the ether oxygen atoms. The coordination numbers (CN) of alkali ions in amorphous PEO increases proportionally with the cation surface. In terms of EO units per cation for the alkali-based thiocyanates salts complexed in PEO, the CN values were 1 for Li⁺, 2 for Na⁺, 3 for K⁺, 5 for Rb⁺, and 7 for Cs⁺.¹⁰⁰ The anion nature gave also the significant effects on ionic conductivity.¹⁰¹ In 1992, Sesner et al.¹⁰² studied the effect of anion polarization on conductivity behavior of PEO complexed with the alkali-based triflate or thiocyanate salts, and reported that the strong coupling between anion and cation mobilities influenced on the conductive behavior as a function of cation size.

The report of conductivity for different alkali-based AsF₆ with temperature (Fig. 23) showed that PEO₈:NaAsF₆ exhibited the highest conductivity among the studied systems with the change of slope at RT for the Arrhenius plots.

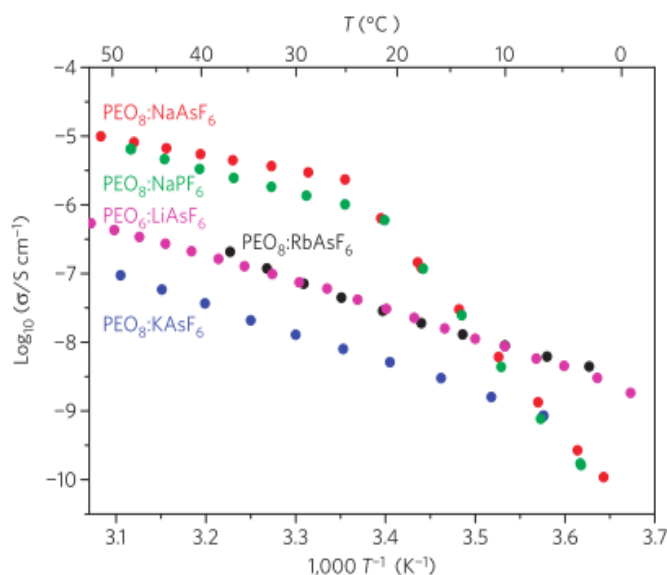


Fig. 23 Conductivity of 8:1 complexes of PEO (methoxy end-capped, M_n 1000 g/mol) with NaAsF_6 , NaPF_6 , KAsF_6 , RbAsF_6 , and $\text{PEO}_6:\text{LiAsF}_6$.

Dhumal et al.¹⁰³ investigated the interaction of alkali/alkaline-earth ions, including Na^+ , K^+ , Mg^{2+} , Ca^{2+} , with the ether oxygen atoms by using ab-initio calculation, and showed that the interaction energies of cation and PEO oligomer $\text{CH}_3\text{O}(\text{CH}_2-\text{CH}_2\text{O})_n\text{CH}_3$ ($n = 2-7$) followed the trend of $\text{K}^+ > \text{Na}^+ > \text{Ca}^{2+} > \text{Mg}^{2+}$. The Mg^{2+} ion bond strongly to the ether oxygen atoms and resulting in lowest conductivity among the series of alkali/alkaline-earth based PEO oligomer.

Later, the effect of different alkali-based iodide salts, RI (with R is the alkali ions), on the gel polymer PEO/salt in acetonitrile was reported by X. Shen et al.¹⁰⁴. These electrolytes exhibit high ionic conductivity above $4 \text{ mS}\cdot\text{cm}^{-1}$ at RT, and changed with the nature of cations. For the alkali cations from Li^+ to K^+ , ionic conductivity increased while increasing the cation radius, and was suddenly decreased for the bigger Cs^+ cation due to the low solubility of CsI in PEO.

In conclusion, the cationic conduction mechanism is very dependent on the size of cation, the anion nature, and the ionic mobility. Therefore, our work will focus on the single conducting polymer where the anions are chemically bonded along the polymer backbone resulting in only the transport of cations in the polymer matrix.

3.3. Single-ion polymer electrolyte based on PEO

The main properties of solid-based electrolyte are briefly resumed in terms of ionic conductivity, transference number, electrochemical stability, flexibility, and safety.¹⁰⁵ Among these factors, cationic transference number displays a remarkable role for ionic plating/stripping performance. In particular, Li^+ cation is generally less mobile than the anion, and its motion couples to that of Lewis basic sites of the polymer which results in the low t^+ for the blend of polymer/salt-based

electrolytes. The t^+ value, generally under 0.5, can cause the charge concentration gradient and reverse the cell polarization rise up, and detrimentally affect the long-term cyclability of the batteries.¹⁰⁶ As an advancement of solid-state electrolytes, the single-ion polymer electrolytes (SIPEs) are highly desirable to overcome the drawbacks of conventional polymer electrolytes. A t^+ value approached to unity prevents the formation of charged concentration gradients in the electrolyte, and limits the lithium dendritic growth that causing the cell's failure.

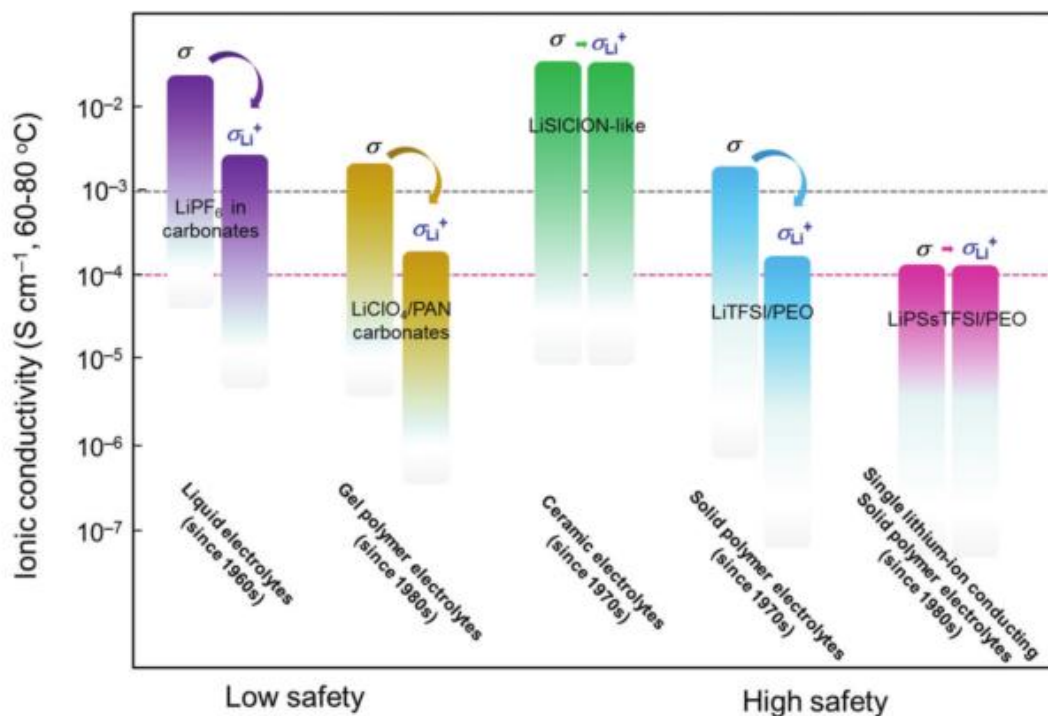


Fig. 24 The development of lithium electrolytes for rechargeable lithium batteries in term of low to high safety, since their first appearance in 1960..¹⁰⁷

In Fig. 24, the world's tendencies focus on the improvement of batteries' safety by using the single-ion materials as solid electrolytes. Back to the 1980s, the first SIPEs proposed by J. Bannister et al.¹⁰⁸ showed that grafting the anionic function on the polymer chain approached the anionic transference number to zero, and resulting in high t^+ . The strategies for grafting anions can be resumed in the three common ways, including

- (i) covalently linking the anions to the polymer backbone
- (ii) grafting the anions to the inorganic backbone
- (iii) using the trapping agents for anions

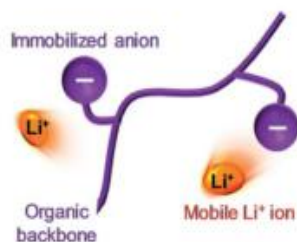


Fig. 25 Schema illustration of a structural single-ion polymer electrolyte.¹⁰⁵

The simplest and straightforward approach in this regard is the covalent tethering of the anionic functions to polymer backbone, as illustrated in Fig. 25. These SIPEs can be synthesized by two basic methods including the direct polymerization of lithium monomers, or the chemical modification of existing polymers. In the next part, a short review of the sulfonate (SO_3^-) or sulfonylimide (TFSI) anions-based SIPEs, which are the most common anions for LPBs due to the highly charge delocalization aspect, and high conductivity are reported.

The sulfonate anion (SO_3^-). They possess a reasonable degree of negative charge delocalization, which is much higher than the carboxylate anion. Starting in 1991, Zhang et al.¹⁰⁹ presented a lithium polymer salt based on SO_3^- anion, called as poly(sulfoalkyl metacrylates) - PSAMM, see Fig. 26a, but the highest Li conductivity of the blend with PEO was only $1.8 \times 10^{-7} \text{ S.cm}^{-1}$ at RT.

Later, C. H. Park et al.¹¹⁰ reported the blend of PEO and lithium poly(4-styrenesulfonate), LiPSS, (Fig. 26b) which showed the RT conductivities of $3 \times 10^{-8} \text{ S.cm}^{-1}$ at $\text{EO/Li} = 8$, up to $10^{-5} \text{ S.cm}^{-1}$ at 80°C , with a t^+ value of 0.85. The low conductivity at RT was linked to the presence of the crystalline PEO regions. Increasing the temperature led to the amorphous behavior of PEO, hence improved the conductivity, but reduced the mechanical properties of electrolyte.

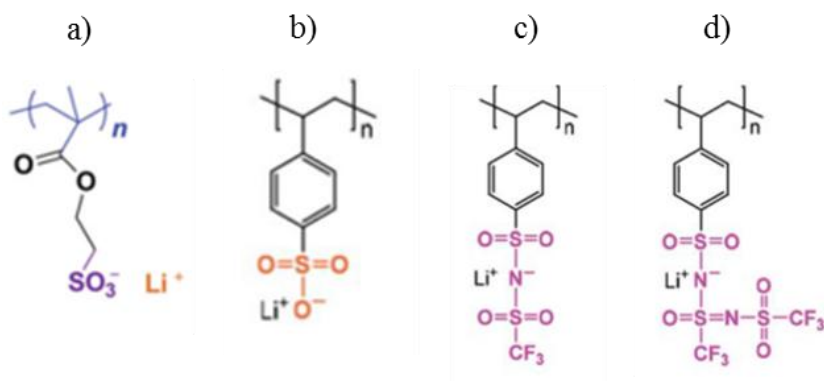


Fig. 26 Chemical structures of single-ion polymers based on SO_3^- anion (a,b) and TFSI anion (c,d).

The sulfonylimide anion (TFSI). This anion was known as the highly delocalized charge distribution, and the plasticizing effect that help to improve the conductivity.¹⁰⁵ In 2000, Watanabe

et al.¹¹¹ presented a poly (2-oxo-1-difluoroethylene sulfonylimide) with a unity transference number. However, the low RT conductivity of 10^{-8} S.cm⁻¹ prevented the development of this material. Later, the single-ion based on a delocalized polyanion i.e. lithium poly (4-styrenesulfonyl (trifluoromethylsulfonyl)imide) – LiPSTFSI (Fig. 26c) was synthesized by R. Meziane et al.¹¹². These polyelectrolytes mixed with PEO reached higher ionic conductivity of 10^{-7} S.cm⁻¹ at RT, and increased to 10^{-5} S.cm⁻¹ at above the melting of polymer.

The effect of charge delocalization of anion on conductive behavior was studied by Zhou et al.¹¹³ using the blends of PEO with LiPSTFSI (Fig. 26c), poly[(4-styrenesulfonyl)(trifluoromethyl(S-trifluoro-methylsulfonylimino)sulfonyl)imide], (LiPSsTFSI, Fig. 26d), and LiPSS (Fig. 26b). The conductivity of 7.61×10^{-7} S.cm⁻¹ was found for PEO/LiPSsTFSI, 8.42×10^{-7} S.cm⁻¹ for PEO/LiPSTFSI, and much lower of 8.35×10^{-8} S.cm⁻¹ for PEO/LiPSS at RT affirmed the highly delocalize charge of anion moiety that enhanced the ionic conductivity. At higher temperature of 90 °C, the blends PEO/LiPSsTFSI reached 1.35×10^{-4} S.cm⁻¹, with the high t^+ value of 0.91, and low T_g of -15 °C indicating the single-ion nature, and the low crystallinity which were suitable for electrolyte applications.

- **Single-ion copolymer**

As knew, the polymer electrolytes based on PEO, even the modified polymers, must be used at the relative high temperature to maintain a reasonable ionic conduction (typically at 80 °C in most of the studies), which limits their applications. Moreover, Li conduction in PEO matrix is dominated by the chain mobility. Higher chain mobility provides higher ionic conductivity, and therefore the poor mechanical properties. Many researches have been suggested to design the single-ion multi-block copolymers, types (AB)_n or (ABA)_n, where each block display a distinct function i.e. ionic conduction or mechanical strength, etc.

Z. Shao and P. Jannasch¹¹⁴ reported the triblock copolymer BAB, where A is the poly(ethylene oxide-*co*-propylene oxide) (PEOPO), and B is the poly(lithium 2,3,5,6-tetrafluorostyrene-4-sulfonate) (PPFSLi), Fig. 27. The copolymer possessed the aromatic ring, type perfluorinated, and due to the electron-withdrawing effect of fluorines, the anion was well dissociated. The conductivity reached 1.5×10^{-6} S.cm⁻¹ at RT, and increased to 1.4×10^{-5} S.cm⁻¹ at 60 °C, which are suitable for the copolymer-based electrolytes. However, grafting the anionic functions on the rigid block resulted in poor conductivity, and low chain mobility.

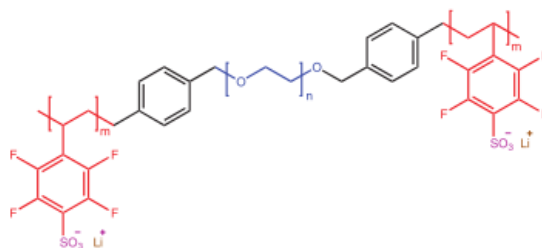


Fig. 27 Chemical structure of the multi-block copolymers based on the SO_3^- anion.¹¹⁴

The TFSI anions were grafted in a rigid block A of an $(\text{ABA})_n$ triblock copolymer i.e. P(LiSTFSI)-b-PEO-b-P(LiSTFSI) (PLiSTFSI: lithium poly(styrene trifluoromethanesulfonylimide)) (Fig.28a).¹¹⁵ This material showed the conductivity of $1.3 \times 10^{-5} \text{ S.cm}^{-1}$ at 60°C , with a t^+ value of 0.85. Later, a number of single-ion multi-block copolymers were investigated such as PEO-b-P(LiSTFSI) (Fig. 28b),^{116,117} P(LiMTFSI)-b-PEO-b-P(LiMTFSI) (Fig. 28c,e)¹¹⁸, PS-b-P(LiSTFSI-r-OEM)-b-PS (Fig. 28d),¹¹⁹ etc. Recently, the structure of BAB copolymer combined a linear PEO (35 kg/mol) block, with the structural blocks PLiSTFSI or P(LiMSTFSI) (Fig. 28e) was also reported.^{117,120}

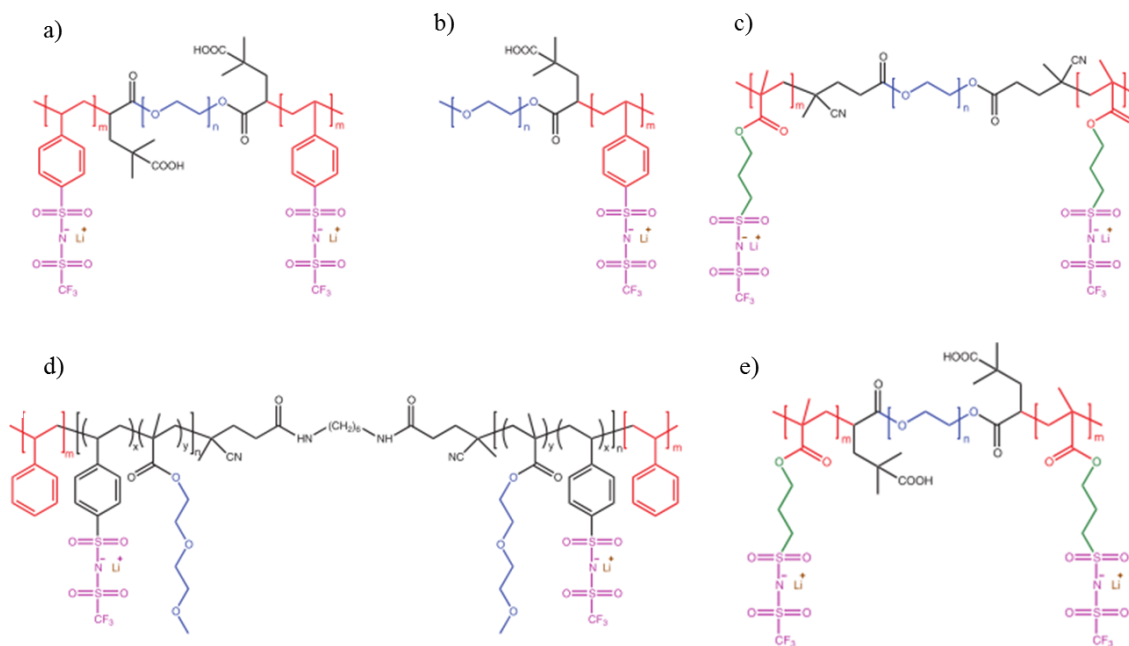


Fig. 28 Chemical structure of several single-ion block copolymers based on PEO, sulfonate and sulfonylimide anions.¹²¹

In a multi-block copolymer structure, the rigid block assures the mechanical strength, but most of the reported copolymers have the anionic functions attached to the rigid block. The lack of phase separation including the lack of mechanical properties. The high conductivity was reported only above the PEO melting point, when the two phases were mixed (due to the interaction of Li^+ and PEO).

In 2015, Balsara et al.¹¹⁷ studied the di-blocks copolymer PEO-b-P(LiSTFSI) and reported that increasing the temperature (above the melting of PEO) resulting in high conductivity due to the mixing of two phases morphology, but poor mechanical strength.¹²¹

In brief, various SIPEs based on PEO and the highly delocalized charge anions such as sulfonate and sulfonylimide have been reported in the past three decades. These anionic groups display an important role on the conductivity of PEO-based electrolytes. The common advantage of these electrolytes relates to the high Li^+ transference number, which can overcome the drawbacks of a blend polymer/salt, including the salt precipitation/aggregation, reserved cell's polarization, Li dendritic growth, etc. However, most of the reported SIPEs exhibit low conductivity, usually about 10^{-7} - 10^{-8} S.cm⁻¹ at RT, and up to 10^{-5} S.cm⁻¹ at above 60 °C, resulting in the unsuitable electrolytes in term of fast charged technologies. The blends of high molecular weight PEO with the lithium poly-anions, as well as the block copolymers exhibit poor mechanical properties above the melting of PEO, and an insufficient conductivity at lower temperature due to the presence of crystalline PEO. Concerning the design of SIPE block copolymers, the anionic functions are usually bonded on the rigid blocks (domain maintains the mechanical strength), which is not favorable neither for Li^+ conduction nor for mechanical strength after the PEO melting.¹⁰⁷ In this work, the design and characterizations of the multi-block copolymer $(\text{AB})_n$ will be presented. The anionic groups are chemically bonded on the PEO conducting block (A block) to provide high Li^+ conduction, and decrease the crystallinity of PEO. Mechanical strength, in a whole range of studied temperatures from RT to 90 °C, is maintained by the presence of an hydrophobic fluorinated poly(ether sulfone) – FPES block (B block), that is not miscible with the PEO domain, as seen in Fig. 29.

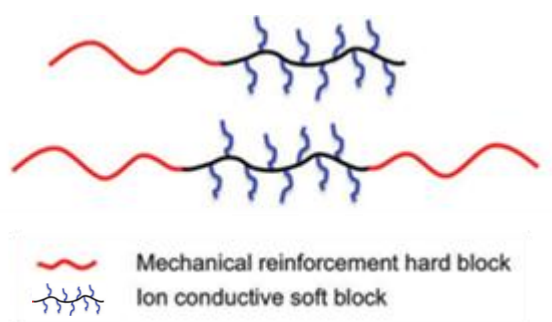


Fig. 29 Schematic structure of the single-ion multi-block copolymer.¹²¹

3.4. Application of SIPEs in all-solid-state lithium metal batteries

In 2013, Bouchet et al.¹¹⁵ studied the cyclability of triblock polymer P(STFSI)-Li-PEO-b-P(STFSI-Li) in the lithium metal coin cells using LiFePO_4 (LFP) as cathode material. The carbon-coated LFP electrodes were prepared by using 60:32:8 wt.% of LFP:SIPE:carbon black. The batteries showed good cycling up to more than 80 cycles at varied power rates without any lithium dendritic growth. The performances of these materials were better than the results from the state of the art

published previously (Fig. 30a). Later, the Armand's group¹²² designed a SIPE by blending high molecular PEO with LiPSTFSI, grafted on Al₂O₃ nano-particles. The SIPE was tested as solid electrolyte and was sandwiched between the Li-metal and the LFP cathode (cathode was casted with 62:18:12:7 wt.% of LFP: PEO: LiPSTFSI: carbon black). The discharge capacity reached 120 mAh.g⁻¹ after 130 cycles at C/2 with an excellent Coulombic capacity of 95 % (Fig. 30b).

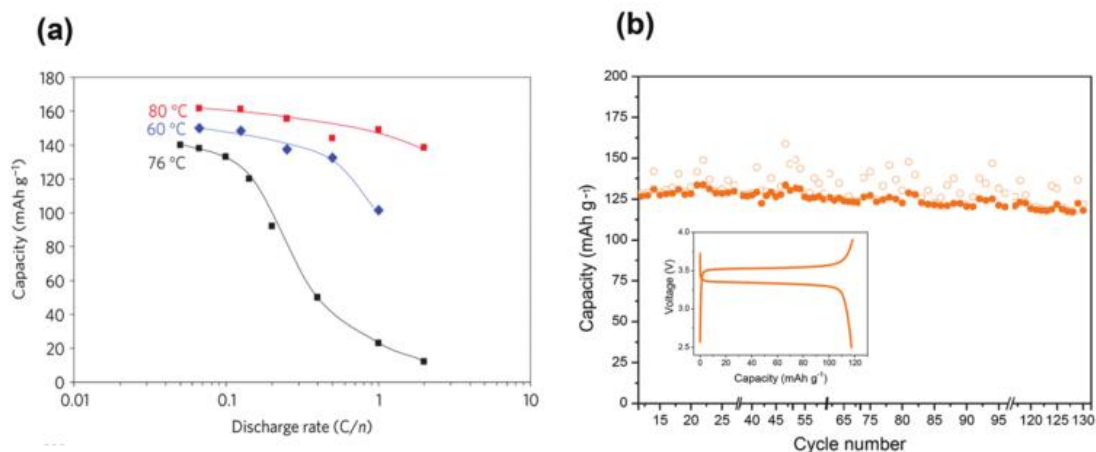


Fig. 30 (a) cycling performances at different temperature as a function of discharge rate for Li|P(STFSI)-Li-PEO-b-P(STFSI-Li)|LFP.¹¹⁵ and (b) The galvanostatic cycling at 70 °C for Li|SIPE|LFP cell reported by Armand' group.¹²²

Recently, the performances of single-ion ABA triblock copolymer electrolytes composed of PEO and poly(lithium 1-[3-(methacryloyloxy) propylsulfonyl]-1-(trifluoromethylsulfonyl) imide) blocks, poly(LiMTFSI), in Li-metal battery using LFP electrode were preported by L. Porcarelli et al.¹¹⁸ The cell delivered 100 mAh.g⁻¹ at C/2, after 300 cycles without any sign of Li dendritic growth (see Fig. 31). These good performances attributed due to the single-ion nature of the electrolyte, with a t^+ value of 0.91.

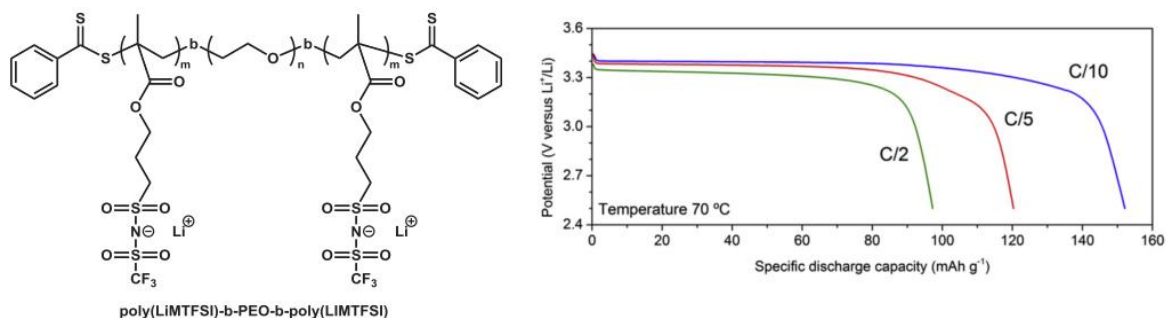


Fig. 31 Chemical structure of poly(LiMTFSI), and the Li/8k-35k-8k/LiFePO4 cell potential versus specific discharge capacity at different C-rates at 70 °C.¹¹⁸

The outstanding cycling performances reported for the SIPEs based on PEO are developed only in a few studies during the last 30 years. These works showed the main advantages of single-ion materials in term of cyclability for LMBs, such as high stabilization without any sign of dendritic

growth after a long cycling, reversibility of lithium plating/stripping, performance. These SIPEs were used not only as electrolytes, but also as binder for cathode casting to ensure an effective conductivity inside the cathode.

4. Electrolyte approaches for future rechargeable batteries

The growing demand of lithium batteries will be quickly constrained by the limit supply of raw material i.e. lithium metal, that leads to the advancement of complementary battery technologies. Been the good candidates for high availability and low-cost materials beside lithium, the alkali/alkaline-earth elements, including sodium (Na), potassium (K), cesium (Cs), magnesium (Mg), and calcium (Ca), etc. become the most promising candidates for future storage devices. Following the development of electrode materials, the electrolytes based on alkali/alkaline-earth metals for rechargeable batteries, in terms of high security and high performance, attract attention from the scientist. The studies of electrolytes using ionic liquids or conducting polymers for safer alkali/alkaline-earth rechargeable batteries are recapped in this part.

4.1. Sodium-ion batteries

Among the next generation, Sodium Ion Batteries (SIBs) have gained much attention due to the rich sodium resource, and the low-cost for potential applications in large-scale energy storage.¹²³ In the 1980s, the first SIB from sodium-lead alloy has been developed by the US and the Japanese companies.¹²⁴ However, the average discharge voltage reached only 3.0 V, which was lower than LIBs of 3.7 V, did not attract much attention. Based on the same mechanism, LIBs and SIBs have similar properties, except their ion carriers. The size of Na⁺ ions (1.02 Å) are bigger than Li⁺ (0.76 Å), and sodium is also heavier than lithium (23 g/mol and to 6.9 g/mol, respectively)¹²⁴, which obstruct the intercalation/ deintercalation of ions in the electrodes. Besides the studies of electrode materials, electrolytes for SIBs are rather similar in detail with the lithium-based electrolyte, such as organic liquid, non-aqueous, and all-solid-state electrolyte.

The blends of ionic liquid/salt or conducting polymers with a fraction of sodium salts gained plenty of attention nowadays as high security electrolytes for SIBs. The early studies used IL, types imidazolium or quaternary ammonium, as electrolyte for Na-ion battery thanks to the dissolution of salt, and the sodium deposition with high efficiency.⁴³ Subsequently, Monti et al.⁵¹ presented the physicochemical behavior of the imidazolium-based TFSI ILs doped NaTFSI (0.4 M) showed high ionic conductivity of 5.3 mS.cm⁻¹ at RT, which was higher than the blend of Li in IL at the same concentration. Later, ILs with TFSI anion, are presented by Nohira et al.¹²⁵, are showed wide electrochemical stabilization up to 4.9 V vs Na⁺/Na, and improved the operating temperature up to

115 °C. The deposition of sodium metal in 1-butyl-1-methylpyrrolidinium TFSI doped NaTFSI at -0.2 V vs Na⁺/Na was also reported by S.A. Mohd Noor et al.⁴³

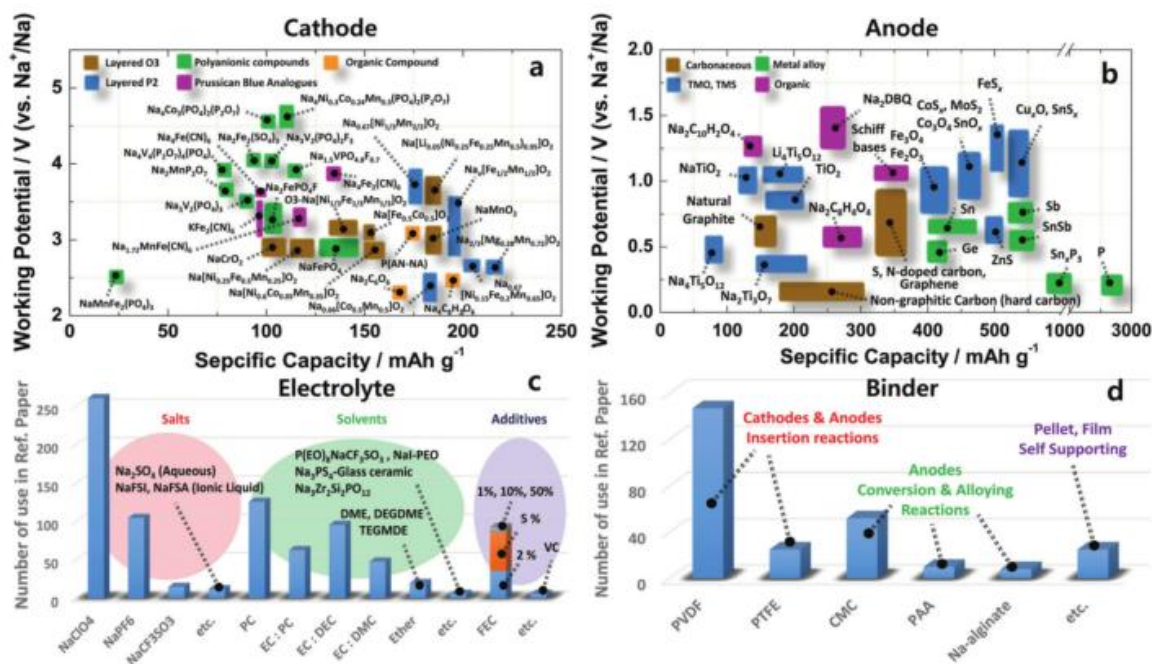


Fig. 32 The recent researches progress for sodium-ion batteries including the cathode, anode, electrolyte, and binder.¹²⁴

Various types of polymers are currently identified instead of a liquid electrolyte. The PEO-based electrolytes with high segmental motion, low T_g , good electrochemical stability, high affinity, and the ability for salt dissolution, ion dissociation/complexation are the most suitable candidate for all-solid-state sodium batteries. Nevertheless, the ionic conductivity of PEO under its melting point (~ 60 °C) is extremely low. Recently, by adding the inorganic fillers (TiO_2 , ZrO_2 or SiO_2) or ionic liquid (more recent approach)¹²⁴, its ionic conductivity can be improved. Very recently, Varun Kumar et al.¹²⁶ presents for the first time the mixture PEO / NaTFSI / BMIm TFSI as an electrolyte for SIBs. Their membranes containing 40 wt.% of IL show a good ionic conductivity (4.1×10^{-4} S.cm⁻¹) at RT. The Na⁺ transference number is around 0.39, and good thermal stability, which makes them very promising material for sodium rechargeable battery.

4.2. Potassium-ion batteries

Recently, potassium-ion batteries (PIBs) have been developed as promising candidate for large-scale energy application. Since 2015, the studies of secondary batteries based on potassium metal have been strongly developing.¹²⁷ These storage devices offer similar principle and advantages as compared to SIBs due to the low-cost and abundant of potassium reserves. The low standard potential of K⁺/K couple (-2.93 V vs SHE), which is close to Li⁺/Li (-3.04 V) and Na⁺/Na (-2.71 V), propose similar cell voltage to those of LIBs and SIBs.¹²⁸ One of the advancements for potassium electrolytes was the reversible potassium plating/stripping (at -0.15 V vs Li⁺/Li) in a

solution of KPF_6 0.5 M in EC:DMC, reported by S. Komaba et al.¹²⁹ Beside a number of studies for electrode materials, the optimization of non-aqueous potassium electrolytes is still in the nascent state.¹³⁰

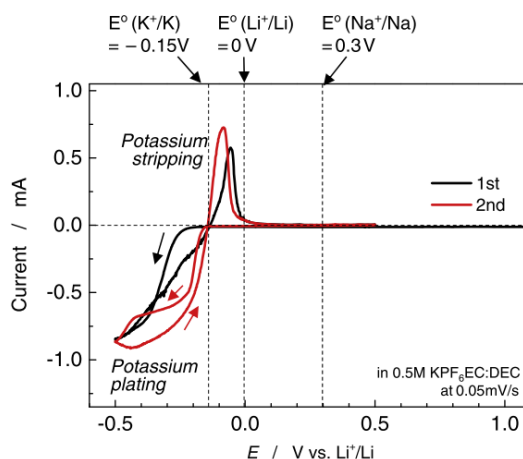


Fig. 33 Cyclic voltammograms of Ni mesh electrode in 0.5 mol.dm⁻³ KPF_6 EC : DMC at 0.05 mV.s⁻¹ scan rate with Li metal as reference electrode.¹²⁹

Electrolytes for PIBs are mainly based on the mixture of KPF_6 , KClO_4 , KBF_4 or $\text{KN}(\text{SO}_2\text{F})_2$ (potassium bis(fluorosulfonyl)amide, KFSa) salts dissolved in carbonate ester solvents.¹³¹ While the KClO_4 , KBF_4 are hardly soluble, the KPF_6 dissolves easily in the carbonate esters, and the PF_6^- anion can also form the SEI with Al current collector as in a LIB. However, the irreversible capacity in high voltage operation (above 4 V), and an insufficiently SEI formation at the negative electrode prevent the use of KPF_6 . The solvent-free and solid electrolytes for rechargeable potassium batteries require the advancement.

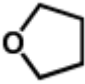

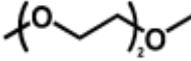
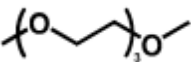
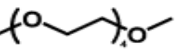
4.3. Magnesium-ion batteries

Rechargeable magnesium batteries (MIBs) are another potential solution, which are considered as a highly promising technology for energy storage and conversion. As a negative electrode, magnesium metal provides two electrons per atom. The divalent nature of Mg^{2+} gives an attractive volumetric capacity of 3832 mAh.cm⁻³, which is twice higher than that of lithium (2062 mAh.cm⁻³) and sodium (1136 mAh.cm⁻³).¹³² In addition, magnesium is the 5th most abundant element in the Earth's crust¹³³, with low atomic weight, and low cost. Magnesium is less reactive (-2.37 V vs. SHE) compared to the alkali metals, environmentally benign, and most of the Mg compounds are usually non-toxic. The MIBs work with the similar principle of intercalation/ de-intercalation as in the LIBs.¹³⁴ In brief, magnesium battery may become one of the best economical solution for electrical storages in the future.

The factors that inhibit the development of MIBs concerned to the availability of magnesium-based electrolytes, such as an electrolyte contained Mg^{2+} with high ionic conductivity and reversible Mg

deposition/dissolution (minimizing the formation of passivation layer on the magnesium metal electrode).¹³⁴ According to the previous studies, the electrolytes consisted of Grignard reagents (R-MgX, R = alkyl; X = Br, Cl), organohaloaluminates, or magnesium organoborates dissolved in several ether solvents (Table 2) presented the reversible electrochemical magnesium deposition. However, these solutions provided the corrosive issue, and unstable in oxidation.

Table 2 Physical properties of cyclic and linear ether solvents.

Solvent		Chemical structure	Boiling point (°C)
THF	Tetrahydrofuran		66
Glyme	Dimethoxy ethane		85
Diglyme	Diethyleneglycol dimethyl ether		162
Triglyme	Triethyleneglycol dimethyl ether		216
Tetraglyme	Tetraethyleneglycol dimethyl ether		275

The ILs, with their unique characteristics, have been highly recommended as safer and green solvents for magnesium electrolytes. As reported in the literature, the combination of high flexibility and low geometric symmetry imidazolium or quaternary ammonium cations⁵⁴, with good electrochemical stability TFSI⁻ anion³⁵ gained many attentions as ILs for dissolving the magnesium salts. The binary system where the Grignard reagents dissolved in TFSI-based IL displayed 90 % Coulombic efficiency for reversible Mg deposition/dissolution, and exhibited high ionic conductivity above 1 mS.cm⁻¹ at 60 °C.^{54,135,136}

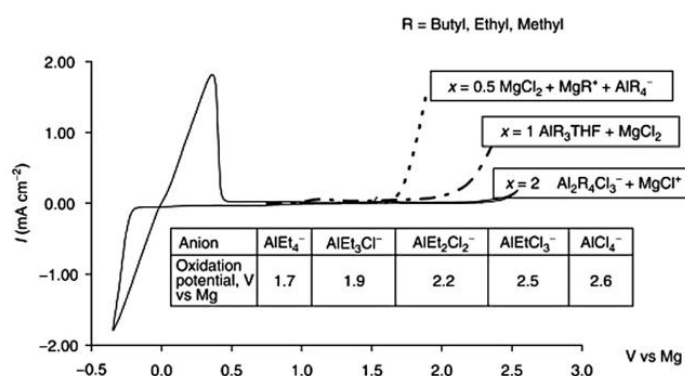


Fig. 34 Cyclic voltammograms of the 0.25 M tetrahydrofuran (THF) solutions, containing Grignard reagents at a scan rate of 20 mV.s⁻¹, from -0.5 to 3 V vs Mg^{2+/Mg}.¹³⁴

The studies of solid polymer electrolytes for MIBs are still restrained. The Mg-based solid electrolytes offered the very low ionic conductivity of about 10⁻⁸ S.cm⁻¹ at RT. Efforts have been changed toward the modified polymers, and the magnesium gel polymer electrolyte to improve the

conductivity while maintaining good mechanical/ electrochemical properties. One of the first encouraged results concerned to the blend $\text{PEO}_n/\text{MgCl}_2$ (with $n = 8, 12, 16,$ and 24)¹³⁷, and $\text{PEO}_{16}/\text{Mg}(\text{ClO}_4)_2$, which exhibited the comparable ionic conductivity to the blend PEO/LiTf .¹³⁸ Later, by adding the molecule of THF, the gel polymer comprised of EtMgBr-PEO-THF showed a reversible magnesium deposition/dissolution due to the activation of EtMgBr complex in THF.¹³⁹ The polymer-IL electrolytes $\text{PEO}/\text{Mg}(\text{Tf})_2/\text{EMImTf}$ showed a Mg transference number $t_{\text{Mg}^{2+}} = 0.45$.¹⁴⁰

5. The aim of this work

The aim of this work includes the characterization of new electrolytes for lithium metal batteries, and the impact of several cations of alkali/alkaline-earth groups such as Na, K, Cs, and Mg on the electrolyte conductivity, diffusivity and thermal properties. Thus, two systems of ionic liquid and solid-state polymer electrolytes are used in this work.

5.1. Ionic liquid electrolyte

The mixture of IL/salt is considered as green electrolyte for safer rechargeable batteries. These physical properties are strongly dependent on the coordination of solvated cation, which dominates the ionic mobility and the solvating/de-solvating processes at the interface electrode/electrolytes. Moreover, ionic conductivity and diffusivity are the two essential factors beside the high thermal and electrochemical stability to describe the usefulness of IL-based electrolytes. This study will investigate the electrolytes based on a common IL i.e. 1-butyl-3-methyl imidazolium bis(trifluoromethanesulfonyl)imide, denoted as BMIm TFSI, and the alkali/alkaline-earth TFSI salts in terms of physical/conductive/diffusivity properties. The IL BMIm TFSI exhibits the exceptional properties including hydrophobicity, electrochemical stability, low viscosity, and very low melting point, which are suitable for electrolyte applications.^{21,141,142} A schematic chemical structure of BMIm TFSI is presented in Fig. 35. The detailed planning includes (i) the study of solubility of several TFSI salts in BMIm TFSI, (ii) the impact of salt concentration for a smallest and a bigger alkali metals coordinated in IL such as Li and Cs, (iii) the evolution of IL properties as a function of ions' nature type alkali/alkaline-earth metals.

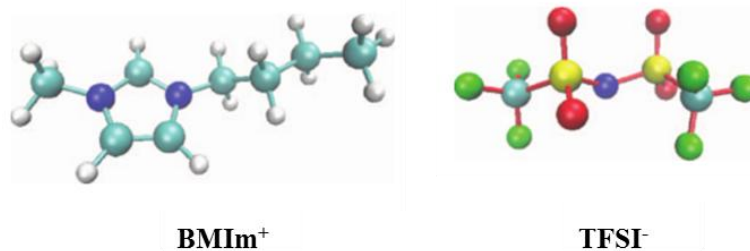


Fig. 35 Schematic structure of BMIm TFSI. Atom's color code: carbon (cyan), nitrogen (blue), hydrogen (white), oxygen (red), fluorine (green), and sulfur (yellow).⁴¹

5.2. Polymer electrolyte

The all-solid-state batteries have been developed due to high volumetric stability, easy handling, no electrolyte leakage, and solvent-free electrolyte. The conducting polymer-based electrolytes gained more attention as safer materials for energy storage devices. The conventional polymer-based electrolytes possess low cationic transference number, generally under 0.5, which is a drawback for battery applications. To overcome this issue, the SIPEs based on PEO and the highly charge delocalized anions i.e. perfluorosulfonate (p-SO₃), or perfluorosulfonylimide (p-TFSI) will synthesized and characterized for lithium metal batteries, the post lithium batteries. A cartoon network of SIPE is presented in Fig. 36. The grafted anions allow reaching the understanding of cationic conduction process since the problems related to anionic mobility, and salt aggregation/precipitation are wholly suppressed.

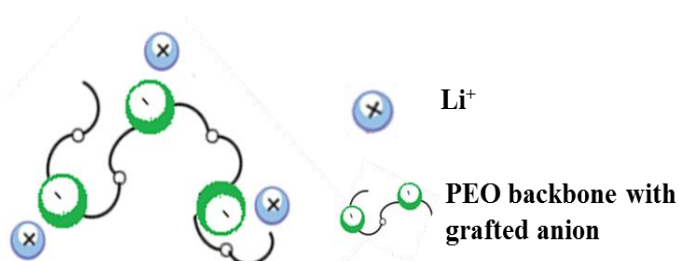


Fig. 36 Cartoon schematic of ionomers based on PEO grafted the anions.

The works involve (i) the syntheses and characterization of SICPs based on PEO as solid electrolytes for lithium metal batteries (this study will be conducted on two types of SICPs: cross-linked SICPs, and multi-block copolymers SICPs), and (ii) the effect of cation's nature on thermal properties and conductive behaviors in these SICP matrixes.

References

1. Tarascon J. M., Armand M., Issues and challenges facing rechargeable lithium batteries, *Nature*, 414, 359–67 (2001).
2. Liu K., Liu Y., Lin D., Pei A., Cui Y., Materials for lithium-ion battery safety, *Sci. Adv.*, 4, (2018).
3. Xu W. et al., Lithium metal anodes for rechargeable batteries, *Energy Environ. Sci.*, 7, 513–537 (2014).
4. Cheng X. B., Zhang R., Zhao C. Z., Zhang Q., Toward safe lithium metal anode in rechargeable batteries: A Review, *Chem. Rev.*, 117, 10403–10473 (2017).
5. D. Aurbach, E. Zinigrad, Y. Cohen, A short review of failure mechanisms of lithium metal and lithiated graphite anodes in liquid electrolyte solutions, *Solid State Ionics*, 148, 405–416 (2002).
6. Lu L., Han X., Li J., Hua J., Ouyang M., A review on the key issues for lithium-ion battery management in electric vehicles, *J. Power Sources*, 226, 272–288 (2013).
7. Cui W., Lansac Y., Lee H., Hong S.-T., Jang Y. H., Lithium ion solvation by ethylene carbonates in lithium-ion battery electrolytes, revisited by density functional theory with the hybrid solvation model and free energy correction in solution, *Phys. Chem. Chem. Phys.*, 18, 23607–23612 (2016).
8. Li Q., Chen J., Fan L., Kong X., Lu Y., Progress in electrolytes for rechargeable Li-based batteries and beyond, *Green Energy Environ.*, 1, 18–42 (2016).
9. Ponrouch, A. et al., Non-aqueous electrolytes for sodium-ion batteries, *J. Mater. Chem. A*, 3, 22–42 (2015).
10. Che H. et al., Electrolyte design strategies and research progress for room-temperature sodium-ion batteries, *Energy Environ. Sci.*, 10, 1075–1101 (2017).
11. Wang Q., Jiang L., Yu Y., Sun J., Progress of enhancing the safety of lithium ion battery from the electrolyte aspect, *Nano Energy*, 55, 93–114 (2019).
12. P. Walden, Molecular weights and electrical conductivity of several fused salts, *Bull. Acad. Imper. Sci. (St. Petersburg)*, 405–422 (1914).
13. Tokuda H. et al., Physicochemical Properties and Structures of Room-Temperature Ionic Liquids. 3. Variation of Cationic Structures, *J. Phys. Chem., B* 110, 2833–2839 (2006).
14. Marsh K. N., Boxall J. A., Lichtenthaler R., Room temperature ionic liquids and their mixtures - A review, *Fluid Phase Equilib.*, 219, 93–98 (2004).
15. Harris K. R., Kanakubo M., Woolf L. A., Temperature and Pressure Dependence of the Viscosity of the Ionic Liquids 1-Hexyl-3-methylimidazolium Hexafluorophosphate and 1-Butyl-3-methylimidazolium Bis (trifluoromethylsulfonyl) imide, *J. Chem. Eng. Data* 52, 1080–1085 (2007).
16. Srouf H. et al., Ionic liquid-based electrolytes for lithium-ion batteries: review of performances of various electrode systems, *J. Appl. Electrochem.*, 46, 149–155 (2016).
17. Tariq M., Forte P. A. S., Gomes M. F. C., Lopes J. N. C., Rebelo L. P. N., Densities and refractive indices of imidazolium- and phosphonium-based ionic liquids: Effect of temperature, alkyl chain length, and anion, *J. Chem. Thermodyn.*, 41, 790–798 (2009).
18. Martins V. L., Torresi R. M., Ionic liquids in electrochemical energy storage, *Curr. Opin. Electrochem.*, 9, 26–32 (2018).

19. Liu H., Yu H., Ionic liquids for electrochemical energy storage devices applications, *J. Mater. Sci. Technol.*, 35, 674–686 (2019).
20. Phung L. M. L., Accumulateurs au lithium a haut potentiel : électrolytes et matériaux d'électrode positives, *PhD thesis, Univ. Grenoble-Alpes* (2010).
21. Bonhote P., Dias A., Papageorgiou N., Kalyanasundaram K., Gra M., Hydrophobic, Highly Conductive Ambient-Temperature Molten Salts, *Inorg. Chem.*, 35, 1168–1178 (1996).
22. Tokuda H., Hayamizu K., Ishii K., Bin A., Susan H., Physicochemical properties and structures of room temperature ionic liquids, variation of anionic species. 16593–16600 (2004).
23. Widegren J. A., Laesecke A., Magee J. W., The effect of dissolved water on the viscosities of hydrophobic room-temperature ionic liquids, *Chem. Commun.*, 1610–1612 (2005).
24. Seddon K. R., Stark A., Torres M.-J., QUILL, Influence of chloride, water, and organic solvents on the physical properties of ionic liquids, *Pure Appl. Chem.*, 72, 2275–2287 (2000).
25. Huddleston J. G. *et al.*, Characterization and comparison of hydrophilic and hydrophobic room temperature ionic liquids incorporating the imidazolium cation, *Green Chem.*, 3, 156–164 (2001).
26. MacFarlane D. R., Meakin P., Sun J., Amini N., Forsyth M., Pyrrolidinium Imides: A new family of molten salts and conductive plastic crystal phases, *J. Phys. Chem., B* 103, 4164–4170 (1999).
27. Vranes M., Dozic S., Djeric V., Gadzuric S., Physicochemical characterization of 1-butyl-3-methylimidazolium and 1-butyl-1-methylpyrrolidinium bis(trifluoromethylsulfonyl) imide, *J. Chem. Eng. Data*, 57, 1072–1077 (2012).
28. Xu W., Cooper E. I., Angell C. A., Ionic Liquids: Ion mobilities, glass temperatures, and fragilities, *J. Phys. Chem. B*, 107, 6170–6178 (2003).
29. Sun, J., Forsyth M., MacFarlane D. R., Room-temperature molten salts based on the quaternary ammonium Ion, *J. Phys. Chem. B*, 102, 8858–8864 (2002).
30. Lewandowski A., Świdarska-Mocek A., Ionic liquids as electrolytes for Li-ion batteries-An overview of electrochemical studies, *J. Power Sources*, 194, 601–609 (2009).
31. Noda A., Hayamizu K., Watanabe M., Pulsed-gradient spin-echo ¹H and ¹⁹F-NMR ionic diffusion coefficient, viscosity, and ionic conductivity of non-chloroaluminate room-temperature ionic liquids, *J. Phys. Chem. B*, 105, 4603–4610 (2001).
32. Tokuda H., Hayamizu K., Ishii K., Susan M. A. B. H. & Watanabe M., Physicochemical properties and structures of room temperature ionic liquids, variation of alkyl chain length in imidazolium cation, *J. Phys. Chem. B*, 109, 6103–6110 (2005).
33. Fuller J., Carlin R. T., Osteryoung R. A., The room temperature ionic liquid 1-Ethyl-3-methylimidazolium tetrafluoroborate: electrochemical couples and physical properties, *J. Electrochem. Soc.*, 144, 3881 (2006).
34. Pitawala J. *et al.*, Phase behaviour, transport properties, and interactions in Li-salt doped ionic liquids, *Faraday Discuss.*, 154, 71–80 (2012).
35. Lassègues J. C., Grondin J., Talaga D., Lithium solvation in bis(trifluoromethanesulfonyl) imide- based ionic liquids, *Phys. Chem. Chem. Phys.*, 5629–5632 (2006).
36. Paolone A., Stabilization of different conformers of bis(trifluoromethanesulfonyl)imide anion in ammonium-based ionic liquids at low temperatures, (2014).
37. Duluard S. *et al.*, Lithium solvation and diffusion in the 1-butyl-3-methylimidazolium

- bis(trifluoromethanesulfonyl)imide ionic liquid, *J. Raman Spectrosc.*, 39, 627–632 (2008).
38. Monteiro M. J., Bazito F. F. C., Siqueira L. J. A., Ribeiro M. C. C., Torresi R. M., Transport coefficients, Raman spectroscopy, and computer simulation of lithium salt solutions in an ionic liquid, *J. Phys. Chem. B*, 112, 2102–2109 (2008).
 39. Andriola A., Singh K., Lewis J., Yu L., Conductivity, viscosity, and dissolution enthalpy of LiNTF₂ in ionic liquid BMINTF₂, *J. Phys. Chem. B*, 114, 11709–11714 (2010).
 40. Lassegues J. *et al.*, Spectroscopic identification of the lithium ion transporting species in litfsi-doped ionic liquids, 305–314 (2009).
 41. Liu H., Maginn E., Effect of ion structure on conductivity in lithium-doped ionic liquid electrolytes: A molecular dynamics study, *J. Chem. Phys.*, 139, (2013).
 42. Borodin O., Smith G. D., Henderson W., Li⁺ cation environment, transport, and mechanical properties of the LiTFSI doped N-methyl-N-alkylpyrrolidinium⁺TFSI⁻ Ionic liquids, *J. Phys. Chem. B*, 110, 16879–16886 (2006).
 43. Mohd Noor S. A., Howlett P. C., Macfarlane D. R., Forsyth M., Properties of sodium-based ionic liquid electrolytes for sodium secondary battery applications, *Electrochim. Acta*, 114, 766–771 (2013).
 44. Kitada A. *et al.*, Enhanced anodic dissolution of magnesium in quaternary-ammonium-based ionic liquid containing a small amount of water, *J. Electrochem. Soc.*, 160, D453–D458 (2013).
 45. Chen F., Forsyth M., Elucidation of transport mechanism and enhanced alkali ion transference numbers in mixed alkali metal-organic ionic molten salts, *Phys. Chem. Chem. Phys.*, 18, 19336–19344 (2016).
 46. H. Yoon, H. Zhu, A. Hervault, M. Armand, D. R. MacFarlane, M. Forsyth, Physicochemical properties of N-propyl-N-methylpyrrolidinium bis(fluorosulfonyl) imide for sodium metal battery applications, *Phys.Chem.Chem.Phys.*, 16, 12350 (2014).
 47. M. Hilder, P. C. Howlett, D. Saurel, E. Gonzalo, A. Basile, M. Armand, T. Rojo, M. Kar, D. R. MacFarlane, M. Forsyth, The effect of cation chemistry on physicochemical behaviour of superconcentrated NaFSI based ionic liquid electrolytes and the implications for Na battery performance, *Electrochim. Acta*, 268, (2018).
 48. N. Wongtharom, C. H. Wang, Y.-C. Wang, C.-H. Yang, Ionic liquid electrolytes with various sodium solutes for rechargeable Na/NaFePO₄ batteries operated at elevated temperatures, *ACS Appl. Mater. Interfaces*, 6, 17564–17570 (2014).
 49. C. Ding, T. Nohira, R. Hagiwara, K. Matsumoto, Y. Okamoto, A. Fukunaga, S. Sakai, K. Nitta, Na[FSA]-[C₃C₁pyrr][FSA] ionic liquids as electrolytes for sodium secondary batteries: Effects of Na ion concentration and operation temperature, *J. Power Sources*, 269, 124–128 (2014).
 50. Méndez-Morales T. *et al.*, MD simulations of the formation of stable clusters in mixtures of alkaline salts and imidazolium-based ionic liquids, *J. Phys. Chem. B*, 117, 3207–3220 (2013).
 51. Monti D., Jónsson E., Palacín M. R., Johansson P., Ionic liquid based electrolytes for sodium-ion batteries: Na⁺ solvation and ionic conductivity, *J. Power Sources*, 245, 630–636 (2014).
 52. J. M. Vicent-Luna, J. M. Ortiz-Roldan, S. Hamad, R. Tena-Zaera, S. Calero, Quantum and classical molecular dynamics of ionic liquid electrolytes for na/li-based batteries: molecular origins of the conductivity behavior, *ChemPhysChem*, 17, 2473–2481 (2016).
 53. J. Fuller, R. T. Carlin, R. A. Osteryoung, P. Koranaios, Anodization and speciation of

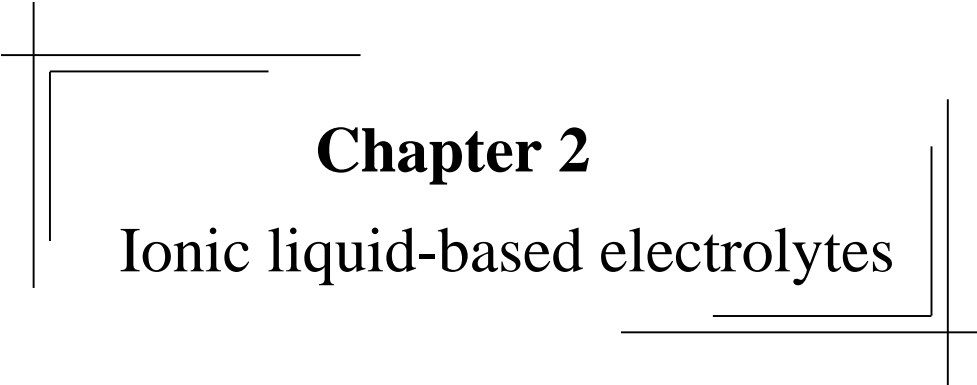
- magnesium in chloride-rich room temperature ionic liquids, *J. Electrochem. Soc.*, 145, 24 (1998).
54. Vardar G. *et al.*, Electrochemistry of magnesium electrolytes in ionic liquids for secondary batteries, *ACS Appl. Mater. Interfaces*, 6, 18033–18039 (2014).
 55. Cheek G. T., O’Grady W. E., El Abedin S. Z., Moustafa E. M., Endres F., Studies on the electrodeposition of magnesium in ionic liquids, *J. Electrochem. Soc.*, 155, (2008).
 56. Giffin G. A., Moretti A., Jeong S., Passerini S., Complex nature of ionic coordination in magnesium ionic liquid-based electrolytes: Solvates with mobile Mg^{2+} cations, *J. Phys. Chem. C*, 118, 9966–9973 (2014).
 57. Fenton D. E., Parker J. M., Wright P. V., Complexes of alkali metal ions with poly(ethylene oxide), *Polymer*, 14, 589 (1973).
 58. Sanchez J. Y., Alloin F., Benrabah D., Arnaud R., Polymer and salt selection for lithium polymer batteries, *J. Power Sources*, 68, 43–51 (1997).
 59. Stephan A. M., Review on gel polymer electrolytes for lithium batteries, *Eur. Polym. J.*, 42, 21–42 (2006).
 60. Karan N. K., Pradhan D. K., Thomas R., Natesan B., Katiyar R. S., Solid polymer electrolytes based on polyethylene oxide and lithium trifluoro- methane sulfonate (PEO – $LiCF_3SO_3$): Ionic conductivity and dielectric relaxation, 179, 689–696 (2008).
 61. Younesi R., Veith G. M., Johansson P., Edström K., Vegge T., Lithium salts for advanced lithium batteries: Li-metal, Li-O₂, and Li-S. *Energy Environ. Sci.*, 8, 1905–1922 (2015).
 62. Foley M. P. *et al.*, Phase behavior and solvation of lithium trifluoromethanesulfonate in propylene carbonate, *ECS Trans.*, 45, 41–47 (2013).
 63. Zhang H. *et al.*, Lithium bis(fluorosulfonyl)imide/poly(ethylene oxide) polymer electrolyte, *Electrochim. Acta*, 133, 529–538 (2014).
 64. Armand M., Duclot M., Chabagnot J. M., Générateurs électrochimiques de production de courant et matériaux pour leur fabrication, (1978).
 65. Armand M., Duclot M. & Chabagnot J. M., *Second International Meeting on Solid Electrolytes, University of St Andrews, Scotland, September 20-22, 1978* (University of St Andrews, 1978).
 66. Gutmann V., Empirical parameters for donor and acceptor properties of solvents, *Electrochim. Acta*, 21, 661–670 (1976).
 67. Takahashi Y., Tadokoro H., Structural studies of polyethers, $(-(CH_2)_m-O)_n$. X. crystal structure of poly(ethylene oxide), *Macromolecules*, 6, 672–675 (1973).
 68. Gray F. M., Polymer electrolytes, *Royal Society of Chemistry, Cambridge, UK, chapter 2*, 34, (1997).
 69. Berthier C. *et al.*, Microscopic investigation of ionic conductivity in alkali metal salts-poly(ethylene oxide) adducts, *Solid State Ionics* 11, 91–95 (1983).
 70. Armand M., The history of polymer electrolytes, *Solid State Ionics*, 69, 309–319 (1994).
 71. Aziz S. B., Woo T. J., Kadir M. F. Z., Ahmed H. M., A conceptual review on polymer electrolytes and ion transport models, *J. Sci. Adv. Mater. Devices*, 3, 1–17 (2018).
 72. McOwen D. W. *et al.*, Concentrated electrolytes: decrypting electrolyte properties and reassessing Al corrosion mechanisms, *Energy Environ. Sci.*, 7, 416–426 (2014).
 73. Zlatka Stoeva, Isabelle Martin-Litas, Edward Staunton, Yuri G. Andreev, Bruce P. G., Ionic conductivity in the crystalline polymer electrolytes $PEO_6:LiXF_6$, X = P, As, Sb, *J. Am.*

- Chem. Soc.*, 125, 15, 4619-4626(2003).
74. Gadjourova Z., Andreev Y. G., Tunstall D. P., Bruce P. G., Ionic conductivity in crystalline polymer electrolytes, *Nature*, 412, 520–523 (2001).
 75. Frenck L., Study of a buffer layer based on block copolymer electrolytes, between the lithium metal and a ceramic electrolyte for aqueous Lithium-air battery, *PhD thesis, Univ. Grenoble-Alpes* (2017).
 76. Marzantowicz M., Dygas J. R., Krok F., Florjańczyk Z., Zygadło-Monikowska E. Conductivity and dielectric properties of polymer electrolytes PEO:LiN(CF₃SO₂)₂ near glass transition, *J. Non. Cryst. Solids*, 353, 4467–4473 (2007).
 77. Ibrahim S., Yassin M. M., Ahmad R., Johan M. R., Effects of various LiPF₆ salt concentrations on PEO-based solid polymer electrolytes, *Ionics (Kiel)*, 17, 399–405 (2011).
 78. Singh T. J., Bhat S. V., Morphology and conductivity studies of a new solid polymer electrolyte: (PEG)_xLiClO₄, *Bull. Mater. Sci.*, 26, 707–714 (2003).
 79. Cameron G. G., Ingram M. D., Harvie J. L., Comparative ion transport in several polymer electrolytes, *J. Power Sources*, 68, 372–376 (1989).
 80. Paillard E. *et al.*, Polymer electrolytes based on new aryl-containing lithium perfluorosulfonates, *J. Fluor. Chem.*, 134, 72–76 (2012).
 81. Fan L. Z., Wang X. L., Long F., Wang X., Enhanced ionic conductivities in composite polymer electrolytes by using succinonitrile as a plasticizer, *Solid State Ionics*, 179, 1772–1775 (2008).
 82. Nagaoka K., Naruse H., Shinohara I., Watanabe M., High ionic conductivity in poly(dimethyl siloxane-co-ethylene oxide) dissolving lithium perchlorat, *J. Polym. Sci. Polym. Lett. Ed.*, 22, 659–663 (1984).
 83. Fonseca C. P., Neves S., Characterization of polymer electrolytes based on poly(dimethyl siloxane-co-ethylene oxide), *J. Power Sources*, 104, 85–89 (2002).
 84. J. F. Le Nest, S. Callens, A. Gandini, A new polymer network for ionic conduction, *Electrochim Acta*, 37, 1585–1588 (1992).
 85. H. Cheradame, A. Gandini, A. Killis, Mechanism of high ionic conductivity in elastomeric networks, *J. Power Sources*, 9, 389 – 395 (1983).
 86. A. Killis, J.F. LeNest, A. Gandini, Correlation among transport properties in ionically conducting cross-linked networks, *Solid State Ionics*, 14, 231–237 (1984).
 87. M.C. Borghini, M. Mastragostino, Reliability of lithium batteries with crosslinked polymer electrolytes, *Electrochim Acta*, 41, 2369–2373 (1996).
 88. J.-Y. Kim, Ionic conduction behavior of network polymer electrolytes based on phosphate and polyether copolymers, *Solid State Ion*, 124, 91–99 (1999).
 89. G. Tillet, B. Boutevin, Chemical reactions of polymer crosslinking and post-crosslinking at room and medium temperature, *Prog. Polym. Sci.*, 36, 191–217 (2011).
 90. D. Benrabah, J.-Y. Sanchez, New polyamide-ether electrolytes, *Electrochim. Acta*, 37, 1737 (1992).
 91. F. Alloin F, J.-Y. Sanchez, Electrochemical behaviour of lithium electrolytes based on new polyether networks, *J. Electrochem. Soc.*, 141, 1915 (1994).
 92. F. Alloin, J.-Y. Sanchez., New solvating polyether networks, *Electrochim. Acta*, 40, 2269 (1995).
 93. Thiam A., Iojoiu C., Leprêtre J. C., Sanchez J. Y., Lithium salts based on a series of new

- aniliny-perfluorosulfonamide salts and their polymer electrolytes, *J. Power Sources*, 364, 138–147 (2017).
94. Visakh P. M., Thomas S., Oksman K., Mathew A. P., Crosslinked natural rubber nanocomposites reinforced with cellulose whiskers isolated from bamboo waste: Processing and mechanical/thermal properties, *Compos. Part A Appl. Sci. Manuf.*, 43, 735–741 (2012).
 95. Paillet M., Dufresne A., Chitin whisker reinforced thermoplastic nanocomposites, *Macromolecules*, 34, 6527–6530 (2001).
 96. Q. Li, J. Zhou, L. Zhang. Structure and properties of the nanocomposite films of chitosan reinforced with cellulose whiskers. *Wiley Intersci.* 48, 2215–2221 (2009).
 97. Azizi Samir, M. A. S., Alloin, F., Sanchez, J. Y., El Kissi, N., Dufresne A., Preparation of cellulose whiskers reinforced nanocomposites from an organic medium suspension, *Macromolecules* 37, 1386–1393 (2004).
 98. Samir M. A. S. A., Alloin F., Sanchez J. Y., Dufresne A., POE-based nanocomposite polymer electrolytes reinforced with cellulose whiskers M., *Electrochem. acta*, 50, 3879–3903 (2005).
 99. Papke B. L., Vibrational spectroscopic determination of structure and ion pairing in complexes of poly(ethylene oxide) with lithium salts, *J. Electrochem. Soc.*, 129, 1434 (1982).
 100. Sesner J. S., Solvation effect upon glass transition temperature and conductivity of poly(ethylene oxide) with alkali thiocyanates, *Macromolecules*, 22, 3029–3037 (1989).
 101. J. J. Fontanella *et al.*, Complexed with alkali metal salts PEO₈-NaClO, 10, 1139–1145 (1983).
 102. Besner S., Vallée A., Bouchard G., Effect of anion polarization on conductivity behavior of Poly(ethylene oxide) complexed with alkali salts, *Macromolecules*, 25, 6480–6488 (1992).
 103. Dhumal N. R., Gejji S. P., Theoretical studies in local coordination and vibrational spectra of M⁺CH₃O(CH₂CH₂O)_nCH₃ (n = 2-7) complexes (M = Na, K, Mg and Ca), *Chem. Phys.*, 323, 595–605 (2006).
 104. Shen X. *et al.*, Quasi-solid-state dye-sensitized solar cells based on gel electrolytes containing different alkali metal iodide salts, *Solid State Ionics*, 179, 2027–2030 (2008).
 105. Jeong K., Park S., Lee S. Y., Revisiting polymeric single lithium-ion conductors as an organic route for all-solid-state lithium ion and metal batteries, *J. Mater. Chem. A*, 7, 1917–1935 (2019).
 106. Sun X. G., Kerr J. B., Synthesis and characterization of network single ion conductors based on comb-branched polyepoxide ethers and lithium Bis(allylmalonato)borate, *Macromolecules*, 39, 362–372 (2006).
 107. Zhang H. *et al.*, Single lithium-ion conducting solid polymer electrolytes: Advances and perspectives, *Chem. Soc. Rev.*, 46, 797–815 (2017).
 108. J. Bannister *et al.*, Ionic conductivities for poly(ethylene oxide) complexes with lithium salts of monobasic and dibasic acids and blends of poly(ethylene oxide) with lithium salts of anionic polymers, *Polymer*, 25, 1291–1296 (1984).
 109. S. Zhang *et al.*, Complexes composed of poly[oligo(oxyethylene) methacrylate] and the alkali metal salts of poly(sulfoalkyl methacrylate), *Polym. J.*, 23, 73–78 (1991).
 110. C. H. Park *et al.*, Blended polymer electrolytes based on poly(lithium 4-styrene sulfonate) for the rechargeable lithium polymer batteries, *Electrochim. Acta*, 50, 375–378 (2004).
 111. Watanabe M., Suzuki Y., Nishimoto A., Single ion conduction in polyether electrolytes

- alloyed with lithium salt of a perfluorinated polyimide, *Electrochim. Acta*, 45, 1187–1192 (2000).
112. Djellab K., Meziane R., Armand M., Bonnet J.-P., Courty M., Single-ion polymer electrolytes based on a delocalized polyanion for lithium batteries, *Electrochim. Acta*, 57, 14–19 (2011).
 113. Q. Ma, H. Zhang, C. Zhou, L. Zheng, P. Cheng, J. Nie, W. Feng, Y.-S. Hu, H. Li, X. Huang, L. Chen, Single lithium-ion conducting polymer electrolytes based on a super-delocalized polyanion, *Angew. Chem. Int. Ed.*, 55, 2521–2525 (2016).
 114. Z. Shaoa et al., Single lithium-ion conducting poly(tetrafluorostyrene sulfonate) – polyether block copolymer electrolytes, *Polym. Chem.*, 8, 785–794 (2017).
 115. Bouchet R. et al., Single-ion BAB triblock copolymers as highly efficient electrolytes for lithium-metal batteries, *Nat. Mater.*, 12, 452–457 (2013).
 116. Inceoglu S. et al., Morphology-conductivity relationship of single-ion-conducting block copolymer electrolytes for lithium batteries, *ACS Macro Lett.*, 3, 510–514 (2014).
 117. Rojas A. A. et al., Effect of lithium-ion concentration on morphology and ion transport in single-ion-conducting block copolymer electrolytes, *Macromolecules*, 48, 6589–6595 (2015).
 118. Luca Porcarelli, M. Ali Aboudzadeh, Alexander S. Shaplov, Claudio Gerbaldi, Single-ion triblock copolymer electrolytes based on poly(ethylene oxide) and methacrylic sulfonamide blocks for lithium metal batteries, *J. Power Sources*, 364, 191–199 (2017).
 119. Chainika Jangu, Alice M. Savage, Zhiyang Zhang, Alison R. Schultz, Louis A. Madsen, Frederick L. Beyer, Sulfonimide-containing triblock copolymers for improved conductivity and mechanical performance, *Macromolecules*, 48, 4520–4528 (2015).
 120. Thelen J. L., Inceoglu S., Venkatesan N. R., Mackay N. G., Balsara N. P., Relationship between ion dissociation, melt morphology, and electrochemical performance of lithium and magnesium single-ion conducting block copolymers, *Macromolecules*, 49, 9139–9147 (2016).
 121. Phan T. N. T., Issa S., Gigmes D., Poly(ethylene oxide)-based block copolymer electrolytes for lithium metal batteries, *Polym. Int.*, 68, 7–13 (2019).
 122. N. Lago, O. Garcia-Calvo, J. M. Lopez del Amo, All-solid-state lithium-ion batteries with grafted ceramic nanoparticles dispersed in solid polymer electrolytes, *ChemSusChem*, 8, 3039–3043 (2015).
 123. Zheng X. et al., Sodium metal anodes for room-temperature sodium-ion batteries: Applications, challenges and solutions, *Energy Storage Mater*, 16, 6–23 (2019).
 124. Hwang J.-Y., Myung S.-T. & Sun Y.-K., Sodium-ion batteries: present and future, *Chem. Soc. Rev.*, 46, 3529–3614 (2017).
 125. Nohira T., Ishibashi T., Hagiwara R., Properties of an intermediate temperature ionic liquid NaTFSA-CsTFSA and charge-discharge properties of NaCrO₂ positive electrode at 423 K for a sodium secondary battery, *J. Power Sources*, 205, 506–509 (2012).
 126. Singh V. K., Singh S. K., Gupta H., Balo L., Tripathi A. K., Electrochemical investigations of Na 0.7 CoO₂ cathode with PEO-NaTFSI-BMIMTFSI electrolyte as promising material for Na-rechargeable battery, *J. Solid State Electrochem.*, 2, 1909–1919 (2018).
 127. Jian Z., Luo W., Ji X., Carbon electrodes for K-ion batteries, *J. Am. Chem. Soc.*, 137, 11566–11569 (2015).
 128. Vaalma C., Buchholz D., Passerini S., Non-aqueous potassium-ion batteries: a review. *Curr. Opin. Electrochem.*, 9, 41–48 (2018).

129. Komaba S., Hasegawa T., Dahbi M., Kubota K., Potassium intercalation into graphite to realize high-voltage/high-power potassium-ion batteries and potassium-ion capacitors, *Electrochem. commun.*, 60, 172–175 (2015).
130. Masese T. *et al.*, Rechargeable potassium-ion batteries with honeycomb-layered tellurates as high voltage cathodes and fast potassium-ion conductors, *Nat. Commun.*, 9, 1–12 (2018).
131. Hosaka T., Kubota K., Kojima H., Komaba S., Highly concentrated electrolyte solutions for 4 v class potassium-ion batteries, *Chem. Commun.*, 54, 8387–8390 (2018).
132. Shao Y. *et al.*, Coordination chemistry in magnesium battery electrolytes: how ligands affect their performance, *Sci. Rep.*, 3, 4–11 (2013).
133. Yoo H. D. *et al.*, Mg rechargeable batteries: an on-going challenge, *Energy Environ. Sci.*, 6, 2265–2279 (2013).
134. Velikokhatnyi O. I. *et al.*, Rechargeable magnesium battery: current status and key challenges for the future, *Prog. Mater. Sci.*, 66, 1–86 (2014).
135. Kakibe T., Hishii J. Y., Yoshimoto N., Egashira M., Morita M., Binary ionic liquid electrolytes containing organo-magnesium complex for rechargeable magnesium batteries, *J. Power Sources*, 203, 195–200 (2012).
136. Shimamura O., Yoshimoto N., Matsumoto M., Egashira M., Morita M., Electrochemical co-deposition of magnesium with lithium from quaternary ammonium-based ionic liquid, *J. Power Sources*, 196, 1586–1588 (2011).
137. L. L. Yang *et al.*, Ionic conductivity in complexes of poly(ethylene oxide) and MgCl_2 . *J. Electrochem. Soc.*, 133, 1380 (2006).
138. Andrew Patrick, Malcolm Glasse, Roger Latham, Novel solid state polymeric batteries, *Solid State Ionics*, 18–19, 1063–1067 (1986).
139. Liebenow C., Mantey S., Preparation of solutions of amidomagnesium chlorides in poly(ethylene oxide) and their characterization by conductivity measurements, *J. Solid State Electrochem*, 7, 313–316 (2003).
140. Tripathi S. K., Jain A., Gupta A., Mishra M., Electrical and electrochemical studies on magnesium ion-based polymer gel electrolytes, *J. Solid State Electrochem.*, 16, 1799–1806 (2012).
141. Li W. *et al.*, Effect of water and organic solvents on the ionic dissociation of ionic liquids, *J. Phys. Chem. B*, 111, 6452–6456 (2007).
142. Watkins T., Buttry D. A., Determination of Mg^{2+} speciation in a TFSI-based ionic liquid with and without chelating ethers using raman spectroscopy, *J. Phys. Chem. B*, 119, 7003–7014 (2015).



Chapter 2
Ionic liquid-based electrolytes

Abstract

In this chapter, the effect of several alkali/alkaline earth cations on the physical and transport properties of ionic liquid (IL) based electrolyte is carried out. The IL 1-butyl-3-methylimidazolium bis(trifluoromethanesulfonyl)imide (BMIm TFSI) combined with different alkali/alkaline-earth metals-based TFSI salts, at certain concentrations of salt, are investigated using multiple characterization techniques, including: differential scanning calorimetry (DSC), electrochemical impedance spectroscopy (EIS), rheology (for viscosity measurement), pulsed-field gradient nuclear magnetic resonance spectroscopy (PFG-NMR) (for ionic diffusivity measurement), infrared spectroscopy (IR), etc. The work aim is to compare the blends BMIm TFSI doped alkali/alkaline-earth metals to determine the impact of concentration and nature of cations on the physical/ conduction/ diffusion behaviors of IL.

1. Introduction

The growing demand for new rechargeable energy storage, beyond lithium batteries, has been requiring more suitable materials for higher performances, long cyclability, and safer devices. The increasing use of lithium batteries in the mobile equipment leads to the fact that lithium mineral resource will be further out of stock. Based on the wide availabilities and the alternative chemical/electrochemical properties, alkali/alkaline earth elements have been considering as the good alternatives for low cost and higher performable batteries.

Safety is a drawback for any successful technology, including the batteries. Recently, the use of ionic liquids (ILs) catches more attention for future energy, thanks to their unique characteristics, such as non-volatility, non-flammability, thermal/electrochemical stability, environmentally friendly, etc. The IL-based electrolytes are generally obtained by mixing and dissolving a fraction of inorganic salt in an IL. The ion transport mechanism of Li^+ cation and its environment in IL have been studied for years by both experimental methods, and molecular dynamic (MD) simulations.^{1,2} Many studies of sodium-based ILs achieved the pretty good results as compared to those of lithium electrolytes,^{3,4} as well as the magnesium-based ILs for secondary magnesium-ion batteries.^{5,6} These studies proposed the new tendencies for developing the alkali/alkaline-earth based ILs for electrolyte application. However, none of them reported the systematic and comprehensive studies about the influence of these coordinated cations inside an IL on the physical and transport properties of the blends (e.g. viscosity, ionic conductivity, transport properties, etc.).

2. Salt solubilization

The ionic liquid (IL) BMIm TFSI purchased from Solvionic[®] was opened in an Argon filled glove box and was used as received. The LiTFSI and CsTFSI purchased from Sigma Aldrich and Solvionic[®], respectively, were used without any additional purification. The other TFSI salts including NaTFSI, KTFSI, $\text{Mg}(\text{TFSI})_2$ and $\text{Ca}(\text{TFSI})_2$ were synthesized via an acid-base reaction between the alkali/alkaline-earth hydroxides with the HTFSI acid. The synthesis and purification protocols are described in the experimental annex.

In this work, the molar fraction of dissolved salt is defined as the number of M^{n+} ions (n) per the number of BMIm⁺ cations (n_{BMIm}), denoted as ' f ', $f = \frac{n}{n_{\text{BMIm}}}$, and the value of molar fraction f was varied between $0.05 \leq f \leq 1.0$. The solubility of TFSI salts is presented in Table 1. The IL/TFSI-based salt electrolytes were prepared by adding a required amount of salt in BMIm TFSI, in a glove box. Magnetic stirring was used to mix these solutions at 80 °C for approximately 72 h. The blends were cool down to room temperature (RT), and the solubility of salt in IL was carefully observed

through the appearance of precipitates or recrystallization of salt after 24 h. The solubility of different salts in IL was asserted from the stability of the homogeneous solution at RT.

Table 1 Solubility of several alkali/alkaline-earth TFSI salts in BMIm TFSI (✓: soluble, X: insoluble)

Molar fraction f	LiTFSI	NaTFSI	KTFSI	CsTFSI	Mg(TFSI) ₂	Ca(TFSI) ₂
0.05	✓	✓	✓	✓	✓	X
0.1	✓	✓	✓	✓	✓	
0.2	✓	✓	✓	✓	✓	
0.3	✓	✓		✓	✓	
0.4	✓	X	X	✓	✓	
0.5 to 1.0	✓			X	✓	

Table 1 presents the solubility limits of the different cation's TFSI salts inside IL (BMIm TFSI). While the LiTFSI is highly soluble in IL up to $f > 1.0$, the bigger alkali ions i.e. Na, K, Cs based TFSI salts become less soluble in IL, for example: until $f = 0.3$ for NaTFSI, $f = 0.2$ for KTFSI, and $f = 0.4$ for CsTFSI. For the alkali-earth metals, while the Mg(TFSI)₂ is dissolved easily in IL up to $f = 1.0$, the Ca(TFSI)₂ is insoluble. Due to the large variations in solubility of the TFSI-based salts in BMIm TFSI, we decided to:

- (1) study the impact of salt concentration for the smallest Li⁺, and the bigger alkali Cs⁺ ion in the concentration range of f between 0.1 to 0.4. Also, these two cations have the isotopes which are NMR sensitive (⁷Li and ¹³³Cs) and are favorable to obtain a full set of data in terms of transport properties (dissociation ratio, alkali transport number, fragility, etc.). The blends of LiTFSI dissolved in BMIm TFSI have been investigated in several studies in the last two decades.^{7,8,9} However, it is necessary to own our reference system to verify the characterization methods and conditions used for the following work.
- (2) extend these analyses to two other less soluble alkali cations e.g. Na⁺ and K⁺ at $f = 0.2$, as well as for the earth alkaline Mg²⁺. For the divalent Mg²⁺ ion, each cation bears two positive charges, so we decided to study the two salt fraction of $f = 0.1$ and 0.2. As these elements do not present a favorable isotope for NMR, the analysis of transport mechanisms will remain more qualitative/comparative than quantitative.

3. Effect of salt concentration

3.1. BMIm TFSI and the binary system [Li][BMIm][TFSI]

3.1.1. Thermal characteristics

The thermal behavior of IL/LiTFSI was measured by DSC measurement from -150 to 100 °C, following two identical heating/cooling cycles, under N₂ flux, with a scan rate of 10 °C/min for both cycles. The IL electrolytes were filled in the aluminum crucible for DSC in a glove box to avoid the contamination of humidity. From the cooling scan (not present), the neat BMIm TFSI shows only one glass transition temperature (T_g), which is also observed during the heating stage (Fig. 1A), at $-87 \pm 2^\circ\text{C}$, as well as two other thermal transitions relating to a cold crystallization, and a melting point at $-42 \pm 2^\circ\text{C}$ and $-1 \pm 2^\circ\text{C}$, respectively. These behaviors fit well to the values reported in the literature for the neat BMIm TFSI.¹⁰

On the other hand, the addition of LiTFSI induces a regular increase of T_g value as the salt concentration increases. As seen in Fig. 1B, all these electrolytes do not show any other phase transitions, such as the melting and recrystallization peaks, from both cooling and heating scans, as it was observed for the neat IL. Similar behavior reported by Pitawala et al.⁹ showed that the crystallization process was completely suppressed with the presence of salt in the LiTFSI based-IL. It is explained due to a large size difference between the Li⁺ ion and IL cation/anion which prevents the ‘efficient packing’ inside the blend IL/LiTFSI. However, the glass transition temperature is very sensitive to the electrolyte composition. As seen in Fig. 1B, at a low concentration of Li ($f = 0.1$), the T_g value of IL/LiTFSI is $-83 \pm 2^\circ\text{C}$, which is slightly higher than the neat IL.

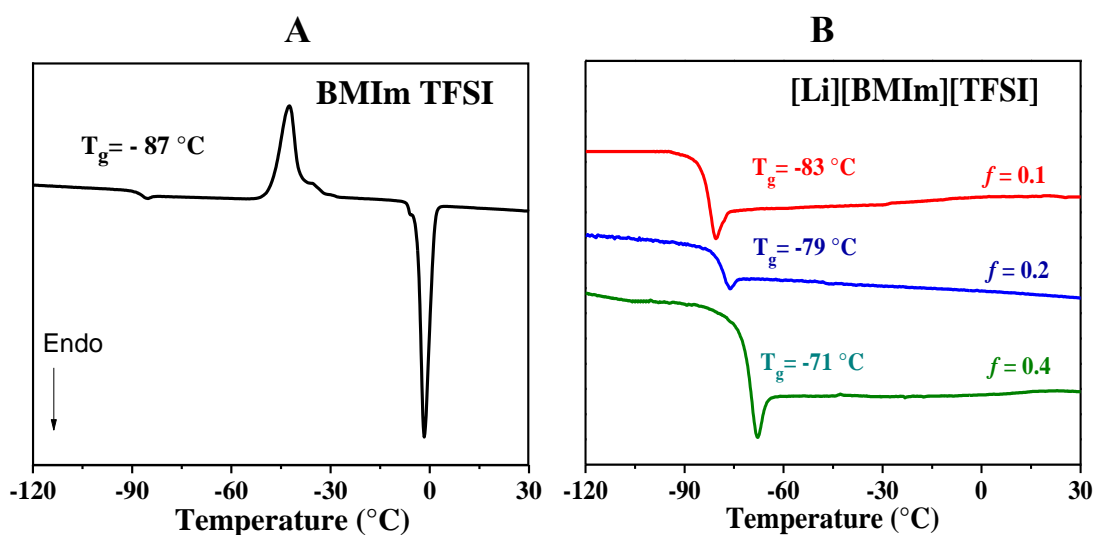


Fig. 1 The second DSC heating scans of (A) the neat BMIm TFSI and (B) the binary systems [Li][BMIm][TFSI] at different molar fraction f .

Moreover, the T_g values increase linearly with the ratio of lithium salt, as observed in Fig. 2. The T_g values of $-79 \pm 2^\circ\text{C}$ and $-71 \pm 2^\circ\text{C}$ are measured for the blends IL/LiTFSI at $f = 0.2$ and 0.4 , respectively. Thus, for $0.1 \leq f \leq 0.4$, Duluard et al.¹¹ reported that the lithium solvation in BMIm TFSI was essentially coordinated by two TFSI⁻ anions and formed the $[\text{Li}(\text{TFSI})_2]^-$ clusters. It is probably the increase in quantity of Li complexes, as well as the formation of bigger macroionic species such as $\text{Li}^+ \dots (\text{TFSI})_n \dots \text{Li}^+$ that could explain a remarkable increase in T_g values for the blends IL/LiTFSI.

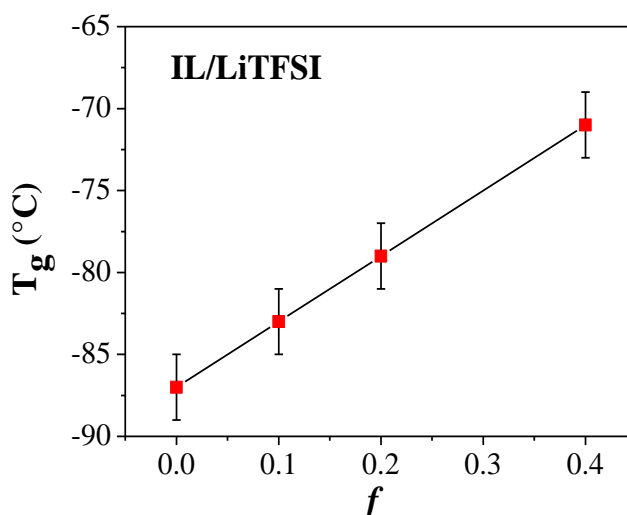


Fig. 2 Evolution of T_g values for the $[\text{Li}][\text{BMIm}][\text{TFSI}]$ systems as a function of molar fraction of salt. The error bars are $\pm 2^\circ\text{C}$ for all samples.

In conclusion, the presence of LiTFSI in BMIm TFSI suppresses the crystallization and melting transitions of the neat IL, and thus increases the T_g values by forming the interactions/coordination between Li^+ and TFSI⁻ anions. From low to an intermediate concentration of salt ($0.1 \leq f \leq 0.4$), the T_g and thus the mobility of ions proportionally decreases. To have more information on mobility the experimental data for viscosity and density of these electrolytes are carried out in the next part.

3.1.2. Density and viscosity

- *Density*

Density of the neat IL and its mixtures was determined by the mass (mg) of a unity volume (mL) of substance. In this study, density of the IL-based electrolytes was measured in a glove box, at 25°C , and detailed protocol is described in the experimental annex. Density of BMIm TFSI is $1.43 \pm 0.01 \text{ g}\cdot\text{cm}^{-3}$, which corresponds to the literature value.⁷ The variation of experimental densities with the molar fraction of salt are plotted in Fig.3. The value increases slightly from $1.43 \pm 0.01 \text{ g}\cdot\text{cm}^{-3}$ for the neat IL, to $1.45 \pm 0.01 \text{ g}\cdot\text{cm}^{-3}$ for $[\text{Li}][\text{BMIm}][\text{TFSI}]$ ($f = 0.1$). Thus, density of the binary system containing Li^+ increases proportionally with increasing the concentration of salt up to $f = 0.4$. These data are in agreement with those reported by Monti et al.¹²

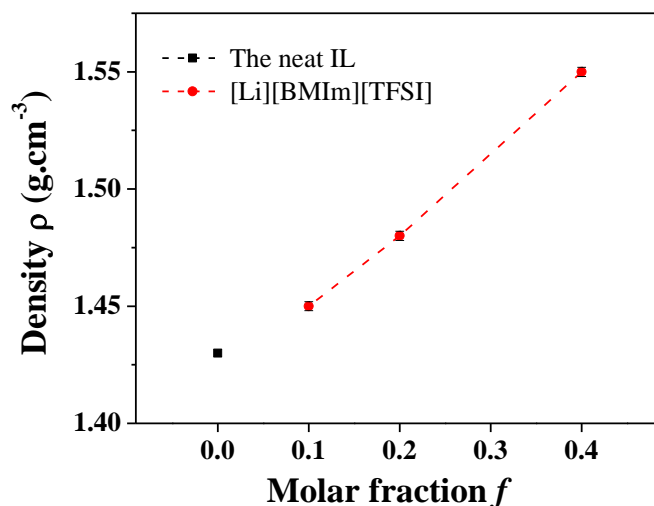


Fig. 3 Density of the neat IL (black) and the binary systems [Li][BMIM][TFSI] (red) with different concentration of salt, at 25 °C. The error bars are ± 0.01 for all samples.

However, our experimental setup for density measurement is not suitable to obtain the values at different temperatures. Meanwhile, the further evaluation of our systems requires these values to calculate the molar conductivity and the degree of dissociation. For this reason, we decided to assume the evolution of density with temperature may exhibit similar behavior as that of the pure ILs¹², and we choose to use the parameters determined experimentally in the literature⁹ for BMIm TFSI. The parameters reported by Tokuda et al.¹³ for the neat BMIm TFSI followed an equation of $\rho(g.cm^{-3}) = b - a.T$ (with $a = 9.40 \times 10^{-4}$ and $b = 1.72$) in the studied range of temperature between -10 and 90 °C. Then for the blends with LiTFSI, the same slope of $a = 9.40 \times 10^{-4}$ was kept for all samples, while recalculating the values of intercept (b) with our experimental density data at 25 °C.

- *Viscosity*

Viscosity is known as an important property which is directly related to the mobility of ions in IL, i.e. the ionic conductivity and diffusivity. Viscosity of the neat IL and the blends IL/Li salt are generally influenced by the nature of IL cation/anion, the interaction between anion-cation, anion-Li, etc. Here, viscosity of BMIm TFSI and the binary systems [Li][BMIm][TFSI] with $0.1 \leq f \leq 0.4$ are measured at the different temperatures from -10 to 90 °C, under a N₂ flux.

At 25 °C, viscosity of the neat IL is 0.051 Pa.s and increases with the presence of LiTFSI such as 0.063 Pa.s at $f = 0.1$ to 0.21 Pa.s for $f = 0.4$. Viscosity data for the IL/LiTFSI systems at 25 °C is plotted linearly with the molar fraction f , as seen in Fig. 4A. Increasing the salt concentration proportionally increases the viscosity of IL. Based on the literature, the neat IL exhibits the lowest viscosity comparing to the blend IL/salt and becomes less viscous while increasing the temperature.^{14,15}

Moreover, viscosity of these blends varies with the temperature and fits well to a VFT model ($\eta = A \exp[E_a/k_B/(T - T_0)]$), where A is the relative parameter, E_a is the pseudo-activation energy (eV), k_B is the Boltzmann constant, and T_0 is the T_g value determined by DSC measurements (in 3.1.1). The VTF plots of $\ln(\eta)$ versus $1000/(T-T_0)$ are in Fig. 4B and the fitting data are shown in Table 2. Adding the LiTFSI increases the energy activation of the binary systems as compared to the neat IL, but the VTF curves show nearly the same slope for all of these blends IL/LiTFSI indicating rather similar E_a values.

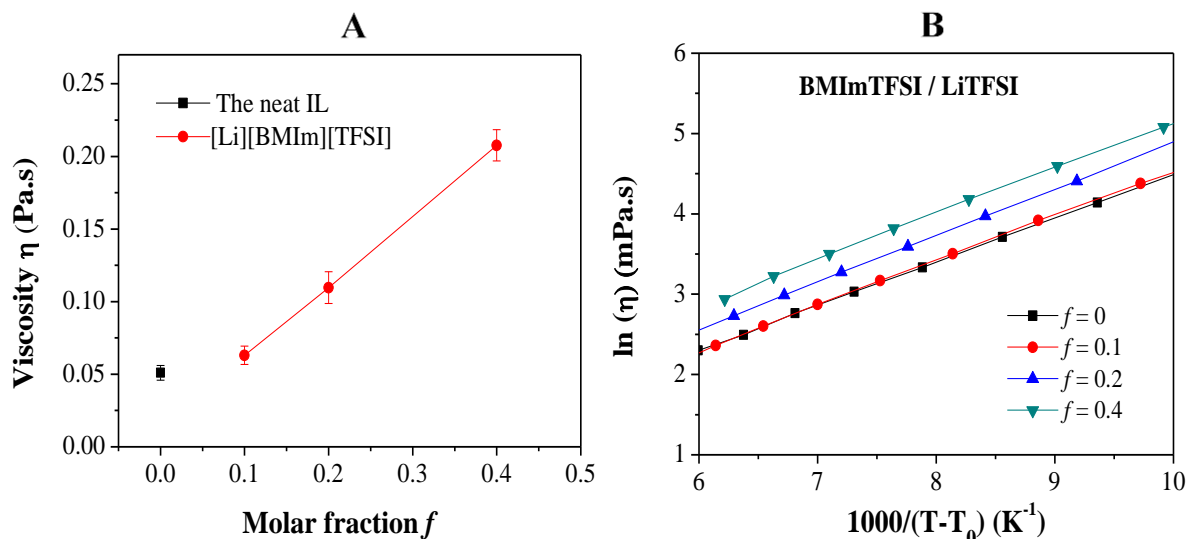


Fig. 4 (A) Viscosity of the neat BMIm TFSI and the binary systems [Li][BMIm][TFSI] with different molar fraction f , at 25 °C; (B) The VTF plots for viscosity data. The error bars are 10 % for all samples.

Table 2 The VTF's fitting factors for viscosity data.

Molar fraction f	$\eta = A \exp[E_a/k_B(T - T_0)]$		
	A (mPa.s)	E_a (meV)	$T_0 \pm 2$ (K)
0	0.83 ± 0.06	37.82 ± 0.46	186
0.1	0.69 ± 0.03	41.89 ± 0.32	190
0.2	0.87 ± 0.06	43.79 ± 0.46	194
0.4	0.47 ± 0.28	44.92 ± 0.60	202

3.1.3. Conductivity

The ionic conductivity represents for the number and mobility of all charged species available in a system and is described as:¹⁶

$$\sigma = F \sum_i Z_i C_i a_i \quad (1)$$

Where F is the Faraday's constant, Z_i is the charge, C_i is the concentration and a_i is the mobility of charged piece ' i '. For the neat IL and the IL doped Li⁺, ionic conductivity is determined from the

Nyquist plot obtained by electrochemical impedance spectroscopy (EIS) measurements, and molar conductivity was calculated from the density and ionic conductivity.

- *Ionic conductivity*

Ionic conductivity of BMIm TFSI and the blends IL/LiTFSI were measured following a heating/cooling process from -10 to 90 °C. The conductivity cell for liquid electrolyte was prepared in a glove box. The data from the heating and cooling cycles are rather similar, and only the cooling scans are reported in this work. An example of a Nyquist plot for the neat BMIm TFSI at 25 °C is presented in Fig. 5. The impedance spectrum is fitted with an equivalent circuit (insert figure in Fig. 5) to determine the resistance of electrolyte (R_{el}) (corresponding to the coupling between the semi-circle and the Warburg line). The ionic conductivity was calculated following the relation below:

$$\sigma = \frac{l}{R_{el} * S} = \frac{\kappa}{R_{el}} \quad (2)$$

Where σ is the ionic conductivity ($S.cm^{-1}$); l is the distance between two electrodes (cm); R_{el} is the electrolyte resistance (Ω), S is the electrodes' surface (cm^2), and κ is the cell constant, and is determined with a KCL 0.1 M solution at 25 °C.

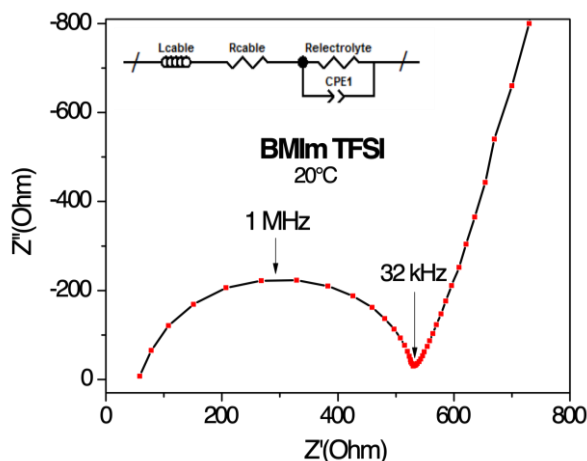


Fig. 5 The Nyquist plot of BMIm TFSI at 20 °C, and the equivalent circuit for impedance spectrum fitting.

The conductivity data obtained were plotted as a function of temperature in Fig. 6A. As seen, conductivity increases while increasing the temperature from 263 to 363 K (0 to 90 °C), which is directly in agreement with the evolution of viscosity for all IL-based electrolytes.¹⁷ When the solution is less viscous, higher conductivity is measured. Thus, at 25 °C, conductivity of the neat commercial BMIm TFSI is 4.0 mS.cm^{-1} , while adding LiTFSI, conductivity of the blends IL/LiTFSI decreases to 3.2 mS.cm^{-1} for $f = 0.1$, and 1.2 mS.cm^{-1} at higher molar fraction of $f = 0.4$. The ionic conductivity of all mixtures remain lower at higher temperature however the difference in conductivity between different concentrations of LiTFSI reduces at higher temperatures as compared with RT. At the highest temperature of 90 °C, conductivity of IL/LiTFSI at $f = 0.1$ is 21.0 mS.cm^{-1} , which is almost similar to the neat IL. Our results are closed to those reported by Monti et al.¹² for the $\text{Li}_{0.15}\text{BMIm}_{0.85}\text{TFSI}$

composition, which contained almost the same salt fraction as our blend IL/LiTFSI at $f = 0.2$, e.g. 8.3 mS.cm^{-1} and 8.1 mS.cm^{-1} at 60°C , respectively.

Moreover, the conductivity is well described with a VTF model ($\sigma = A \exp[E_a/k_B(T-T_0)]$). The fitting's data are showed in Table 3 and the VTF graphs are presented by plotting the $\ln(\sigma)$ with $1000/(T-T_0)$ in Fig. 6B. The fitting curves for these electrolytes are linear (in a $\ln(\sigma) = f(1000/(T-T_0))$ scaled plot), and the addition of salt significantly changes the slopes as compared to the neat IL. However, the blends IL/LiTFSI exhibit the parallel curves relating to nearly similar energy activation with the increasing the salt concentration.¹⁵

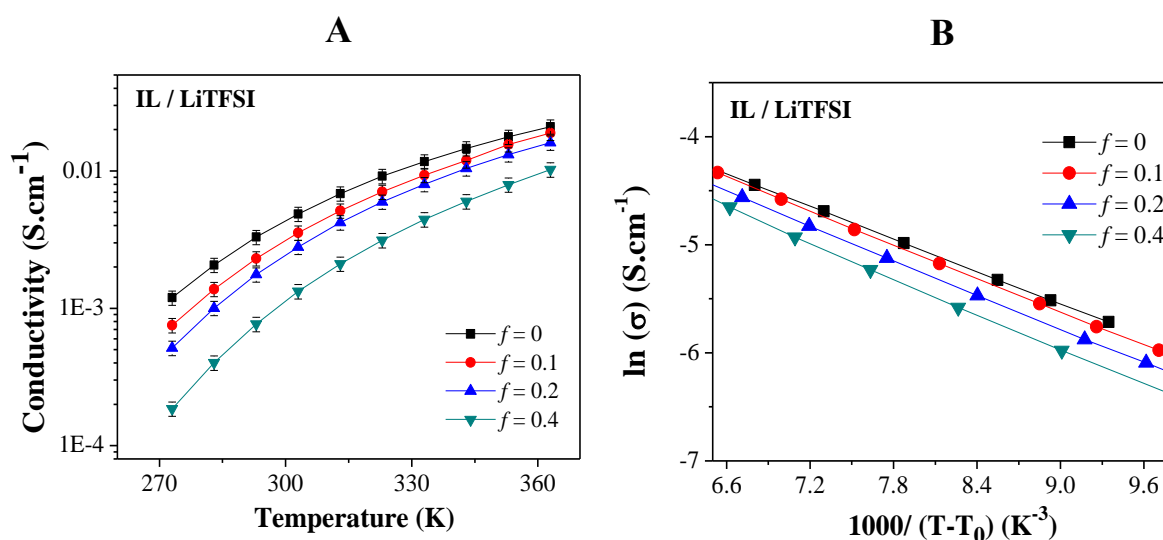


Fig. 6 (A) Ionic conductivity as a function of temperature (K) for the neat BMIm TFSI and the binary systems [Li][BMIm][TFSI]; (B) the VTF plots for conductivity data. The error bars are less than 10 % for all samples.

Table 3 VTF's fitting factors for conductivity data

Molar fraction f	$\sigma = A \exp[E_a/k_B(T-T_0)]$		
	A (S.cm^{-1})	E_a (meV)	$T_0 \pm 2$ (K)
0	0.36 ± 0.01	43.31 ± 0.10	186
0.1	0.55 ± 0.03	48.47 ± 0.88	190
0.2	0.38 ± 0.01	46.23 ± 0.18	194
0.4	0.41 ± 0.02	48.90 ± 0.47	202

To further observe the proportional effect of Li concentration and determine how increasing temperature can affect the ionic conductivity, the conductivity data are also plotted as a function of T_g/T in Fig. 7.

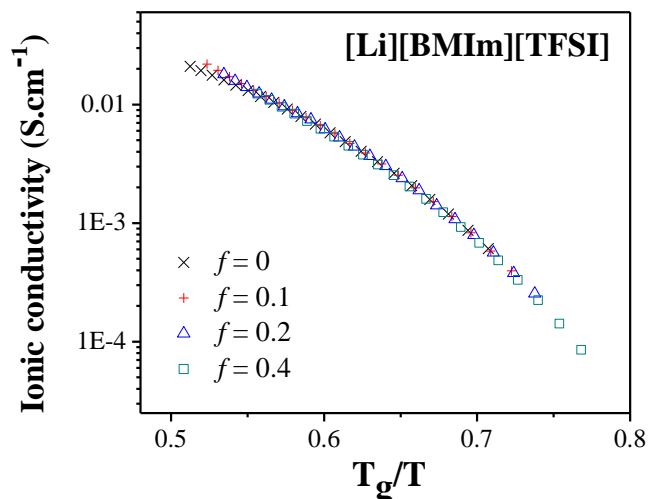


Fig. 7 Ionic conductivity with T_g/T for the neat BMIm TFSI and the binary systems [Li][BMIm][TFSI].

As seen, all of the data for a neat IL and the binary systems [Li][BMIM][TFSI] are plotted in an identical scaled representation as a function of T_g/T . All of the curves are lying on the same master curve, which means that the fragility of these systems does not change with the addition of lithium salts. These results are similar to those reported by Pitawala et al.⁹, on various IL/salt systems. This also means that the structuration/ inhomogeneity of the IL is not perturbed by the addition of salt and that the conduction processes inside these electrolytes are dominated by the viscous properties of these liquids.

In conclusion, ionic conductivities of the neat IL and the binary systems IL/LiTFSI are dominated by the overall ionic mobility. The presence of LiTFSI decreases the IL conductivity by increasing the IL viscosity, which is strongly related to the evolution of glass transition temperatures. Thus, conductivity decreases proportionally with the quantity of salt dissolved in IL from low to intermediate concentration and increases with the temperature following a VTF model. Moreover, the data show identical scaled representation with T_g/T indicating the same temperature dependence for all IL-based electrolytes.

- *Molar conductivity*

Another important parameter is the molar conductivity of IL-based electrolytes. The term ‘ionic conductivity’ does not involve the ionic concentration but only their mobility. In order to overcome the ionic concentration, the molar conductivity (Λ_m) is determined following the equation:

$$\Lambda_m = \frac{\sigma}{c} = \frac{\sigma^* M}{d} \quad (3)$$

Where σ is the ionic conductivity measured by EIS ($\text{S}\cdot\text{cm}^{-1}$); c is the ionic concentration ($\text{mol}\cdot\text{cm}^{-3}$); M is the molecular weight of the compound ($\text{g}\cdot\text{mol}^{-1}$); and d is the density ($\text{g}\cdot\text{cm}^{-3}$). Here, the molecular weight M of the blends are determined as:

$$M = \frac{f}{1+f} * M_{LiTFSI} + \frac{1}{1+f} * M_{BMImTFSI} \quad (4)$$

where f is the molar fraction of the blend IL/salt, and M_{LiTFSI} , $M_{BMImTFSI}$ are the molar mass of LiTFSI and the neat IL, corresponding to 287.07 g.mol⁻¹ and 419.36 g.mol⁻¹, respectively.

The molecular weight, ionic conductivity, and molar conductivity of these IL-based electrolytes at 25 °C are presented in Table 4. As seen, the molar mass decreases while increasing the salt concentration meaning that the big BMIm⁺ cation in IL is partially replaced by the smaller and lighter Li⁺ ions. Thus, molar conductivity shows a significant decrease when increasing the concentration of dissolved salts. At low concentration of Li ($f = 0.1$), the Λ_m is 0.9 S.cm².mol⁻¹, which is lower than the neat IL of 1.2 S.cm².mol⁻¹, and decreases even more to 0.6 S.cm².mol⁻¹ for $f = 0.2$, and 0.3 S.cm².mol⁻¹ for $f = 0.4$. Indeed, the molar conductivity is inversely proportional with the electrolyte's concentration, following the equation (3). When the blend becomes more concentrated, its viscosity significantly increases with the concentration of salt and leads to the decrease of conductivity.

In conclusion, the presence of salt shows the obvious impacts for both ionic conductivity and molar conductivity of the Li-based IL electrolytes relating to the increase of viscosity. Higher the concentration of salt dissolved in IL, lower the conductivity of the binary systems IL/LiTFSI obtains.

Table 4 Molecular weight and conductivity of the neat BMIm TFSI and the blends IL/LiTFSI at 25 °C.

Molar fraction f	$d \pm 0.01$ (g.cm ⁻³)	$M \pm 0.01$ (g.mol ⁻¹)	σ (mS.cm ⁻¹)	Λ_m (S.cm ² .mol ⁻¹)
0	1.43	419.36	4.0	1.2
0.1	1.45	405.21	3.2	0.9
0.2	1.48	392.92	2.3	0.6
0.4	1.55	362.82	1.2	0.3

3.1.4. Walden plot

The correlation between conductivity and the fluidity of an electrolyte is usually presented in a Walden diagram. The perfectly dissociated electrolytes at infinite dilution follows the Walden rule: $\Lambda \eta = constant$.¹⁸ A deviation from this rule is often observed, especially for the ionic liquids, and allows to have a qualitative estimation of the ionicity of a system (by observing the deviation from a reference line of KCl 0.01 mol.L⁻¹ solution¹⁸), even if the interpretation is still widely debated.^{19,20} Walden diagrams of the neat IL and the binary systems IL/LiTFSI are obtained by plotting the logarithm of molar conductivity (Λ_m) with the logarithm of the inverse of viscosity ($1/\eta$) from -10 to 90 °C. Thus, it is necessary to use the estimated data of density as a function of temperature, as mentioned in 3.1.2,

to calculate the Λ_m values. This hypothesis may add some uncertainty in the calculation of molar conductivities.

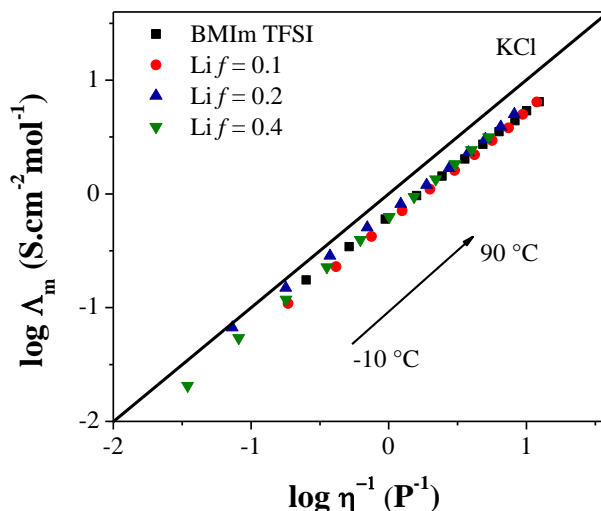


Fig. 8 The Walden plots of the neat BMIm TFSI and the blends IL/LiTFSI from -10 to 90 °C. The referenced line is the data of a KCl 0.01 mol.L⁻¹ solution.

The Walden diagrams present in Fig. 8 for BMIm TFSI and the binary electrolytes. As seen, all the curves are linear and lie slightly under the referenced line, corresponding to 'good ionic liquid' behavior such as stated in the classification of Xu et al.¹⁸ It could state that these IL-based mixtures are near the ideal case where all the ions are completely dissociated and they move independently from one to another. Here, the conductivity obtained for these IL-based electrolytes are slightly lower and the deviations indicate the formation of complexes between Li⁺ cation and TFSI anions. The evolution of these data with temperature shows the slopes which are different from the ideal electrolyte KCl which is explained by different energy activation calculated for viscosity and ionic conductivity data with the VTF model (see Table 2 and 3). Follow K. Hayammizu et al.¹⁵, the E_a values for viscosity are slightly different as compared to those of conductivity for the binary systems EMIm BF₄/LiBF₄. While decreasing the temperature, the data approach the ideal line of KCl indicating higher ionic dissociation at low temperature.

Also, remarkably, all the points are lying nearly on the similar master curve, whatever is the ratio of salt dissolved inside the IL. This result is rather different from those reported by M. Monterio et al.¹⁴, who studied the system of BMMIm TFSI/LiTFSI (BMMIm is 1-butyl-2,3-dimethyl-imidazolium cation) and found a significant evolution of the slope with the Li concentration. They explained this phenomenon by the formation of aggregates and 'tighter structure' which also increases the IL viscosity. However, the structure of the BMMIm cation is slightly different from ours BMIm cation, where a methyl group replaces the acidic hydrogen between the two nitrogen, and their results are reported with a salt fraction of $f=0.6$, which is higher than those used in our work.

These results prove that even if the neat IL and the IL-based electrolytes are entirely made of ions, their intricate structure leads to partial dissociation. It means that only a part of ions will, therefore, contribute to the conduction process. This will be also detailed from the measurements of self-diffusion coefficient by PFG-NMR technique.

3.1.5. Self-diffusion coefficient

Self-diffusion coefficients (D) of all species i.e. BMIm⁺ cation, TFSI⁻ anion, and Li⁺ ion were measured by ¹H, ¹⁹F and ⁷Li PFG-NMR method, respectively. Complementary to the ionic conductivity measurements, which are limited to charged species, the NMR method allows measuring the diffusivity of each chemical species whatever is the charged or neutral ion, as a well as the strong ion pair. The diffusion data for the neat IL and the binary systems IL/LiTFSI are plotted as a function of 1000/T in Fig. 9, and the values at RT are reported in Table 3. For the neat IL, the diffusion coefficient of BMIm⁺ is slightly higher as thus of the anion TFSI⁻, as it was also depicted in the previous studies.²¹ It is related to the high dissociation of the melting salt and the smaller size of the cation. A similar phenomenon was reported in the literature for most of imidazolium TFSI-based ILs.²¹ The D values of the two species increase with increasing the temperature from 298 K to 353 K (20 - 80 °C) in following with a VTF like behavior and rather similar evolutions. These phenomena have been reported in the literature.¹³

With the addition of Li salt, the diffusivity of both IL cation and anion significantly decrease, meanwhile the diffusion of Li⁺ cation is much lower. Even if it is counterintuitive because the Li⁺ cation is much smaller than the other ions, this characteristic behavior was depicted in all IL electrolytes^{9,14,22,23} and related to the strong complexation of Li⁺ cation by the TFSI⁻ anions. It is also confirmed by the reduction of D_{TFSI} values by a factor of two compared to the D_{BMIm} values while increasing the salt concentration. For example at highest temperature of 80 °C, the neat IL has a D_{BMIm} value of $17.1 \times 10^{-11} \text{ m}^2 \cdot \text{s}^{-1}$ and a D_{TFSI} value of $14.0 \times 10^{-11} \text{ m}^2 \cdot \text{s}^{-1}$, whereas for the IL/LiTFSI at $f = 0.4$, the self-diffusion coefficients of $8.7 \times 10^{-11} \text{ m}^2 \cdot \text{s}^{-1}$ and $4.8 \times 10^{-11} \text{ m}^2 \cdot \text{s}^{-1}$ are measured for the IL cation and anion, respectively. It indicates that with the presence of Li salt, the TFSI⁻ anion does not diffuse as a single ion. One reason that should be pointed out is the formation of the anionic cluster between Li⁺ and TFSI⁻ which significantly decreases the self-diffusion coefficients of anion. Thus, Li⁺ is always the slowest component despite its smaller/lighter size. A relative order of $D_{\text{BMIm}} > D_{\text{TFSI}} > D_{\text{Li}}$ is observed for all IL-based electrolytes.

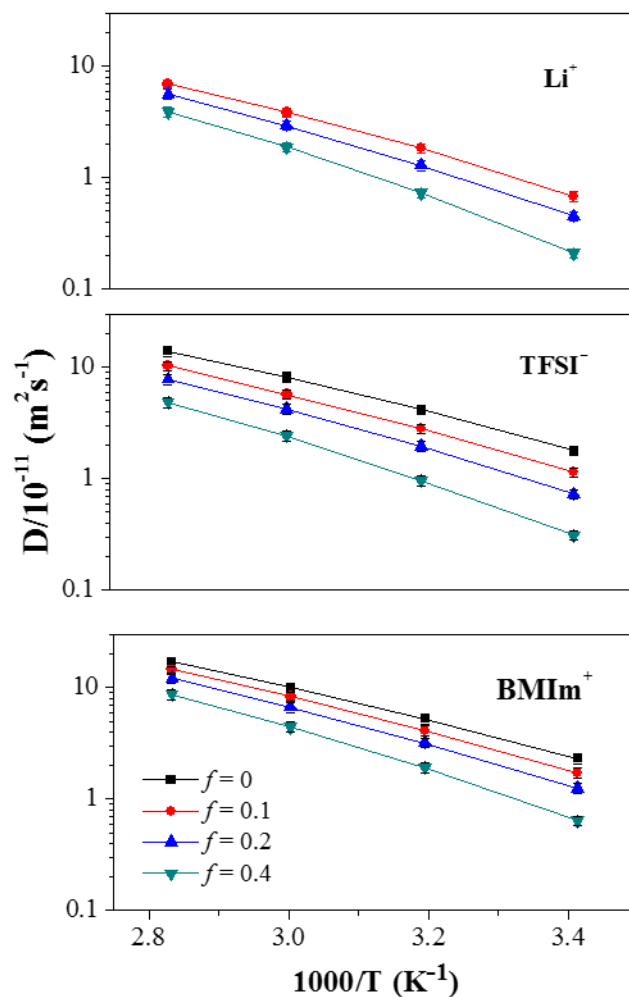


Fig. 9 The self-diffusion coefficient of Li^+ ion, TFSI $^-$ anion, and BMIm $^+$ cation for the neat BMIm TFSI and the blends IL/LiTFSI as a function of $1000/T$. The error bars are 10 % for all samples.

- *Analysis of mobility mechanisms*

The self-diffusion coefficient measured by PFG-NMR allows to reach a theoretical value of ionic conductivity (in assumption of the full ionic dissociation) following the equation.¹⁵

$$\Lambda_{NMR} = e^2 (N_{BMIm} D_{BMIm} + N_{TFSI} D_{TFSI} + N_{Li} D_{Li}) / (kT) \quad (5)$$

Where N_{BMIm} , N_{TFSI} , N_{Li} are the number of ions per a unit volume for BMIm $^+$, TFSI $^-$ and Li^+ ions, respectively, and D_{BMIm} , D_{TFSI} , D_{Li} are the self-diffusion coefficients of IL cation, anion, and Li^+ measured by ^1H , ^{19}F and ^7Li PFG- NMR spectroscopies, respectively. Conductivity at 20 °C for the neat IL and the binary systems IL/LITFSI calculated by equation (5) are presented in Table 5.

As seen, conductivity values determined by this equation are somehow extensively higher than those measured by EIS method (in 3.1.3), which is in agreement to the literature.²⁴ This difference is explained due to the assumption of the equation model. In fact, by PFG-NMR, we measure the self-diffusion for a define ion, and the method can not distinguish the differences between a free ion, ion

pairs, and aggregates. Moreover, the presence of LiTFSI in IL causes an important decrease of conductivity while increasing the salt concentration relating to higher viscosity of the blends IL/LiTFSI.

3.1.6. Dissociation degree and Li⁺ transference number

- *Dissociation degree*

Other interesting parameters of IL based electrolyte are the dissociation degree and Li transference number. Dissociation degree ‘ τ ’ is determined by the ratio between molar conductivity, measured by EIS, and those estimated by Nernst-Einstein equation¹³:

$$\tau = \frac{\Lambda_{imp}}{\Lambda_{NMR}} \quad (6)$$

where Λ_{imp} , Λ_{NMR} are the molar conductivity obtained by impedance and NMR spectroscopy, respectively. The τ value uses indicates directly the proportion of active ions which contributing to the ionic conduction in the diffusing species.²⁵ When the value of τ approaches to 1, all of the ions are supposed to be completely dissociated. Nevertheless, lithium dissolution in the IL is distinct from what happens in organic solvents, the IL compose completely by the ions at high concentration resulting in Li⁺ ion can easily form strong coordination with the TFSI anions. These hyper complexes consequently increase the viscosity and simultaneously decrease the ionic conduction/ diffusion ability. Thus, the dissociation degree does not significantly involve with the temperature.²⁶ The τ value of the neat IL and the blends IL/LiTFSI determined at 20 °C are shown in Table 5. A τ value of 0.63 is calculated for the neat IL which is in agreement to the value reported by H. Tokuda et al.²⁵. Moreover, the addition of salt increases the dissociation rate from 0.63 to 0.70 for the blend IL/LiTFSI at $f = 0.1$. And the τ value slightly increases while increasing salt concentration up to $\tau = 0.77$ for $f = 0.4$.

- *Li⁺ transference number*

Even the good ionic conductivity up to 1 mS.cm⁻¹ at RT is measured for these IL-based electrolytes, this measurement involves the contribution of all charged species and does not reflect the ability of lithium conductive in IL which is an essential property of a lithium electrolyte. To obtain the mobility of Li⁺ ion for these binary system IL/LiTFSI, the transference number of lithium, denoted as t_{Li}^+ , is calculated from the self-diffusion coefficients obtained by NMR following the equation below (the parameters were described in the equation (5)):

$$t_{Li}^+ = \frac{N_{Li}D_{Li}}{N_{BMIm}D_H + N_{TFSI}D_F + N_{Li}D_{Li}} \quad (7)$$

The lithium transference number, determined from equation (7), is presented in Table 5. Based on these values, the binary system IL/LiTFSI exhibit low transference number due to small concentration of Li^+ in a concentrated ionic environment. Thus, the ability of lithium transport increases with increasing the salt concentration such as $t_{\text{Li}}^+ = 0.023$ for the $f = 0.1$ sample to 0.072 for $f = 0.4$.

Table 5 Self-diffusion coefficient, molar conductivity, dissociation degree, and Li transference number of BMIm TFSI and the blends IL/LiTFSI at 20 °C.

Molar fraction f	D_{BMIm}	D_{TFSI}	D_{Li}	$\Lambda_{\text{imp}} * 10$	$\Lambda_{\text{NMR}} * 10$	$\tau * 10$	$t_{\text{Li}}^+ * 10^2$
	(* $10^{-11} \text{ m}^2 \cdot \text{s}^{-1}$)			(S.cm ² .mol ⁻¹)			
0	2.3	1.8	-	9.7	15.3	6.3	-
0.1	1.7	1.1	0.7	7.1	10.1	7.0	2.3
0.2	1.3	0.7	0.5	5.1	6.6	7.3	4.6
0.4	0.6	0.3	0.2	2.3	2.9	7.7	7.2

In conclusion, the study of physical and transport properties for the neat BMIm TFSI and the binary systems IL/LiTFSI with $0.1 \leq f \leq 0.4$ are carried out by the variety of experimental techniques. Most of the obtained results are in good agreement with those reported by different researched groups for years. Moreover, our work represents a nearly-full understanding about the dissociation of Li^+ in a define IL, from low to intermediate salt concentration, which was rarely reported in the literature.

The main purpose here is to set up the processes and conditions for investigating the systems based on IL doped alkali/alkaline-earth elements. In the next part, a binary system containing a bigger alkali ion i.e. the cesium Cs^+ cation in BMIm TFSI will be carried out. The effect of salt concentration on physical and transport properties of the blends IL/CsTFSI, with $0.1 \leq f \leq 0.4$, will be studied following the experimental approaches developed for Li-based electrolytes.

3.2. The binary system [Cs][BMIm][TFSI]

In this part, the behaviors of a binary system [Cs][BMIm][TFSI] is carried out by various techniques, as used for the blend IL/LiTFSI. The molar fraction of CsTFSI salt is varied from 0.1 to 0.4. To our knowledge, very few studies are dealing with the behavior of Cs⁺ salts dissolved in IL, and they are mainly focused to environmental issues such as extraction solvents, and also with the help of complexed molecules such as calixarene.^{27,28,29} Furthermore, none of these studies are dealing with a systematic study of the influence of such big alkali cation to the physicochemical properties of ternary systems.

Then, our focus will be to make a systematic study of the ternary system [Cs][BMIM][TFSI] in comparison with the [Li][BMIM][TFSI], with similar analytical tools (taking the opportunity that ¹³³Cs is the only other alkali nuclei very sensitive to NMR experiments) and highlight the effect of a larger dissolved cation.

3.2.1. Thermal characteristics

The Fig. 10A presents the DSC curves for the IL/CsTFSI mixtures ($f = 0.1, 0.2, 0.4$) recorded at the second heating stage with a scan rate of 10 °C/min. For all this composition range, they present only a glass transition, the crystallization process being suppressed, as it was also depicted inside Li based electrolytes. Moreover, the evolution of T_g values with the salt fraction for both Li and Cs systems are presented in Fig. 10B. The addition of salt proportionally increases the T_g values of both systems, but the effect is less pronounced in the case of Cs-based ILs. Actually, at $f = 0.1$, the difference of T_g value for two systems is only 2 °C, then increases to 4 °C for $f = 0.2$, and up to 8 °C different for $f = 0.4$ indicating a stronger effect of salt content for LiTFSI than its neighbor CsTFSI.

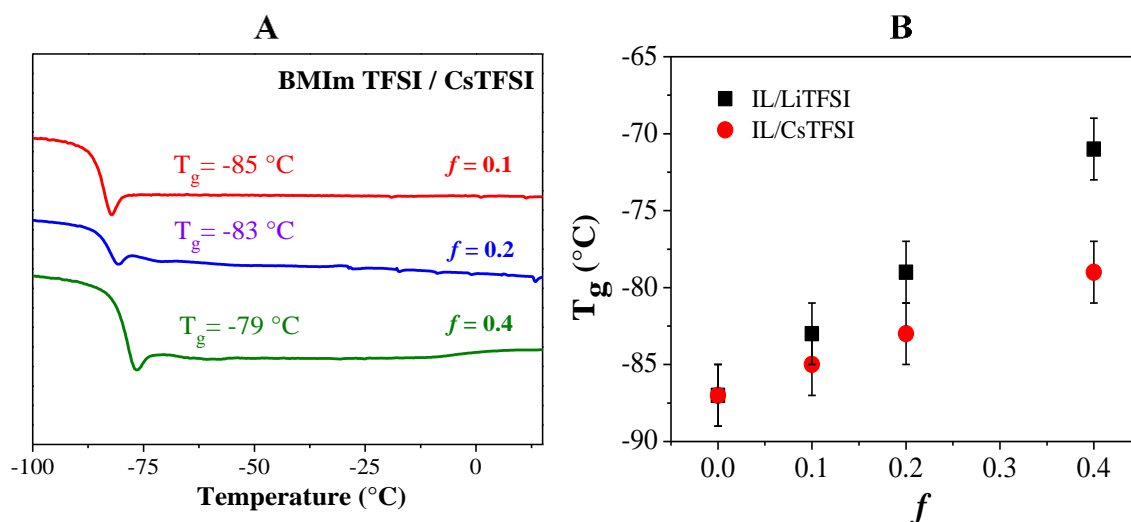


Fig. 10 (A) the second DSC heating scans of IL/CsTFSI, and the evolution of T_g values for LiTFSI and CsTFSI in IL at different molar fraction f , the error bars are ± 2 for all samples.

The Cs⁺ ions are bigger than the Li⁺ one ($r_{\text{Cs}^+}=1.67\text{-}1.88 \text{ \AA}$ and $r_{\text{Li}^+} = 0.59\text{-}0.92 \text{ \AA}$ depending on the alkali coordination³⁰) and their size is nearer from thus of the BMIM⁺ cation (a value of 2.75 \AA was reported by G. Feng et al.³¹ for the radius of the cation ring in using a free volume model approximation) which induce a lower perturbation to the IL nanostructure. However, it is well known that these alkali ions are strongly coordinated by the TFSI⁻ anions. In the case of Li⁺, the most favorable structure reported with two TFSI⁻ ions [Li(TFSI)₂]⁻,¹¹ while this number increases to 3 for Na⁺ [Na(TFSI)₃]⁻¹² and then may be even 3 or more for the larger cations.

3.2.2. Density and viscosity

- *Density*

Density of the binary systems IL/CsTFSI at 25 °C and the references of IL/LiTFSI with $0.1 \leq f \leq 0.4$ are presented in Table 6. As seen, the values are rather similar on the whole range of salt concentration. The negligible difference includes the difference of molar masses of LiTFSI and CsTFSI e.g. 287.07 g/mol and 413.05 g/mol, respectively. However, the small quantities of dissolved salt in IL do not remarkably change the density of the blends. Density increase while increasing the salt concentration from low to high. Moreover, for the next evaluations, we estimate the density of the Cs-based electrolytes as a function of temperature using the experimental data reported in Table 6 and the assumption for the Li-based ILs as discussed in 3.1.2.

Table 6 Density for the IL/LiTFSI and IL/CsTFSI systems at 25 °C.

Molar fraction f	Density ± 0.01 (g.cm ⁻³)	
	IL/LiTFSI	IL/CsTFSI
0.1	1.45	1.46
0.2	1.48	1.49
0.4	1.55	1.56

- *Viscosity*

Viscosity of these Cs-based IL are presented as a function of inverse temperature ($1000/T$) with a blend of IL/LiTFSI at $f = 0.4$, as seen in Fig. 11. Viscosity of the blends IL/CsTFSI increases with increasing the salt concentration and become less viscous at high temperature, as reported for the Li-based ILs. The curves for both Li and Cs systems exhibit similar behavior with the increase of temperature following a VTF model. These results are significantly correlated to the evolution of T_g values measured by DSC. Moreover, it is interesting to point out that the CsTFSI has less impact on the IL viscosity as compared to LiTFSI. For example, while increasing the f value from 0.1 to 0.4, viscosity at 25 °C increases from 0.06 Pa.s to 0.09 Pa.s, respectively, for the blends IL/CsTFSI, whereas it is from 0.06 to 0.17 Pa.s for the Li-based ILs. A huge difference between two alkaline

systems may relate to the different size of Li^+ and Cs^+ cations which influences on the ionic mobility (or viscosity).

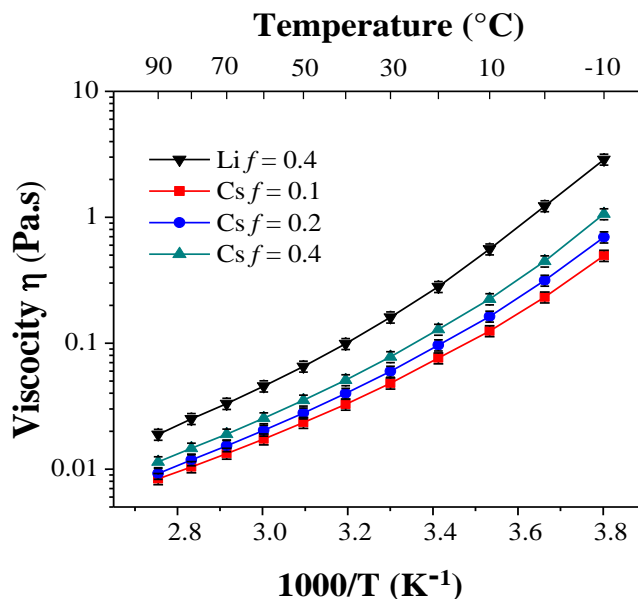


Fig. 11 Viscosity of IL/LiTFSI at $f = 0.4$ (black line) and the systems $[\text{Cs}][\text{BMIm}][\text{TFSI}]$ at different molar fraction f as a function of $1000/T$. The error bars are 10 % for all samples.

3.2.3. Conductivity

- *Ionic conductivity*

The ionic conductivity of IL/CsTFSI systems and the reference IL/LiTFSI at $f = 0.4$ measured by EIS method are presented as a function of $1000/T$ in Fig. 12. The conductivity is relatively high for these blends (above 1 mS.cm^{-1} at RT) even at the highest molar fraction of salt of $f = 0.4$, which is suitable for electrolyte applications. The effect of salt concentration is once again less important for Cs compositions and correlates to the evolution of viscosity discussed above. For example, conductivity decreases from 3.3 to 2.2 mS.cm^{-1} for IL/CsTFSI systems, whereas it is 3.2 to 1.2 mS.cm^{-1} for the Li compositions, corresponding to the molar fraction of salt $f = 0.1$ and 0.4 , respectively.

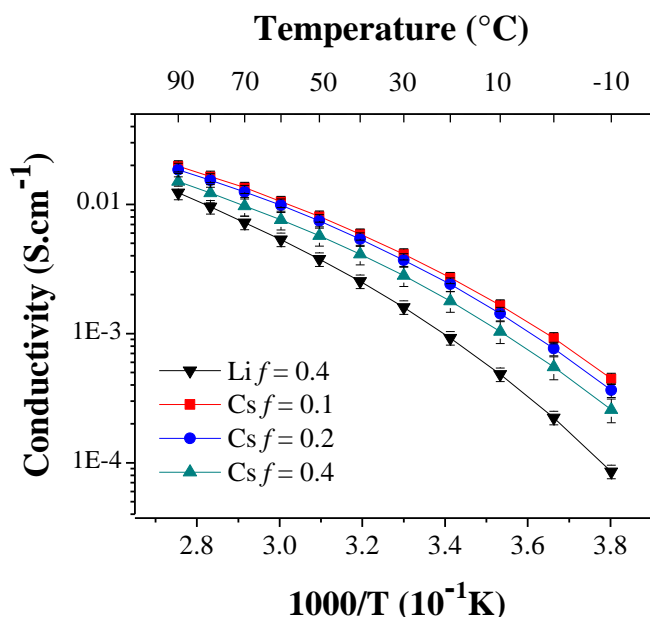


Fig. 12 Ionic conductivity of IL/LiTFSI at $f = 0.4$ and the systems $[Cs][BMIm][TFSI]$ at different molar fraction f as a function of $1000/T$. The error bars are 10 % for all samples.

The conductivity data plot as a function of T_g/T , (T_g determined by DSC), for the Cs-based ILs at different salt concentration are presented in Fig. 13, and compared to the curve obtained for LiTFSI, BMIm TFSI at $f = 0.4$. Obviously, these data lie on the same curve indicating similar scaled-temperature dependence of these electrolytes. It means that the fragility of these systems is not changed while increasing the size of cation, and even the salt concentration. It means that the conductive properties of any blend IL/salt are only dependent from the viscosity (or ionic mobility) in the whole range of temperature from -10 to 90 °C, and that the nanostructure of these electrolytes is not noticeably modified by the amount or the nature of the alkali ion added.

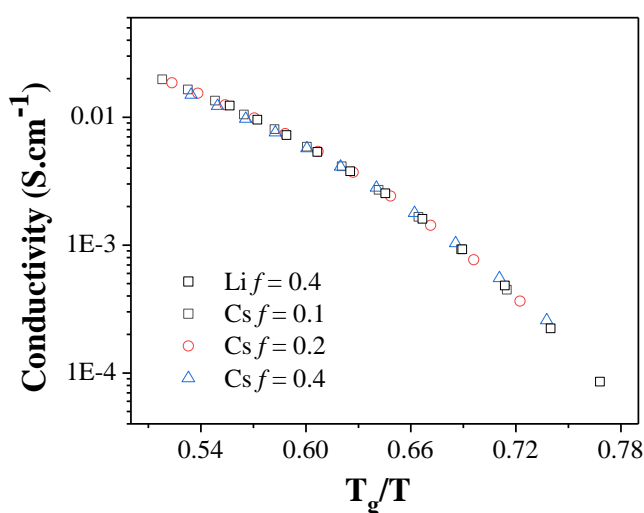


Fig. 13 Ionic conductivity as a function of T_g/T for the IL/LiTFSI at $f = 0.4$, and the binary systems $[Cs][BMIm][TFSI]$ at different salt contents.

- *Molar conductivity*

The molecular mass and molar conductivity at RT of the blends IL/CsTFSI are calculated from the equation (3) and (4), and the results are presented in Table 7. As seen, the molar mass of Cs-based IL shows a negligible change with salt concentration due to the very close molar mass of CsTFSI (413.05 g/mol) and BMIm TFSI (419.36 g/mol). It means by addition of salt, each IL molecule is replaced by nearly the same molar weight of CsTFSI. Nonetheless, conductivity decreases while increasing the amount of salt. At low concentration of $f = 0.1$, conductivity is $0.77 \text{ S.cm}^2.\text{mol}^{-1}$, and decreases to $0.68 \text{ S.cm}^2.\text{mol}^{-1}$ for $f = 0.2$, or $0.47 \text{ S.cm}^2.\text{mol}^{-1}$ for $f = 0.4$. Comparing to the Li-based ILs (in Table 4), the addition of CsTFSI in IL has even less impact on molar conductivity of the blends. For example, when the f varies from 0.1 to 0.4, a decrease of 68 % in conductivity obtained for the Li-based ILs, whereas it is only about 39 % for the Cs-based electrolytes.

Table 7 Density, mass molar, and conductivity of the binary systems IL/CsTFSI at different molar fraction f .

Molar fraction f	$d \pm 0.01$ (g.cm^{-3})	$M \pm 0.01$ (g.mol^{-1})	σ (mS.cm^{-1})	$\Lambda_m * 10$ ($\text{S.cm}^2.\text{mol}^{-1}$)
0.1	1.46	418.81	2.7	7.7
0.2	1.48	418.34	2.4	6.8
0.4	1.56	417.52	1.8	4.7

The Walden plots of these Cs-based ILs and a referenced sample IL/LiTFSI at $f = 0.4$ are presented in Fig. 14. As seen, similar behavior with those reported for the neat IL and the Li-based electrolytes (in 3.1.4) is observed i.e. (i) the curves are linear and lie slightly under the KCl reference line, (ii) these electrolytes are classified as 'good ionic liquid' behavior, (iii) the data plot slightly lower than the KCl line which corresponds to the formation of complexes, and this difference relates to the different in energy activation for viscosity and ionic conductivity, (iv) the data approach the ideal line meaning higher ionic dissociation at low temperature.

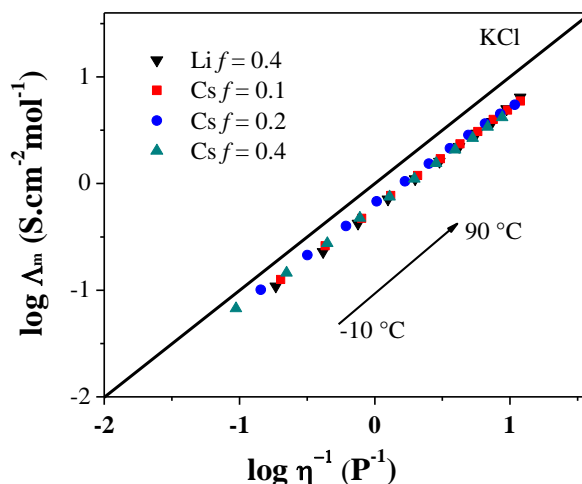


Fig. 14 Walden plots for the blends IL/LiTFSI at $f = 0.4$ and IL/CsTFSI at different molar fraction of salt, from -10 to 90 °C. The referenced line is the data of a KCl 0.01 mol.L⁻¹ solution.

3.2.4. Self-diffusion coefficient, dissociation, and transport properties

The self-diffusion coefficient D of BMIm⁺, TFSI⁻ and Cs⁺ ions were measured by PFG-NMR method of the ¹H, ¹⁹F and ¹³³Cs nuclei, respectively. The ¹³³Cs data were obtained in collaboration with A-L. Rollet from Phenix laboratory (Paris). All of the evolution observed for Cs- based IL systems (as seen in Fig. 15) are similar to those reported for the blend IL/LiTFSI (in 3.1.5) including:

- (i) the diffusivity of both IL cation/anion decrease strongly with addition of CsTFSI salt and then slightly with increasing the salt concentration,
- (ii) the D_{TFSI} value is always lower than D_{BMIm} and is more affected by the Cs⁺ concentration.
- (iii) Cs⁺ ion is always the slowest component. The relative order of diffusion coefficient is $D_{\text{BMIm}} > D_{\text{TFSI}} > D_{\text{Cs}}$.

Thus, comparing the impact of alkali's nature at highest molar fraction of salt ($f = 0.4$), from the black curves (IL/LiTFSI) and the cyan curves (IL/CsTFSI) in Fig. 15, the influence of Li⁺ ion on ionic diffusivity is more important than the Cs⁺ cation e.g. at 20°C, the D_{Li} value is $0.21 \times 10^{-11} \text{ m}^2 \cdot \text{s}^{-1}$, meanwhile the D_{Cs} value is three times higher of $0.63 \times 10^{-11} \text{ m}^2 \cdot \text{s}^{-1}$. The big difference of self-diffusion coefficients observed for two systems indicates different coordination shells of alkali ions in IL which is strongly depended on the ionic radius.

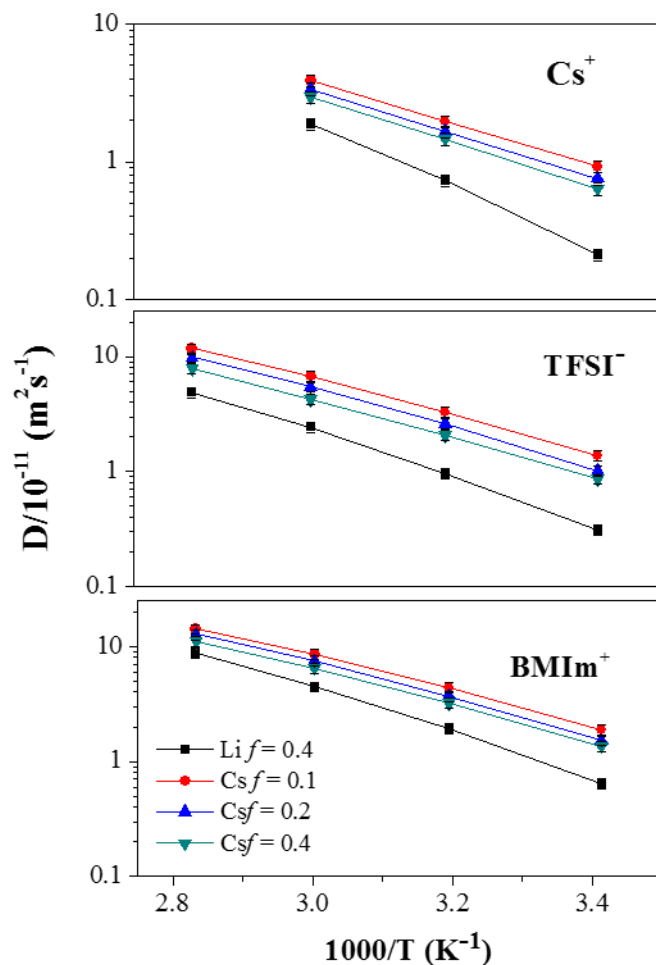


Fig. 15 Self-diffusion coefficient of Cs^+ , TFSI^- , and BMIm^+ ions for the blend of IL/LiTFSI at $f=0.4$ and the blends IL/CsTFSI as a function of $1000/T$. The error bars are 10 % for all samples.

Table 8 Self-diffusion coefficient, conductivity, dissociation degree and Cs transference number of the blends IL/CsTFSI at 20 °C.

Molar fraction f	D_{BMIm}	D_{TFSI}	D_{Cs}	$\Lambda_m * 10$	$\Lambda_{\text{NMR}} * 10$	$\tau * 10$	$t_{\text{Cs}}^+ * 10^2$
	(* $10^{-11} \text{ m}^2 \cdot \text{s}^{-1}$)			(S.cm 2 .mol $^{-1}$)			
0.1	1.9	1.4	0.9	7.7	11.9	6.4	2.6
0.2	1.5	1.0	0.7	6.8	8.8	7.7	5.2
0.4	1.3	0.8	0.6	4.8	7.1	6.7	9.4

Moreover, the dissociation degree obtained from the ratio of molar conductivity determined by EIS method and by NMR spectroscopy for the IL/CsTFSI systems are presented in Table 8. Comparing the two values of molar conductivity, the Λ_m value is always lower than the Λ_{NMR} value. The evolution of τ values with salt concentration for the Li and Cs-based ILs is rather similar at low concentration of salt, and increases up to $f=0.4$ for Li, but only limits to $f \leq 0.2$ for the Cs. Clearly, these

values are influenced by the CsTFSI concentration. However at higher concentration of CsTFSI dissolved in IL, a drop of τ values e.g. 0.77 for $f = 0.2$ to 0.67 for $f = 0.4$ may relate to the formation of aggregates. These non-conductive aggregates significantly decrease the conductivity determined by EIS method (contribute to only the charged pieces) but not the conductivity determined by NMR. On the other hand, increasing the amount of Cs^+ in IL helps to enhance the cationic transference number of the blends IL/CsTFSI from $t_{\text{Cs}^+} = 0.026$ to 0.094 for $f = 0.1$ and 0.4 due to the higher cation contents. Similar evolution was also observed for the blends of IL/LiTFSI (Table 5).

3.3. Conclusions

The effects of salt concentration ($0.1 \leq f \leq 0.4$) in two alkali-based BMIm TFSI, including IL/LiTFSI and IL/CsTFSI are carried out as electrolytes for future storage devices in term of physical and transport properties. Along with this work, the evolution of the physical properties such as glass transition temperature, density, viscosity, ionic conductivity, self-diffusion coefficient, etc., with the salt concentration for these systems are investigated by various methods and techniques. A part of the obtained results are comparable to those reported in the literature for the Li-based electrolytes.

Thus, by comparing the similar compositions of a small ion (Li^+) and a bigger alkali ion (Cs^+) coordinated in IL, we noticed that the addition of both Li^+ and Cs^+ ions lead to the relatively similar trends.

The behaviors observed for both systems can be resumed as

- The addition of salt suppresses the crystallization of IL and resulting in only the glass transition behavior is observed by DSC measurement. The T_g values increase with increasing the salt reflecting the lower ionic mobility.
- The IL density and viscosity increase by adding more salt in IL and their evolutions with temperature fit to a VTF model.
- The presence of salt reduces significantly the overall ionic conductivity and self-diffusion coefficient of both IL cation/anion, and more important for the TFSI⁻ anion while increasing the amount of salt. The alkaline ion is always the slowest component, and the D values follow an order of $D_{\text{BMIm}} > D_{\text{TFSI}} > D_{\text{Alkaline}}$ in every salt concentration from low to intermediate.

The nature of ion has a minor influence on these IL properties. The Cs^+ ion seems to have less impact on IL properties at the same salt concentration in term of viscosity and ionic transport properties as compared to the Li^+ one, which relates to the lower T_g values measured for the identical alkali concentration, and the data can be easily renormalized in using scaled T_g/T representations.

These experimental data may help to figure out the overall hypotheses for any alkali-based IL systems, even for the alkaline-earth metal, with the salt concentration following:

- (i) the physical and transport properties of any alkali-based IL with the salt concentration may follow similar trends for Li and Cs compositions, from low to intermediate salt fraction ($f \leq 0.4$).
- (ii) how big the coordinated cations is, how low the remarkable effects on IL properties obtain while increasing the salt concentration.

To further verify the second hypothesis, we chose to study the series of alkali/alkaline-earth based IL, including Li, Na, K, Cs, and Mg, at the definite molar fractions of salt. This fundamental study is expected to give a better understanding of the effect of cation's nature on the physical and transport properties of IL. But these elements including Na, K, and Mg are not the good NMR nuclei which will restraint the availability for determining the self-diffusion coefficients of alkali /alkaline-earth cations, transference number, and ionic dissociation degree. Nonetheless, because of the nature of these cations, especially for Na and Mg, these blends IL/alkali/alkaline-earth –based TFSI salt are proposed as promising electrolytes for future rechargeable devices using the same concept of the well-known lithium batteries.

4. Alkali/ alkaline-earth based BMIm TFSI

While the Li-based ILs attracted the scientist's attention as safer electrolyte for lithium batteries, the systems of IL doped alkali/alkaline-earth metals are less reported in the literature. For the growing demand of new energy storable devices, the overall understanding of electrolyte based on abundant element resources should be satisfied and alkali/alkaline-earth including especially sodium (Na) and magnesium (Mg) become the promising candidates for future technologies. Thus, based on the results obtained for the blends of IL doped Li^+ and Cs^+ cations with the salt concentration, the physical and transport properties of any similar binary system 'IL/TFSI-based salt' may follow the same trends of evolution. In this part, the effect of cation's nature on the alkali/alkaline-earth based ILs are carried out using the definite salt concentration ($f = 0.2$) at 25 °C. This value of f is chosen due to the limited solubility of KTFSI in BMIm TFSI. In addition, for the divalent metal, two compositions at $f = 0.1$ and 0.2 are prepared to further observe the effect of charged number on IL properties.

4.1. Thermal characteristics

The second heating thermograms for the alkali/alkaline-earth based BMIm TFSI, from – 130 to - 30 °C, with a scan rate of 10 °C/min, under N_2 gas flux, are presented in Fig. 16. These mixtures exhibit only one heat capacity change corresponding to their T_g . In detail, none of them show the crystallization as seen for the neat IL, and this behavior correlates to those observed for the IL doped Li and Cs. Comparing the T_g values obtained for these alkali-based electrolytes at the same molar fraction of $f = 0.2$, the presence of the smallest ions i.e. Li^+ and Na^+ ions in IL exhibit similar T_g of -

79 ± 2 °C. How bigger the cation is, how lower the T_g value observes such as -84 ± 2 °C for IL/KTFSI, and -83 ± 2 °C for IL/CsTFSI. The relative order of T_g values for alkali-based ILs is Li, Na > K \approx Cs.

The presence of Mg^{2+} ion in IL increases significantly the T_g value up to -74 ± 2 °C, at the same molar fraction of salt of $f = 0.2$, whereas a value of $T_g = -83 \pm 2$ °C was measured for $f = 0.1$. Obviously, for the divalent ion Mg^{2+} , the T_g value is much higher than the alkali-based ILs (if we compare them at $f = 0.2$). Meanwhile they remain rather similar (if we consider the number of added charges) for the compositions of Mg ($f=0.1$) and the alkali ($f=0.2$), and even for the Mg ($f=0.2$) to alkali ($f=0.4$), which is related to the divalent nature of magnesium. It is obvious that for each Mg^{2+} ion, two TFSI⁻ anions are added in IL to compensate the charges, but it is only one for the case of alkali ions. This fact causes an increase in viscosity of the blend, and further increases the T_g value.

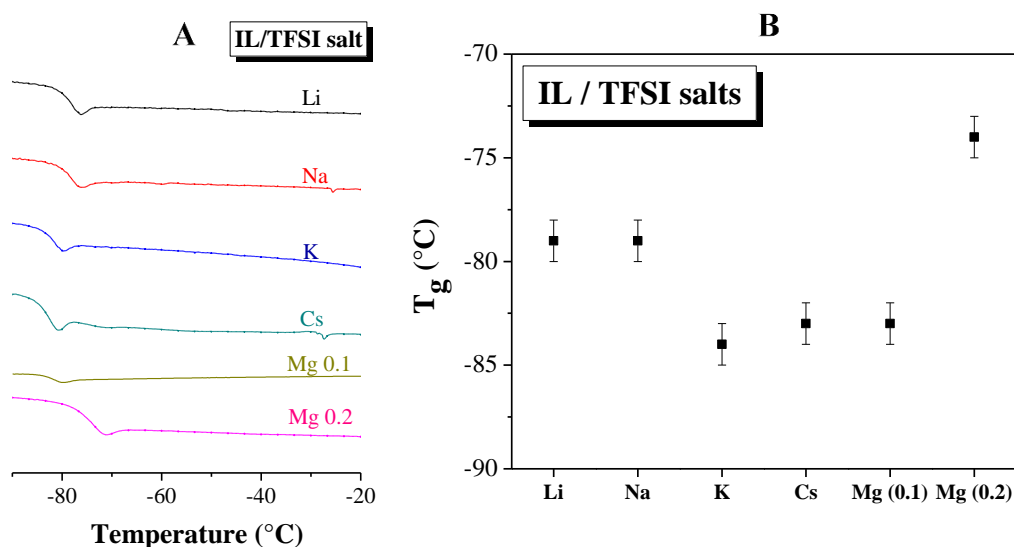


Fig. 16 (A) The second heating DSC thermograms of the blends IL/TFSI-based salt, including LiTFSI (black line), NaTFSI (red), KTFSI (blue), CsTFSI (green), $Mg(TFSI)_2$ ($f = 0.1$) (dark yellow), and $Mg(TFSI)_2$ ($f = 0.2$) (rose). (B) the T_g values of the blends IL/salts with the cation nature.

In brief, the blends of BMIm TFSI with the TFSI-based salts type alkali/alkaline-earth metals exhibit one glass transition temperature in the large range of characteristic temperature as observed by DSC measurement. Increasing the cation size decreases the ionic mobility by increasing the T_g values for the alkali-based ILs. Meanwhile, the divalent nature of Mg causes a huge increase of T_g comparing to the alkali-based electrolytes. The different T_g values observed for these ILs may concern the number of surrounding anions, the cation's size, and the solvation of cation in IL. In the next studies, the density and viscosity of these electrolytes are carried out.

4.2. Density and viscosity

- *Density*

Density of these blends IL/salt measured at 25 °C in a glove box are presented in Table 9. It is obvious that these alkali-based ILs exhibit rather similar density of $1.47 \pm 0.02 \text{ g.cm}^{-3}$. Alternatively, for the blend of IL/Mg(TFSI)₂, the densities at two concentrations of salt i.e. $f = 0.1$ and 0.2 increase with increasing the salt concentration. At $f = 0.2$, Mg-based IL exhibits the density of $1.49 \pm 0.01 \text{ g.cm}^{-3}$, which is rather similar to the alkali electrolytes.

- *Viscosity*

Viscosity at RT of these blends IL/ TFSI-salts are presented in Table 9. As seen, the alkali-based ILs exhibit close viscosity at 25 °C. The viscosity data are slightly changed by adding different alkali cations in IL. The lowest viscosity of Cs-based IL (at 7.53 cPa.s) obtained may relate to the compromise between the coordinated cation size, solvation shell, and ionicity of the blend. On the other hand, viscosity of IL doped Mg²⁺ at $f = 0.1$ is 8.91 cPa.s which is in the same order of magnitude to the alkali-based ILs. However, the blend of Mg at $f = 0.2$ shows much higher viscosity of 20.19 cPa.s indicating the influence of adding similar number of charge versus similar molarities. All of the experimental viscosity values possess the incertitude of 10 %.

Table 9 Density, molecular weight, and viscosity of BMIm TFSI and the blends IL/TFSI salt at 25 °C.

Sample	Density $\rho \pm 0.01 \text{ (g.cm}^{-3}\text{)}$	Molecular weight $M \pm 0.01 \text{ (g.mol}^{-1}\text{)}$	Viscosity $\eta \text{ (cPa.s)}$
IL/ LiTFSI ($f = 0.2$)	1.48	392.91	10.96
IL/ NaTFSI ($f = 0.2$)	1.48	396.12	11.60
IL/ KTFSI ($f = 0.2$)	1.46	399.31	10.87
IL/ CsTFSI ($f = 0.2$)	1.48	418.14	7.53
IL/ Mg(TFSI) ₂ ($f = 0.1$)	1.46	452.45	8.91
IL/ Mg(TFSI) ₂ ($f = 0.2$)	1.49	435.91	20.19

In conclusion, density of these binary systems IL/salt slightly increases with the order of cation size. The viscosity increases with the presence of salt in IL, and decreases while increasing the cation size.

4.3. Ionic conductivity

Ionic conductivity of the blends IL/salt, measured by EIS method, are presented as a function of inverse temperature in Fig.18. The conductivity data are very close and increases with the temperature from low to high. At low temperature, the effect of cation size on IL conductivity is more obvious. Conductivity increases with increasing the cation size following a trend of $\text{Li} < \text{Na} < \text{K} < \text{Cs}$ for the

alkali-based ILs. Bigger the cation is, higher the conductivity observes. The differences of conductivity vanish at higher temperatures. Thus, an interested thing relating to the evolution of viscosity and conductivity between the Li and Na-based electrolytes is observed. The viscosity determined at 25 °C for Na-based IL is very slightly higher than the Li electrolyte e.g. 11.60 and 10.96 cPa.s, respectively, meanwhile conductivity of the less viscous blend is found to be lower. A roughly same behavior was reported by Monti et al.¹² with different salt fractions for these two systems which was explained by the different coordinated shells of Li and Na and the TFSI anions i.e. $[\text{Li}(\text{TFSI})_2]^-$ and $[\text{Na}(\text{TFSI})_3]^{2-}$ anionic clusters. While the complexes of Na^+ are bigger, their mobility is quite lower than the lithiated one, but the weaker interactions between Na^+ and TFSI^- resulting in higher ionic conductivity of the Na-based IL.³²

Furthermore, for the divalent system, lower conductivity is observed at the same molar fraction of $f = 0.2$ due to higher viscosity of the blend (see the pink curve in Fig. 17). However, at $f = 0.1$, conductivity of the blend IL/ $\text{Mg}(\text{TFSI})_2$ is in the same order of magnitude with the alkali-based ILs at $f = 0.2$. One of the advantages, in term of electrolyte behavior, is that the IL contained the divalent ions only needs a half of quantity of dissolved salt to reach similar conductivity with the monovalent charge. The ionic conductivity of these electrolytes at 25 °C are presented in Table 10. Conductivity is $2.06 \text{ mS}\cdot\text{cm}^{-1}$ for the lithiated IL and increases to $2.43 \text{ mS}\cdot\text{cm}^{-1}$ for Na, $2.65 \text{ mS}\cdot\text{cm}^{-1}$ for K, and 3.01 for Cs electrolyte. Meanwhile, a lower conductivity of $1.19 \text{ mS}\cdot\text{cm}^{-1}$ is measured for IL/ $\text{Mg}(\text{TFSI})_2$ at the same molar fraction $f = 0.2$.

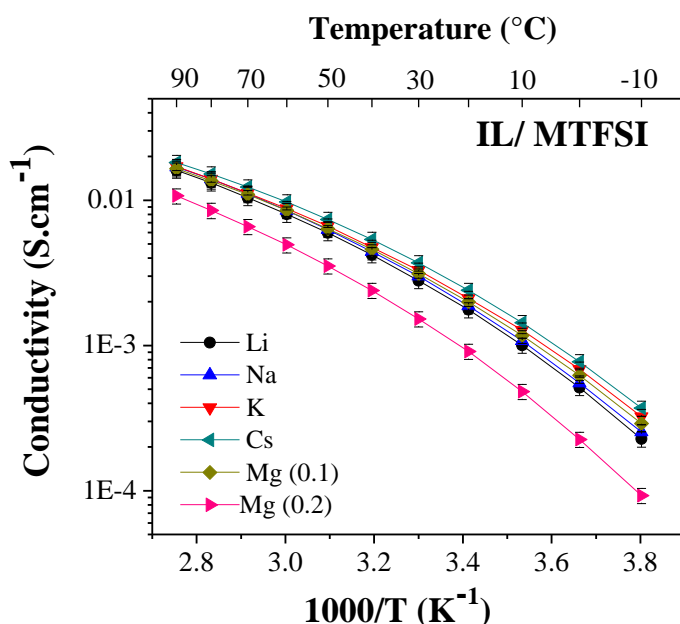


Fig. 17 Ionic conductivity as a function of inverse temperature for the binary system IL/ TFSI salts.

The conductivity data are also fitted to a VTF model, and the VTF's fitting parameters are presented in Table 10. The energy activation (E_a) and the A factors for these electrolytes are presented in Fig

18. As seen, the E_a which represents for the charge carriers mobility and the A factors are very close for the alkali-based ILs (at $f = 0.2$), and the IL doped Mg^{2+} (at $f = 0.1$) indicating the negligible influences of cation size on the transport properties.

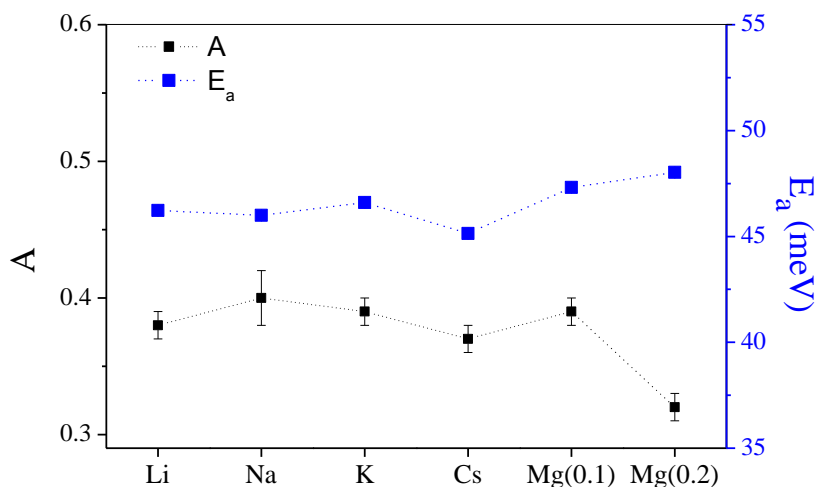


Fig. 18 The pre-exponential factor and energy activation of the blends IL/TFSI salt calculated from the VTF's fitting for conductivity data.

Table 10 Ionic and molar conductivity at 25 °C, and the VTF's fitting parameters for conductivity data.

Sample	σ mS.cm ⁻¹	Λ_m S.cm ² .mol ⁻¹	VTF's fitting parameters		
			A (S.cm ⁻¹)	E_a (meV)	T_0 (K)
IL/ LiTFSI ($f=0.2$)	2.38	0.59	0.38 ± 0.01	46.23 ± 0.18	194
IL/ NaTFSI ($f=0.2$)	2.43	0.65	0.40 ± 0.02	46.00 ± 0.24	194
IL/ KTFSI ($f=0.2$)	2.65	0.72	0.39 ± 0.01	46.64 ± 0.01	189
IL/ CsTFSI ($f=0.2$)	3.01	0.84	0.37 ± 0.01	45.14 ± 0.09	190
IL/ Mg(TFSI) ₂ ($f=0.1$)	2.55	0.78	0.39 ± 0.01	47.31 ± 0.12	190
IL/ Mg(TFSI) ₂ ($f=0.2$)	1.19	0.34	0.32 ± 0.01	48.03 ± 0.02	199

These data are also represented with a T_g/T scaled in Fig. 19. The data lie on two nearly similar master curves with similar shape and curvatures e.g. the upper one for pure BMIm TFSI and the alkali-based ILs, another curve is slightly shifted under for the two compositions of [Mg][BMIM][TFSI]. It means that the fragility for pure IL both alkali and alkaline-earth electrolytes are rather similar, and the structural perturbation induced by these two families of ions are very small compared to the initial nano structuration of the IL. Thus, the ionic conductivity and the difference between the two families of electrolytes are governed by their viscosity.

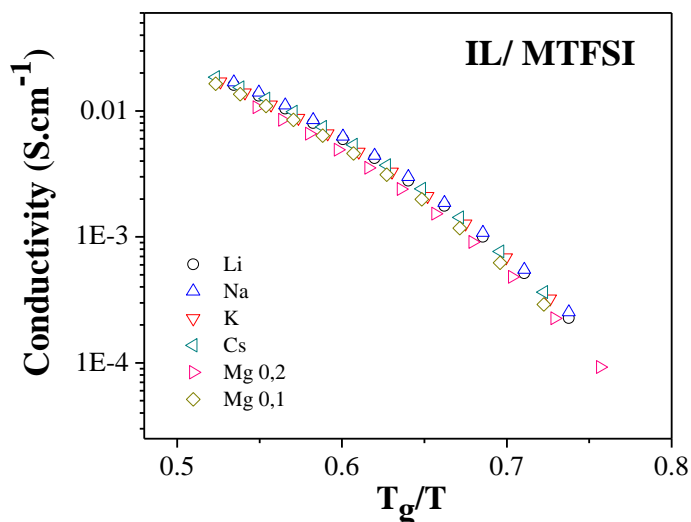


Fig. 19 Ionic conductivity as a function of T_g/T for the binary systems $[M][BMIm][TFSI]$

The molar conductivity of these IL-based electrolytes at 25 °C, calculated from the ionic conductivity measured by EIS method with the corresponded density and the molecular weight, are presented in Table 10. These Λ_m values increase with the cation size for the alkali-based IL from Li to Cs. For the Mg-based electrolytes, a lower value of 0.34 S.cm².mol⁻¹ is measured relating to the effect of Mg divalent nature which was previously mentioned. At lower concentration of $f=0.1$, the blend exhibits a Λ_m value of 0.78 S.cm².mol⁻¹ which is rather close to the alkali-based ILs.

In conclusion, ionic conductivity for the binary systems IL/salt exhibit the same evolution with temperature, as seen for two IL doped Li and Cs systems. Thus the effect of cation size, observed at the definite concentrations of salt, shows that the conductive process is dominated by IL cation/anion mobility, and the presence of different alkali/alkaline-earth cations in IL exhibits small impact on IL transport properties. Thus, for the alkali systems, ionic conductivity increases with increasing the ionic radius from Li to Cs.

For a better understanding of the relation between conductivity and fluidity of these IL/salt systems, their Walden plots at 25 °C are presented in Fig. 20. These blends could be classified as ‘good ionic liquids’ due to the fact that all of the data lie slightly under the reference line of KCl. In brief, the behaviors reported for both Li and Cs-based ILs are rather similar for any IL doped alkali/alkaline-earth cations system whatever the cation nature.

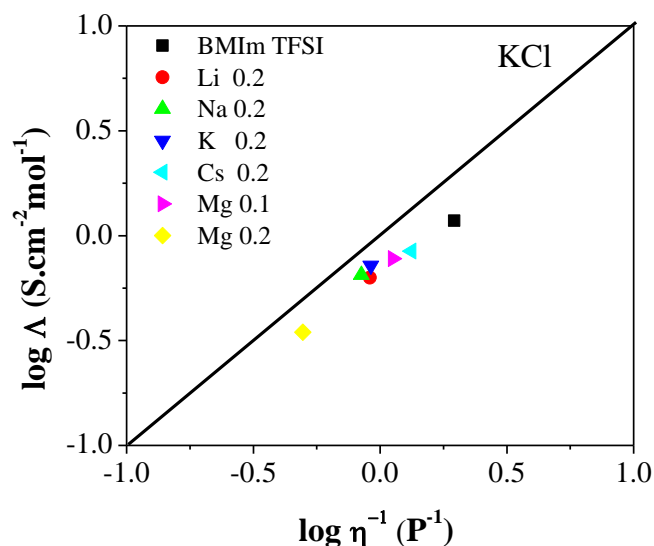


Fig. 20 Walden plots of the neat IL and the binary systems IL/TFSI-salt at 25 °C.

4.4. Self-diffusion coefficient

The self-diffusion coefficients of IL cation/anion for these binary systems IL/TFSI salt were measured by PFG-NMR at 25 °C, and the results are presented in Fig. 21. As seen, the presence of the TFSI salts causes a decrease of diffusion coefficient for both IL cation and anion, and the D_{BMIIm} values are higher than the D_{TFSI} values for all systems. For the alkali ions, diffusivity of TFSI anion increases with increasing the cation size from Li to Cs. How bigger the cation is, how faster the diffusivity of anion is relating to weaker interaction between alkali cation and TFSI anions. In case of a divalent cation, the charged carriers diffuse much slower than in the alkali-based IL at the same salt fraction of $f=0.2$, and rather similar at lower Mg concentration of $f=0.1$. Obviously, the blends' viscosity is an imperative effect resulting in the decrease of ionic diffusion.

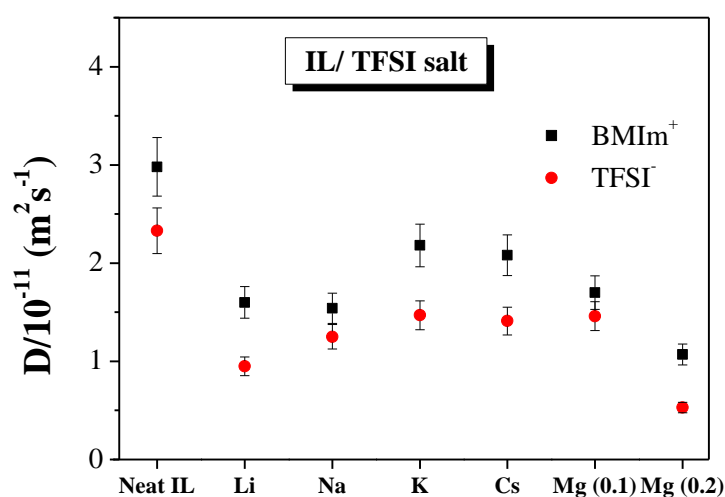


Fig. 21 Self-diffusion coefficient of BMIIm⁺ and TFSI⁻ for the neat IL and the blends of IL/TFSI salts at 25 °C.

Following the Stokes-Einstein equation^{15,18}

$$D_i = \frac{k_B T}{6\pi\eta r_i} \quad (8)$$

Where D_i is the self-diffusion coefficient and r_i is the radius of the specie i , η is the viscosity, k_B is Boltzmann constant, and T is the definite temperature. The D value of each charged specie presented in the binary systems [M][BMIm][TFSI], where M is the alkali/alkaline-earth cations, is inversely proportional to the viscosity of the blend and the size of ion.

Indeed, an evolution trend of $D_M \gg D_{TFSI} > D_{BMIm}$ should be suggested due to the difference in size of these three ions. However, an opposite behavior previously reported for both Li and Cs-based ILs indicates that the alkali cation does not diffuse separately but together in complexed with the TFSI anions. It was a shame that we couldn't measure the diffusivity of other alkali metals by NMR, apart from the Li^+ and Cs^+ ions. Many attempts have been performed to measure the diffusion of Na^+ , but its NMR active nucleus (^{23}Na) is strongly quadrupolar, and the corresponding nuclear relaxation times are very short, as it was also noticed in a published study.³³ The T_2 relaxation time between 400 to 800 μs was measured in a temperature range of 20 to 120 °C which is disabled to obtain the diffusion coefficient by both PFG-NMR and the alternative Stray-Field NMR technique (a technique developing in LPS-Orsay Laboratory by P. Judeinstein and colleagues). Nevertheless, based on the results obtained for two systems of IL doped Li^+ and Cs^+ , we suggest that the diffusion of any alkali/alkaline-earth ion in BMIm TFSI may exhibit the similar behavior, and the D_M values are always smaller than the D_{TFSI} , and D_{BMIm} values.

4.5. Cisoid and Transoid TFSI conformers

Based on the previous studies, TFSI anion is a flexible molecule that can exist in two inequivalent conformations (see Fig. 22) e.g. cisoid (or cis) TFSI (forms of C_1 symmetry with the CF_3 groups on the same side of the S-N-S plane) and transoid (or trans) TFSI (forms of C_2 symmetry and the two CF_3 groups are on the opposite sides of the S-N-S plane).³⁴ Both conformers are usually observed in the liquid or the glass state of the TFSI-based ILs, and their concentration can give the definite influences on the IL physical and conductive properties.³⁵ In this work, the ratio between two TFSI conformers in coordination with different alkali/alkaline-earth cations is only investigated in the liquid state (at 25 °C). The dependence of TFSI conformations for these blends IL/salt was carried out by using infrared spectroscopy (IR) measurement, in transmission from 400 to 4000 cm^{-1} , under a N_2 flux, and the detailed protocol is described in the annex.

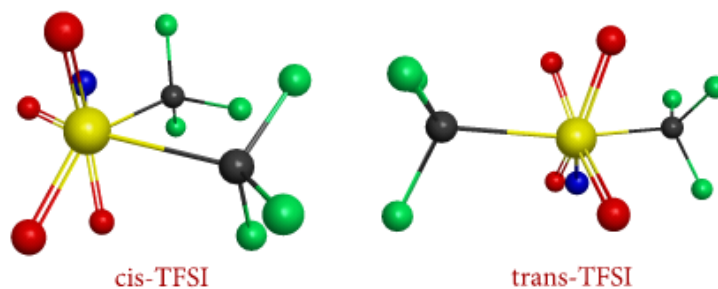


Fig. 22 Geometry of *cis*-TFSI and *trans*-TFSI.³⁶

Indeed, the characteristics bands of both *cis* and *trans*-TFSI were reported in the literature for the neat TFSI ILs^{37,38,36} and the Li-based TFSI ILs³⁹. The difference between two conformers of TFSI is mainly observed below 700 cm⁻¹ in the IR spectra, especially in the 460 – 680 cm⁻¹ region, following M. Herstedt et al.³⁴. They also reported that the IR bands of the C₁ *cis*-TFSI were typically at 602 and 656 cm⁻¹, whereas the C₂ *trans*oid band was found at 618 cm⁻¹. In this work, the IR spectrum of several alkali/alkaline-earth based BMIm TFSI are presented from 580 to 680 cm⁻¹ region, and only the electrolytes contained a salt fraction of 0.2 are shown in Fig. 23. For the obvious reason, the band at 556 cm⁻¹ is normalized to 1 for all spectra.

The ratio between two conformers is calculated following a relation below:

$$r = \frac{I_{\text{Cis}}}{I_{\text{Trans}}} = \frac{I_{602} + I_{656}}{I_{618}} \quad (9)$$

Where I_{Cis} and I_{Trans} are the intensity of the bands corresponded to the two conformers. The ratio r for all of the electrolytes are shown in Table 11. Obviously for the neat IL, the quantity of two conformers is nearly equivalent and rather for the *trans*-TFSI. The presence of TFSI salts in IL probably increases the *cis*-TFSI in the binary systems.

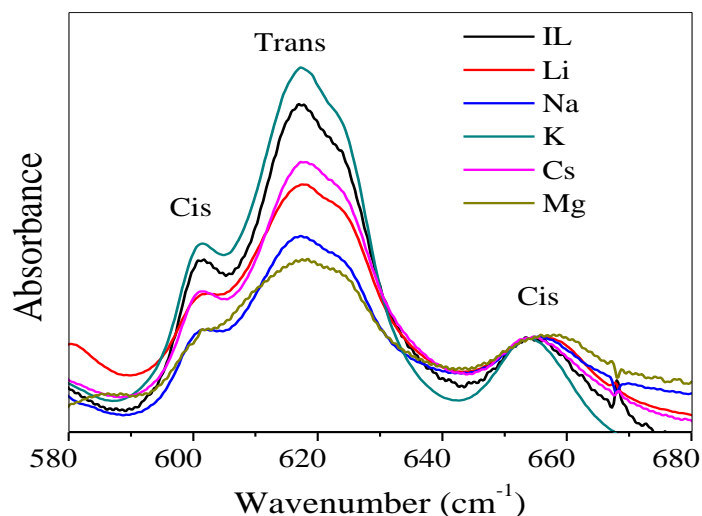


Fig. 23 IR spectra from 580 to 680 cm⁻¹ of BMIm TFSI and the blends IL/salts at $f = 0.2$ at 25°C.

Table 11 The ratio of cis and trans-TFSI concentration in BMIm TFSI and different IL/salt systems at 25 °C.

Electrolyte	Salt fraction (<i>f</i>)	cis-TFSI/trans-TFSI (<i>r</i>)
BMIm TFSI	0	0.90
[Li][BMIm][TFSI]	0.1	0.81
	0.2	1.12
	0.4	0.95
[Na][BMIm][TFSI]	0.2	1.10
[K][BMIm][TFSI]	0.2	0.99
[Cs][BMIm][TFSI]	0.1	0.83
	0.2	0.95
	0.4	0.79
[Mg][BMIm][TFSI]	0.1	1.50
	0.2	1.78

Firstly, the ratio *r* increases with the addition of salt at $f \leq 0.2$ for the Li-based ILs, and suddenly decreases at higher concentration of $f = 0.4$. Let's back to the literature, Lassegues et al.⁴⁰ studied the binary systems [Li][BMIm][TFSI] by both DFT calculations and IR spectroscopy and concluded that at a salt concentration of $f \leq 0.2$, the TFSI anions in the complexes with Li⁺ adopted both cis and trans-TFSI, and the [Li(TFSI)₂]⁻ anionic clusters where Li⁺ complexed by two TFSI anions was confirmed. Similarly, K. Pilar et al.⁴¹ reported that the [Li(TFSI)₂]⁻ complex is stable and contains one in the cisoid and one in the transoid conformer of TFSI. These studies help to explain the rather similar quantity of cis and trans-TFSI conformers at low concentration of salt. However, higher than this concentration, the [Li(TFSI)₂]⁻ complex may be replaced by the nano-structuring where Li⁺ is coordinated with less than two anions and forms the [Li_m(TFSI)_n]^{(n-m)-} aggregates with $n = 2m - 1$,⁴⁰ and liberating the free anions. Also, the trans-TFSI is more stable³⁴ resulting in higher concentration of the trans conformer than the cis one (the *r* values lower than 1). The similar behaviors are observed for the Cs-based ILs, and even with the two blends of IL doped Mg(TFSI)₂. Next, comparing the effect of cation nature such as the alkali cations, at the salt fraction of $f = 0.2$, the blends exhibit roughly same concentration of the two TFSI conformers (the *r* values approach to 1). This is in agreement with the IL/LiTFSI systems that the complexes of alkali-TFSI contain both cis and trans-

TFSI, and that each alkali cation is coordinated with at least two anions, and even three for the bigger cations i.e. $[\text{Na}(\text{TFSI})_3]^{2-}$ as reported in the literature for the Na-based ILs^{12,32}.

On the other hand, the addition of a divalent cation increases significantly the r value indicating the presence of higher cis-TFSI concentration in the blends. At $f = 0.2$, the quantity of cis conformer is nearly twice comparing to the trans-TFSI. However, the complexes of Mg^{2+} and TFSI anions are very complicated due to the presence of both ion pair and solvated aggregates which are the main reasons causing the huge reduction of ionic mobility and resulting in lower conductivity. The average number of TFSI anion surrounded the Mg^{2+} ion is about 3 to 4, and each anion has different potential energy environments.³² In brief, it can be concluded that the cisoid conformers are favorable for the formation of complexes between a divalent cation and the TFSI anions.

5. Conclusions

Ionic liquid-based electrolytes, defined as electrolyte of an inorganic salt dissolved into an RTIL, are largely investigated for battery technologies in the past three decades. In such electrochemical devices, the RTIL are considered as potentially interested solvent for dissolving the salt. While most of the studies (from fundamental to application aspects) are dealing with the lithium-based ILs, the growing interest concerned the post lithium batteries, principally sodium and magnesium batteries, as the promising alternatives is attracting more attention.

The advancement of such new systems reclaims to gain more fundamental knowledge, and this work, as our knowledge, is one of the first systematic studies about the influence of cation's nature i.e. alkali/alkaline-earth metals on the physical and transport properties of the binary systems IL/salt. This study mostly focuses on the cationic transport process which is a key parameter for any electrolyte application. Besides, by using multi-technical approaches, physical properties of the blends IL/salt including their density, viscosity, conductivity, self-diffusion of the various components are carried out. These data allow to reach the important information such as cation transference number, ionic dissociation degree, and ionicity of the blends.

The first mandatory step of this work is to determine the solubility of different TFSI based salts in a homologous IL i.e. BMIm TFSI. A large solubility range is observed for Li^+ and Mg^{2+} ($f \gg 1.0$), the other cations e.g. Cs^+ , Na^+ , and K^+ are less soluble in IL, and the Ca^{2+} is apparently insoluble. Due to the large solubility of TFSI salts in BMIm TFSI, we are investigated the impact of cation concentration on two cations i.e. Li^+ , Cs^+ , and cation nature for all samples (at $f = 0.2$) on IL properties.

At first glance, the presence of alkali/alkaline-earth cations in a common IL leads to similar evolutions of IL properties (at RT) such as the significant increase of viscosity and the consequent decrease

of both ionic conductivity and diffusion coefficients. It is also noteworthy that the decrease of diffusion coefficient is larger for the TFSI⁻ anion than the BMIm⁺ cation, and the alkali cations (only measurable for Li⁺ and Cs⁺ ions) are always the slowest component despite their smallest sizes. It affirms the strong complexation of alkali cation by the TFSI⁻ anions. This behavior is more obvious while decreasing the size of coordinated cation, and (or) increasing the salt concentration. Moreover, the presence of salt increases the dissociation degree of these blends as compared to the neat IL, and the cationic transference number, even it is rather inefficient for electrolyte application, increases proportionally to the salt concentration.

Moreover, our results also deal with the variation of IL properties as a function of temperature, ranging from -10 to 90 °C. By DSC measurements, the adding of salt exhibits as a crystallization inhibitor or glass former for IL. Thus, the T_g of the blends IL/salt is strongly depended on the concentration and nature of coordinated cations e.g. larger effect is observed for the smaller ions and increases with the salt ratio. Remarkably, the evolution of these electrolytes, whatever is their composition, with temperature leads to the unified results:

- the master curve of Walden plot obtained with the variation of temperature affirms a rather similar ionicity.
- scaling of ionic conductivity by the glass transition temperature (T_g/T) leads to a master curve, evidencing similar fragility.

Thus, for a binary system, the ionic transport properties are driven by its viscosity,⁴² and its nanostructuration is not so different comparing to the neat IL.⁴³

Nevertheless, the challenge is to clarify the dependence of T_g value (or ionic mobility) inside the blends IL/salt with the cation nature, but the original molecular, or the description of T_g are still rather debated in the literature. Through our results, the glass transition behavior is obviously connected to the coordination shell of alkali/alkaline-earth cation, and even the possibility for forming the big aggregates which comprise more than one cations through bridging anions ($X^+ \dots (\text{TFSI})^- \dots X^+$) inside these blends.^{18,44} While the combination of some direct measurements (IR, EXAFS, Raman spectroscopies) can help to obtain description of the average coordination shells, the second order neighboring, and the formation of alkali-based clusters, etc., these techniques are very difficult to assess experimentally because the dynamic equilibrium and the lifetime of these complex species are not measurable.

Facing a lot of difficulties relating to the inaccessible of several direct experimental techniques, a molecular dynamic approach has been paralleled started by Dr. P. Judeinstein and B. Coasne (LiPhy, Grenoble) to further reach such full knowledge. This work consists to use the published force fields description and a classical molecular dynamic approach to compute the trajectories, then extract the

relevant data. However, the used force fields were developed in a different context (as an example, the force field for alkali/earth alkaline in aqueous solutions), so our approximations need to be verified. In the following work, the experimental results (presented in this chapter) and those obtained by simulations will be compared. The first encouraged results are presented in Fig. 24 including the evolution of X-Ray scattering pattern, in collaboration with F. Cousin from LLB in Saclay, for the system [Cs][BMIM][TFSI] ($f = 0.1; 0.2; \text{ and } 0.4$) and the evolution of self-diffusion coefficients at 300 K for [alkali][BMIM][TFSI] electrolytes ($f=0.2$). We expect that the comparison between adequate MD method and reproduce experimental results will allow us to get more sensitive information about the physicochemical properties of these electrolytes.

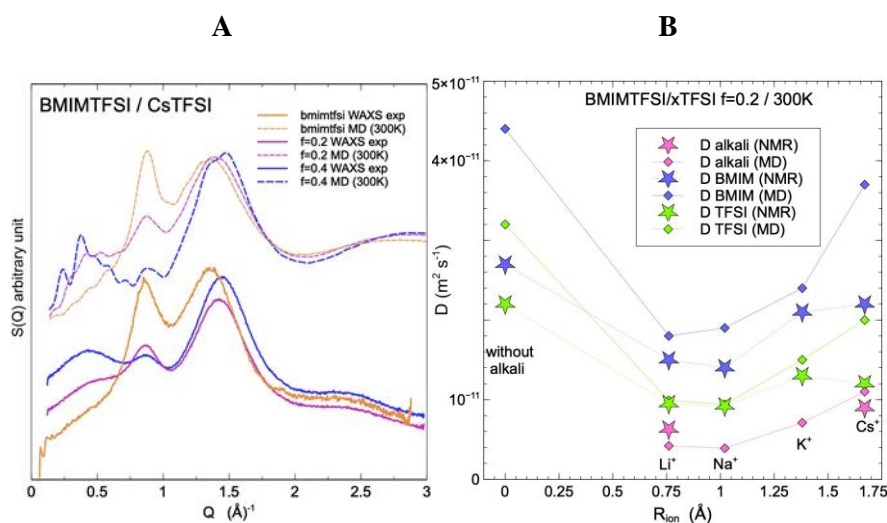


Fig. 24 Comparison between experimental and molecular dynamic approach for structural and dynamic approaches (A) Wide angle X-Ray scattering, to characterize IL and electrolyte nanostructuring, of [Cs][BMIM][TFSI] system at $f = 0.1; 0.2; \text{ and } 0.4$; and (B) the evolution of self-diffusion coefficients for [M][BMIM][TFSI] systems (M is Li, Na, K, Cs), at 300 K and $f=0.2$.

References

1. Borodin O., Smith G. D., Henderson W., Li⁺ cation environment, transport, and mechanical properties of the LiTFSI doped N-methyl-N-alkylpyrrolidinium⁺TFSI⁻ Ionic liquids, *J. Phys. Chem. B*, 110, 16879–16886 (2006).
2. Kirchner E. B., Ionic liquids, *Top. Curr. Chem.*, 290, (2010).
3. H. Yang, J. Hwang, Y. Wang, K. Matsumoto, N-Ethyl-N-propylpyrrolidinium Bis(fluorosulfonyl)amide Ionic Liquid Electrolytes for Sodium Secondary Batteries: Effects of Na Ion Concentration, *J. Phys. Chem.C*, 123, 22018–220262 (2019).
4. C. Ding, T. Nohira, K. Kuroda, R. Hagiwara, A. Fukunaga, Sh. Sakai, K. Nitta, NaFSA–C₁C₃pyrFSA ionic liquids for sodium secondary battery operating over a wide temperature range, *J. Power Sources*, 238, 296–300 (2013).
5. T. Kakibe, N. Yoshimoto, M. Egashira, Optimization of cation structure of imidazolium-based ionic liquids as ionic solvents for rechargeable magnesium batteries. *Electrochem. Commun*, 12, 1630–1633 (2010).
6. Mohd Noor S. A., Howlett P. C., Macfarlane D. R., Forsyth M., Properties of sodium-based ionic liquid electrolytes for sodium secondary battery applications, *Electrochim. Acta*, 114, 766–771 (2013).
7. Vranes M., Dozic S., Djeric V., Gadzuric S., Physicochemical characterization of 1-butyl-3-methylimidazolium and 1-butyl-1-methylpyrrolidinium bis(trifluoromethylsulfonyl) imide, *J. Chem. Eng. Data*, 57, 1072–1077 (2012).
8. Talaty E. R., Raja S., Storhaug V. J., Dölle A., Carper W. R., Raman and infrared spectra and ab initio calculations of C 2-4MIM imidazolium hexafluorophosphate ionic liquids, *J. Phys. Chem. B*, 108, 13177–13184 (2004).
9. Pitawala J. et al., Phase behaviour, transport properties, and interactions in Li-salt doped ionic liquids, *Faraday Discuss*, 154, 71–80 (2012).
10. Harris K. R., Kanakubo M., Woolf L., a. Temperature and Pressure Dependence of the Viscosity of the Ionic Liquids 1-Hexyl-3-methylimidazolium Hexafluorophosphate and 1-Butyl-3-methylimidazolium Bis (trifluoromethylsulfonyl) imide, *J. Chem. Eng. Data*, 52, 1080–1085 (2007).
11. Duluard S. et al., Lithium solvation and diffusion in the 1-butyl-3-methylimidazolium bis(trifluoromethanesulfonyl)imide ionic liquid, *J. Raman Spectrosc.*, 39, 627–632 (2008).
12. Monti D., Jónsson E., Palacín M. R., Johansson P., Ionic liquid based electrolytes for sodium-ion batteries: Na⁺ solvation and ionic conductivity, *J. Power Source*, 245, 630–636 (2014).
13. Tokuda H. et al., Physicochemical Properties and Structures of Room-Temperature Ionic Liquids, 3. Variation of Cationic Structures, *J. Phys. Chem. B*, 110, 2833–2839 (2006).
14. Monteiro M. J., Bazito F. F. C., Siqueira L. J. A., Ribeiro M. C. C., Torresi R. M., Transport coefficients, Raman spectroscopy, and computer simulation of lithium salt solutions in an ionic liquid, *J. Phys. Chem. B*, 112, 2102–2109 (2008).
15. Hayamizu K., Aihara Y., Nakagawa H., Nukuda T., Price W. S., Ionic conduction and ion diffusion in binary room-temperature ionic liquids composed of [emim][BF₄] and LiBF₄, *J. Phys. Chem. B*, 108, 19527–19532 (2004).
16. Yu L., Pizio B. S., Vaden T. D., Conductivity and spectroscopic investigation of bis(trifluoromethanesulfonyl)imide solution in ionic liquid 1-butyl-3- methylimidazolium bis(trifluoromethanesulfonyl)imide, *J. Phys. Chem. B*, 116, 6553–6560 (2012).
17. Tokuda H., Hayamizu K., Ishii K., Susan M. A. B. H., Watanabe M., Physicochemical

- properties and structures of room temperature ionic liquids, 2. variation of alkyl chain length in imidazolium cation, *J. Phys. Chem. B*, 109, 6103–6110 (2005).
18. Xu W., Cooper E. I., Angell C. A., Ionic Liquids: Ion mobilities, glass temperatures, and fragilities, *J. Phys. Chem. B*, 107, 6170–6178 (2003).
 19. Harris K. R., Can the transport properties of molten salts and ionic liquids be used to determine ion association, *J. Phys. Chem. B*, 120, 12135–12147 (2016).
 20. Schreiner C., Zugmann S., Hartl R., Fractional walden rule for ionic liquids: examples from recent measurements and a critique of the so-called ideal KCl line for the walden plot, *J. Chem. Eng. Data*, 55, 1784–1788 (2010).
 21. Kunze M., Appetecchi G. B., Jeong S. S., Balducci A., Melting behavior and ionic conductivity in hydrophobic ionic liquid-based electrolytes, 12981 (2007).
 22. Haskins J. B., Bennett W. R., Wu J. J., Hernández D. M., Borodin O., J. D. Monk, C. W. Bauschlicher, Computational and experimental investigation of Li-Doped Ionic Liquid Electrolytes: [pyr₁₄][TFSI], [pyr₁₃][FSI], and [EMIM][BF₄], *J. Phys. Chem. B*, 118, 11295–11309 (2014).
 23. F. Castiglione, A. Famulari, G. Raos, S. V. Meille, A. Mele, G. B. Appetecchi, Pyrrolidinium-based ionic liquids doped with lithium salts: how does Li⁺ coordination affect its diffusivity, *J. Phys. Chem. B*, 118, 13679–13688 (2014).
 24. Aihara Y., Arai S., Hayamizu K., Ionic conductivity, DSC and self diffusion coefficients of lithium, anion, polymer, and solvent of polymer gel electrolytes: The structure of the gels and the diffusion mechanism of the ions, *Electrochim. Acta*, 45, 1321–1326 (2000).
 25. Tokuda H., Hayamizu K., Ishii K., Bin A., Susan H., Physicochemical properties and structures of room temperature ionic liquids, Variation of anionic species, 16593–16600 (2004).
 26. Li W. et al., Effect of water and organic solvents on the ionic dissociation of ionic liquids, *J. Phys. Chem. B*, 111, 6452–6456 (2007).
 27. Dietz M. L., Ionic liquids as extraction solvents: Where do we stand?, *Sep. Sci. Technol.*, 41, 2047–2063 (2006).
 28. H. Luo, S. Dai, P. V. Bonnesen, A. C. Buchanan, J. D. Holbrey, N. J. Bridges, Extraction of cesium ions from aqueous solutions using Calix[4]arene-bis(tert-octylbenzo-crown-6) in ionic liquids, *Anal. Chem.*, 76, 3078–3083 (2004).
 29. N. Sieffert et al., Comparing an ionic liquid to a molecular solvent in the cesium cation extraction by a calixarene: a molecular dynamics study of the aqueous interfaces, *J. Phys. Chem. B*, 110, 19497–19506 (2006).
 30. <http://abulafia.mt.ic.ac.uk/shannon/ptable.php>.
 31. Feng G., Chen M., Bi S., Goodwin Z. A.H., Postnikov E. B., Urbakh M., Kinetics of ion transport in ionic liquids: two dynamical diffusion states (2018).
 32. Giffin G. A., Moretti A., Jeong S., Passerini S., Complex nature of ionic coordination in magnesium ionic liquid-based electrolytes: Solvates with mobile Mg²⁺ cations, *J. Phys. Chem. C*, 118, 9966–9973 (2014).
 33. Yoon H., Zhu H., Hervault A., Armand M., MacFarlane D. R., Physicochemical properties of N-propyl-N-methylpyrrolidinium bis(fluorosulfonyl)imide for sodium metal battery applications, *Phys. Chem. Chem. Phys.*, 16, 12350 (2014).
 34. Herstedt M. et al., Spectroscopic characterization of the conformational states of the bis(trifluoromethanesulfonyl)imide anion (TFSI), *J. Raman Spectrosc.*, 36, 762–770 (2005).

35. Capitani F. et al., The complex dance of the two conformers of bis(trifluoromethanesulfonyl) imide as a function of pressure and temperatures, *J. Phys. Chem. B*, 120, 1312–1318 (2016).
36. Palumbo O. et al., An infrared spectroscopy study of the conformational evolution of the Bis(trifluoromethanesulfonyl)imide ion in the liquid and in the glass state, *Adv. Condens. Matter Phys.*, 2015, (2015).
37. Paolone A., Stabilization of different conformers of bis(trifluoromethanesulfonyl)imide anion in ammonium-based ionic liquids at low temperatures (2014).
38. Paschoal, V. H., Faria, L. F. O., Ribeiro, Vibrational spectroscopy of ionic liquids, *Chem. Rev.*, 117, 7053–7112 (2017).
39. Lassegues J. et al., Spectroscopic identification of the lithium ion transporting species in litfsi-doped ionic liquids spectroscopic identification of the lithium ion transporting species in LiTFSI-doped ionic, 305–314 (2009).
40. Lassègues J. C., Grondin J., Talaga D., Lithium solvation in bis(trifluoromethanesulfonyl) imide-based ionic liquids, *Phys. Chem. Chem. Phys.*, 5629–5632 (2006).
41. Pilar K. et al., Communication: Investigation of ion aggregation in ionic liquids and their solutions with lithium salt under high pressure, *J. Chem. Phys.*, 148, (2018).
42. Sippel P., Lunkenheimer P., Krohns S., Thoms E., Importance of liquid fragility for energy applications of ionic liquids, *Sci. Rep.*, 5, 13922 (2015).
43. Ueno K., Tokuda H., Ionicity in ionic liquids: correlation with ionic structure and physicochemical properties, *Phys. Chem. Chem. Phys.*, 12, 1649–1658 (2010).
44. Fraser K. J., Izgorodina E. I., Forsyth M., Scott J. L., Liquids intermediate between ‘molecular’ and ‘ionic’ liquids: Liquid Ion Pairs, *Chem. Comm.*, 3817–3819 (2017).



Chapter 3

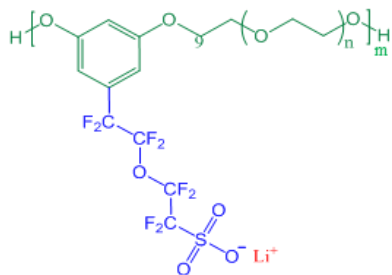
Polymer-based electrolyte for Li-metal battery

Abstract

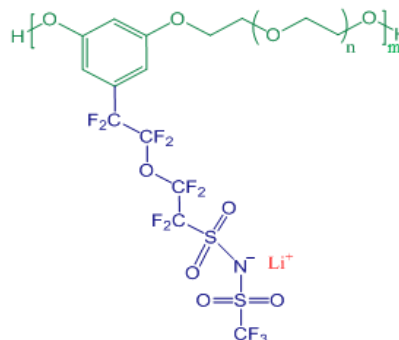
In this chapter, two types of single-ion conducting polymers were synthesized and characterized as solid polymer electrolytes. The first part presents a new family of polymer electrolytes based on the cross-linked SIPEs, which was obtained in three steps e.g. two polycondensation reactions, following by a radical polymerization under UV irradiation. Two types of anions were bonded to the PEO backbone: phenyl-oxoperfluoropentane sulfonate (p-SO₃), (SIPEs named as I_xp-SO₃-db, x corresponds to the molecular weight of precursor used in the first synthesis step i.e. poly(ethylene glycol) – PEG), and phenyl-oxoperfluoropentane sulfonylimide (p-TFSI), (SIPEs named I_p-TFSI-db). The polymer electrolytes Li-form were characterized as a function of anion's nature, and of EO/Li ratio. The electrochemical performances of I₁₀₀₀ p-SO₃-cr in a symmetrical Li-metal cell (Li/SIPE/Li), and in a full battery (Li-metal/SIPE/LFP) were evaluated.

In the second part, the synthesis and characterizations of multi-block copolymers (named as Co_x p-SO₃), obtained by the copolymerization of a linear I_x p-SO₃ block and a hydrophobic partially fluorinated poly(ether sulfone) - (FPES) block were presented. To improve the conductivity of material, low molecular weight poly(ethylene glycol)dimethyl ether (DMPEG) was added as plasticizer. Electrochemical behaviors of the resulted polymer were studied as solid electrolytes for Li-metal battery using LFP cathode.

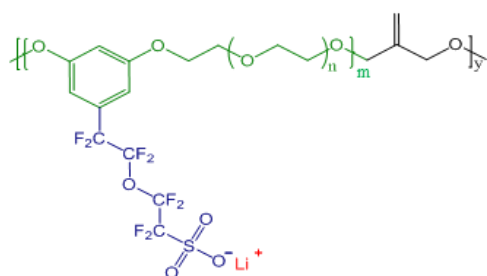
Chemical structure of polymers study in this chapter



Ip-SO₃

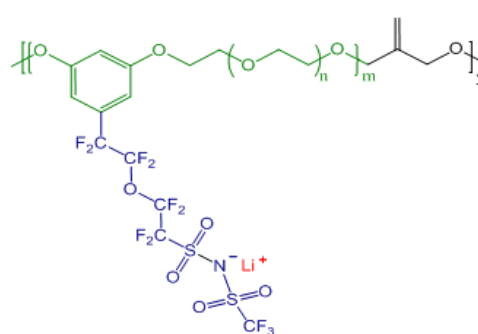


Ip-TFSI

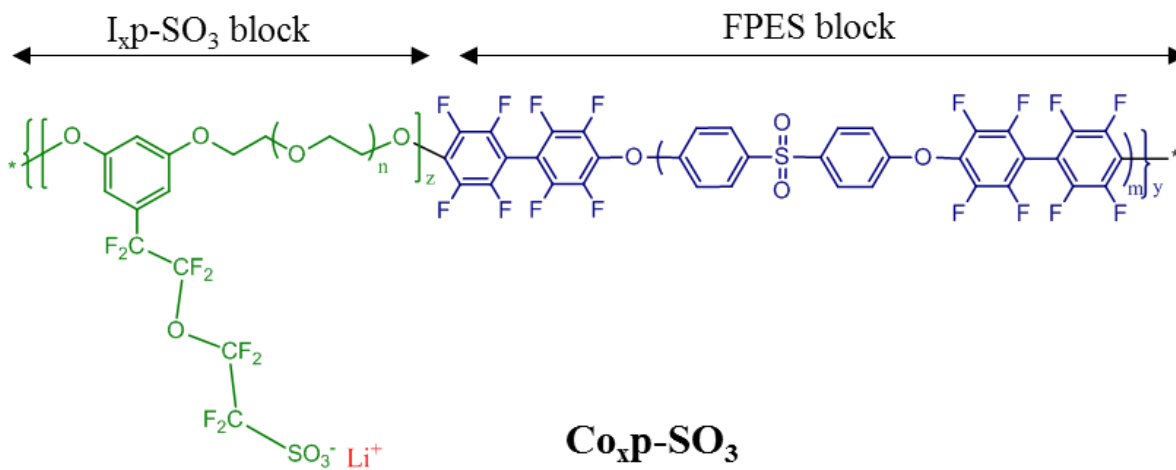


I_xp-SO₃-db

where x = 1000; 600; 400



I₁₀₀₀p-TFSI-db



Co_xp-SO₃

where x = 1000; 400

1. Cross-linked single-ion polymer electrolyte (SIPE)

The SIPEs were obtained in three steps:

- 1) Synthesis of ionic block (ionomer) $I_x\text{p-SO}_3$ and $I_{1000}\text{p-TFSI}$ by polycondensation reaction between PEG and potassium-5-(3',5'-difluorophenyl)-3-oxoperfluoropentane sulfonate - (p-SO_3), or sodium-N-(trifluoromethane)-5-(3',5'-difluorophenyl)-3-oxoperfluoropentanesulfonylimide (p-TFSI). Where x is the length of PEG e.g. 1000; 600; 400 g/mol.
- 2) Synthesis of $I_x\text{p-SO}_3\text{-db}$, and $I_{1000}\text{p-TFSI-db}$ with double-bonds side chain by polycondensation reaction of the ionic block performed in the first step and 1,3-dichloro-2-methyl-propene.
- 3) Film casting and double-bonds polymerization under UV irradiation (cross-linked films named as $I_x\text{p-SO}_3\text{-cr}$ and $I_{1000}\text{p-TFSI-cr}$).

Additionally, two linear ionomers, i.e. $I\text{p-SO}_3$ and $I\text{p-TFSI}$, with the desired molecular weight of 10 kg/mol were synthesized and comparatively characterized.

1.1. Syntheses of ionic block (ionomers)

Ionic blocks with the molecular weights of 10 and 5 kg/mol were synthesized by polycondensation reaction between the PEG, with different molecular weights (400, 600, 1000 g/mol), and the ionic monomer, based on difluorobenzene grafted with the anions types perfluoropentane sulfonate - (p-SO_3), or perfluoropentane sulfonylimide (p-TFSI). The two monomers (Fig. 1) were provided by ERAS Labo.

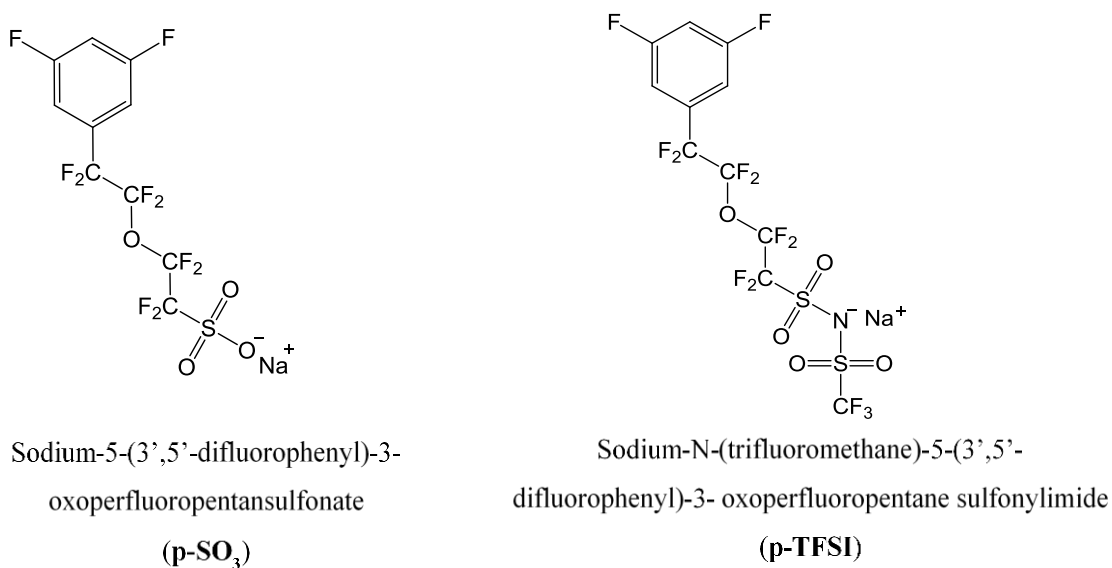


Fig. 1 Schematic presentation of the monomers used for SIPEs syntheses.

For this work, about 3 g of the p-TFSI monomer was provided by Eras labo. The synthesis and purification of this monomer are more complicated, and resulting in much lower reaction yield as compared to its homologue p-SO₃ monomer. Therefore the majority of studies was conducted with the sulfonated monomer.

In this polycondensation reaction, molecular weight of ionomer was predicted by the ratio of PEG and ionic monomer. To control the molar mass and functionalized the ionomer, the monomer terminating the block must be taken in excess. The ratio r of two monomers was calculated by Carother's equation, as seen below:

$$MW_{\text{block}} = \frac{1(1+r)}{2(1-r)} MW_0 + MW_{\text{end}} \quad (1)$$

where MW_{block} is the previewed molecular weight of a block, MW_0 is molecular weight of a structural unit, MW_{end} is molecular weight of a terminating monomer. A schema illustrates the parameters of Carother's equation for ionomer synthesis is presented in Fig. 2, and these calculated values for the previewed molecular weights of 10 and 5 kg/mol are resumed in Table 1.

To obtain the predicted molecular weight, highly purified monomers were required. Therefore, all the reagents used for ionomer syntheses were carefully prepared and stored in an Argon filled glove box prior use. This polycondensation reaction is also very sensitive to the presence of water, the reaction was performed under an Argon flux. For the ionomers possessed double-bonds along the backbone, the OH functions from the end chain of ionomer after the first synthesis step reacted with 3-dichloro-2-methyl-propene. The quantity of OH end-chain corresponds to $[(1-r) \times \text{moles}]$ of PEG, and a stoichiometric amount of 3-dichloro-2-methyl-propene was used to obtain the highest molecular weight.

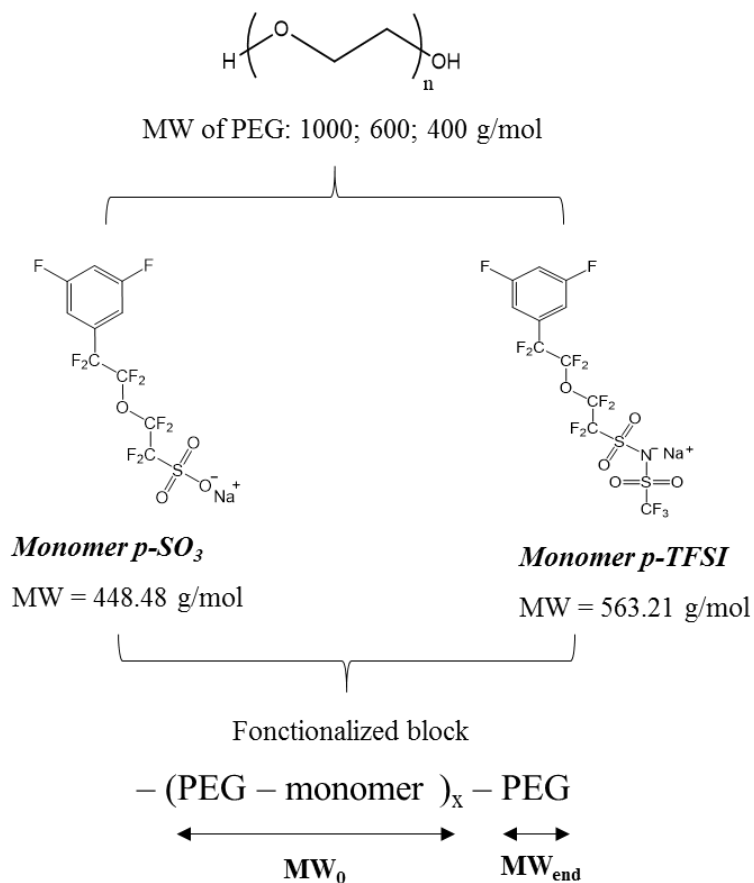


Fig. 2 Schema illustrates the parameter of Carother's equation for ionomer synthesis.

Table 1 Parameters of Carother's equation used for ionomer synthesis.

Ionomer	MW _{POE} g.mol ⁻¹	EO/M ratio	MW _{block} g.mol ⁻¹	MW ₀ g.mol ⁻¹	MW _{end} g.mol ⁻¹	<i>r</i>
I ₁₀₀₀ p-SO ₃	1000	23	10 000	1408	999	0.855
I ₁₀₀₀ p-SO ₃ -db	1000	23	5000	1408	999	0.701
I ₆₀₀ p-SO ₃ -db	600	14		1008	599	0.794
I ₄₀₀ p-SO ₃ -db	400	9		808	399	0.839
I ₁₀₀₀ p-TFSI	1000	23	10 000	1523	999	0.844
I ₁₀₀₀ p-TFSI-db	1000	23	5000	1523	999	0.680

This synthesis approach lead to a very homogeneous distribution of anions along the polymer backbone, and the distance between two anions is always fixed by the length of PEG, as illustrated in Fig. 3.

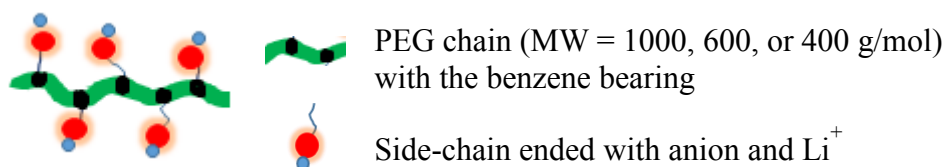


Fig. 3 Cartoon schematic of ionomer based on PEO and the grafted the anions.

1.1.1. Synthesis of Ip-SO₃

The Ip-SO₃ was synthesized via a polycondensation reaction (see Fig. 2) with the desired molecular weight (MW_{block}) of 10 kg/mol. The PEG (MW 1000 g/mol) and NaH dissolved bis(2-methoxyethyl) ether (diglyme) were heated at 60 °C, under Argon flux to form the O⁻,Na⁺ groups at the end-chain of PEG. A change of color from colorless to dark-brown, after about 2 h, indicated the formation of the expected O⁻ Na⁺ functions. In the next step, a required quantity of sodium-5-(3',5'-difluorophenyl)-3-oxoperfluoropentansulfonate, noted as monomer sulfonate, dissolved in DGME was added. The mixture was heated at 140 °C for at least 2h, and the formation of ionomer was followed by ¹⁹F-NMR spectrometry until the aromatic fluorines at -108 ppm (see the insert photo in Fig. 5) disappeared. The resulting yellowish gel polymer was purified, then exchanged into Li-form, following the processes described in the annex (1.3.2.). Ionomer was filtered under vacuum in a plastic ultra-filtration cell, using the Millipore ultrafiltration membrane of 3 kDa, to remove residual inorganic salts, low molecular weight polymer (lower than 3000 g/mol), remaining traces of solvents, and un-reacted monomer. This reaction was repeated multiple times to affirm the reproducibility.

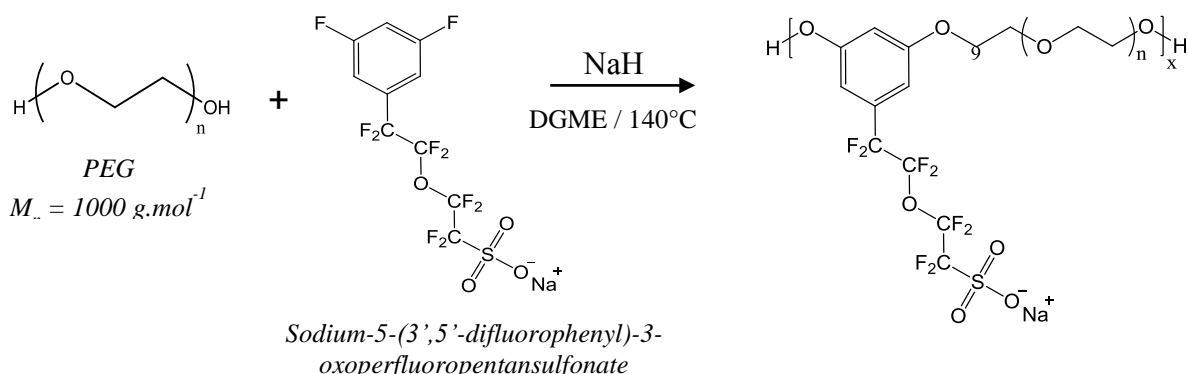


Fig. 2 Synthesis process of I_{1000p}-SO₃.

Fig. 5 illustrates the ¹H and ¹⁹F-NMR spectra of the neat Ip-SO₃ in deuterated acetone (acetone-d₆), which proved high purity of the final product. As seen in Fig. 5, where only the peaks corresponding to ionomer protons are presented, the single peaks at 6.93 and 6.84 ppm relate to the aromatic protons of benzene bearing, the multi-peaks at 4.31 and 3.93 ppm attribute to (CH₂-CH₂-O) bonds near the aromatic ring, and the protons of PEG appear at 3.70 ppm. The ratio of integrals correspond perfectly to the expected structure of ionomer I_{1000p}-SO₃. The ¹⁹F-NMR spectrum shows four single peaks

corresponding to the CF_2 groups of anionic function. The aromatic fluorines at -108 ppm of the unreacted ionic monomer (insert figure) were disappeared completely after the reaction.

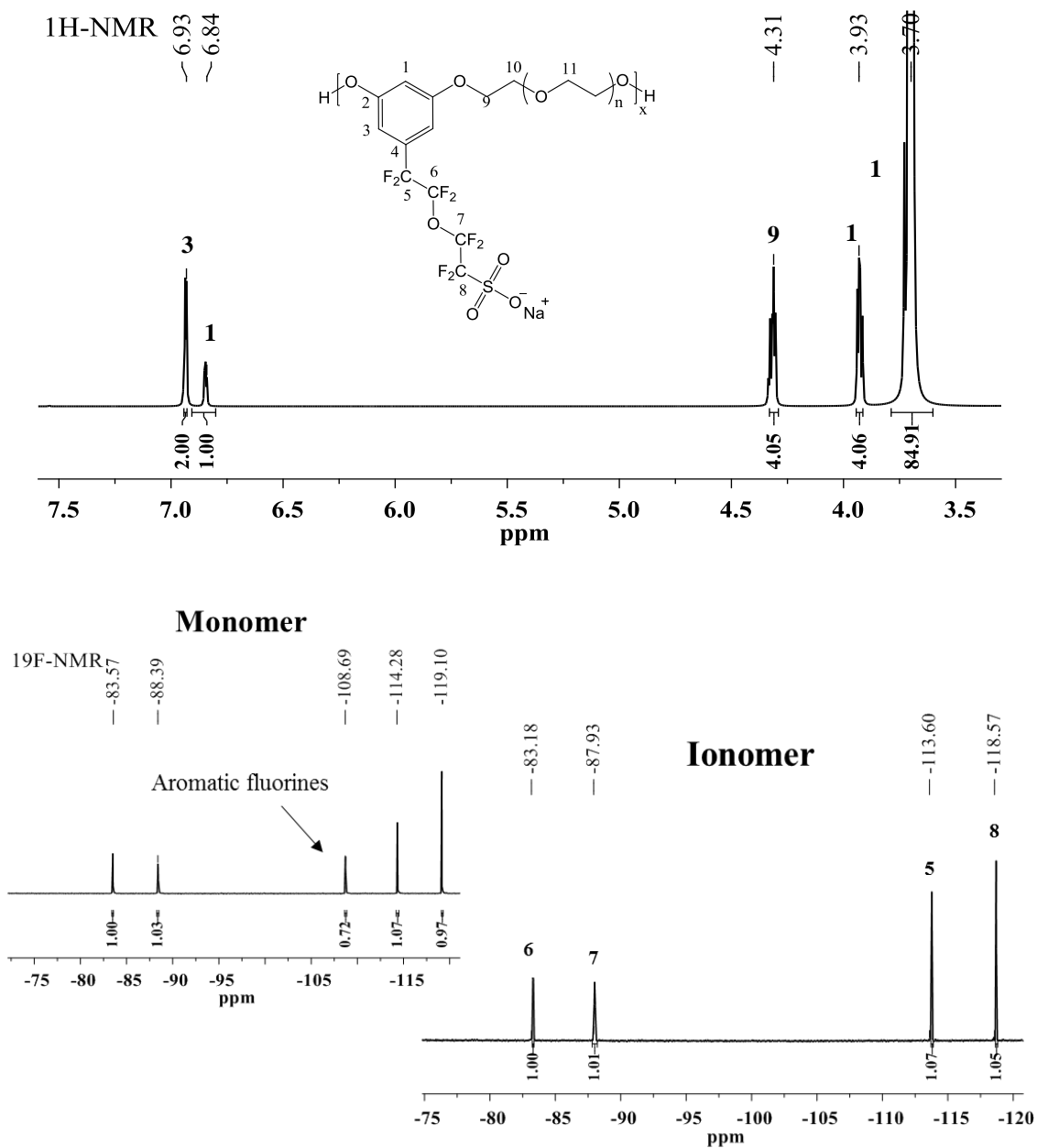


Fig. 3 ^1H and ^{19}F -NMR spectra of $I_{xp}\text{-SO}_3$ in acetone- d_6 , inset figure presents the ^{19}F -NMR spectrum of the un-reacted monomer.

1.1.2. Synthesis of $I_x p\text{-SO}_3\text{-db}$ with double-bonds along the chain

The $I_x p\text{-SO}_3\text{-db}$ were synthesized via a two-step polycondensation reaction, with the desired molecular weight of 5 kg/mol. The PEG with different molecular weights of 1000, 600, and 400 g/mol were used to vary the ratio of EO units per Li^+ ion, denoted as EO/Li, from 23, 14, to 9, respectively.

The ionomer was synthesized using the same process as for $I_p\text{-SO}_3$ (in 1.1.1). When the peak of aromatic fluorines disappeared in ^{19}F -NMR spectrum, the reaction was cooled down to $70\text{ }^\circ\text{C}$, and a desired quantity of 1,3-dichloro-2-methyl-propene was added. The synthesis process of the second polycondensation step is presented in Fig. 6.

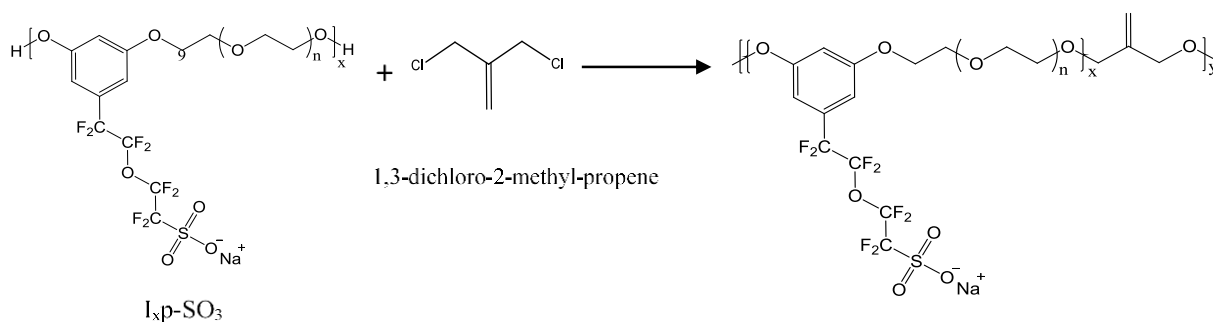


Fig. 4 Synthesis schema of $I_x p\text{-SO}_3\text{-db}$.

This reaction step was monitored by ^1H -NMR spectrum (in acetone- d_6). The spectrum of $I_{1000} p\text{-SO}_3\text{-db}$ is given in Fig. 5 as an example. At the beginning of the second step, the protons of 1,3-dichloro-2-methyl-propene were found at 5.44 and 4.32 ppm, then shifted to 5.25 and 4.09 ppm when the reaction finish. The integral ratio between aromatic and double-bonds protons was about 1: 0.47, corresponding perfectly to one double-bonds for each ionic block of 5 kg/mol. ^{19}F -NMR spectrum of the resulted ionomer was similar to that of $I_p\text{-SO}_3$ (Fig. 5), where four single peaks corresponding to the CF_2 groups of perfluorosulfonic side chain were observed. Ionomers were recovered and purified using the same protocol as for $I_p\text{-SO}_3$.

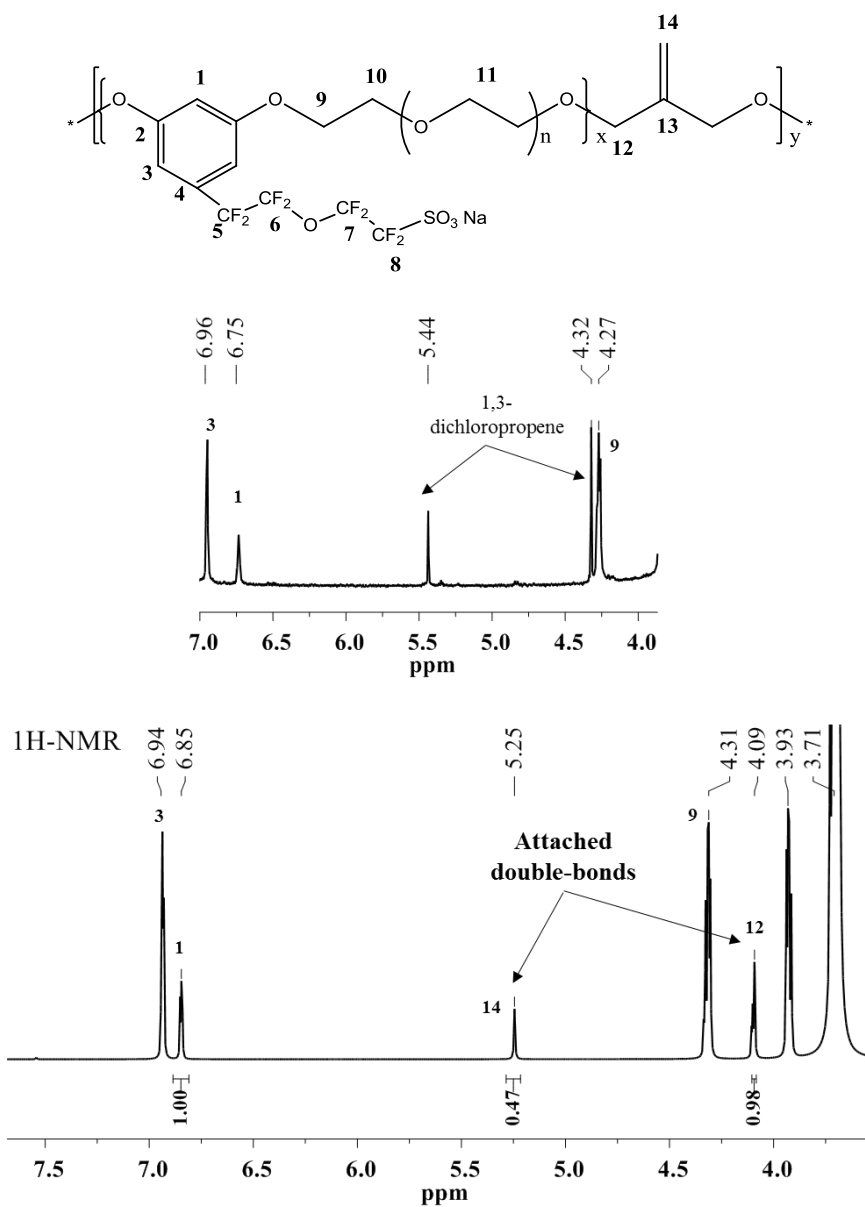


Fig. 5 The $^1\text{H-NMR}$ spectrum of $I_{1000}p\text{-SO}_3\text{-db}$.

1.1.3. Synthesis of Ip-TFSI

Based on the same protocols described in 1.1.1, the ionomer Ip-TFSI were synthesized via a polycondensation reaction (Fig. 8) between the PEG (MW 1000 g/mol) and the monomer perfluoropentanesulfonylimide (**p-TFSI**), with a desired MW of 10 kg/mol. The ^{19}F -NMR spectra of unreacted monomer, and Ip-TFSI in acetone- d_6 are shown in Fig. 7. The peak at -79.7 ppm corresponds to the fluorines of $-(\text{NSO}_2\text{CF}_3)$ sulfonylimide anion, and four others single peaks represent the fluorines of CF_2 groups from the side chain. The ^1H -NMR spectrum of Ip-TFSI is similar to that of Ip- SO_3 (Fig. 3). The obtained yellowish gel polymer was purified, and exchanged into Li^+ form.

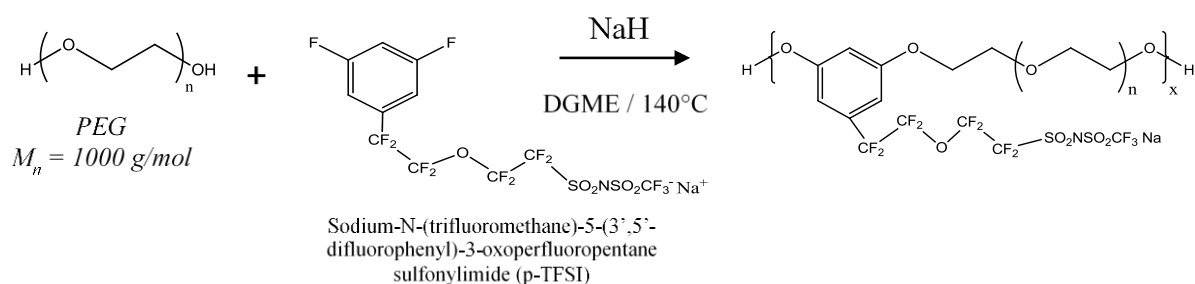


Fig. 6 Synthesis process of Ip-TFSI.

The synthesis of Ip-TFSI faced the multiple difficulties. Despite adding the PEG in excess as compared to the ionic monomer, the aromatic fluorines were not completely reacted (peak at -108 ppm in ^{19}F -NMR spectrum). Increasing the temperature, as well as the reaction time did not help to consume the whole quantity of aromatic fluorines. Therefore, new amount of NaH was added to finish the reaction. We did not understand the lower reactivity of TFSI monomer than the perfluorosulfonic one, because the only difference between two monomers concerns the function at the end of side chain i.e. sulfonate or sulfonylimide, which locates so far from the aromatic ring, and should not change the reactivity of aromatic fluorines.

Regarding the NMR spectra, the protons' integrals correspond perfectly to the expected structure of Ip-TFSI. In the ^{19}F spectrum, the integral ratio between four CF_2 groups from the side chain are rather similar for ionomer, without any additional fluorine peaks, or the specific peaks of perfluorosulfonic side chain. Integrals of $(\text{NSO}_2\text{CF}_3)$ fluorines and CF_2 groups' fluorines for monomer and ionomer have not a good ratio e.g. a slight reduction of integrals ratio from 1.2: 1 to 1:1 is observed, respectively, while it should be 1.5:1 for the correct spectrum of monomer. An elementary analysis performed by Eras-labo proved the high purity of monomer, so this lower integral ration for the monomer is mainly related to the difference in relaxation time of different fluorines. To reach the good ratio, the NMR acquisition time should to be modified.

1.1.4. Synthesis of I₁₀₀₀ p-TFSI-db with double-bonds along the chain

Ionomer I₁₀₀₀ p-TFSI-db was synthesized using the same protocol described in 1.1.2 for the PEG (MW 1000 g/mol) and the monomer perfluorosulfonylimide (p-TFSI). The final product was followed by ¹H-NMR spectrum in acetone-d₆ (Fig. 10). The integral ratio between the protons of aromatic ring (6.84 ppm) and of double-bonds (5.25 ppm) is approximately 1:0.5, which is slightly lower than the expected one of 1:0.6 (corresponds to one double-bonds for one functionalized block of 5 kg/mol) resulting in the longer chain i.e. about 6 kg/mol instead of 5 kg/mol between two double-bonds. The ¹⁹F-NMR spectrum of I₁₀₀₀ p-TFSI-db was similar to that presented in Fig. 9.

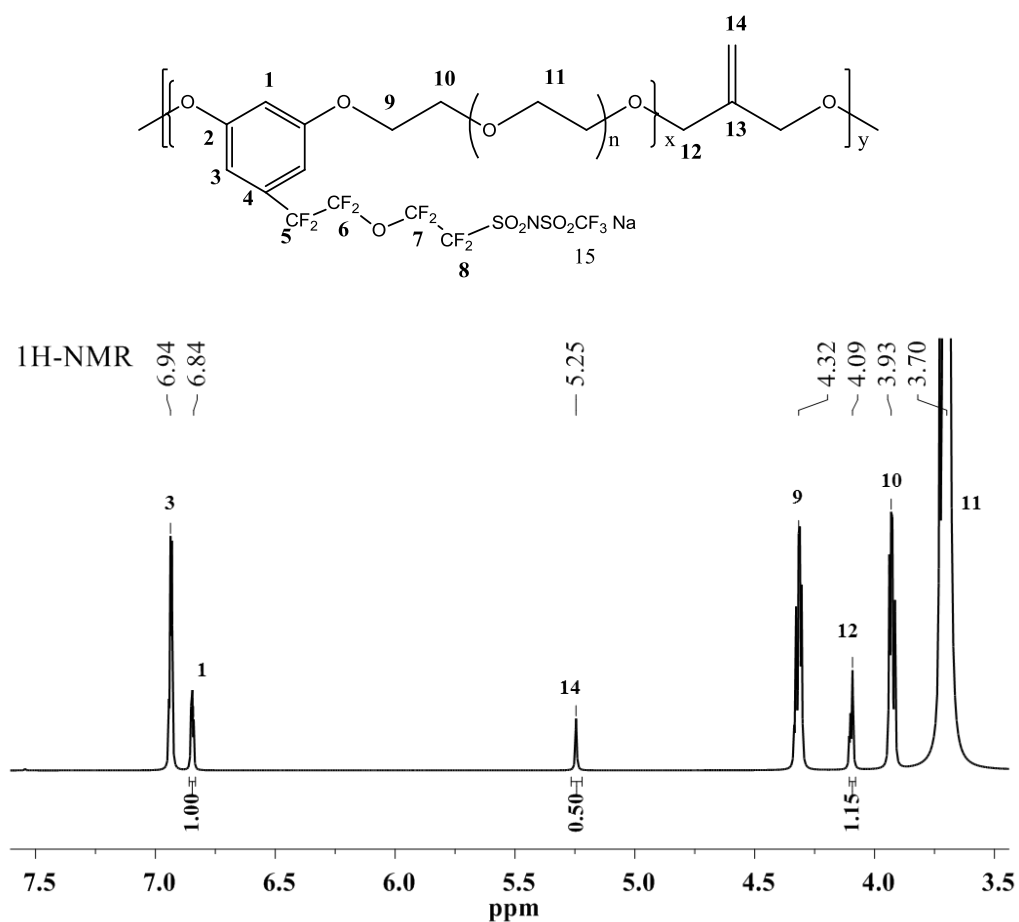


Fig. 8 The ¹H-NMR spectrum of I₁₀₀₀ p-TFSI in acetone-d₆.

1.2. Characterization

1.2.1. Molar mass and cation exchange efficiency

The molecular weight is an important characteristic that can influence the mechanical properties of a polymer. A longer chain leads to higher chain entanglements and cross-linking degree, hence better mechanical properties. Besides, the syntheses of ionomers was performed in the presence of NaH, and the starting aromatic monomers contained the Na⁺ or K⁺ ions. Since these materials are used as electrolyte for lithium batteries, the high efficiency of cation exchange needed to be ensured. The ion exchange was performed on chromatography column containing the Amberlite™ IR120 resin in Li-form. The lithiated resin was prepared by mixing the Amberlite H-form, purchased from Sigma Aldrich, with an excess of LiOH in aqueous solution (detailed protocol is described in the annex). The molecular weight of the synthesized ionomers, measured by size exclusion chromatography coupled multi-angle laser light scattering (SEC-MALLS), and the content of cations detected by absorption spectroscopy (AAS) are presented in Table 2.

The linear ionomers i.e. Ip-SO₃ and Ip-TFSI have similar molecular weight of $M_w = 17$ kg/mol, and a polydispersity index (DPI) of 1.3 ($M_n = 12$ and 13 kg/mol respectively). The I_xp-SO₃-db (with x = 1000, 600, 400) have molecular weights (M_w) ranging between 24 and 35 kg/mol, with a DPI from 1.4 to 1.7. The low DPI (usually for a polycondensation reaction the DPI is 2) of these polymers is due to the filtration step that eliminated the low molecular weight (< 3 kg/mol) oligomers. Molecular weight is much higher in the case of I₁₀₀₀p-TFSI-db, and ranging between 49 and 61 kg/mol, with a DPI of 1.3. From the obtained results, the number of double-bonds side chain along the polymer chain are between 3 and 5 in the case of I₄₀₀p-SO₃-db and I₁₀₀₀p-SO₃-db, and between 4 and 7 for I₆₀₀p-SO₃-db chain. Possessing the higher molecular weight, the I₁₀₀₀p-TFSI-db has approximately 10 to 12 double-bonds in a chain polymer.

The cation's concentration detected by absorption atomic spectroscopy (AAS) is an important factor that indicates the yield of ion exchange process. The ionomers Li-form, dissolved in distilled water, were passed through the flame detectors for Li, Na and K elements to determine the alkali concentration in the sample. The solution of 5 ppm of cation (estimated to Li⁺ ions) was prepared by dissolving a desired quantity of ionomer in water (the mass of Li was calculated from the mass of a unit block MW_0 in Table. 1). Concentration of the three elements Li, Na, K, measured by AAS, were transferred into percentages, as seen in Table 2. All of the lithiated ionomers contain more than 95 % of Li⁺ ions that reflecting an excellent yield of ion exchange reaction.

Table 2 Properties of synthesized ionomers including molecular weight and composition of cations.

Ionomer Li form	EO/ Li ratio	SEC-MALLs			AAS		
		M _n (kg.mol ⁻¹)	M _w (kg.mol ⁻¹)	DPI	Li %	Na %	K %
I _p -SO ₃	23	12	17	1.3	100	-*	-
I _{1000 p} -SO ₃ -db	23	18	24	1.3	97.1	2.9	-
I _{600 p} -SO ₃ -db	14	21	35	1.7	97.4	1.2	1.4
I _{400 p} -SO ₃ -db	9	19	24	1.3	96.1	1.5	2.3
I _p -TFSI	23	13	17	1.3	95.0	-	4.9
I _{1000 p} -TFSI-db	23	49	61	1.3	96.8	-	3.1

* (-) Concentration non-detectable

1.2.2. Cross-linking degree and NCC dispersion

i. Cross-linking degree

The lithiated ionomers with double-bonds were casted into membrane, and cross-linked using an UV irradiation with the presence of 2-hydroxy-4'-(2-hydroxyethoxy)-2-methylpropiophenone (Irgacure 2959). This photoinitiator is known as a good photo-caged radical source¹, and the photochemical decomposition, studied by Scaiano et al.², is presented in Fig. 9. Under UV irradiation, the radicals of photoinitiator initiate the radical polymerization of double-bonds from ionomer. Due to the presence of the double-bonds along the polymer chain, the polymerization reaction can create a 3D network (cross-linked ionomer). Cross-linking reaction of the synthesized ionomers possessed the double-bonds is illustrated in Fig. 10, and a detailed process is described in the annex.

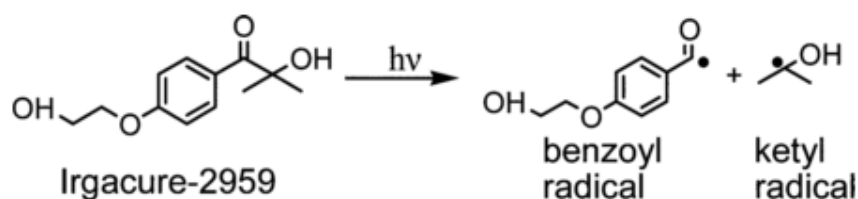


Fig. 9 The photochemistry pathway of Irgacure 2959 demonstrated by Scaiano et al.²

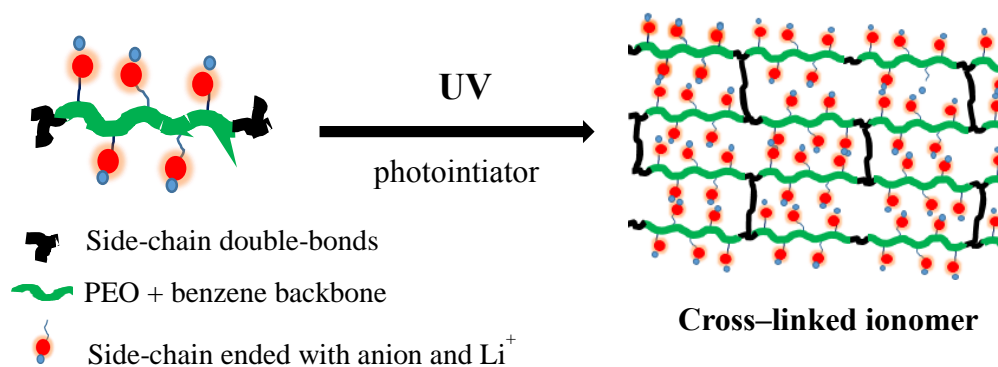


Fig. 10 Cross-linked process of the synthesized ionomers with the double-bonds using an UV irradiation.

The yield of reaction was evaluated by FT-IR spectroscopy. Ionomers before and after cross-linking were observed from 4000 to 400 cm^{-1} , in transmission, with 16 accumulations, and a resolution of 1 cm^{-1} , at RT. The IR spectra of the interested zone from 1750 to 1400 cm^{-1} for $I_{1000}\text{p-SO}_3\text{-db}$, $I_{1000}\text{p-SO}_3\text{-cr}$ (Fig. 3A), and for $I_{1000}\text{p-TFSI-db}$, $I_{1000}\text{p-TFSI-cr}$ (Fig. 3B) are illustrated.

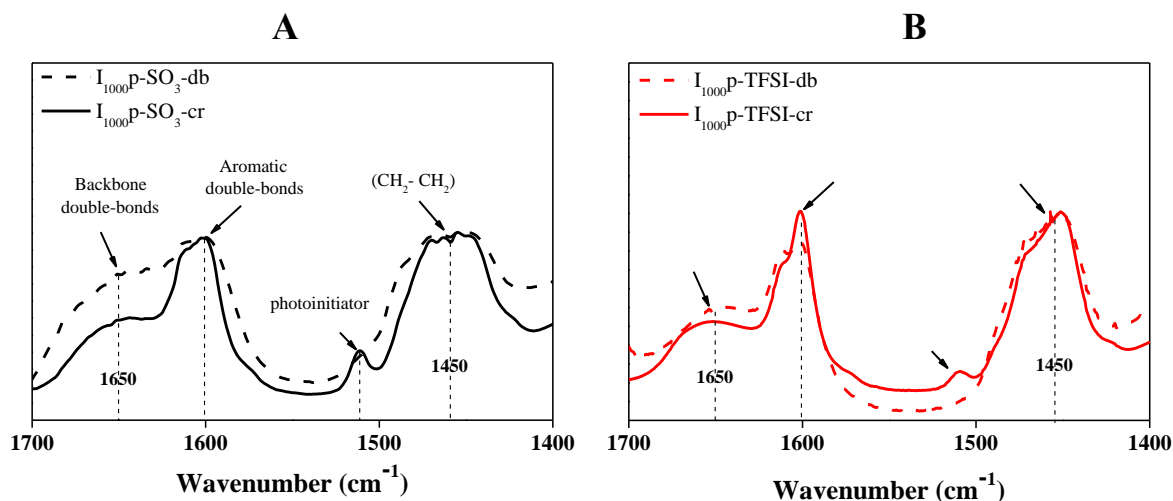


Fig. 11 FTIR spectra of (A) $I_{1000}\text{p-SO}_3$ and (B) $I_{1000}\text{p-TFSI}$ from 1750 to 1400 cm^{-1} ; before cross-linking (dash line), and after cross-linking (straight line).

Intensities of the bands at 1600 cm^{-1} , and 1450 cm^{-1} corresponding to the aromatic double-bonds and the $-\text{CH}_2\text{-CH}_2$ bonds of PEG did not evolve after the cross-linking. The IR spectra were normalized to obtain the same intensity for the bands at 1450 cm^{-1} . The peak at 1510 cm^{-1} in the cross-linked ionomer's spectrum is a characteristic peak of photoinitiator Irgacure 2959.¹ Intensity of the peak at 1650 cm^{-1} , corresponding to the double-bonds side chain, decreased significantly after irradiation.³ The yield of reacted double-bonds was determined by the ratio of intensities of the peaks at 1650 cm^{-1} for ionomer's before and after cross-linking, following the relation:

$$\text{degree of crosslinking} = 1 - \frac{I_{1650} \text{ crosslink}}{I_{1650} \text{ initial}} * 100$$

Where $I_{1650} \text{ crosslink}$ and $I_{1650} \text{ initial}$ represent intensities of the peaks at 1650 cm^{-1} for cross-linked

and non-cross-linked ionomers, respectively. The cross-linking density of ionomers are showed in Table 3.

Table 3 Cross-linking degree of synthesized ionomers with double-bonds obtained by FTIR spectroscopy.

Ionomer	Intensity of the band at 1650 cm ⁻¹		Degree of cross-linking (%)
	Non cross-linked	Cross-linked	
I ₁₀₀₀ p-SO ₃	0.75	0.49	35
I ₆₀₀ p-SO ₃	0.69	0.39	43
I ₄₀₀ p-SO ₃	0.67	0.42	38
I ₁₀₀₀ p-TFSI	0.49	0.42	15

Crosslinking yield of the I_x p-SO₃ is ranging from 35 to 43 %, while it is only 15 % for I₁₀₀₀ p-TFSI. The lower crosslinking yield of I₁₀₀₀p-TFSI may correlate to the higher molecular weight, thus higher viscosity, as well as lower concentration of double-bonds (as proved in 1.1.4). Cross-linking degree of I₁₀₀₀ p-SO₃ are comparable to those reported for the non-ionic polycondensate³. This low cross-linking density may induce poor mechanical properties of the resulted ionomer films. However, the main objective was to form the 3D ionomers with good chain mobility (a moderate cross-linking density), and further reinforced by the nano-fillers (NCC), because high density of cross-linking can dramatically decrease the ionic conductivity.⁴

The solubility tests in a solvent were also performed to check the suitable cross-linking density of the resulted ionomer films. The cross-linked ionomers immersed in deuterated acetonitrile for 24 h, and the extracted liquid phase were analyzed by ¹H and ¹⁹F-NMR spectroscopies. A definite mass of dried membrane weighted in the glove box was put in a volume of solvent. The vial was closed carefully to prevent the evaporating of organic solvent. After 24 h, the liquid phase contained the soluble ionomer was extracted by filtration, and filled in an NMR tube (d = 4mm). A reference solution of 0.5 M tetrabutyltetrafluoroborate, filled in a small insert tube(d = 3mm), was inserted in the NMR tube to quantify the amount of ionomer dissolved in acetonitrile by observing the ratio of integrals between the ionomer's characteristic peaks and the reference solution. The quantity of ionomer dissolved in acetonitrile after 24 h was less than 5 wt.% for all cross-linked matrix indicating a sufficient cross-linking density for further application as solid electrolytes.

ii. Nano cellulose dispersion

The performed membranes, generally for I₁₀₀₀ p-SO₃-cr and I₁₀₀₀ p-TFSI-cr, even after crosslinking were very sticky and impossible to handle or manipulate correctly in the glove box. To improve the

mechanical properties of these films, the nano crystals cellulose (NCC) fillers were used to reinforce the cross-linked ionomers. The used NCC has diameter of 2 to 20 nm with a factor form L/d of 10-100, and can be dispersed in water up to 4 wt.%. In a previous work of M. Bolloli⁵, the evolution of mechanical properties for the reinforced PVdF films (used the same type of NCC) proved that only from 6 wt.% of NCC content, these polymer films exhibited a noticeable improvement of mechanical strength with low impact on conductivity. However, above this concentration, the chain mobility was significantly affected, hence a decrease of the conductivity was also noticed.⁶

In this work, all of the cross-linked films were reinforced with 6 wt.% of NCC to enhance their mechanical strength. However, we were not able to measure the mechanical properties of these resulted films because our instruments performed in the ambient atmosphere, and these materials (based on PEO) absorbed quickly humidity from the environment and became very sticky and impossible to handle. Meanwhile, these reinforced films after drying under vacuum were able to manipulate in the inert atmosphere (without the presence of water) e.g. in an Argon-filled glove box.

The dispersion of the nanofillers was observed by Scanning Electron Micrograph (SEM) on the cross-section surface of membrane (cryo-fractured). The sample was prepared by immersing in liquid nitrogen for few seconds, then brook into pieces. The cross-section surface of sample was observed to determinate the aggregates or the inhomogeneous distribution of NCC in polymer matrix. The SEM image of I₁₀₀₀p-SO₃-cr reinforced with 6 wt.% NCC, and its corresponding treated binary image obtained by ImageJ are presented in Fig. 12 A,B. ImageJ is a useful free tool for image analysis and the sizes of distributions were determined using the “analyze particle” function of this software. The obtained data were presented by histogram by plotting the number of particles with their diameters in Fig. 12 C.

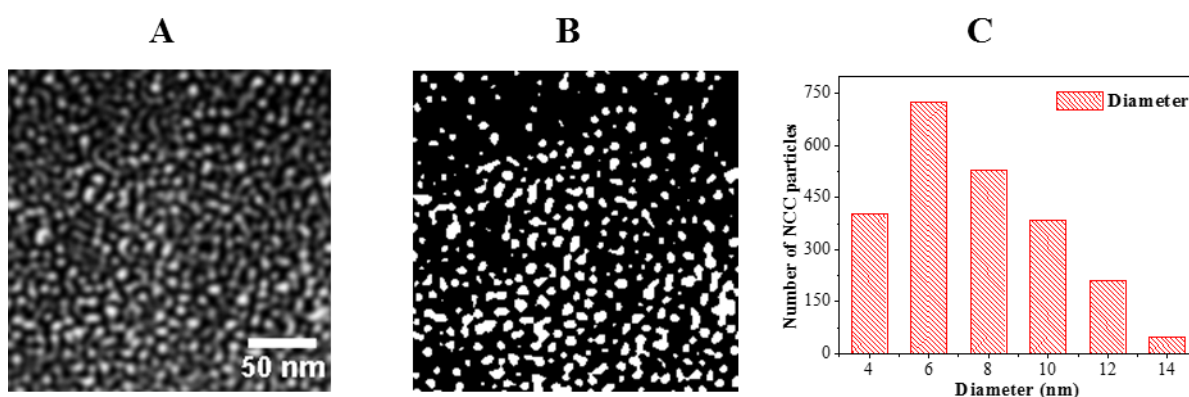


Fig. 12. (A) SEM images of the cryo-fractured surface for I₁₀₀₀p-SO₃-cr + 6 wt.% NCC, (B) with the corresponding ImageJ treated images, and (C) the number of NCC particles and their size distribution.

A homogenous dispersion of nano-fillers (NCC is the gray nodules in Fig. 14A or white nodules in the treated Fig. 14B) in the cross-linked matrix (black background) was observed indicating a successful process. The distribution of particles sizes is narrow and varies between 4 to 14 nm

corresponding to the average sizes of used NCC (theory value of $d = 2$ to 20 nm). Thus, an absence of aggregates is also observed in these SEM images. This homogenous distribution of NCC attributed to the absence of the crystalline domains (illustrate in 1.2.3) because the aggregates may formed during the POE spherulite growth, and the added NCC were ejected into interspherulitic regions.⁷

1.2.3. Thermal properties

i. *Thermal stability*

The thermal stability of materials was determined by thermogravimetric analysis (ATG). The dried samples weighted in a glove box, and the measurements performed under nitrogen atmosphere with a scan rate of 10 °C/min. The thermogravimetric curves from 250 to 450 °C, showing the degradation behaviors of synthesized ionomers are presented below. In Fig. 13, the ATG thermograms of Ip-SO₃ (black curve) and Ip-TFSI (red curve) are compared. These two ionomers exhibit high thermal stability (above 300 °C) that are very promising for safer solid electrolytes. This excellent thermal stability relates to the high thermal degradation temperatures of both PEO⁸, and the anionic monomers⁹ under nitrogen. The polymer degradation seems to take place by a sharp weight loss at about 300 °C, and the T_d value is determined at 5% weight loss for all samples.

A T_d value of 332 ± 2 °C is observed for Ip-SO₃, and 318 ± 2 °C for TFSI-based ionomer. This step relates to the degradation of PEG chain (reported T_d value of PEG under N₂ was between $250 - 340$ °C)¹⁰. Whereas the degradation of perfluorinated moiety reported in the previous work of O. Danyliv was above 300 °C⁹ under oxygen, and up to 414 ± 2 °C under N₂ flux. However, the degradation of ionomer based on TFSI starts sooner than that of sulfonated ionomer (about 14 °C lower), and its weight loss is not correlated to the weight fraction of PEG (1000 g/mol) in a unit block (MW_0 of 1523 g/mol), as seen in Table 4. We suspected that the presence of impurities from the synthesis may initiate the degradation of PEO segment at lower temperature.

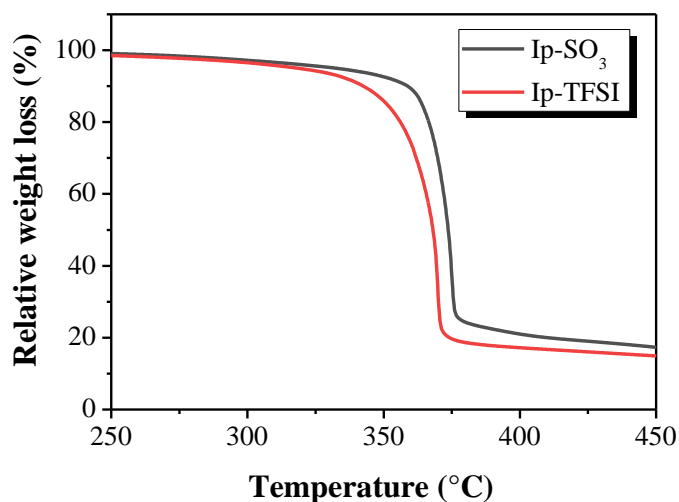


Fig. 13 Thermogravimetric curves of synthesized ionomers $I_{1000p}\text{-SO}_3$, and $I_{1000p}\text{-TFSI}$ from 250 to 450 °C.

Effect of Li concentration on thermal stability for the I_xp-SO_3-cr were also investigated (see Fig. 16). High thermal stability above 330 °C was reached for the three ionomers despite a difference of PEG length and Li content. The T_d value decreases with the length of PEG (from 1000 to 400 g/mol) as seen in Table 4. These values are very close for $I_{1000}p-SO_3-cr$ and $I_{600}p-SO_3-cr$ i.e. 356 ± 2 °C and 354 ± 2 °C, respectively, and decreases with more than 20 °C for $I_{400}p-SO_3-cr$ (334 ± 2 °C). Based on this results it can be assumed the degradation starts with the bonds ether aliphatic-aromatic (resulted by condensation of PEG with the ionic monomer), and due to the shorter PEG lengths of $I_{400}p-SO_3-cr$, the volatile fragments were formed at lower temperature, as compared with the two other ionomers possessed the longer PEG chain. The weight loss percentage in the first step calculated from ATG and theoretical mass fraction of PEG are presented in Table 4. The relative weight loss matches well to the weight fraction of PEG in ionomer.

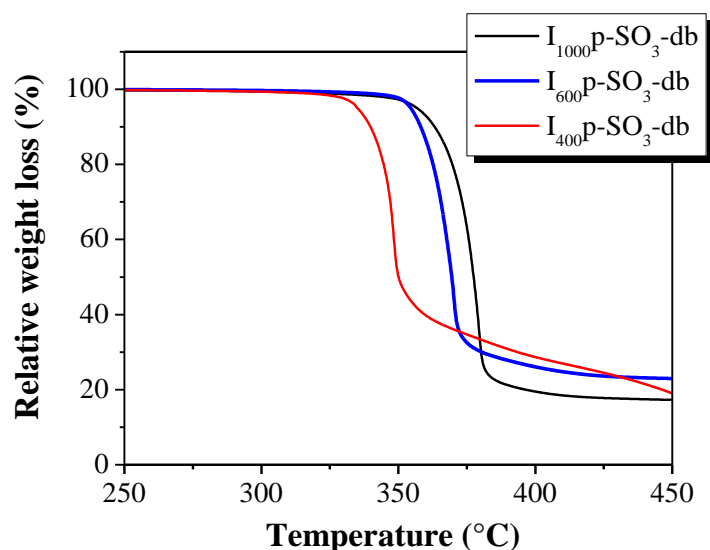


Fig. 14 Thermogravimetric curves of ionomers I_xp-SO_3-db (with $x = 1000; 600; 400$) from 250 to 450°C.

Table 4 Analysis of thermal degradation temperature for the synthesized ionomers.

Sample	$T_d \pm 2$ (°C)	Wt.% of PEG	
		Experimental	Theory
Ip-TFSI	318	79	66
Ip-SO ₃	332	74	71
$I_{1000}p-SO_3-cr$	356	75	71
$I_{600}p-SO_3-cr$	354	67	60
$I_{400}p-SO_3-cr$	334	55	50

ii. Differential scanning calorimetry (DSC)

Phase transitions of the synthesized ionomers were observed by Differential Scanning Calorimetry (DSC) following two identical heating/cooling cycles, under N_2 flux, and only the second heating scans are presented. A scan rate of $10\text{ }^\circ\text{C}/\text{min}$ was applied for both heating and cooling scans. The samples placed in the aluminum crucible in a glove box to avoid the presence of water. The DSC thermograms of synthesized ionomers are presented in Fig. 15.

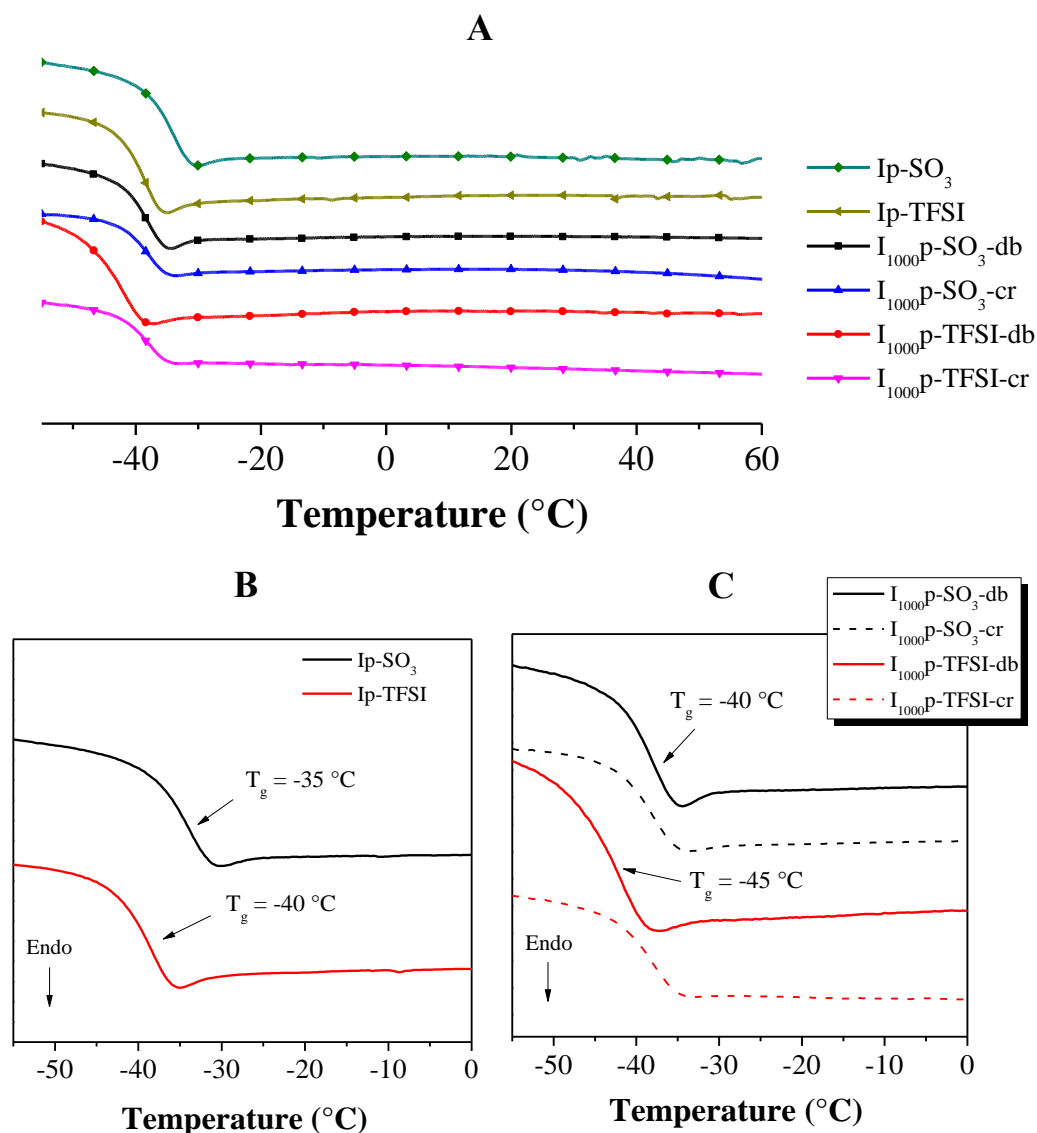


Fig. 15 DSC thermograms of (A) synthesized ionomers from -60 to $60\text{ }^\circ\text{C}$; and the zoom of glass transition behavior for (B) the linear $I_p\text{-SO}_3$, $I_{1000}p\text{-TFSI}$ ionomers, and (C) the linear $I_{1000}p\text{-SO}_3\text{-db}$, $I_{1000}p\text{-TFSI-db}$ (straight lines), the cross-linked $I_{1000}p\text{-SO}_3\text{-cr}$, $I_{1000}p\text{-TFSI-cr}$ (dash lines), from -60 to $0\text{ }^\circ\text{C}$, scan rate of $10\text{ }^\circ\text{C}/\text{min}$, under N_2 flux.

In the large range of studied temperatures, from -100 to $150\text{ }^\circ\text{C}$, these ionomers show only one phase transition related to their glass transition temperature, which indicates their completely amorphous state (even for linear or cross-linked ionomers) without any melting point and recrystallization on

both heating and cooling scans. P. Eiamlamai¹¹ reported previously that the linear or cross-linked PEO blended with lithium salt (having similar structures as the aromatic perfluorosulfonate moiety), exhibited a melting temperature associated with the crystalline phase. In the case of ionomer, the tethering of salt to the polymer chain prevents completely the crystallization. Similar behavior was also reported by G. Luo et al.¹², and M. Watanabe et al.¹³ for their single-ion materials.

The SO₃-based ionomer show about 5 °C higher in T_g as compared to the TFSI one e.g. -35 ± 2 °C and -40 ± 2 °C, respectively (Fig. 15B), which is related to the larger delocalization of negative charge, and the bulkiness of TFSI anion inducing a plasticized effect on the ionomer.^{14,15} Our measurements with the blends contained PEO (MW 300 kg/mol) and LiTf or LiTFSI, at the same EO/Li of 23, show the T_g values of -30 ± 2 °C and -40 ± 2 °C, respectively. In brief, grafting of ionic functions along the polymer chain exhibits a weak effect on the T_g value.

The thermograms of linear ionomers with double-bonds, and the corresponded cross-linked matrix for I₁₀₀₀p-SO₃ and I₁₀₀₀p-TFSI are presented in Fig. 17C. After cross-linking, the T_g value is slightly increased to -37 ± 2 °C for I₁₀₀₀p-SO₃-cr, and -40 ± 2 °C for I₁₀₀₀p-TFSI-cr, which are about 3 °C and 5 °C higher than the non-crosslinked ionomers e.g. I₁₀₀₀p-SO₃-db and I₁₀₀₀p-TFSI-db, respectively. Cross-linking is an effective method that helps to enhance the mechanical properties of polymer, but simultaneously decreases the chain mobility, and resulting in an increase of T_g.¹⁶ Because the cross-linked density of these films is quite low (as disused in 1.2.2), their T_g values may not exhibit a remarkable change. Noted also that not only the cross-linking effect, but also the presence of NCC may contribute to the slightly increase of T_g, since all of the studied films were reinforced with 6 wt.% of NCC.

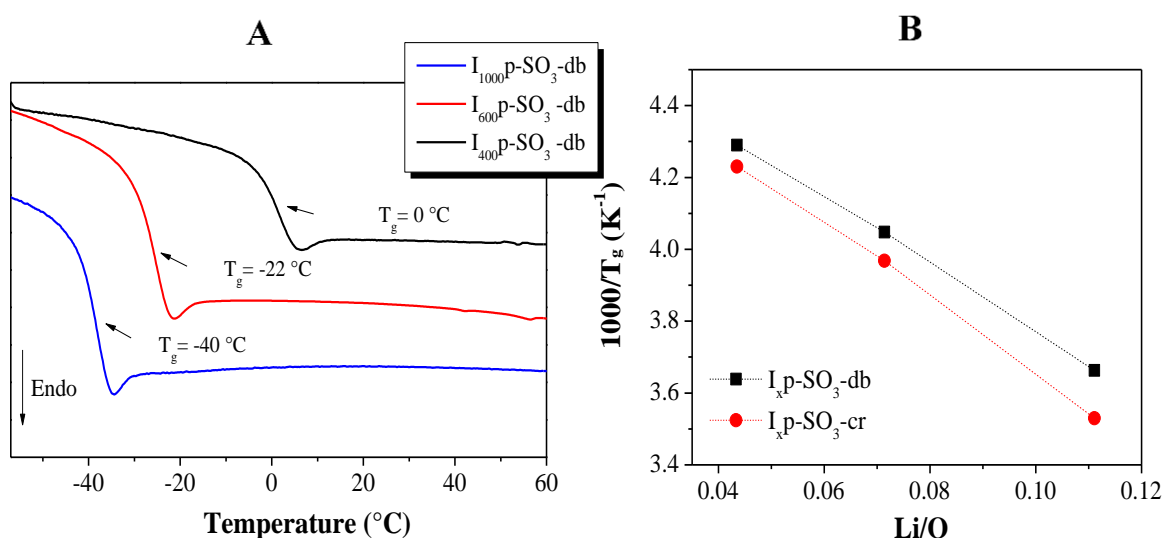


Fig. 16 (A) The DSC thermograms of I_xp-SO₃-db from -60 to 60 °C, and (B) evolution of 1000/T_g with Li/O for the cross-linked I_xp-SO₃-cr (red), and non-crosslinked I_xp-SO₃-db (black).

The effect of Li concentration, represented by EO/Li, was studied for the series I_x p-SO₃-db ionomers, and their DSC thermograms are presented in Fig. 16A. The decrease of EO/Li (from 23 to 9) induces a huge increase of T_g with about 40 °C different. In detail, the T_g value increases from -40 ± 2 °C for EO/Li = 23, to -22 ± 2 °C for EO/Li = 14, and 0 ± 2 °C for EO/Li = 9. Moreover, the cross-linking effect also induces an increase in T_g, as discussed above. The increase of 1/T_g with decreasing Li/O is linear for both cross-linked and non-cross-linked ionomers, which is a typical behavior for the amorphous polymer.¹⁷ Generally, the increase of T_g with increasing Li concentration relates to more interactions between Li⁺ and PEO structural units.¹⁸ However, for the blend polymer/salt, particularly the POE/LiTf system, T_g values are negligible influenced by the addition of salt, including the studied zone of EO/Li from 9 to 23.¹⁹

Amorphous blend of cross-linked PEO and aromatic perfluorosulfonated salt PhSCF₂CF₂SO₃Li (the salt has similar structure with the grafted anionic functions of ionomer) reported by E. Paillard et al.²⁰ showed an increase in T_g with only 10 °C when increased the EO/Li from 10 to 28, that means the presence of an aromatic impact more the T_g than an aliphatic one. The huge difference in T_g for ionomers with Li concentration may explain due to (i) the absence of salt aggregates, and (ii) the rigidity of aromatic ring that affects the PEO chain mobility when it is incorporated to the backbone. For example, in the I₄₀₀p-SO₃-cr structure, when each Li⁺ is grafted in a well-controlled distance of EO/Li = 9, and about 5 EO units have interactions with Li⁺,²¹ for at least two EO (close to aromatic ring), the Li⁺ mobility is affected by the rigidity of aromatic ring.

1.2.4. Conductive and transport properties

i. Conductivity and transference number of gelled ionomers

The lithiated ionomers' conductivity are measured by impedance spectroscopy from RT to 90 °C, following a heating/cooling process, with a step of 10 °C, and an isotherm of 1 h between each step of temperature. The ionomers I₁₀₀₀p-SO₃ and I₁₀₀₀p-TFSI are very viscous liquid (or gel polymer), which were not possible to cast into membrane. Their conductivities were carried out using the conductivity Radiometer micro-cell for liquid electrolyte. The cells were prepared in the glove box to avoid the water contamination. The values of conductivities performed on both heating and cooling cycles are identical as shown in Fig.19A (an example of I₁₀₀₀p-TFSI), meaning highly reproductive measures without any degradation, and hydration/dehydration of sample taking place during the measurements. In Fig. 19B, conductivities of I₁₀₀₀p-TFSI and I₁₀₀₀p-SO₃ are represented as a function of 1000/T.

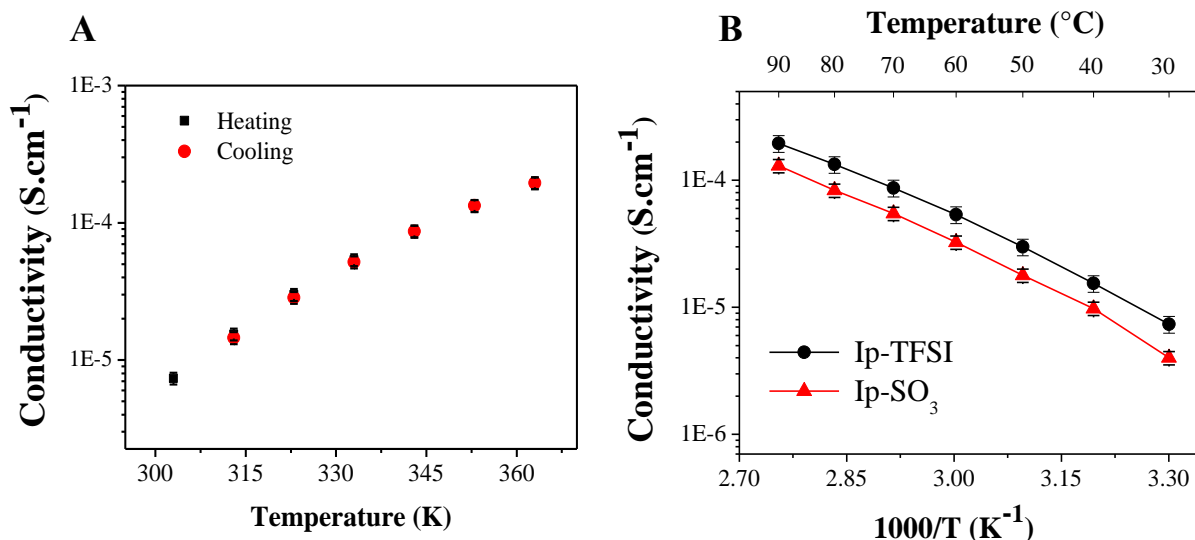


Fig. 17 Plots of conductivity (A) with temperature from the heating and cooling scans of I_{1000p} -TFSI, and (B) with inverse temperature ($1000/T$) for the synthesized ionomers. Three measurements are performed, the error bar is lower than 10%.

Conductivity data increase with increasing the temperature, and the highest values at 90°C are above $10^{-4} \text{ S}\cdot\text{cm}^{-1}$ for both linear ionomers, which are promising for electrolyte applications. However, conductivity of I_{1000p} -TFSI is almost two times higher than that of I_{1000p} -SO₃ that correlates to the mobility of polymer chain (the T_g value of TFSI-based ionomer is about 5°C lower than the SO₃ one). As concerned the ionic concentration, these two ionomers possess the same EO/Li of 23, but the Li dissociation in polymer matrix also depends on the anion delocalization which is better for TFSI, hence resulting in higher conductivity.

Another factor that may influence the conductivity is Li transference number (t_{Li^+}). Possessing the grafted anions and the high molecular weights, which are much higher than the entanglement threshold of PEO (3 kg/mol), these two ionomers are expected to have the t_{Li^+} values close to unity. The transport properties of these gel polymer were investigated by PFG-NMR technique for ^{19}F and ^7Li nuclei. The self-diffusion coefficients of these two linear ionomers were obtained at high temperature of 80°C (the temperature favorable for ionic transport in polymer, found in most of the studies of polymer electrolytes). The ionomers were filled in a tube of 4 mm of diameter in a glove box, and sealed under an Argon atmosphere. The performed conditions for measuring the diffusion of charged carriers are described in the annex. Noted that the ionic functions were chemically bonded along the polymer chain, hence the hydrogenated backbone (PEG and aromatic ring) should diffuse in same rate with the anions. The D value of backbone, related to the diffusion of ^1H nuclei, is lower than 10% different comparing to the anion diffusion coefficient, hence affirming the roughly same diffusivity of backbone and side chains. The t_{Li^+} is obtained from the relation:

$$t_{\text{Li}}^+ = \frac{D_{\text{Li}}}{D_{\text{F}} + D_{\text{Li}}} \quad (2)$$

where D_{Li} and D_{F} are the self-diffusion coefficients of Li^+ and anion, at 80 °C, determined by PFG-NMR technique. The D values and t_{Li}^+ for two ionomers are presented in Table 5.

Table 5 Self-diffusion coefficients of fluorine, lithium, and the Li transference number of ionomers obtained from the equation (1) at 80 °C.

Ionomer	First component		Second component		$D_{\text{Li}} * 10^{-12}$ ($\text{m}^2 \cdot \text{s}^{-1}$)	t_{Li}^+
	$D_{\text{F}} * 10^{-12}$ ($\text{m}^2 \cdot \text{s}^{-1}$)	%	$D_{\text{F}} * 10^{-13}$ ($\text{m}^2 \cdot \text{s}^{-1}$)	%		
I ₁₀₀₀ P-TFSI	4.4	43	8.7	57	8.8	0.65
I ₁₀₀₀ P-SO ₃	1.3	48	1.9	52	4.1	0.74

Although the high molecular weight of ionomers, the diffusion of anion was still measurable. From the ^{19}F diffusion spectra, two diffusion coefficients corresponding to two different components were observed for both ionomers. The first component (with about 43 - 48 %) diffused more than 5 times faster than the second one, that relates to the polydispersity of polymer (DPI of 1.3 for both ionomers), and the shorter chains diffused much faster than the longer chains. The transport number was obtained using an average value for anion diffusion coefficients by multiplying the D_{F} value of each component with its corresponding percentages. The t_{Li}^+ values for the two linear ionomers are rather lower than unity e.g. $t_{\text{Li}}^+ = 0.65$ for I₁₀₀₀P-TFSI and 0.74 for the SO₃-ionomer, which are unexpected for the SIPEs.

To better understand the difference in conductivity of two ionomers, in Fig. 18, the Li^+ conductivity was plotted as a function of $T = T_{\text{g}} + X$, where X is the constant ranging between 70 and 130 (associated with the scanning temperature range), to minimize the polymer segmental mobility effect. The Li^+ conductivities are obtained by multiplying ionic conductivity value with the corresponded t_{Li}^+ . Surprising that the Li^+ conductivity curves for two ionomers are nearly superposed, as plotted with the $T_{\text{g}} + X$ scale. The dissociation degree of these ionomers (at the same EO/Li of 23) is not dependent on the anion nature e.g. SO₃⁻ or TFSI, and seems to be similar despite the well-known higher anion delocalization of TFSI. The blends PEO/salt, consisted of high molecular weight PEO and LiTFSI or LiTf as dissolved salts at EO/Li=23, were also prepared for comparing. Their ionic conductivities performed in the roughly same conditions were multiplied to the cationic transport number of 0.14 for PEO/LiTFSI²², and 0.35 for PEO/LiTf (which were previously determined by our team), then represented as a function of $T_{\text{g}} + X$ in Fig 20 B. Contrarily to the ionomers, the blend PEO/LiTFSI exhibits higher Li conductivity with at least 30% than the PEO/LiTf in the large range of temperatures. So the behavior observed for ionomers may relate to (i) the anions are chemically

bonded to the backbone that prevents the precipitation/ aggregations of salt, which is an issue of the blend polymer/salt, (ii) the regular spacing of anions along the polymer chain (a PEG chain of 1000 g/mol for these linear ionomers).

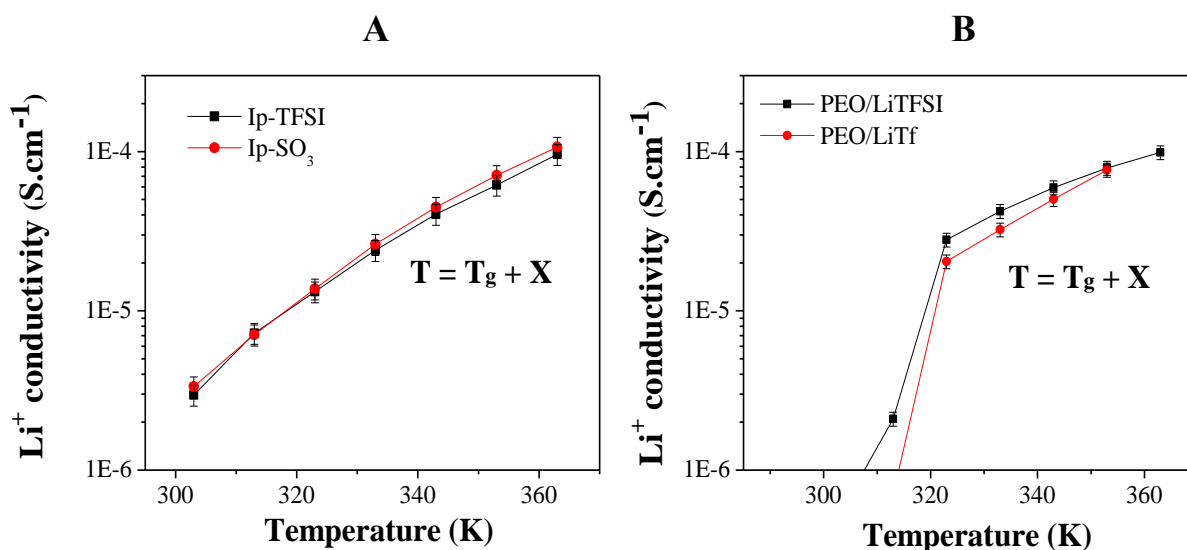


Fig. 18 The Li⁺ conductivities of (A) $I_{1000p}\text{-SO}_3$ (red) and $I_{1000p}\text{-TFSI}$ (black); (B) the blend PEO/LiTf (red) and PEO/LiTFSI (black) as a function of $T = T_g + X$, at the same EO/Li of 23, where X is constant.

ii. Conductivity and transference number of cross-linked ionomers

The conductivity of the cross-linked films was measured in a Swagelok cell, where the solid membrane sandwiched between two disks of stainless-steel (SS) electrodes. The linear ionomers with double-bonds are like the ‘chewing gum’, and their conductivities were impossible to measure with good accuracy. Therefore, conductivity of the cross-linked films reinforced with 6 wt.% NCC are discussed in this work.

The reinforced cross-linked ionomer shows a lower conductivity, in the whole range of temperatures from RT to 90 °C, comparing to the non-reinforced one, as seen in Fig. 21A, e.g. a value of 1×10^{-5} S.cm⁻¹ for the cross-linked ionomer decreases to 8.1×10^{-6} S.cm⁻¹ for the reinforced polymer at 60 °C, with about 20 % lower. Noted that the non-reinforced NCC film is very sticky with poor mechanical strength, even in the inert environment of a glove box, so that the irreproducibility of conductivity measurements was predicted. However, the obtained result still agrees to the state of the art reported by Samir et al.²³ Even if the reinforcing effect of NCC obviously decreases the conductivity of material, a quantity of 6 wt.% of NCC was added to improve the manipulation of membranes in the glove box, and to ensure the reproducible results. The Fig. 21B illustrates the reproducibility of both synthesis and crosslinking protocols for ionomers by plotting the conductivity of $I_{1000p}\text{-SO}_3\text{-cr} + 6$ wt.% NCC membranes, from two different batches, versus $1000/T$. These curves lie in the pretty same scale, indicating the high reproducibility of membrane preparation and conductivity measurements.

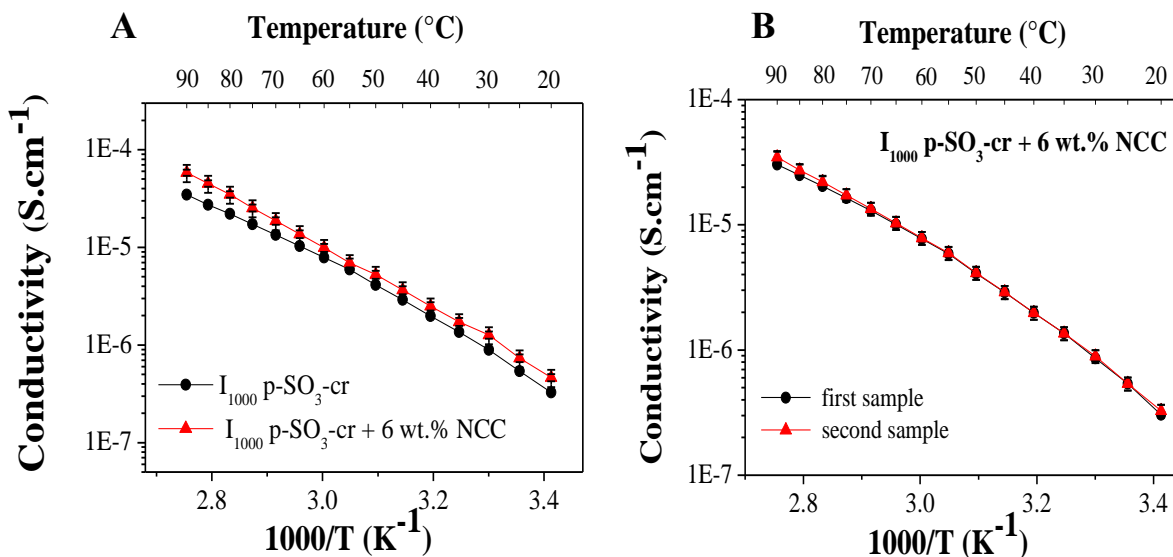


Fig. 19 (A) Conductivity of cross-linked I_{1000} p-SO₃-cr with 6 wt.% NCC (red line) and without NCC (black line); (B) two different cross-linked I_{1000} p-SO₃-cr films prepared by the same protocol.

The conductivity of I_{1000} p-SO₃-cr + 6 wt.% NCC and I_{1000} p-TFSI-cr + 6 wt.% NCC are compared in Fig. 20A. At 60°C, the conductivities of both electrolytes are superior to 10⁻⁵ S.cm⁻¹, which are comparable, or even higher than those reported in the literature²⁴ (the best reported value for SIPEs was 1.3 x 10⁻⁵ S.cm⁻¹ at 60°C). Conductivities of I_{1000} p-TFSI-cr are slightly higher in the whole temperature range. Noted that the error bars for I_{1000} p-TFSI-cr (from 6 measures of conductivity includes 3 from the same batch, and 3 from different batches of ionomer) are much higher as compare to the I_{1000} p-SO₃-cr. This disparity in conductivity is explained by the fact that the TFSI membranes are stickier, hence harder to determine their thickness, and to control the geometric interface electrolyte/ electrode in the glove box. Representing the conductivity data as a function of $T_g + X$ (to minimize the impact of chain mobility) induces similar behavior to the linear ionomers i.e. a superposition of the two curves, that proves the delocalization of anion has a negligible impact on the salt dissociation, see Fig. 20B.

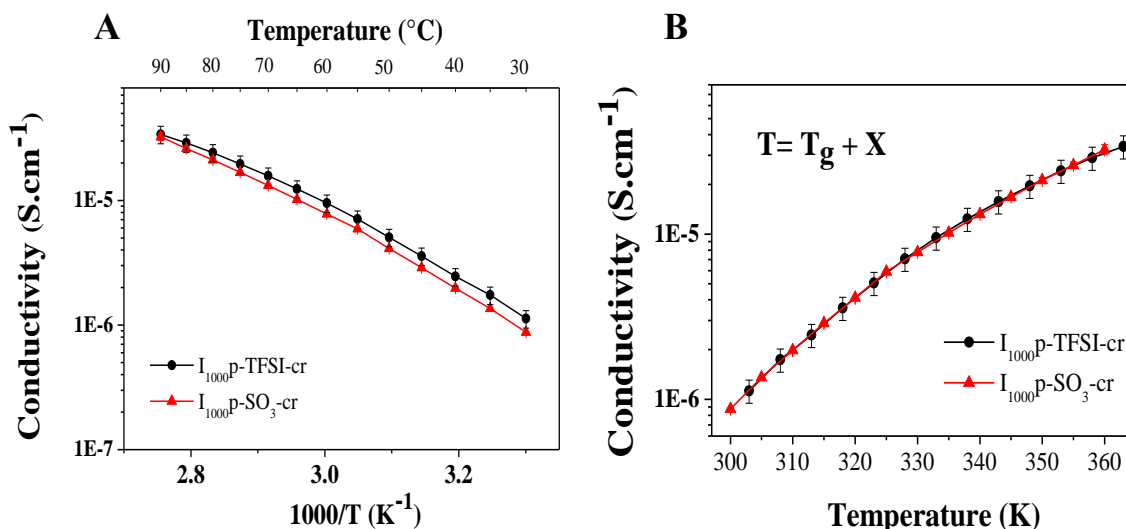


Fig. 20 Conductivity of the cross-linked ionomers $I_{1000}p\text{-SO}_3\text{-cr}$, and $I_{1000}p\text{-TFSI-cr}$ as a function of (A) inverse temperature $1000/T$; and (B) at $T = T_g + X$, where X is constant.

In Fig. 21, conductivities of the $I_xp\text{-SO}_3\text{-cr}$ with $1000/T$ are compared to evaluate the impact of lithium content on conductivity behavior. Decreasing EO/Li from 23 to 9 decreases drastically the conductivity. This strong reduction in conductivity is correlated to the increase of T_g values, with more than $50\text{ }^{\circ}\text{C}$ with EO/Li (see 1.2.3), hence to the strong decrease in segmental motions of PEG chain. The highest conductivity at $90\text{ }^{\circ}\text{C}$ is $3.5 \times 10^{-5}\text{ S}\cdot\text{cm}^{-1}$ for $I_{1000}p\text{-SO}_3\text{-cr}$, $1.9 \times 10^{-5}\text{ S}\cdot\text{cm}^{-1}$ for $I_{600}p\text{-SO}_3\text{-cr}$, and $4.5 \times 10^{-6}\text{ S}\cdot\text{cm}^{-1}$ for $I_{400}p\text{-SO}_3\text{-cr}$.

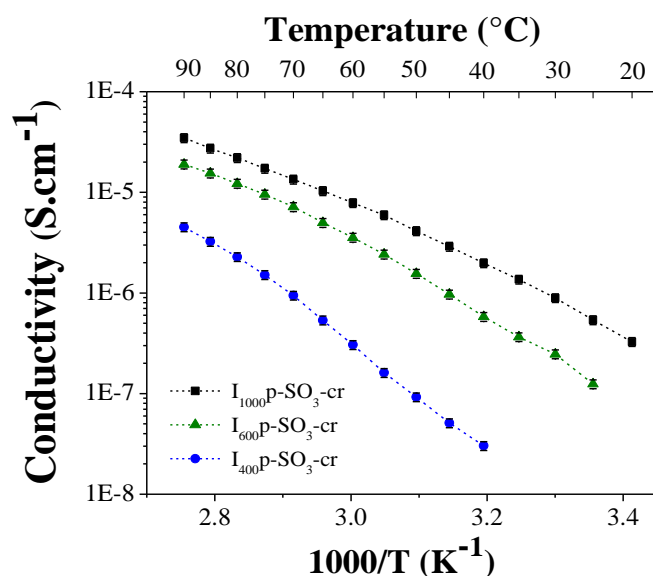


Fig. 21 Conductivity as a function of inverse temperature of the $I_xp\text{-SO}_3\text{-cr}$ (with $x = 1000, 600, 400$).

To minimize the influence of chain mobility related to Li concentration and cross-linking density, conductivities of the $I_xp\text{-SO}_3\text{-cr}$ at $T = T_g + 90$ as a function of Li/O (black curve in Fig. 24) are presented. The Li conductivity data of the blends PEO/LiTf performed in the roughly same

conditions were added for comparison (red curve). Cationic conductivity of the blends PEO/LiTf, contained similar Li concentration with the ionomers, was calculated by multiplying the ionic conductivity to the t_{Li^+} value of 0.35. It is important to notice that at $T = T_g + 90$, the blends are amorphous (temperature above the melting of the polymer, determined by DSC measurements).

The conductivity behavior of two types of polymer electrolytes are different, as seen in Fig. 24. Conductivity of the blends reaches a maximum at $\text{Li}/\text{O} = 0.073$ (corresponding to the $\text{I}_{600} \text{p-SO}_3\text{-cr}$), then decreases. While for the ionomers (black curve), conductivity increases with increasing the Li content. This increase in conductivity is approximately equal to 2.5 time that is roughly close to the increase of Li content in ionomers, from $\text{I}_{1000} \text{p-SO}_3\text{-cr}$ to $\text{I}_{400} \text{p-SO}_3\text{-cr}$. The behaviors observed for the blend PEO/salt agree with the literature that conductivity reached a maximum before decrease due to the formation of aggregates at high salt concentration.²⁵ In brief, conductivity of ionomers is proportionally increased when increasing the Li content, from Li/O of 0.04 to 0.11, proving the advantages of single-ion materials.

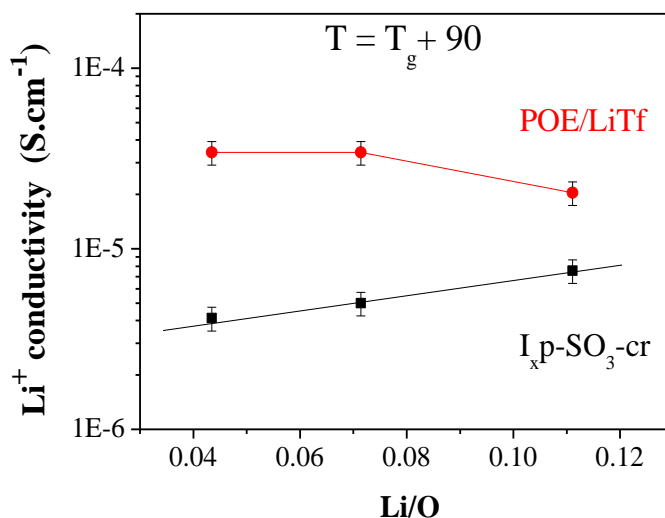


Fig. 22 Li^+ conductivities of cross-linked ionomers (black) and blends of PEO/LiTf (red) at $T_g + 90$ with Li/O .

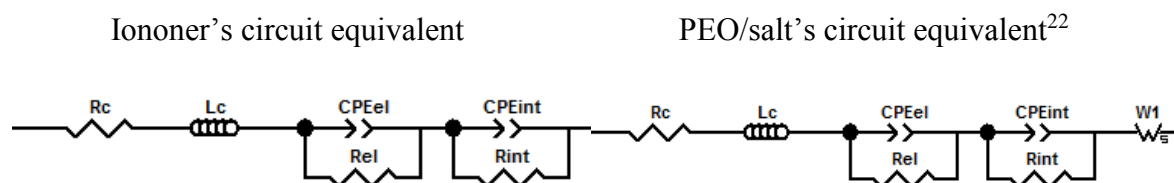
In conclusion, these linear ionomers exhibit high conductivity, close to $10^{-4} \text{S}\cdot\text{cm}^{-1}$ at 90°C , for both SO_3 and TFSI anions. The cross-linking effect and Li concentration give an obvious reduction of conductivity that agrees with the higher T_g . At 60°C , the highest Li content ionomer ($\text{I}_{400} \text{p-SO}_3\text{-cr}$) has a conductivity lower than $10^{-7} \text{S}\cdot\text{cm}^{-1}$, which is not suitable for electrolyte applications. Therefore, the electrochemical behaviors were conducted only for the membranes possessed the highest conductivity i.e. $\text{I}_{1000} \text{p-SO}_3\text{-cr}$ and $\text{I}_{1000} \text{p-TFSI-cr}$.

❖ Transference number

The lithium electroplating tends to lead to dendritic deposits, which originate from various physical phenomenon, involving or not the formation of solid electrolyte interphase (SEI). Fast dendrite

growth occurs when the current reach a limit, which corresponds to full anion depletion at the lithium/electrolyte interface, which is a direct result of the anionic mobility.²⁶ Indeed, a concentration gradient occurs due to the consumption of lithium at one electrode, creating a depletion and the migration of anions in the opposite direction. Fixing these anions would theoretically solve this issue, by virtue of charge neutrality, and prevent the establishment of concentration gradients.

Therefore, the design of polymer electrolyte with a unity transference number is required. Different methods have been used in the literature to determine the Li transference number, and electrochemical impedance is the simplest one. The symmetric lithium metal coin cell was prepared by sandwiching the solid electrolyte film between two electrodes of Li-metal in a glove box. The cell was heated at 80 °C in a controlled temperature oven, and performed using a Biologic VMP3 potentiostat. The Nyquist plots of the Li || electrolyte || Li cell from 1 MHz to 1 mHz for the cross-linked ionomers and the blends PEO/salt are presented in Fig. 25. These impedance spectra were fitted to the corresponded equivalent circuits, as seen below.



where R_c , R_{el} , R_{int} are the resistances of the cable, of the solid electrolyte and of the Li-electrolyte interface, respectively. The L_c represents the inductor of the cable, CPE are the constant phase elements, and W_s is the Warburg element.

For systems which exhibit a t^+ lower than 1, the typical Warburg loop can be observed at low frequencies, corresponding to the diffusion response of Li^+ , as seen in the Nyquist plots of the blends PEO/LiTf and PEO/LiTFSI (Fig. 23 B,D). The impedance plots of cross-linked ionomers exhibit two definite demi-cycles relating to the resistance of electrolyte (R_{el}) and of Li/electrolyte interface (R_{int}), without any sign of Li diffusion at low frequencies (up to 1 mHz).

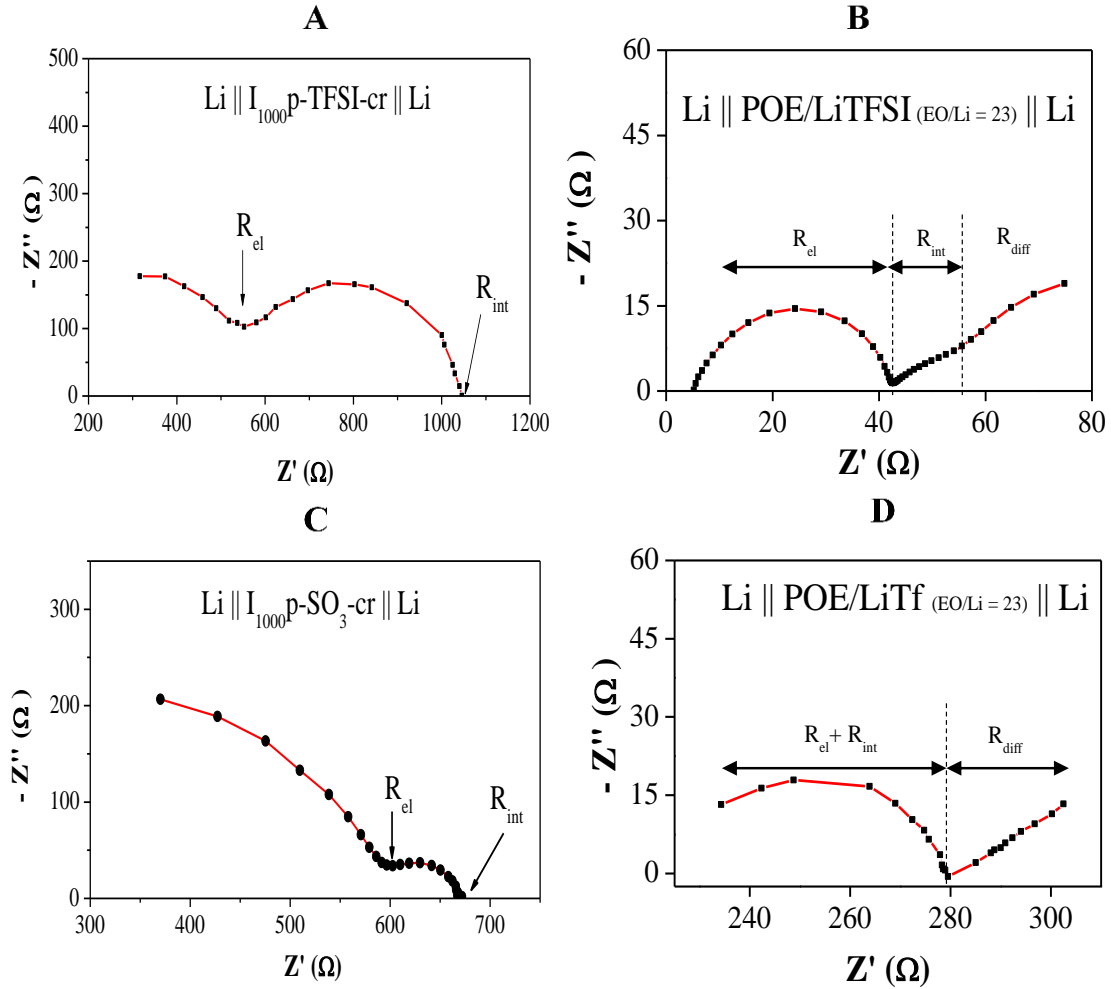


Fig. 23 Nyquist plots of the symmetric Li || electrolyte || Li cells at 80 °C for (A) I₁₀₀₀p-TFSI-cr, (B) PEO/LiTFSI, (C) I₁₀₀₀p-SO₃-cr, and (D) PEO/LiTf at the same EO/Li of 23.

According to Mac Donald²⁷, the transference number of a binary system is calculated following:

$$t_{Li}^+ = \frac{R_{el}}{R_{el} + R_{diff}} \quad (3)$$

where t_{Li}^+ is the Li transference number, R_{el} and R_{diff} are the electrolyte resistance and the lithium diffusion resistance, respectively. Following the relation (3), t_{Li}^+ value for both ionomers are equal to 1 due to the absence of R_{diff} , thus affirming the successful syntheses of single-ion materials. Moreover, the R_{int} value of I₁₀₀₀p-SO₃-cr (about 50 Ω) is a degree of magnitude lower than the TFSI ionomer (about 495 Ω), indicating better Li/electrolyte interface. This phenomenon may relate to the impurities content in TFSI-based ionomer that are unstable with the lithium metal.

The t^+ value of cross-linked I₁₀₀₀p-SO₃-cr was also determined by two other techniques including the steady-state current, and PFG-NMR to further compare the behaviors observed above. Noted that the two electrochemical methods i.e. low frequency EIS and steady-state current are somehow similar, but they propose the different ways to get the t_{Li}^+ . For the steady-state current method, a constant

potential of 40 mV was applied across the symmetric Li-metal cell, and the current was recorded with time. The impedance spectroscopies were measured every 15 minutes until a constant current was reached to further determine the interface resistances before and after polarization. The transference number of Li^+ was calculated following the Bruce and Vincent equation²⁸:

$$t_{\text{Li}}^+ = \frac{\frac{\Delta V}{I_0} - R_{\text{int}}}{\frac{\Delta V}{I_\infty} - R_{\text{int}}} = \frac{I_\infty - (\Delta V - I_0 R_{0 \text{ int}})}{I_0 - (\Delta V - I_\infty R_{\infty \text{ int}})} \quad (4)$$

where ΔV is the applying potential of 40 mV, I_0, I_∞ are the intensities current, and $R_{0 \text{ int}}, R_{\infty \text{ int}}$ are the interface resistances taken before and after the measurements. The t_{Li}^+ calculated from the relation (4) for $\text{I}_{1000\text{p-SO}_3\text{-cr}}$ is 0.95, indicating a transference number very close to unity. This result is comparable to the behavior observed by the low frequency EIS method.

Furthermore, the self-diffusion coefficients of ^{19}F and ^7Li nuclei for $\text{I}_{1000\text{p-SO}_3\text{-cr}}$, measured by PFG-NMR technique, are presented in Table 6. The t_{Li}^+ obtained from the equation (2), where $D_{\text{Li}}, D_{\text{F}}$ are self-diffusion coefficients of Li^+ and anion, respectively, is 0.97 for the cross-linked $\text{I}_{1000\text{p-SO}_3\text{-cr}}$.

Table 6 Diffusion coefficients of ^7Li and ^{19}F nuclei, and the t_{Li}^+ of $\text{I}_{1000\text{p-SO}_3}$ at 80 °C measured by PFG-NMR.

Electrolyte	$D_{\text{F}} * 10^{-12} \text{ (m}^2 \cdot \text{s}^{-1}\text{)}$	$D_{\text{Li}} * 10^{-12} \text{ (m}^2 \cdot \text{s}^{-1}\text{)}$	t_{Li}^+
$\text{I}_{1000 \text{ p-SO}_3\text{-cr}}$	0.048	2.0	0.97

It should be noticed that in most of the studies for the blend polymer/salt, cationic transference number obtained by electrochemical characterization, and by PFG-NMR spectroscopy were usually incomparable. As reported by Chauvin et al.²⁹, this is probably due to:

<u>PFG-NMR method</u>	<u>Electrochemical method</u>
<ul style="list-style-type: none"> - Counts all of the species including ion pairs, isolated, solvated ions. - The species mobility are associated with the auto-diffusion mechanism. 	<ul style="list-style-type: none"> - Measures only the charged carriers. - The mobility of ions is ensured by not only the diffusion but also the migration phenomena.

Nevertheless, the cross-linked ionomer $\text{I}_{1000\text{p-SO}_3\text{-cr}}$ exhibits the rather similar behaviors of nearly unity transference number determined by three different techniques. These t_{Li}^+ values are very close to one e.g. 0.95 for the steady-state current method, and 0.97 for the PFG-NMR method, affirming the successful synthesis of single-ion polymer electrolytes.

1.2.5. Electrochemical stability

Electrochemical stability window of the cross-linked $\text{I}_{1000\text{p-SO}_3\text{-cr}}$ and $\text{I}_{1000\text{p-TFSI-cr}}$ films were carried out by cyclic voltammetry (CV) technique, using a Biologic VMP3 (multichannel

potentiostat), at 80 °C. The coin cells were prepared by sandwiching the membrane between a lithium metal and a stainless-steel (SS) electrodes in a glove box. The electrochemical stability performed from -0.1 V to 4.1 V vs Li^+/Li , with a scan rate of $0.1 \text{ mV}\cdot\text{s}^{-1}$ and the cyclic voltammograms of these materials are presented in Fig. 26.

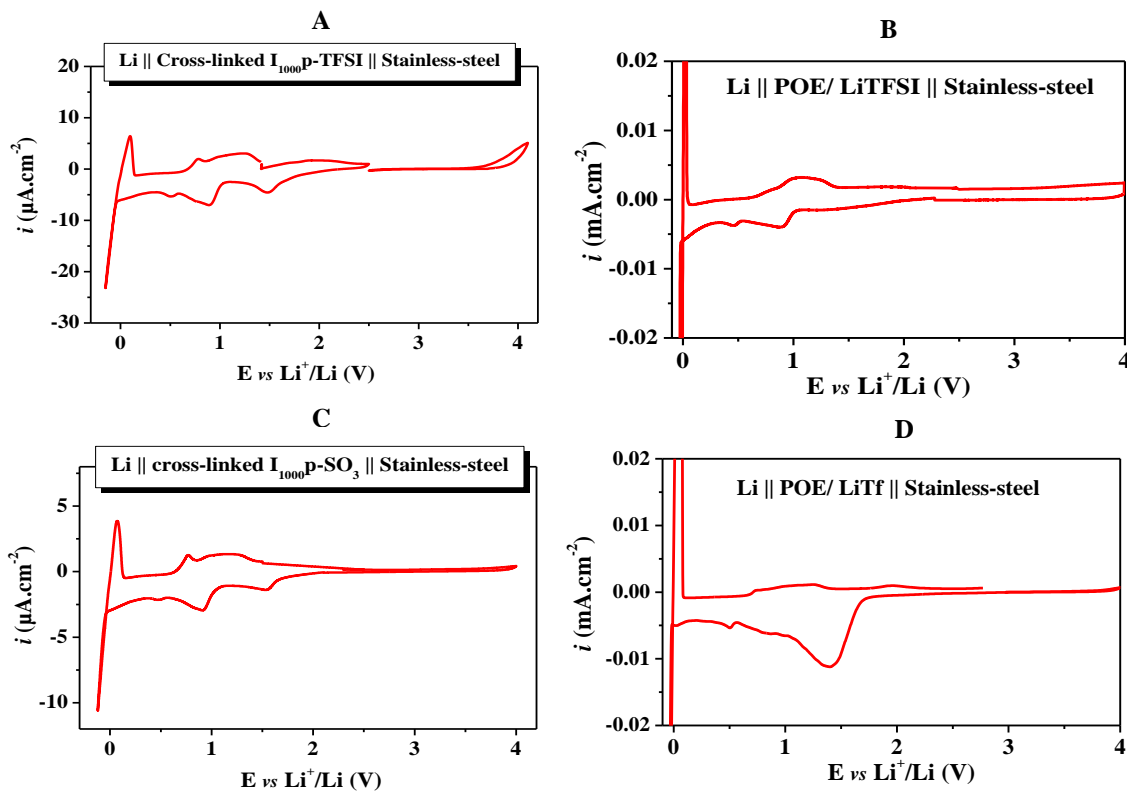


Fig. 24 The CV curves of (A) $I_{1000} \text{ p-TFSI-cr}$, (B) PEO/LiTFSI , (C) $I_{1000} \text{ p-SO}_3\text{-cr}$, and (D) PEO/LiTf at the same EO/Li of 23, from -0.1 to 4.1 V versus Li^+/Li in the $\text{Li}|\text{electrolyte}|\text{SS}$ cells with $0.1 \text{ mV}\cdot\text{s}^{-1}$ scanning rate, at 80 °C.

The CV curves from -0.1 to 4.1 V vs Li^+/Li of the two cross-linked membranes are compared with those obtained for the blends PEO/LiTf and PEO/LiTFSI , at the same EO/Li of 23, in Fig. 26. The lithium plating/stripping ability is observed through the appearance of a redox peak started at 0 V vs Li^+/Li . The peaks appear from 0.7 to 1.5 V vs Li^+/Li on both anodic and cathodic scans are also observed for two cross-linked films, and even for the blends PEO/salt , at same operation's conditions. These peaks, as reported previously in the literature,³⁰ may relate to the impurities or the specific characteristics of PEO -based electrolytes in contact with the SS electrode. In all of the voltammograms, the electrolyte exhibits a good stability in oxidation up to 4 V vs Li^+/Li , except for $I_{1000} \text{ p-TFSI-cr}$ (limit at 3.7 V vs Li^+/Li , affirming the impurities content in ionomer). Although the very promising properties obtained for both cross-linked ionomers, the next parts focuses only on the applications of $I_{1000}\text{p-SO}_3\text{-cr}$ as solid electrolyte due to the simplest synthesis, high purity, with lower price comparing to the TFSI-based ionomer.

1.2.6. Lithium plating/stripping test

The main issue of lithium metal batteries concerns the formation of Li dendrites during either fast charge (tip growth), or over cycling (bottom/tip growth). A good electrolyte can strongly contribute and overcome these issues. The cycling test used a symmetric Li-metal coin cell, where the electrolyte was sandwiched between two Li-metal electrodes in a glove box. To conduct this study, the polarization times and the applied current densities are modified from the cycling route reported by L. Frenck³¹ (see Fig. 25).

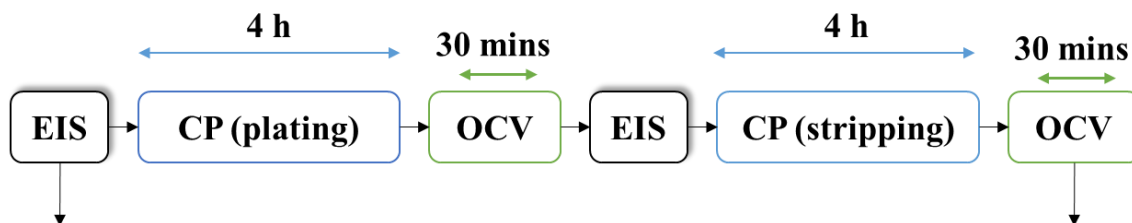


Fig. 25 The cycling routine for dendritic growth test in a $\text{Li} // \text{I}_{1000}\text{p-SO}_3 // \text{Li}$ cell at 80°C .

Before applying a certain constant current, the cell was heated at 80°C until equilibrium, and followed by impedance measurements in every 2h, for 24h. When the identical Nyquist plots obtained (the equilibrium of the cell was immediately reached after the first 2h), the cycling routine at different currents was applied. The test started with 10 pre-conditioning cycles at low current of $0.01\text{ mA}\cdot\text{cm}^{-2}$ for 4h in both charge and discharge, following by 30 min of rest (OCV) between each cycles, and an impedance measurement (EIS). The applied current density were increased from 0.01 up to $0.2\text{ mA}\cdot\text{cm}^{-2}$. At the highest current of $0.2\text{ mA}\cdot\text{cm}^{-2}$, the thickness of the lithium transferred in each side was about $3.8\ \mu\text{m}$ in 4 h. After a long cycling at various applied currents, the cell was continuously cycled at $0.01\text{ mA}\cdot\text{cm}^{-2}$ to investigate the reversibility of the system.

Following the proposed protocol, materials with a t_{Li^+} much lower than 1 may exhibit the polarization at both charge/discharge, resulting in the non-linear voltage steps. Meanwhile, for the single-ion material, the reversibility of lithium plating/stripping between two electrodes was predicted, without polarization evolution. The voltage steps typically for the electrolytes with a unity t_{Li^+} are the straight-stair steps, as seen in Fig. 26.

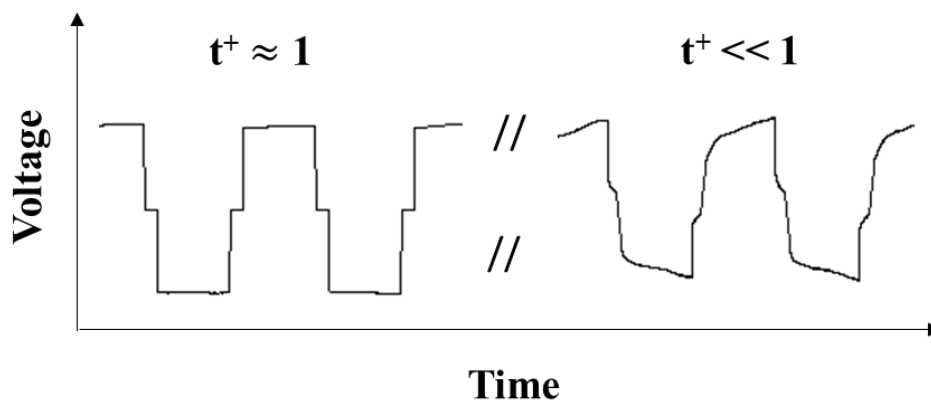


Fig. 26 Schema of the straight-stair steps for $t^+ \approx 1$ (left) and the polarization steps for $t^+ \ll 1$ (right).

To further verify this behavior, Fig. 27 illustrates the evolution of the voltage under 0.1 mA.cm^{-2} for the blend PEO/LiTf (EO/Li = 23), in a symmetric Li-metal cell, at 80°C , using the cycling routine proposed in Fig. 25. Before short circuit, the potentials obtained at charge/discharge, and even during 30 min of rest did not reach any constant value. At higher applied current of 0.1 mA.cm^{-2} , the appearance of dendritic growth was observed through a suddenly drop of voltage, indicating the short circuit.

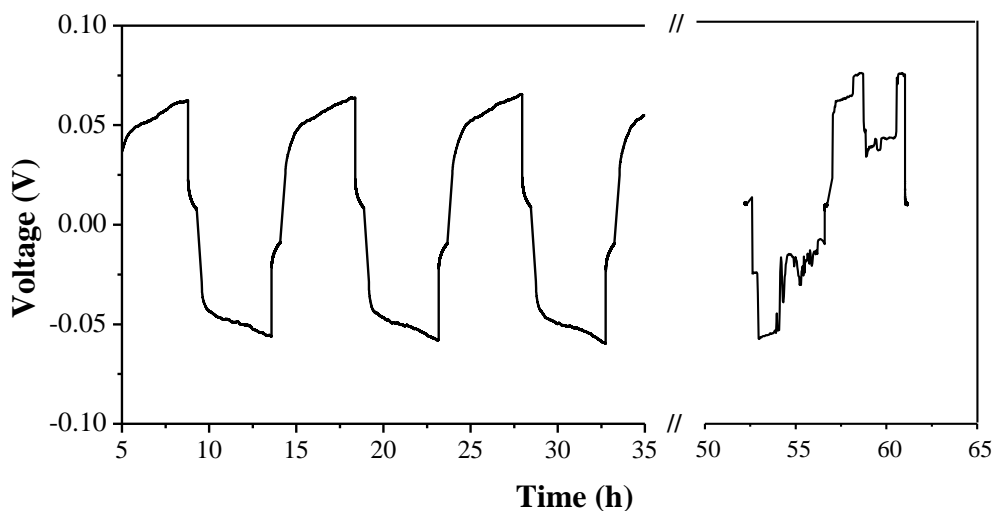


Fig. 27 Schema of Li plating/stripping inside a Li || PEO/LiTf || Li cell at 80°C under 0.1 mA.cm^{-2} .

The evolution of lithium plating/stripping in a Li || I₁₀₀₀p-SO₃-cr || Li cell, at 80°C , is presented in Fig. 28, where the over-potentials at various applied currents were plotted with time. From the first inspection of this figure, the cell exhibits an excellent stability over 78 days, corresponding to 250 cycles of charge/discharge, without the short circuit and any sign of Li dendritic growth. This result is especially impressive, meaning a big successful of design and synthesis SIPE.

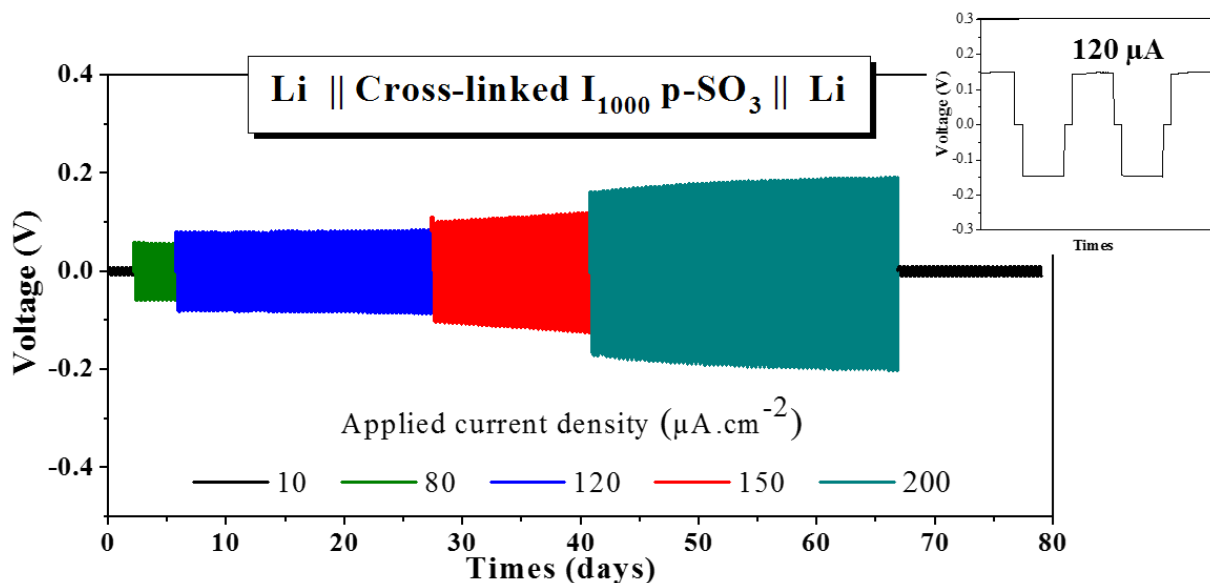


Fig. 28 Typical Li plating/stripping in a symmetric Li || $I_{1000}p-SO_3-cr$ || Li cell at 80 °C at different applied currents from 0.01 to 0.2 mA.cm⁻² as a function of time; insert figure presents the straight-stair steps at both charge/discharge directions and even during relaxing at 0.12 mA.cm⁻².

The potential reached at both charge/discharge sides are likely identical in absolute value, and increase with increasing the applied current across the cell. The typically straight-stair steps for single-ion electrolyte are also observed during plating/stripping as showed in the insert figure, affirming a nearly unity transference number of $I_{1000}p-SO_3-cr$. While at rather low current of 0.01 mA.cm⁻², represented in black color, the voltage is negligible i.e. ± 13.8 mV, the value obtained with an applied current of 0.2 mA.cm⁻² is equal to 0.18 V (the cyan curves).

Evolution of the over-potential values with current density is presented in Fig. 29. The voltages increase with the increase of current densities indicating the stable resistance interface Li-metal/electrolyte following the relation $U = IR$.³² By extracting the impedance spectra at a constant applied current of 0.12 mA.cm⁻², the interface Li/polymer is extremely stable (about 50 Ω), and reaches immediately constant at a define current density. The Nyquist plots in Fig. 30 represent the response of electrolyte (the incomplete demi-cycle at high frequencies), and of the Li/electrolyte (demi-cycle at low frequencies) interface, before and after polarization at 0.12 mA.cm⁻². The resistance values remain stable even at high applied current, which is an exclusive advantage beyond a unity transference number of $I_{1000}p-SO_3-cr$ in term of non-polarized material. Similar experiments were performed for the single-ion materials of L. Porcarelli et al.³³, but even at low current density, their systems need more than 10 days to reach a stable Li/electrolyte interface.

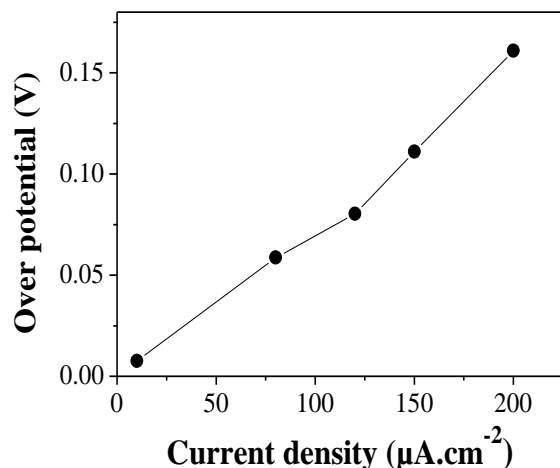


Fig. 29 The over-potentials as a function of current density for a symmetric Li || $I_{1000}\text{p-SO}_3\text{-cr}$ || Li cell at 80 °C.

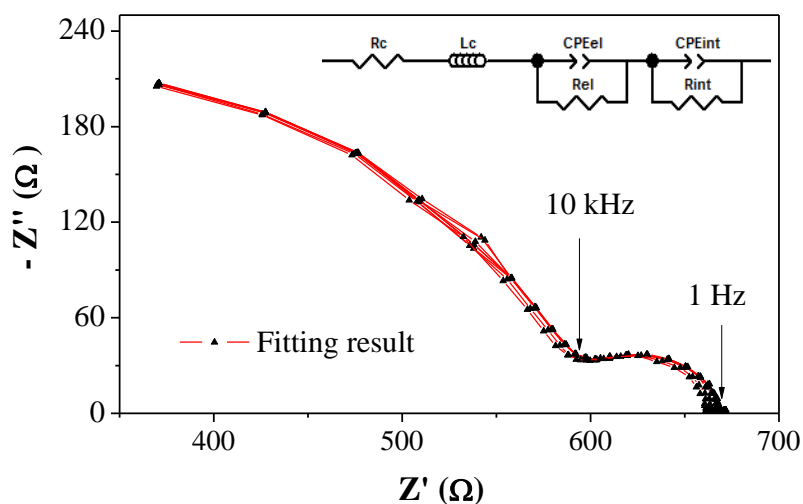


Fig. 30 Nyquist plots of a symmetric Li || $I_{1000}\text{p-SO}_3\text{-cr}$ || Li cell at 80 °C under 0.12 $\text{mA}\cdot\text{cm}^{-2}$ as applied current.

Let's back to Fig. 29, the over-potential values reached at different applied currents, for example 0.18 V at 0.2 $\text{mA}\cdot\text{cm}^{-2}$, are significantly lower than the reported results of L. Frenek³¹ (0.23V at 0.17 $\text{mA}\cdot\text{cm}^{-2}$), or L. Porcarelli et al.³³ (0.25V at 0.2 $\text{mA}\cdot\text{cm}^{-2}$) for the single-ion electrolytes. Moreover, after an extremely long polarization of about 150 charge/discharge at different currents density, the cell was continually performed at low current of 0.01 $\text{mA}\cdot\text{cm}^{-2}$ (the black curve at the end of the cycling test in Fig. 28). The over-potentials reach nearly the same values as that of the pre-conditioning stage, which definitely affirms an excellent reversibility versus lithium metal of the ionomer.

In brief, the polymer electrolyte has an excellent stability versus lithium metal, with a long cyclability in a symmetric Li-metal cell, without any sign of dendrite formation up to 80 days. These impressive results for a SIPE based on PEO are rarely found in the literature. The next part of this work presents the performances of $I_{1000}\text{p-SO}_3\text{-cr}$ as solid electrolyte for the lithium metal battery with the LFP

cathode.

1.2.7. Cycling tests

i. LFP cathode preparation

The cycling tests of electrolyte material require the LFP cathode. The ionic mobility in the cathode is ensured by the homogenous fill of liquid electrolyte into the electrode's porosity. In contrast, for an all-solid-state battery, the solid electrolyte is not able to maintain a suitable conductivity inside the cathode, even by hot pressing the components. The enable Li circulation inside the 'home made' LFP cathodes is provided by the addition of ionomer (contained the ionic functions) as Li⁺ conductor and also as binder, for cathode preparation.

The ionomers before cross-linking are like the gel polymers and need to be cross-linked. However, the cathode consists of activated carbon that can absorb the UV light, and prevents the cross-linking reaction of side chain double-bonds, hence resulting in poor mechanical properties. To solve this issue, the blend of high molecular weight PEO (MW = 300 kg/mol) with I₄₀₀p-SO₃-db, in a weight ratio of 1:1, corresponding also to an EO/Li of 23, was added to the cathode. This blend has similar EO/Li with the cross-linked I₁₀₀₀-p-SO₃-cr electrolyte, and was also characterized in term of conductive and ionic transport properties. The conductivity and cationic transference number of the blend determined by impedance spectroscopy in the symmetric stainless steel and Li-metal coin cells, respectively. The conductivity as function of 1000/T for the blend polymers (red line), and the cross-linked I₁₀₀₀-p-SO₃-cr (black line) are showed in Fig. 31.

Conductivity of the blend PEO/I₄₀₀-p-SO₃-db is slightly higher than that of I₁₀₀₀-p-SO₃-cr. However, a drop of conductivity at about 45 °C relating to the melting of the semi-crystalline PEO phase is observed for only the blend polymers. The Li transference number of 0.95, determined by steady-state current method in a symmetric Li-metal cell at 80 °C, was obtained for PEO/I₄₀₀-p-SO₃-db indicating the single-ion behavior. These results promote a promising electrolyte for lithium metal batteries operating at high temperature.

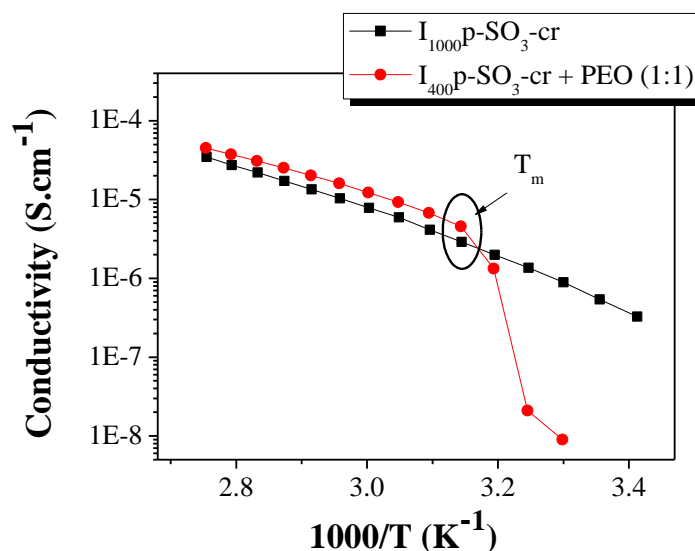


Fig. 31 Conductivity of the blend PEO/ $I_{400}p-SO_3-cr$ (1:1) and the cross-linked $I_{1000}p-SO_3-cr$, at EO/Li of 23, as a function of $1000/T$.

To evaluate the impact of polymer content in the cathode, the two compositions of cathode i.e. 75:15:10 (A-LFP) and 60:30:10 (B-LFP) in weight ratio of $LiFePO_4$ (LFP): PEO/ $I_{400}p-SO_3-cr$: carbon black, respectively, were prepared. The PEO (MW = 300 kg/mol) and $I_{400}p-SO_3-cr$, (1:1 in weight ratio), were dissolved in water at 60 °C, using magnetic stirring, for 48 h, until homogenous. The volume of water is diminished as possible to maintain an enable ink's viscosity. About 1.0 mL of water was used for the A-LFP, and 1.8 mL for the B-LFP composition.

The mixture of material powders consisted of LFP material and activated carbon black were prepared by gently grinding in a hand mortar with cyclohexane. After about 30 min of mixing, solvent was gently evaporated at RT, then the fin powders were added into a vial contained the blend of polymers. The ink was magnetic stirred for 2 h, and homogenized using an Ultra-Turrax® mixer for 1 h. Water was frequently added during the mixing to maintain an enable ink's viscosity. Finally, the ink was casted onto an aluminum current collector using a doctor-blade, with the thickness of 100 μm . The process is illustrated in Fig. 32.

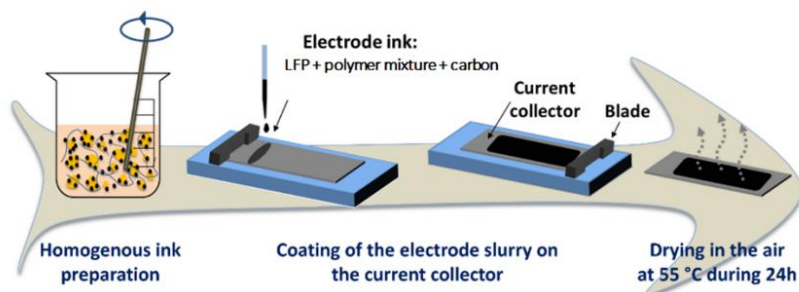


Fig. 32 LFP cathode preparation process.

The resulted cathodes were gently dried at RT overnight, and moved to an oven at 55 °C for slowly drying over 48 h. The SEM images of the bulks A-LFP and B-LFP cathodes, with thickness after

drying of 33 and 23 μm , respectively, are presented in Fig. 35. Both of the electrodes exhibit a homogeneous distribution of materials, however for the B-LFP electrode, the particules seem to be better covered by the polymer. The cathode porosity was calculated from the difference between the electrode density (the ratio of loading mass/loading volume of a bulk electrode), and the theoretical density including the densities of all the components. Noted that density of the blend polymers used for cathode casting is 1.25 g/cm^3 . These hand-casting electrodes exhibit low estimated porosity of 26 % for A-LFP, and 22 % for B-LFP cathode, which are the excellent results. Back to the state of the arts, the lowest estimated porosity of LFP cathode using SIPE as binder was about 45%.³⁴ The low porosity of 26 % and 22 % for the hand-casting cathodes are meaningful in term of gravimetric energy density, allowing to increase the interface electrode/electrolyte in the all-solid-state batteries, and providing the low charge-transfer resistance.³⁵

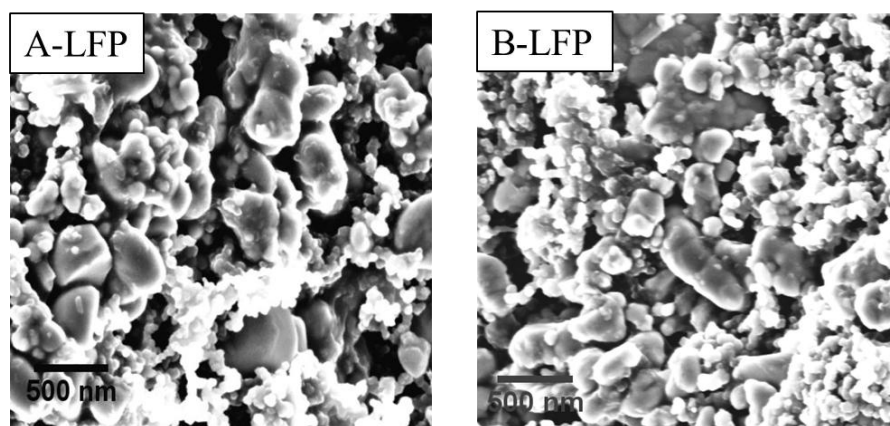


Fig. 33 SEM images of the bulk LFP cathodes, including A-LFP (75:15:10) (left) and B-LFP (60:30:10) (right) in weight ratio of (LFP, PEO: I_{400p} -SO₃-db (1:1) and carbon black), respectively.

i. Cycling tests in a lithium metal battery

To further be used in lithium metal polymer battery, the cathodes were dried under vacuum at 80 °C for 24 h, and stored in a glove box. The batteries combined a LFP as positive electrode, a cross-linked electrolyte film I_{1000p} -SO₃-cr, and a negative Li-metal anode were prepared in the glove box. The coin cell's assembly is illustrated in Fig. 34. All the cycling tests were conducted at 80 °C with various Galvanostatic rates of C/n, meaning the capacity C per n hours, from C/20 up to 2C, and a potential range between 2.5 to 3.8 vs Li⁺/Li.

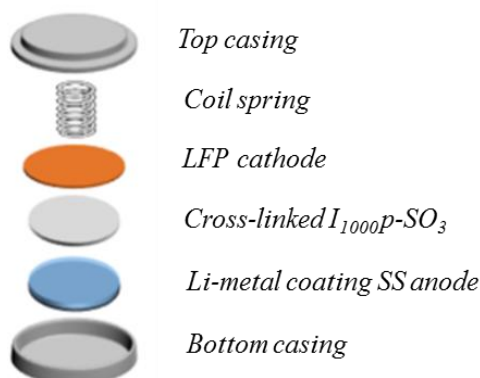
COIN CELL ASSEMBLY

Fig. 34 Coin cell assembly for the cycling test using a cross-linked $I_{1000P-SO_3-cr}$ as solid electrolyte, sandwiching between a LFP cathode and a Li-metal anode.

A-LFP cathode

The cycling tests using A-LFP cathode were performed at different scan rates from C/20 up to 1C at 80 °C. The assembled A-LFP || $I_{1000P-SO_3-cr}$ || Li shows an excellent charge/discharge reversibility up to C/5. The flat-shaped charge/discharge curves are observed at different power rates from low to high, as seen in Fig. 35. The discharge capacity calculated (theoretically 170 mAh.g⁻¹ for the LFP material) are presented in the right side of Fig. 35. The cell delivers 140 mAh.g⁻¹ in the first discharge at C/20, and the capacity decreases with the increasing of the C-rate whereas the polarization increase proportionally to the scan rate. At C/2.5, a ‘well-defined’ plateau is observed during the discharge corresponding to 68 % of the capacity obtained at low C-rate. However, at high rate, 1C, a sudden drop of the discharge capacity is observed, with a capacity of 60 mAh.g⁻¹, this huge decrease can be associated with the high polarization of the cell probably associated with an non-optimal ionic pathway due to the low amount of solid polymer electrolyte into the electrode and the presence of residual porosity. At the different scan rates from C/20 to C/2.5, the Coulombic efficiency is higher than 96 % that prove the very good cyclability of the cell (as seen in Fig. 35).

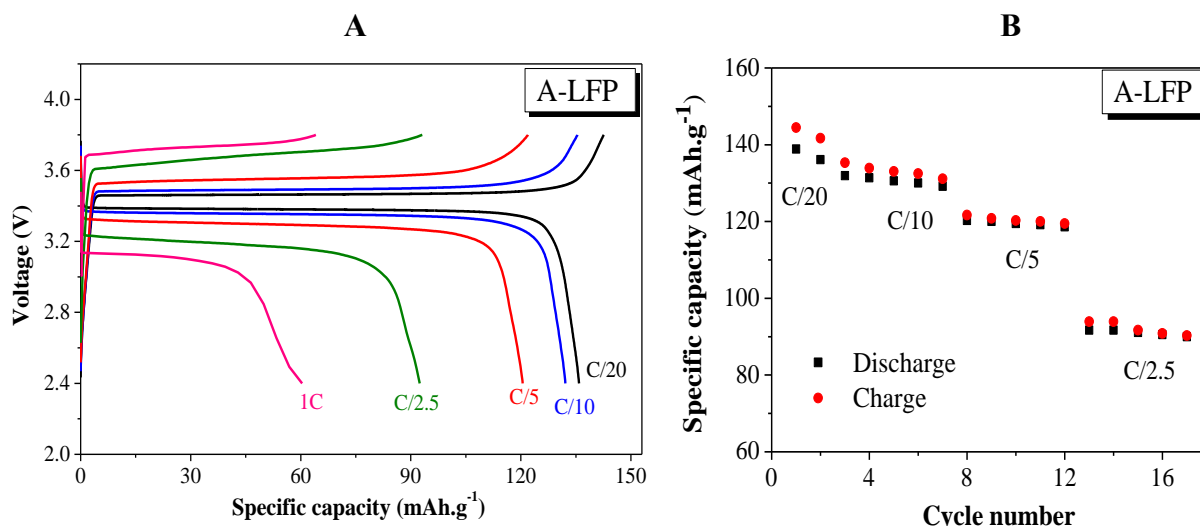


Fig. 35 Charge/discharge curves at different scan rates from C/20 to C/2.5 for A-LFP || I₁₀₀₀p-SO₃-cr || Li cell at 80 °C (left), and capacity as a function of cycles (right).

To understand the effect of polymer content in the cathode on the final performances of battery, the assembly of B-LFP || I₁₀₀₀p-SO₃-cr || Li were cycled. The B-LFP cathode has higher polymer content of 30 wt.%, with more efficient percolated ionic pathway, so a better ionic conductivity in the electrode was expected.

B-LFP cathode

The cycling tests performed with the same charge/discharge rates from C/20 up to 2C for the B-LFP || I₁₀₀₀p-SO₃-cr || Li cell, at 80 °C. The cycling test conducted at C/20 for the first 5 cycles, then for 10 cycles at every C-rate up to 2C. At the end of the schedule, two cycles at C/20 were performed to verify the cell's stability. The charge/discharge capacity obtained at different C-rates, and the Coulombic efficiency are presented in Fig. 36.

As seen, the cell is stable during the long cyclability test, without dendritic growth, and an excellent coulombic efficiency (above 98 %) is reached during more than 60 cycles at the various C-rates. Noted that, the cell delivers for the first discharge a capacity of 143 mAh.g⁻¹ at C/20, which is similar to the assembled A-LFP || I₁₀₀₀p-SO₃-cr || Li. The capacity decreases while increasing the C-rates that can be related to the polarization of the cell, but the decrease of capacity is much lower as compared to that obtained with A-LFP cathode. Moreover, the cell shows an excellent reversibility up to an extremely high 2C scan rate.

The capacities obtained from C/20 to 2C are very stable, during the 10 cycles at each rate with any significant decrease. However, at higher constant C-rates of C and 2C, both charge and discharge capacities decrease slightly with the cycle number. This reduction can be probably due to the low

ionic conductivity of ionomers, and the presence of residual porosity that can induce ionic transport limitation at high C-rates. At the rate of 2C, the cell delivers more than 75 % of capacity obtained at C/20 that is a very good result for all-solid-state-lithium batteries. These results are comparable and even better than several studies in this field including the one of H. Oh and al.³⁶ (discharged capacity reached 120 mAh.g⁻¹ at C, at 80 °C), or those reported by L. Porcarelli et al.³³ with a capacity loss of about 80 % at C/5 in a Li/SIPE/LFP battery at 70 °C.

The two final cycles at low C-rate exhibit an excellent capacity with a value of 139 mAh.g⁻¹ that are close to the one obtained at the first discharge (143 mAh.g⁻¹) at the same scan rate of C/20. This excellent behavior proves the advantage of using single-ion based polymer electrolyte, where the Li⁺ ions are the only mobile species in this system that avoids the polarization phenomena at the interface due to concentration gradient.

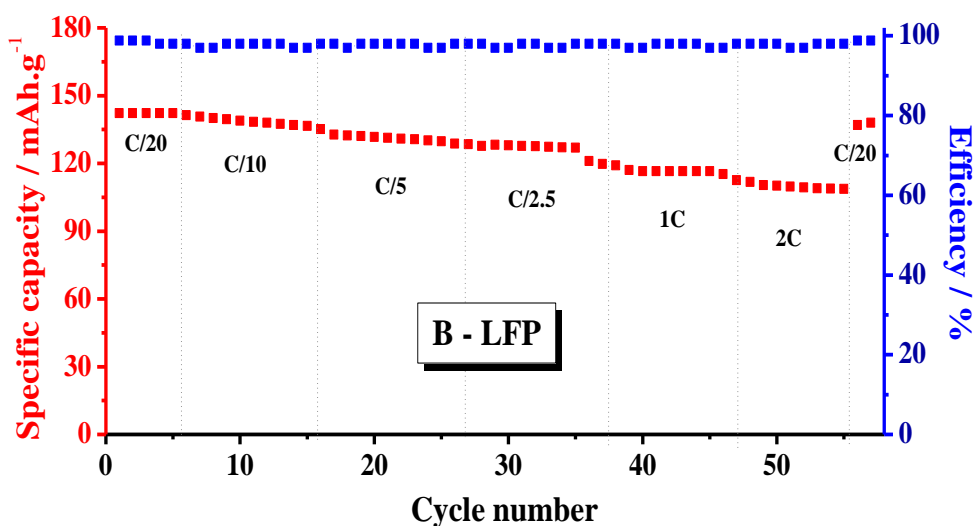


Fig. 36 Cyclability of B-LFP // I_{1000P}-SO₃-cr // Li cell at 80 °C with different scan rates from C/20 to 2C, including the discharge capacity and the corresponded Coulombic efficiencies.

The porosity of both cathodes are very close e.g. 26 % and 22 % for A-LFP and B-LFP, respectively. In the first approximation, this difference has a negligible effect on the performances of batteries at low C-rate. The capacity evolution versus C-rates for two systems using A-LFP and B-LFP cathodes is presented in Fig. 37. At C/20 the two systems exhibit almost similar capacity of about 140 mAh.g⁻¹, but at high C-rates, the A-LFP cell is more polarized, and the discharge capacities decrease faster with increasing the C-rates. The cell based on A-LFP electrode delivers lower discharge capacity as compared to the B-LFP cell e.g. 5 % lower at C/10, 10 % at C/5, up to 28 % at C/2.5. The better performance of B-LFP cell is explain by the formation a more connected, and more efficient ionic pathway due to the increase of the polymer content in cathode.

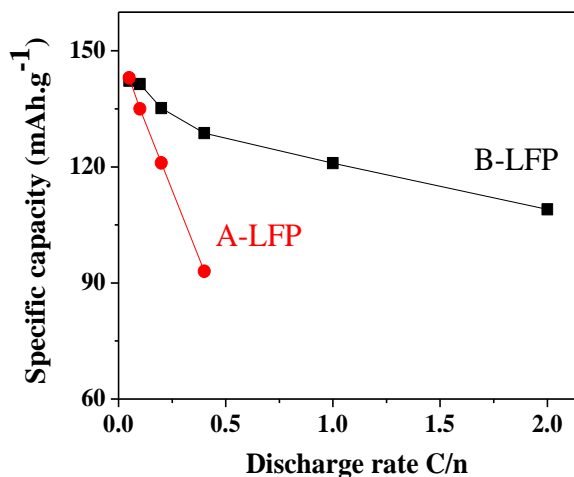


Fig. 37 Discharge capacities obtained for A-LFP (red line) and B-LFP (black line) as a function of C-rates in the LFP || I₁₀₀₀p-SO₃-cr || Li battery at 80 °C.

ii. Cyclability of battery improvement

To improve the discharge capacity at high C-rates, the charge of the cell was reached at low C-rate (C/20 or C/10) whatever the discharge C-rates. This cycling test with low charging rate and fast discharging rate was previously reported by Bouchet et al.³⁴, used the unipolar block copolymer as electrolyte. In this conditions, named as regime 2, a new battery was cycled from C/20 to C rate using the following: the first cycles are charged and discharged at the same rate e.g. C/20 and C/10, meanwhile for higher discharge C-rates, the cell was always charged at C/10 before discharge to ensure a fully charging process.

Fig. 38 shows the discharge curves of two identical assembled B-LFP || I₁₀₀₀p-SO₃-cr || Li cell, at 80 °C, using the regime 1 (charge/discharge at the same C-rates), and the regime 2 (charge at low C-rate, discharge at higher C-rates) with different power rates from C/20 up to C. The discharge capacities at low scan rates e.g. C/20, C/10, up to C/5 for the two cells are nearly the same e.g. 142 mAh.g⁻¹ at C/20, 139 mAh.g⁻¹ at C/10, and 132 mAh.g⁻¹ at C/5. At a relative high 1C rate, the cell performed with regime 1 delivers about 116 mAh.g⁻¹, and 119 mAh.g⁻¹ for the regime 2, but the difference is negligible to consider as an improvement.

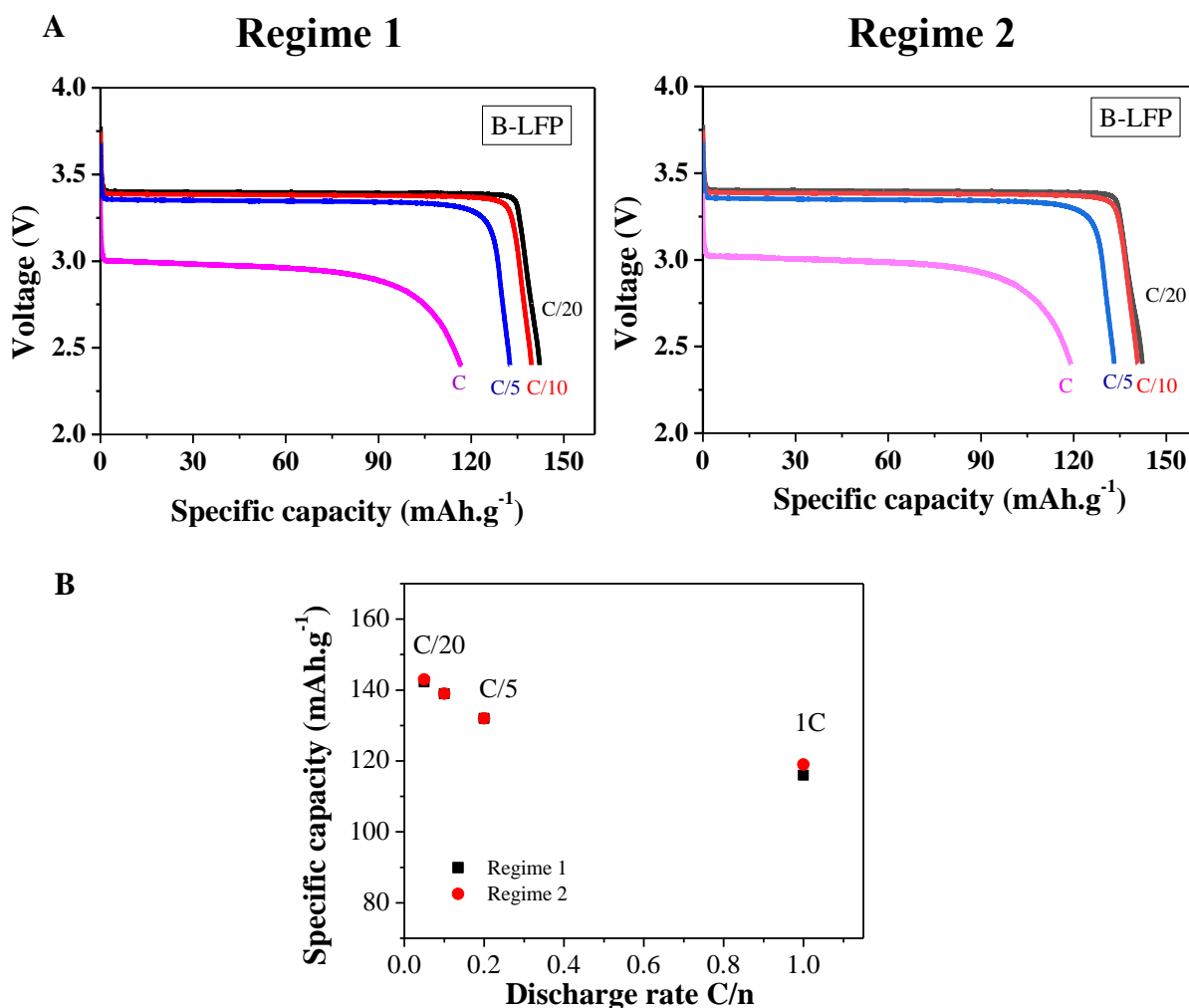


Fig. 38 A. Discharge curves obtained at different power rates from C/20 to 1C for regime 1: charge/discharge at the same rate (left), and regime 2: charge at low C-rate (C/20, C/10) and discharge at different C-rates for the B-LFP || I₁₀₀₀p-SO₃-cr || Li cells at 80 °C; and B. the specific capacities obtained for two regimes as a function of discharge rate.

In brief, the rate of charging has negligible impact on cell performances, and the transport limiting process occurs more accurately during the discharge. The cell cycled using the regime 2 was then submitted to a durability test with a charge-discharge at C/5. From the Fig. 39, the capacity of the battery is extremely stable during 57 cycles with the excellent Coulombic efficiencies of nearly 100 %. A higher capacity could be obtained with the porosity-free electrode,³⁵ therefore the hot pressing of the electrode B-LFP is suggested to improve the capacity at high C-rates.

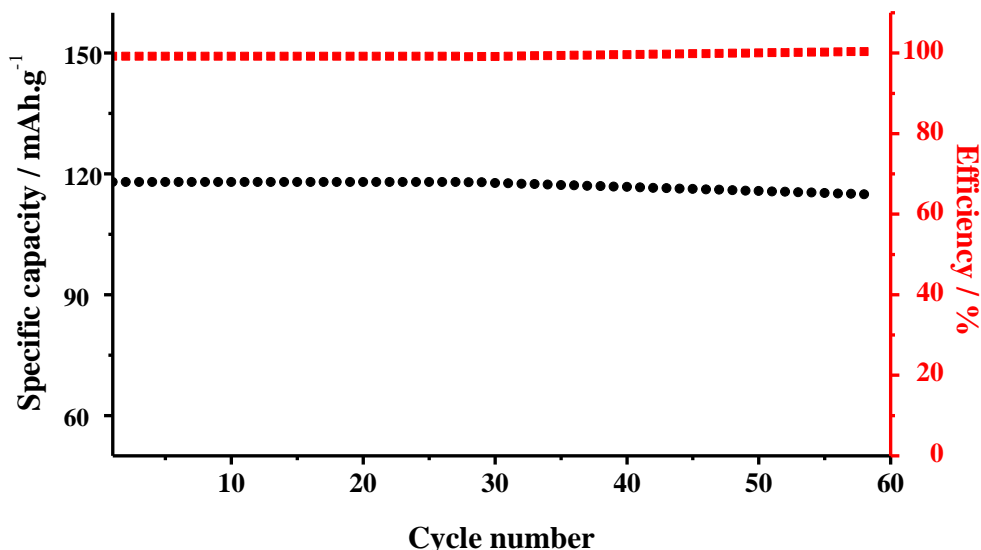


Fig. 39 Cyclability of B-LFP // I_{1000p}-SO₃-cr // Li cell at 80 °C at C/5 rate, including the discharge capacity and the corresponded coulombic efficiencies.

1.3. Conclusions

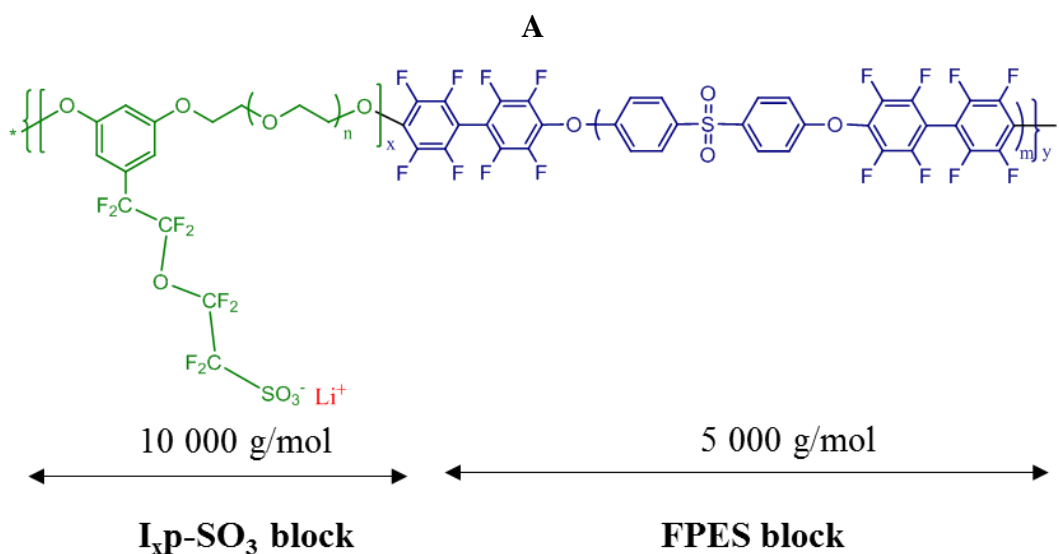
We were successfully designed and synthesized the single-ion structures based on PEO and the highly delocalized charge anions such as perfluorosulfonate or perfluorosulfonylimide. These materials were characterized as solid polymer electrolyte for safer lithium metal batteries.

This work proved that the SIPEs are amorphous and are thermal stable over 300 °C. By cross-linking and reinforcing with 6 wt.% of NCC, the solid electrolyte films exhibit good electrochemical behaviors versus lithium. The cycling tests in the symmetric Li-metal cell confirmed an excellent reversibility of Li plating/stripping, and a nearly unity transference number of Li⁺ for the cross-linked matrixes. The cycling tests in the LFP // I_{1000p}-SO₃-cr // Li-metal batteries demonstrated an excellent reversibility, which are higher than the best results reported in the state of the arts. In brief, the obtained results proved that single-ion materials are well adapted for future high performances, and safer all-solid-state Li-metal batteries.

To simplify the elaboration method, and casting membrane with better mechanical properties, the SIPEs based on block copolymer were also synthesized and characterized in the following part. The new multi-block copolymers combined an ionic block (based on the single-ion structure of I_{1000p}-SO₃), and a hydrophobic fluorinated poly(ether sulfone) (FPES) block to reinforce the mechanical properties. These materials help to perform the membranes with better mechanical properties, without the addition of NCC, and the UV irradiation step.

2. Multi-block copolymer

The multi-block copolymers $(AB)_n$ were synthesized and characterized. The A block is a high T_g polyaromatic sulfone (FPES) which permits to maintain good mechanical properties, whereas the B block is an ionic block providing the Li^+ ions mobility (a PEO-based ionomer). The chemical structure, and the expected network of block copolymer are presented in Fig. 41. The two blocks are selected to be incompatible, and to form during the casting process a nano-phase separation morphology with hydrophobic (FPES) domains and ionic domains. The design of this structure allows to obtain the block copolymer with the ionic function attached to the conducting block, thus keep the phase separation, and the mechanical properties even at high temperature. In the state of the arts, for most of reported block copolymers, the ionic functions were attached to the rigid blocks, hence once the PEO melts, the two phases are mixed and drastically degrading the mechanical properties.^{34,37} The ionic block is obtained from different molecular weight PEG (MW = 1000, 400 g/mol), and sodium-5-(3',5'-difluorophenyl)-3-oxoperfluoropentansulfonate (monomer p-SO₃). The synthesized copolymers are named as Co_xp-SO₃, where x represents the molecular weight of PEG used for ionic block synthesis.



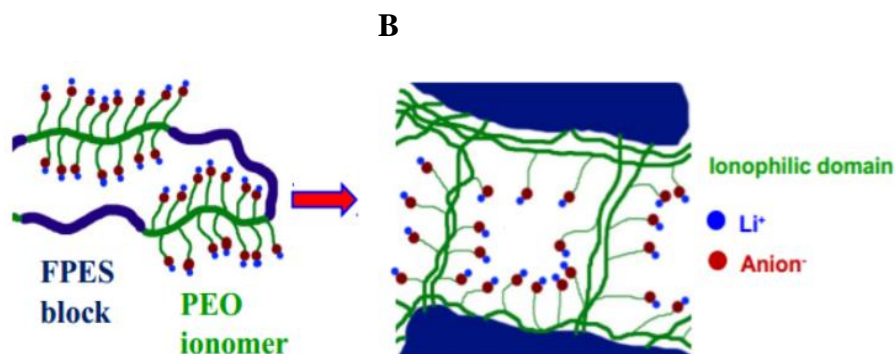


Fig. 40 (A) chemical structure of multi-block copolymer based on a hydrophobic FPES block and an ionic I_xp-SO_3 block; (B) expected cartoon network of copolymer.

2.1. Synthesis of Co_xp-SO_3

2.1.1. Synthesis of hydrophobic fluorinated poly(ether sulfone) (FPES) block

The FPES block with a desired molecular weight of 5000 g/mol is synthesized using dihydroxy diphenylsulfone (DPS), K_2CO_3 and decafluorobiphenyl (DFB) in DMAc as solvent. After 2 h of mixing at 70 °C, the obtained yellowish viscous mixture was precipitated in HCl 1 M aqueous solution and then washed with deionized water up to neutral pH. The hydrophobic block is dried under vacuum at 80 °C for 24 h and stored in a glove box.

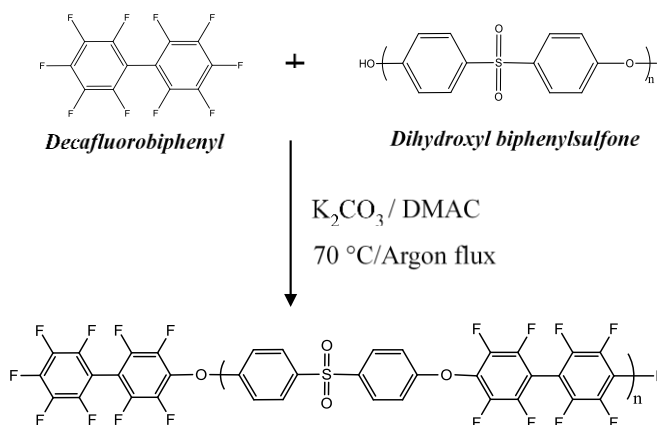


Fig. 41 Synthesis of hydrophobic FPES block.

The NMR spectra in deuterated chloroform were performed to confirm the structure of the final product (see Fig.44). In the 1H -NMR spectrum, the peaks at 7.1 and 7.9 ppm correspond to the aromatic protons of diphenylsulfone in ortho ether position and ortho SO_2 position, respectively are observed. For the ^{19}F spectrum (Fig.44), the triplet at -149.41 ppm relates to the fluorine in para position of biphenyl from the end of chain. The peaks at -160.06 and -137.15 ppm represent the ortho and meta-fluorine of the fluorinated biphenyl from the end of chain. The two intense peaks at -136.74 and -151.93 ppm correspond to the fluorine at meta and ortho ether positions of the octafluorobiphenyl ether.

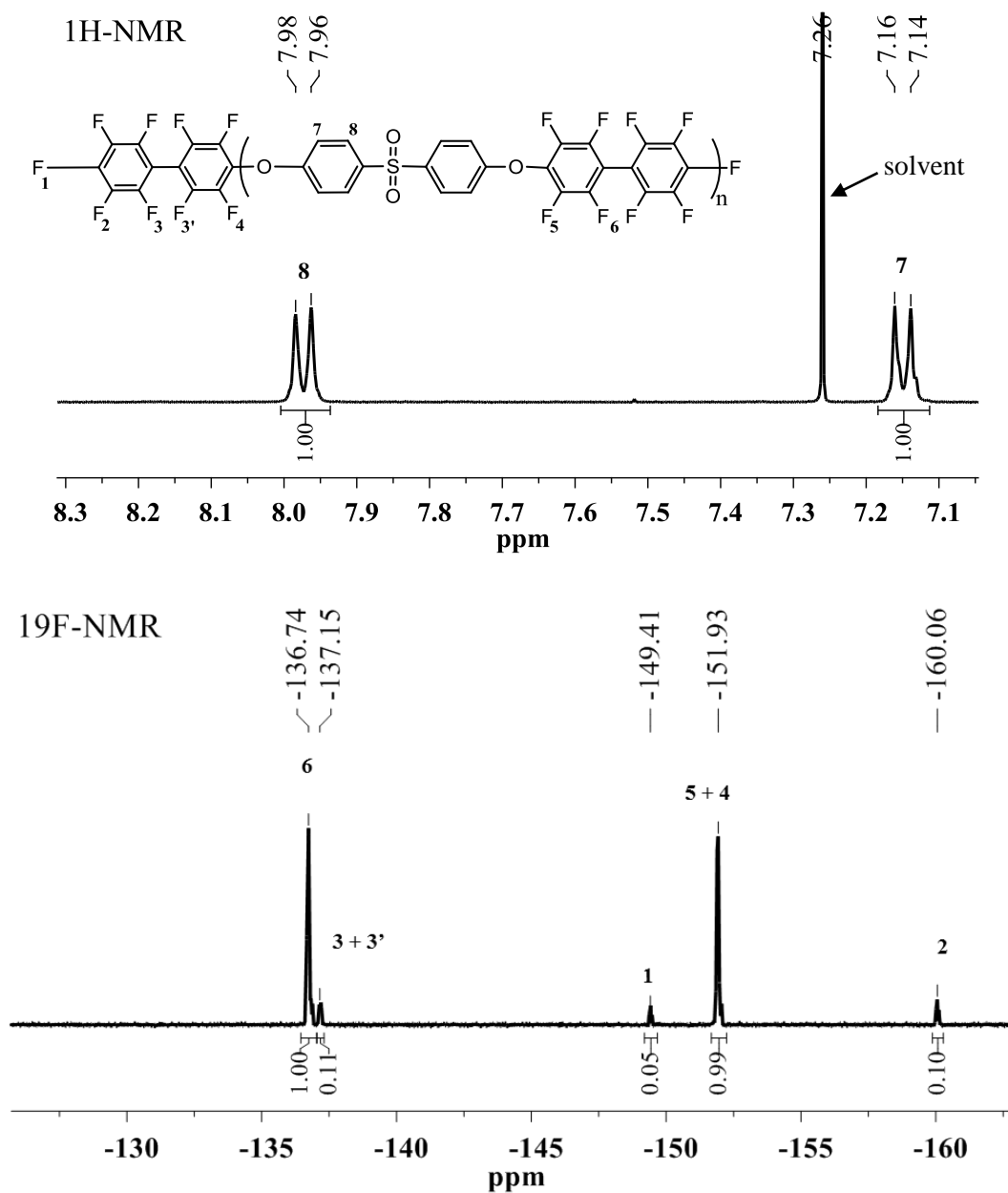


Fig. 42 The ^1H and ^{19}F -NMR spectra of FPES block in deuterated chloroform.

2.1.2. Synthesis of $\text{Co}_x\text{p-SO}_3$

The copolymers $\text{Co}_x\text{p-SO}_3$ were synthesized via a two-step polycondensation reaction, as described in Fig. 43. The amount of monomers was calculated to obtain an ionic block $\text{I}_x\text{p-SO}_3$ with a mass of 10 kg/mol. The synthesis performed following the same procedure as described in 1.1.1. After the formation of ionic block (the reaction was followed by the disappearance of aromatic fluorines in the ^{19}F -NMR spectrum), the hydrophobic FPES block was added directly into the flask at 50 °C. The final product was monitored by ^{19}F -NMR in DMSO-d_6 through the disappearance of the fluorines from the end-chain of FPES block. When the reaction finished, copolymer was precipitated in distilled water, under magnetic stirring to remove the inorganic salts in excess or formed during the synthesis. The NMR spectra of pure copolymer are showed in Fig. 44.

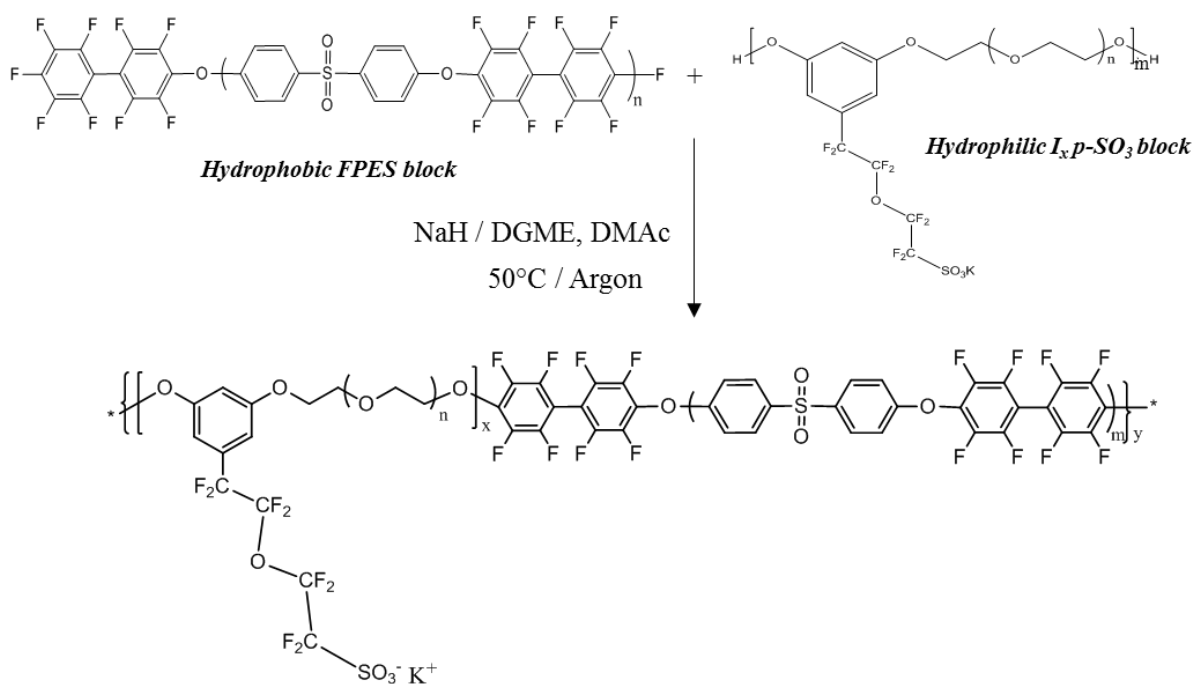


Fig. 43 Synthesis procedure of $\text{Co}_x\text{p-SO}_3$.

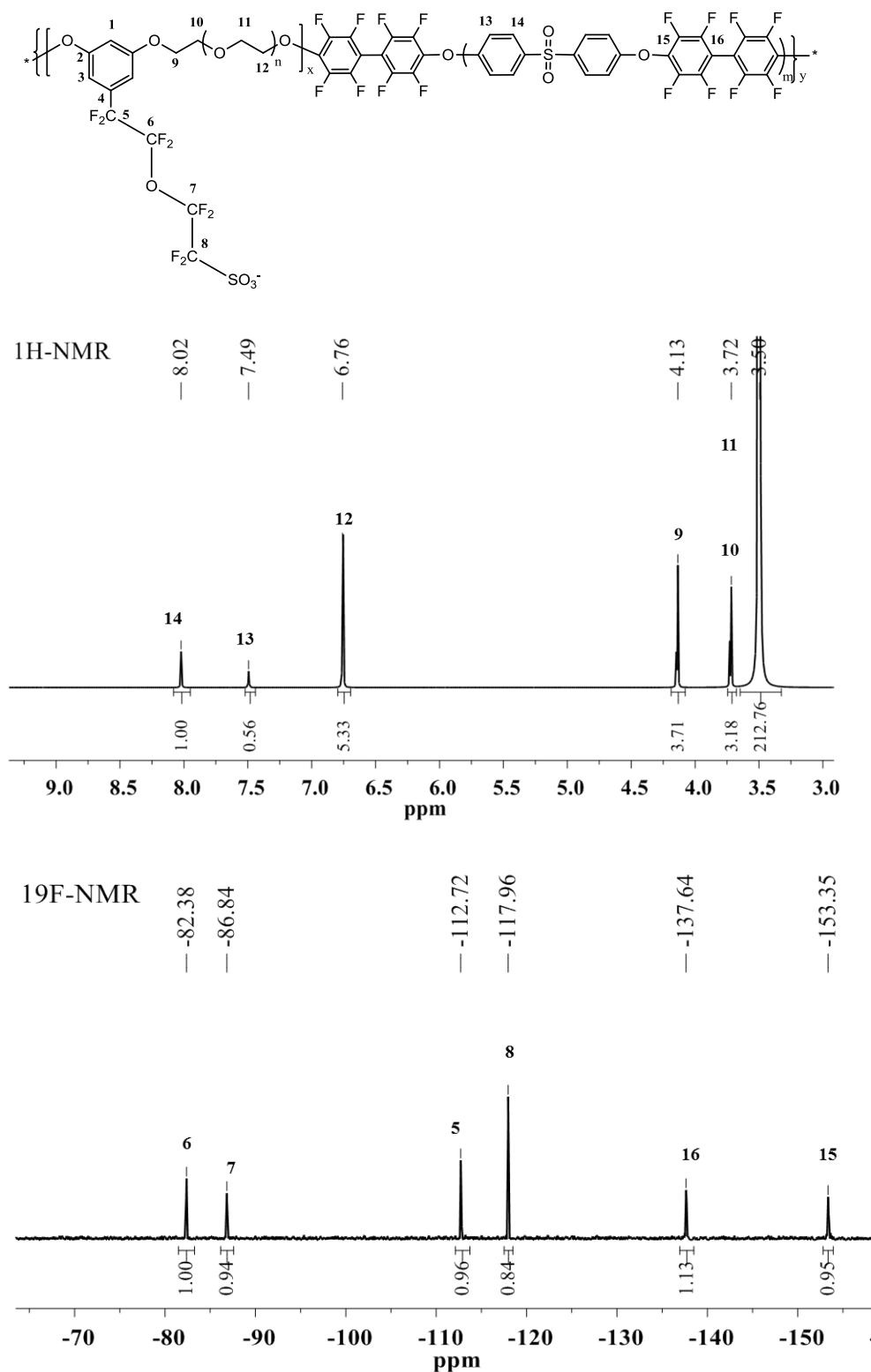


Fig. 44 The ^1H and ^{19}F -NMR spectra of $\text{Co}_{1000}\text{p-SO}_3$ in DMSO-d_6 .

The copolymers molecular weights were determined by SEC MALLs. The high molecular weights were obtained i.e. 300 kg/mol for $\text{Co}_{1000}\text{p-SO}_3$ and 250 kg/mol for $\text{Co}_{400}\text{p-SO}_3$, with a polydispersity of 3.6 and 2.7, respectively (see Table 7). The synthesized copolymers are exchanged into Li^+ form

for further characterizing as solid electrolytes for lithium battery. Thanks to the presence of hydrophobic block, and the high molecular weight, the copolymers are insoluble in aqueous solution. Therefore, the ion exchange process is quite simple and was performed by immersing the thin film membranes in 1M LiCl aqueous solution (see the annex). To measure the ion exchange capacity, since the $\text{Co}_x\text{p-SO}_3$ are insoluble in water, a definite quantity of copolymer was degraded in extra-pure HNO_3 (65%), and filtrated to extract only the ionic block (eliminate the insoluble FPES block) contained the interested cations. An excellent yield of ion exchange is found with nearly 100 % for both copolymers Table 7.

Table 7 Properties of synthesized copolymers including molecular weight and composition of cations.

Ionomer Li form	EO/ Li ratio	SEC-MALLs		AAS		
		M_n kg.mol ⁻¹	DPI	Li %	Na%	K %
$\text{Co}_{1000}\text{p-SO}_3$	23	300	3.6	100	-*	-
$\text{Co}_{400}\text{p-SO}_3$	9	250	2.7	99	-	-

* (-) Concentration non-detectable

These lithiated copolymers were cast into membrane, from a solution of 0.2 g copolymer in DMSO, and dried under vacuum at 80 °C for 48 h. To enhance the conductivity of copolymers, a polymer blend consisted of $\text{Co}_{400}\text{p-SO}_3$ and poly(ethylene glycol)dimethyl ether (DMPEG) (MW = 1000 g/mol) was also prepared. The DMPEG content was 36 wt.% corresponding to an EO/Li = 23 for the blend polymers (the same Li concentration as in $\text{Co}_{1000}\text{p-SO}_3$). The performed films with thickness ranging from 100 to 120 μm were dried and stored in a glove box prior to use.

2.2. Characterization

2.2.1. Thermal properties

i. Thermal stability

The analysis of the relative weight loss versus temperature for the synthesized copolymers, and the blend copolymer was observed by TGA measurements. The dried samples were heated from RT to 800 °C, under N_2 flux, with a scan rate of 10 °C.min⁻¹. The thermograms from 200 to 450 °C (Fig. 47), exhibit a sharp weight loss at about 340 °C. As previously discussed for the cross-linked ionomers' degradation (1.2.3.), this weight loss corresponds to the degradation of PEG chain. Noted that, the T_d values show in Table 8 are determined at 5 % of relative weight loss for all the samples. The membrane cast from a blend of $\text{Co}_{400}\text{p-SO}_3$ and DMPEG exhibits nearly similar behaviors with the $\text{Co}_{1000}\text{p-SO}_3$ contained the same EO/Li of 23.

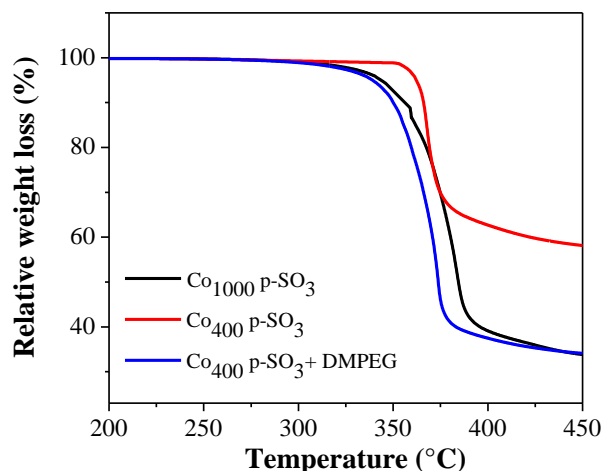


Fig. 45 Thermograms for the synthesized copolymers and the blend $\text{Co}_{400}\text{p-SO}_3 + \text{DMPEG}$ from 200 to 450°C

Table 8 Thermal analysis of polymer including the degradation for the synthesized copolymers and the blend $\text{Co}_{400}\text{p-SO}_3 + \text{DMPEG}$.

Sample	$T_d \pm 2$ (°C)	Wt.% of PEG
$\text{Co}_{1000}\text{p-SO}_3$	343	60
$\text{Co}_{400}\text{p-SO}_3$	362	35
$\text{Co}_{400}\text{p-SO}_3 + \text{DMPEG}$	339	60

ii. Differential scanning calorimetry

The thermal characteristics of these copolymers were investigated by DSC measurements. The thermograms in Fig. 46A run at 10 °C/min, and show only the glass transition behavior that means these materials are completely amorphous in the large range of temperatures. The $\text{Co}_{400}\text{p-SO}_3$ exhibits clearly two T_g i.e. the first T_g at 30 ± 2 °C corresponds to the phase transition of ionic I-pSO₃ block (see 1.2.3.), and the second one at 235 ± 2 °C attributes to the polyaromatic polysulfone FPES block.³² The appearance of the second T_g proves a sharp phase separation between the ionic and hydrophobic chains. However, using the same conditions, the thermograms of $\text{Co}_{1000}\text{p-SO}_3$ exhibits only one T_g at -23 ± 2 °C of the ionic block, and the phase transition of the FPES block is non observable (see the black line in Fig. 46A). Increasing the scan rate of both heating and cooling cycles to 20 °C/min helps to clearly determinate the second T_g value of the FPES block at 162 ± 2 °C, as seen in Fig. 46B. This T_g is much lower than the $\text{Co}_{400}\text{p-SO}_3$ suggesting a poorer phase separation.

Concerning the ionic blocks of the two copolymers, a huge difference in the T_g values is obtained e.g. 53 °C. This significant increase of T_g values with decreasing EO/Li (from 23 to 9) was also reported for the cross-linked ionomers in 1.2.3, but here the gap of T_g values is even higher.

Additionally, the T_g of ionic block for $\text{Co}_{1000}\text{p-SO}_3$ and $\text{Co}_{400}\text{p-SO}_3$ are 20°C and 30°C , which are higher than those obtained for $\text{I}_{1000}\text{p-SO}_3\text{-cr}$ and $\text{I}_{400}\text{p-SO}_3\text{-cr}$, respectively. This strong increase of T_g for these copolymers mainly relates to the presence of more than 30 wt.% of rigid block e.g. $M_n = 10$ kg/mol for the ionic block, and $M_n = 5$ kg/mol for the FPES block, which could largely affect the mobility of ionic chain.

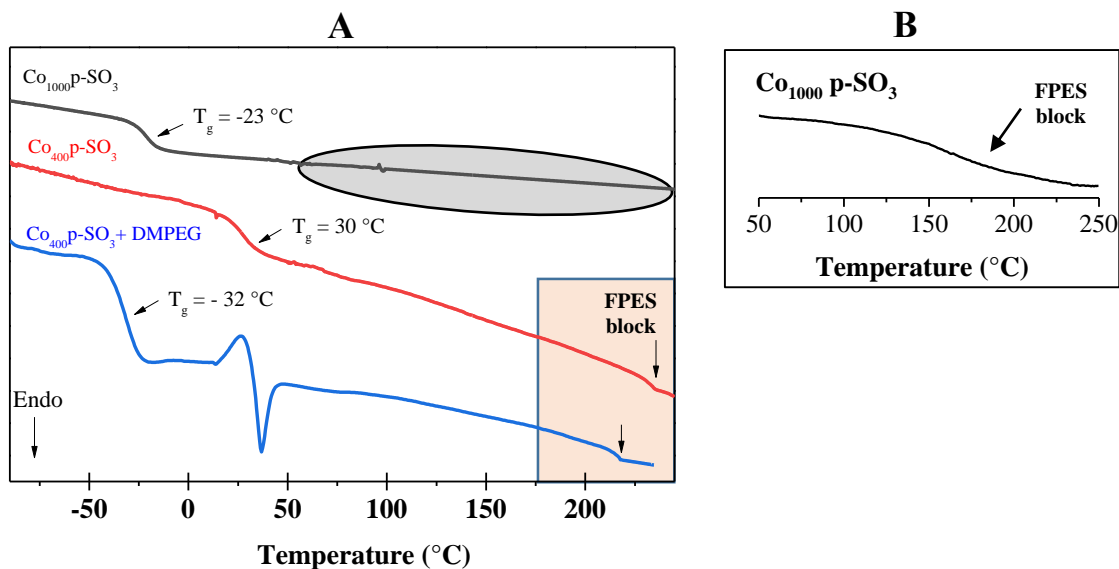


Fig. 46 (A) The DSC thermograms of the $\text{Co}_x\text{p-SO}_3$ and the blend $\text{Co}_{400}\text{p-SO}_3 + \text{DMPEG}$ from -80 to 250°C with a scan rate of $10^\circ\text{C}/\text{min}$; (B) DSC thermogram of $\text{Co}_{1000}\text{p-SO}_3$ from 50 to 250°C with a scan rate of $20^\circ\text{C}/\text{min}$.

The high T_g of ionic blocks testify on low mobility of Li^+ , thus a low conductivity for these copolymers is predicted. Therefore, a blend of polymers was prepared by adding an amount of free DMPEG as plasticizer in $\text{Co}_{400}\text{p-SO}_3$ to get the $\text{EO}/\text{Li} = 23$ (same as in $\text{Co}_{1000}\text{p-SO}_3$), and was casted into membrane. As concerned the thermal behaviors of this membrane, in Fig. 46, the blue thermogram exhibits three separated phases transition corresponding to the T_g of $\text{I}_{400}\text{p-SO}_3$ block and DMPEG at $-32 \pm 2^\circ\text{C}$, to the crystallization and melting processes of the free DMPEG at $33 \pm 2^\circ\text{C}$, and the T_g of FPES block at $216 \pm 2^\circ\text{C}$. The addition of DMPEG strongly shifts the T_g of ionic block from $30 \pm 2^\circ\text{C}$ to $-32 \pm 2^\circ\text{C}$. Calculating the theoretical T_g of a blend formed with the ionic blocks and the DMPEG by using Flory-Fox equation, and considering the DMPEG ($T_g = -65 \pm 2^\circ\text{C}$) interacts only with the ionic chains, gives a value of -20°C , which is weakly higher than the behavior observed by DSC measurements. The T_g value of the hydrophobic block decreases as compared to that of $\text{Co}_{400}\text{p-SO}_3$ meaning the FPES block are also plasticized by the DMPEG.

In conclusion, the synthesized copolymers exhibit high thermal stability over 340°C , an amorphous character, and their glass transition temperature are influenced by the Li^+ concentration. The $\text{Co}_{400}\text{p-SO}_3$ shows much higher T_g than its homologue $\text{Co}_{1000}\text{p-SO}_3$, which was also observed for the ionomers. Two well defined T_g obtained for the $\text{Co}_{400}\text{p-SO}_3$ indicating a better phase separation

behavior. The addition of plasticizer i.e. low molecular weight DMPEG decreases significantly the T_g values of both hydrophilic and hydrophobic blocks, while keeping the shape phase (ionic/hydrophobic) separation. This blend is expected to have higher conductivity comparing to the $Co_{1000}p-SO_3$ due to a difference of about 9 °C in T_g of the ionic blocks.

2.2.2. Conductivity

The conductivity of the two copolymers and the polymer blend are measured by EIS method using a Swagelok cell SS || polymer || SS. The measures are performed to a heating/cooling process, from 90 to 10 °C, following the same conditions as for the cross-linked ionomers (1.2.3), and the conductivities are presented as a function of the inverse of temperature in Fig. 49.

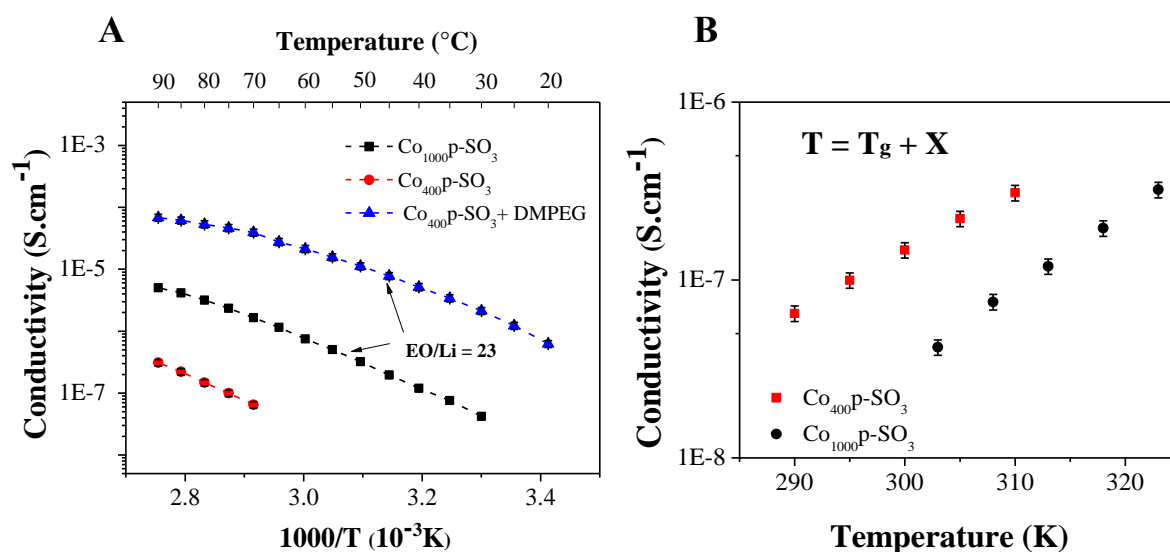


Fig. 47 (A) Conductivity versus $1000/T$ of the Co_xp-SO_3 and the blend $Co_{400}p-SO_3 + DMPEG$; (B) Conductivity of Co_xp-SO_3 at $T = T_g + X$.

The conductivity for all the samples increases with increasing temperature following a VTF behavior. The $Co_{1000}p-SO_3$ (black line) exhibits conductivity of 5.0×10^{-6} at 90 °C, meanwhile the $Co_{400}p-SO_3$ shows lower conductivity of 3.1×10^{-7} at the same temperature. This behavior is somehow similar to the one observed for the I_xp-SO_3-cr ionomers, and the huge difference in conductivity relates to the difference of T_g i.e. the T_g value of ionic block for $Co_{400}p-SO_3$ is 53 °C higher than that of $Co_{1000}p-SO_3$. Moreover, if we compare the conductivity at $T = T_g + X$ (where X is constant) to avoid the effect of the rigidity (see Fig. 47B), at a same temperature of $T_g + X$, the $Co_{400}p-SO_3$ show higher conductivity and its value is almost 2.6 higher than those of $Co_{1000}p-SO_3$, value which corresponds, similarly to what has been observed with the cross-linked ionomers, to the difference in Li concentration. If we compare $Co_{1000}p-SO_3$ with $I_{100}p-SO_3-cr$, the conductivity is almost an order of magnitude lower. This decrease could be explained by (i) the lower mobility (higher T_g) and (ii) the presence of about 33 wt.% of rigid block which is not conducting (dilution effect). Moreover, this

non-conducting phase would provide a high tortuosity of ionic pathway, and/or the presence of isolated ionic domains.

The blend $\text{Co}_{400}\text{p-SO}_3 + \text{DMPEG}$ exhibits pretty good conductivity of $7.4 \times 10^{-5} \text{ S.cm}^{-1}$ at 90°C , which is about one order of magnitude higher than $\text{Co}_{1000}\text{p-SO}_3$, despite their similar Li content ($\text{EO/Li} = 23$). Additionally, conductivities of this blend are twice higher than that of cross-linked $\text{I}_{1000}\text{p-SO}_3\text{-cr}$, despite the lower T_g of the last one ($\text{Co}_{400}\text{p-SO}_3 + \text{DMPEG}$ exhibits of $T_g = -32 \pm 2^\circ\text{C}$ against to $-37 \pm 2^\circ\text{C}$ for $\text{I}_{1000}\text{p-SO}_3\text{-cr}$, respectively), and the presence of a non-conducting FPES fraction (21 wt.% after the addition of DMPEG). This may be explaining by the strong contribution of ‘free DMPEG’ in Li^+ transport. One more thing that needs to be mention here is a good phase separation between the rigid block and the ionic chain (two distinct phase transitions in the DSC curve) which can contribute to enhance the conductivity by creating well organized and efficient Li^+ ions conducting pathways.

2.2.3. Electrochemical stabilization

The electrochemical stability window of the copolymer films was carried out by CV technique. The coin cells were prepared by sandwiching the copolymer membrane between a lithium metal foil and a stainless-steel (SS) electrode, in a glove box. The electrochemical stability tests were performed from -0.3 V to 4.1 V vs Li^+/Li , with a scan rate of 0.1 mV.s^{-1} , at 80°C . The voltammograms of $\text{Co}_{1000}\text{p-SO}_3$ and $\text{Co}_{400}\text{p-SO}_3 + \text{DMPEG}$, which are the highest conductivity samples, are presented in Fig. 48.

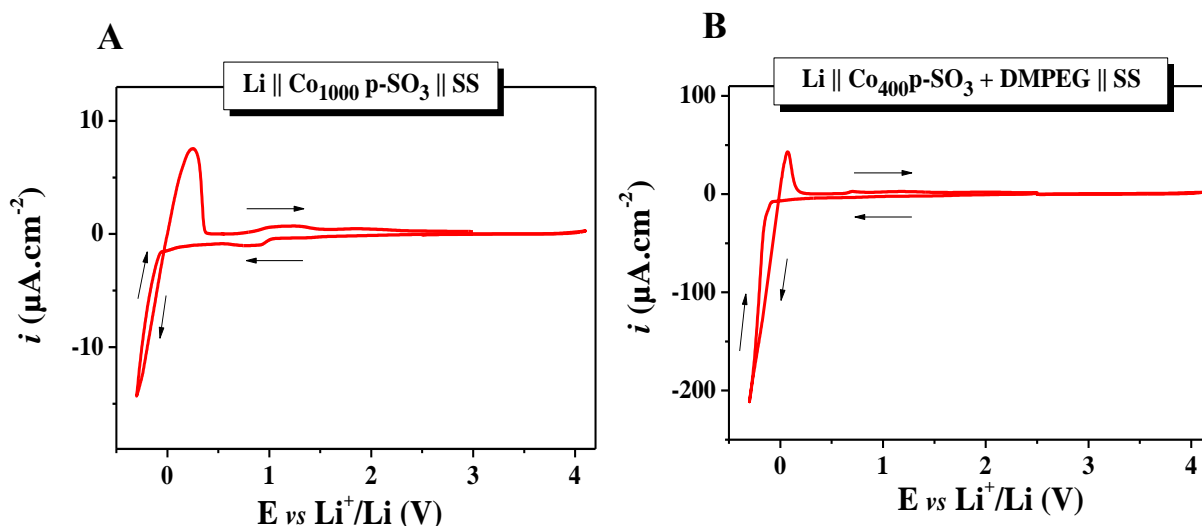


Fig. 48 Cyclic voltammograms of $\text{Co}_{1000}\text{p-SO}_3$ (left) and $\text{Co}_{400}\text{p-SO}_3 + \text{DMPEG}$ (right) from -0.3 to 4.1 V vs Li^+/Li in a $\text{Li}||\text{electrolyte}||\text{SS}$ cell, with 0.1 mV.s^{-1} scanning rate, at 80°C

In the anodic scans, both electrolytes exhibit high stability over 4 V vs Li^+/Li , which is comparable to the SO_3 -based ionomers, and even slightly higher than the conventional PEO/salt electrolyte (limit

at 3.9 V vs Li⁺/Li). The reduction of lithium started at -0.1 V vs Li⁺/Li for both electrolytes. The blend polymer performed a current intensity significantly higher (roughly 10-fold order of magnitude) as compared to that of Co₁₀₀₀p-SO₃ relating to the higher conductivity. In the next part, the membrane possessed highest conductivity i.e. Co₄₀₀p-SO₃ + DMPEG was characterized as solid electrolyte in the Li-metal batteries. Before, the single-ion nature of these electrolytes are affirmed by the tests of Li⁺ transference number.

2.2.4. Lithium transference number

The transference number of the blend Co₄₀₀p-SO₃ + DMPEG was measured by low frequencies EIS and PGSE-NMR methods. For the EIS method, the symmetric Li-metal coin cell was prepared in a glove box by sandwiching the polymer film between two electrodes of Li-metal. Before the cycling tests, the cell was heated and stabilized at 80 °C in a controlled temperature oven. The EIS measurements were applied at every 2 h, for 24 h, to reach the constant impedance spectra. The cell was performed following a cycling route used for the cross-linked ionomers. The Nyquist plot from 1 MHz to 1 mHz of the assembly Li || Co₄₀₀p-SO₃ + DMPEG || Li, is presented in Fig. 49, and the spectrum was fitted with an equivalent circuit (insert figure).

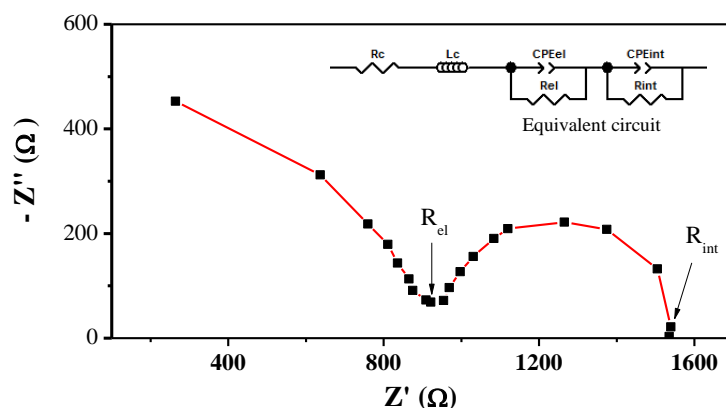


Fig. 49 Nyquist plot of Li || Co₄₀₀p-SO₃ + DMPEG || Li at 80 °C and the fitting result (red line).

The impedance spectrum shows two semi-circles corresponding to the electrolyte response (R_{el} , CPE_{el}), and Li/electrolyte interface response (R_{int} , CPE_{int}), respectively, without any sign of Li diffusion at low frequencies. This plot exhibits similar behavior to the cross-linked I₁₀₀₀p-SO₃-cr meaning a unity Li transference number of the blend Co₄₀₀p-SO₃ + DMPEG.

The self-diffusion coefficients (D) measured by NMR spectroscopy at 80 °C, for ¹⁹F and ⁷Li nuclei, shows only the Li diffusion with a D_{Li} value of $4.8 \times 10^{-12} \text{ m}^2\text{s}^{-1}$. The diffusion of fluorines corresponding to the anionic function was non-detectable, indicating the absence or the extremely low diffusion of anions. The cationic transport number of the blend is considered to unity.

2.2.5. Lithium dendritic growth test

The tests were performed using the same cycling protocol for the cross-linked ionomer (in 1.2.6) at 80 °C. The typical voltage steps with time recorded as a function of the constant applied current densities from 0.01 to 0.1 mA.cm⁻² are presented in Fig. 50. The cell is stable up to 400 h without any sign of Li dendrite growth at different applied currents from low to high. The corresponded over-potentials increase proportionally with increasing the currents as observed for the cross-linked I₁₀₀₀P-SO₃-cr. However, the cell became unstable at 0.2 mA.cm⁻², and polarized leading to the short circuit. This behavior is surprising because the I₁₀₀₀P-SO₃-cr cycled well at this current density, despite the lower conductivity.

Moreover, a zoom in Fig. 50 shows the nearly straight stair steps of lithium plating/stripping during charge/discharge cycles, and even at OCV. However, the over-potential takes time to reach constant plateau, which is an unexpected behavior of single-ion polymer. These phenomena is assumed due to the presence of free plasticizer, which causes the slight polarization at the beginning of each cycle, and can be related to the lithium reactivity.

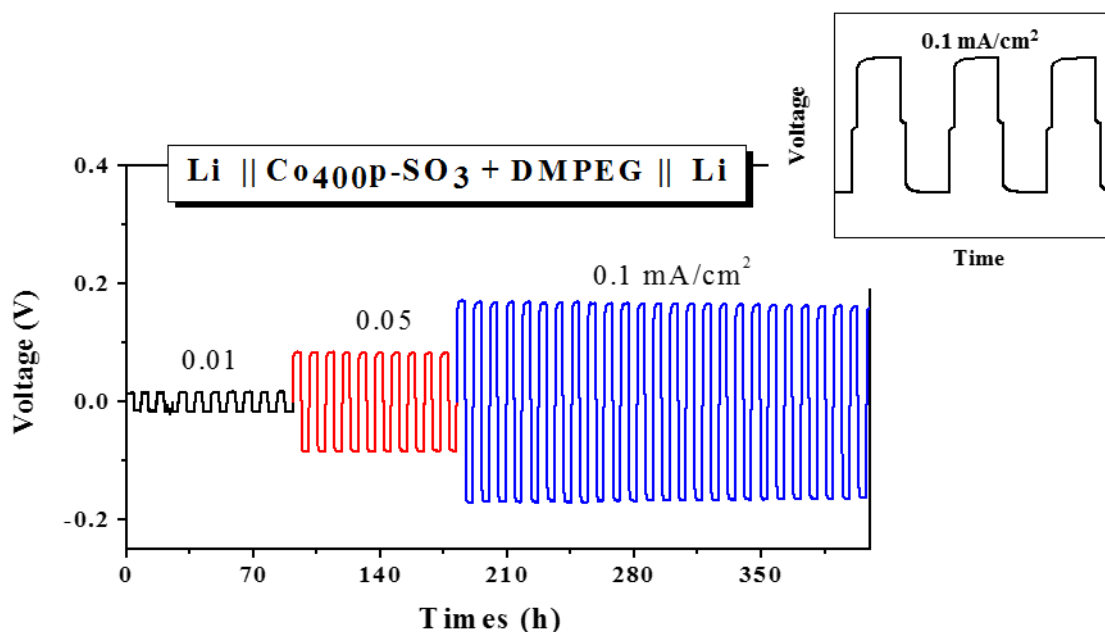


Fig. 50 Typical Li plating/stripping in a symmetric Li || Co₄₀₀P-SO₃ + DMPEG || Li cell at 80 °C at different applied currents from 0.01 to 0.1 mA.cm⁻² as a function of time. Insert figure presents the voltage steps at both charge/discharge directions and during OCV at 0.1 mA.cm⁻².

2.2.6. Cycling tests

The cycling test in a Li-metal battery using the B-LFP electrode and the blend Co₄₀₀P-SO₃ + DMPEG as solid electrolyte was performed at 80 °C. Fig. 51 shows the charge/discharge curves at different power rates from C/20 to C. The charge and discharge performed at the same C-rate. The cell

delivers about 140 mAh.g^{-1} at C/20 which is comparable to that of $\text{I}_{1000}\text{p-SO}_3\text{-cr}$ electrolyte, and exhibits the well-defined potential plateau up to C/2.5 rate. The discharge capacity decreases slowly from 140 to 123 mAh.g^{-1} at C/20 and C/2.5, respectively, and shows a stable cyclability with high Coulombic efficiency of above 98 % during more than 40 cycles (Fig 53B). However, at 1C we observe a strong polarization (Fig. 51), and an important decrease in capacity as compared to $\text{I}_{1000}\text{p-SO}_3\text{-cr}$ (only 60% of the initial capacity was reached, where 81% was obtained with the cross-linked ionomer) is observed (Fig 52). Meanwhile, when the cycling rate was reduced to C/10, about 86% of the first cycle capacity were recovered, indicating the high reversibility of the battery without detrimental degradation process.

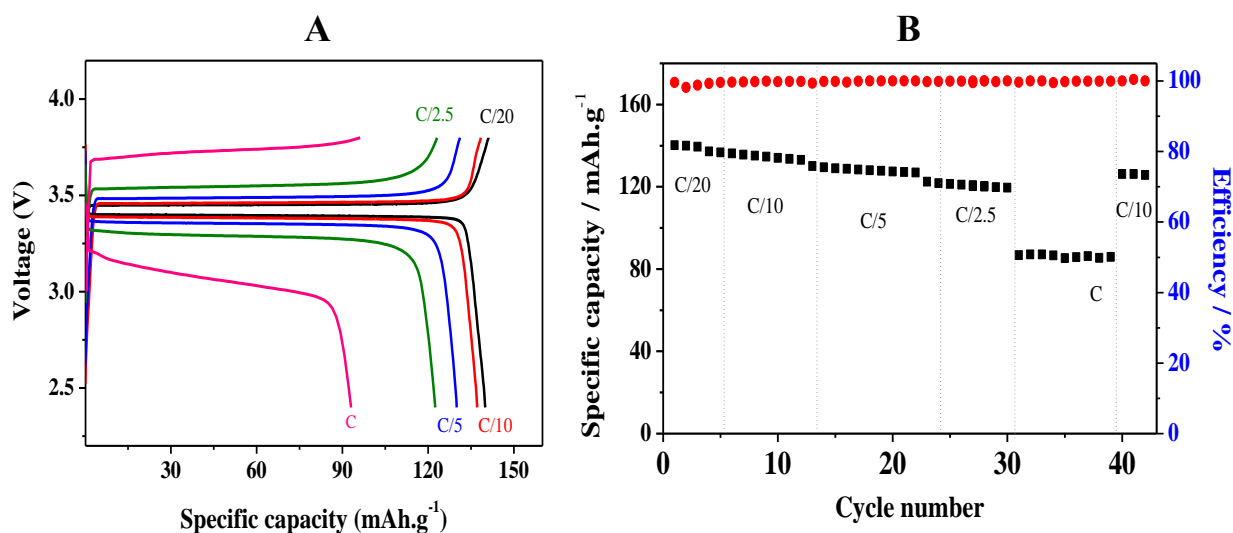


Fig. 51 Cyclability at different scan rates from C/20 to 1C for B-LFP // $\text{Co}_{400}\text{p-SO}_3 + \text{DMPEG}$ // Li cell at 80°C .

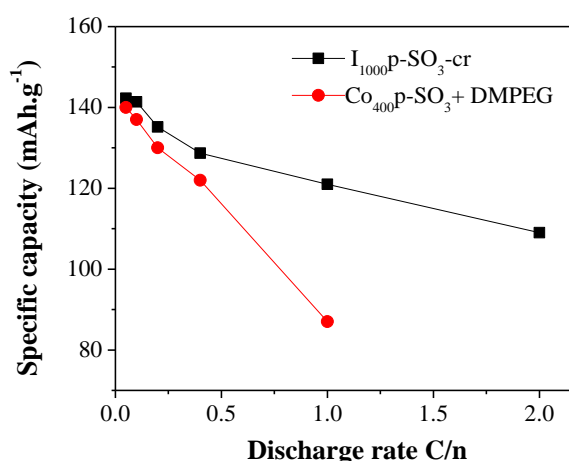


Fig. 52 Discharge capacities obtained for the B-LFP // electrolyte // Li batteries at 80°C using the $\text{I}_{1000}\text{p-SO}_3\text{-cr}$ (black) and $\text{Co}_{400}\text{p-SO}_3 + \text{DMPEG}$ (red) as solid electrolytes as a function of discharge rates.

The durability tests were performed at C/10 using the same battery, and the performances as

well as the Coulombic efficiency are presented in Fig. 53. The cell was still stable over 48 cycles with an excellent Coulombic efficiency of 98 %.

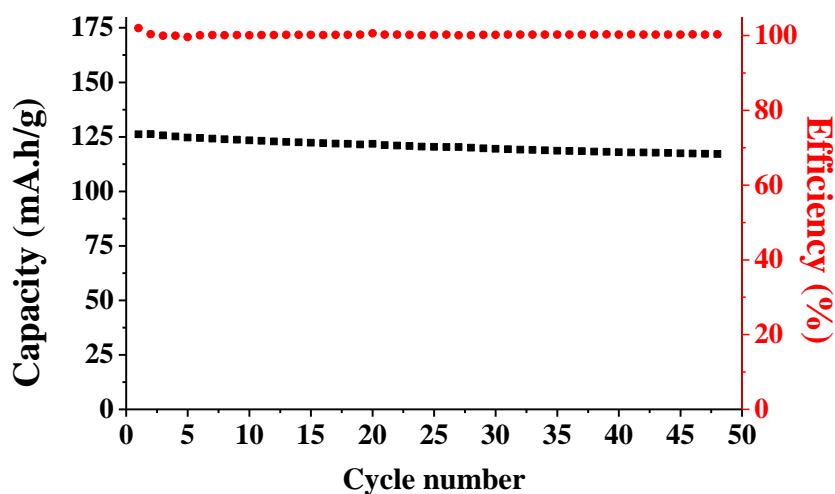


Fig. 53 Durability tests at C/10 for B-LFP // Co_{400p}-SO₃ + DMPEG // Li cell at 80 °C.

This is a surprising result because the conductivity of the blend polymer is higher than the cross-linked ionomer, hence lower cell polarization was expected. These behavior may be caused by the presence of free DMPEG as plasticizer. The DMPEG is moving with Li⁺ during charge/discharge, and at high C-rates it can induce a DMPEG concentration gradient into the membrane. The blend PEO+ I_{400p}-SO₃-db from the electrode is also compatible with the DMPEG, thus, a part of DMPEG can be retained in the electrode and inducing a decrease in electrolyte conductivity.

2.3. Conclusions

The multi-block copolymers based on the Ip-SO₃ ionic block and the rigid FPES block were synthesized and characterized. These materials have the ionic functions attached directly on the PEO block contrarily to the block copolymers reported in the literature, where the anions are fixed on the rigid block. The addition of free DMPEG as plasticizer causes a strong decrease of T_g, while keeping the clear phase separation, resulting in higher conductivity due to a good percolation, and high mobility of ionic domains.

The presence of about 33 wt.% of the hydrophobic block induces the insoluble characteristic of copolymers in aqueous solution that facilitated the purification, and ionic exchange processes. The membranes obtained by casting directly from the solution of copolymer dissolved in solvent, without any additional processes, such as the cross-linking or the NCC reinforcing, as for the ionomers. The resulted copolymer films possess good mechanical properties and high thermal stability that help to recover the material after characterization.

The single-ion nature of these polymers was affirmed by both electrochemical and PFG-NMR techniques. The blend $\text{Co}_{400}\text{p-SO}_3 + \text{DMPEG}$ was investigated as solid electrolyte in a lithium metal battery using the B-LFP electrode. At low C-rate the performances of the blend and the cross-linked ionomers were comparable, while at high C-rate the blend induced higher cell polarization.

The presence of free DMPEG affected on the performances at high C-rate. For the evolution of this materials, and preventing the use of plasticizer, the copolymers possessed the longer ionic block for improving conductivity due to the percolation of the ionic domains are required. The LFP electrode contained the same ionic composition to the electrolyte is required to limit the migration of plasticizer from electrolyte to electrode.

References

1. Liu M., Li M., De Xue J., Phillips D. L., Time-resolved spectroscopic and density functional theory study of the photochemistry of Irgacure-2959 in an aqueous solution, *J. Phys. Chem. A*, 118, 8701–8707 (2014).
2. Scaiano J. C., Stampelcoskie K. G., Hallett-Tapley, G. L., Photochemical Norrish type I reaction as a tool for metal nanoparticlesynthesis: importance of proton coupled electron transfer, *Chem. Commun.*, 48, 4798–4808 (2012).
3. Thiam A., Antonelli C., Iojoiu C., Alloin F., Sanchez J. Y., Optimizing ionic conduction of poly(oxyethylene) electrolytes through controlling the cross-link density, *Electrochim. Acta*, 240, 307–315 (2017).
4. Sakakibara T. *et al.*, Cross-linked polymer electrolyte and its application to lithium polymer battery, *Electrochim. Acta*, 296, 1018–1026 (2019).
5. Bolloli M., Nouvelles membrane polymères et électrolytes liquides pour batteries Li-ion. (Université de Grenoble, 2014).
6. Bolloli M. *et al.*, Nanocomposite poly(vinylidene fluoride)/nanocrystalline cellulose porous membranes as separators for lithium-ion batteries (2016).
7. Azizi Samir M. A. S., Alloin F., Sanchez J. Y., Dufresne A., Cellulose nanocrystals reinforced poly(oxyethylene), *Polymer*, 45, 4149–4157 (2004).
8. Alloin, F., D'Apréa, A., Kissi, N. El, Dufresne, A., Bossard F., Nanocomposite polymer electrolyte based on whisker or microfibrils polyoxyethylene nanocomposites, *Electrochim. Acta*, 55, 5186–5194 (2010).
9. Danyliv O., Nouvelles membranes à squelette haute performance pour les piles à combustible PEMFC. *PhD thesis, Université Grenoble-Alpes* (2015).
10. Cameron G. G. *et al.*, The thermal degradation of poly(ethylene oxide) and its complex with NaCNS, 25, 779–784 (1989).
11. Eiamlamai P., Polymer electrolytes based on ionic liquids for lithium batteries Electrolytes polymères à base de liquides ioniques pour batteries au lithium, *PhD thesis, Université Grenoble-Alpes* (2015).
12. Luo G. *et al.* Synthesis of Single Lithium-Ion Conducting Polymer Electrolyte Membrane for Solid-State Lithium Metal Batteries, *ACS Appl. Energy Mater*, 2, 3028–3034 (2019).
13. Watanabe M., Suzuki, Y., Nishimoto, A., Single ion conduction in polyether electrolytes alloyed with lithium salt of a perfluorinated polyimide, *Electrochim. Acta*, 45, 1187–1192 (2000).
14. Ngai K. S., Ramesh S., Ramesh K., Juan J. C., A review of polymer electrolytes: fundamental, approaches and applications, *Ionics (Kiel)*, 22, 1259–1279 (2016).
15. Elmore C. *et al.*, Ion Transport in Solvent-Free, Crosslinked, Single-Ion Conducting Polymer Electrolytes for Post-Lithium Ion Batteries, *Batteries*, 4, 28 (2018).
16. Sanchez J. Y., Alloin F., Benrabah D., Arnaud, R., Polymer and salt selection for lithium polymer batteries, *J. Power Sources*, 68, 43–51 (1997).
17. E. Paillard, Nouveaux électrolytes polymères pour batteries au lithium. *PhD thesis, Université Grenoble-Alpes* (2008).
18. Aihara Y., Arai S., Hayamizu K., Ionic conductivity, DSC and self diffusion coefficients of lithium, anion, polymer, and solvent of polymer gel electrolytes: The structure of the gels and the diffusion mechanism of the ions, *Electrochim. Acta*, 45, 1321–1326 (2000).

19. P. Pietro Bucci *et al.*, Characterization of PEO-lithium triflate polymer electrolytes: Conductivity, DSC and Raman Investigations. *Ionics (Kiel)*, 8, 36–43 (2002).
20. Paillard E. *et al.*, Polymer electrolytes based on new aryl-containing lithium perfluorosulfonates, *J. Fluor. Chem.*, 134, 72–76 (2012).
21. Lightfoot P., Mehta M. A., Bruce P. G., Crystal structure of the polymer electrolyte poly(ethylene oxide)₃:LiCF₃SO₃, *Science*, 262, 883–885 (1993).
22. Devaux D., Bouchet R., Glé D., Denoyel R., Mechanism of ion transport in PEO/LiTFSI complexes: Effect of temperature, molecular weight and end groups, *Solid State Ionics*, 227, 119–127 (2012).
23. Azizi Samir M. A. S., Alloin F., Sanchez J. Y., El Kissi N., Dufresne A., Preparation of cellulose whiskers reinforced nanocomposites from an organic medium suspension, *Macromolecules*, 37, 1386–1393 (2004).
24. Zhang H. *et al.*, Single lithium-ion conducting solid polymer electrolytes: Advances and perspectives, *Chem. Soc. Rev.*, 46, 797–815 (2017).
25. Ramesh, S., Yuen, T. F., Shen, C. J., Conductivity and FTIR studies on PEO-LiX [X: CF₃SO₃⁻, SO₄²⁻] polymer electrolytes, *Spectrochim. Acta - Part A Mol. Biomol. Spectrosc.*, 69, 670–675 (2008).
26. Chazalviel J.-N., Electrochemical aspects of the generation of ramified metallic electrodeposits, *Phys. Rev. A*, 42, 7355–7367 (1990).
27. Macdonald J. R., Binary electrolyte small-signal frequency response, *J. Electroanal. Chem.*, 53, 1–55 (1974).
28. Vincent P. G. B. C. A., Transport in associated polymer electrolytes, *Solid State Ionics*, 40/41, 607–611 (1990).
29. Chauvin C., Alloin F., Iojoiu C., Sanchez J. Y., New polymer electrolytes based on ether sulfate anions for lithium polymer batteries. Part II: Conductivity and transport properties of blended and cross-linked ionomers, *Electrochim. Acta*, 51, 5954–5960 (2006).
30. Armand M., Polymer solid electrolytes - an overview, *Solid State Ionics*, 9–10, 745–754 (1983).
31. Frenck L., Study of a buffer layer based on block copolymer electrolytes, between the lithium metal and a ceramic electrolyte for aqueous Lithium-air battery, *PhD thesis, Université Grenoble-Alpes* (2017).
32. Nguyen H. D. *et al.*, Nanostructured multi-block copolymer single-ion conductors for safer high-performance lithium batteries, *Energy Environ. Sci.*, 11, 3298–3309 (2018).
33. Porcarelli L. *et al.*, Single-ion block copoly(ionic liquid)s as electrolytes for all-solid state lithium batteries, *ACS Appl. Mater. Interfaces*, 8, 10350–10359 (2016).
34. Bouchet R. *et al.*, Single-ion BAB triblock copolymers as highly efficient electrolytes for lithium-metal batteries, *Nat. Mater.*, 12, 452–457 (2013).
35. Cameron W., Tanner K. F., The effect of porous composite electrode structure on solid oxide fuel cell performance, *J. Electrochem. Soc.*, 144, 21–30 (1997).
36. Oh H. *et al.*, Poly(arylene ether)-based single-ion conductors for lithium-ion batteries, *Chem. Mater.*, 28, 188–196 (2016).
37. Inceoglu S. *et al.*, Morphology-conductivity relationship of single-ion-conducting block copolymer electrolytes for lithium batteries, *ACS Macro Lett.*, 3, 510–514 (2014).



Chapter 4

Impact of alkali cations on conductive
behavior of polymer electrolytes



Abstract

In this chapter, the single-ion polymers, which were successfully performed in the Li-metal batteries in chapter 3, were exchanged into different alkali cations, including Na⁺, K⁺ and Cs⁺. Two types of SIPE i.e. ionomer I₁₀₀₀ p-SO₃-db with the cross-linked I₁₀₀₀ p-SO₃-cr, and block copolymer Co₁₀₀₀ p-SO₃ based on different alkali metals are investigated. The advantage of these materials relates to the nearly unity cationic transference number that can suppress or limit the anion mobility, and allows to reach the transport properties of the cations. The thermal stability and phase transition behaviors of these electrolytes were determined by TGA and DSC measurements. The conductivity was carried out in the Swagelok cell, using EIS method, in the range of temperatures from 20 to 90 °C. The evolution of conductivity for these SICPs as a function of cation nature are discussed and compared to get better understanding about the impact of cation on transport properties in the solid state.

1. Introduction

The growing demand of renewable energy sources has been dominated by the Li-ion batteries in a large scale of applications e.g. mobile devices, electric vehicles, etc. However, the rising of lithium costs, and a limit of raw material resource will enhance the advancement of new technologies based on the abundant elements, including the alkaline metals. Moreover, the use of polymer-based electrolytes for safer rechargeable lithium-metal batteries has been gained more success these recent years. The all-solid-state devices based on alkali elements are requiring a step forward, especially for electrolyte materials. The use of poly(ethylene oxide) – PEO, as polymer host for dissolving alkali salts, is suggested as a promising solution for these future batteries.

Since the first discovery by Wright and co-workers¹ in 1973, the complexes of alkali metals with PEO gained much attention due to their electrical conductivities. Later, a number of studies in this field have been reported by different researched groups.²⁻⁴ Nevertheless, the first commercial of Li-ion batteries in 1991 restrained the advancement of other alkali-based electrolytes. Back to the previous studies, Besner et al.⁴ investigated the influence of anion polarization (CF_3SO_3^- , SCN^- , ClO_4^-) on ionic conductivity of the complexes PEO/alkali salts. They proved that not only ion pairing, but also ion-dipole interaction, and anion polarization contributed to ionic conductivity in the concentrated PEO electrolytes. Although many efforts, the conduction process and the effect of cation size on transport properties in PEO matrix were still unclear. The work of M. Perrier et al.³ demonstrated the alkali-polymer interaction in the blends of PEO and the alkali-based TFSI or SCN salts, and affirmed that the ionic conductivity was influenced by not only the cation size, but also by the other non-negligible factors including the short-range interactions with anions, anion nature, etc.

As mentioned previously in the literature review, ionic conductivity in polymer essentially occurs in the amorphous phase (above the melting of polymer), which limits the important applications at high temperature. The issues related to the use of conventional blend polymers, where an inorganic salt dissolved in the polymer host, as solid electrolytes prevent the development lithium metal batteries, hence the post lithium storage devices. Therefore, the single-ion polymers can overcome these drawbacks, and are required as the most effective solution for all-solid-state batteries (as also proved in the chapter 3). The anion polarization, whatever is SO_3^- or TFSI, exhibits a negligible effect on conductive process of SIPEs due to the grafting of anionic functions on the PEO chain. This advantage minimizes the effect of anion mobility, and provides better understanding of cation transport in the polymer matrix.

In this work, the cross-linked ionomer I_{1000} p- SO_3 , and the block copolymer CO_{1000} p- SO_3 exchanged into different alkaline cations including Na^+ , K^+ , and Cs^+ were prepared and characterized. These resulted alkali-based SIPEs were compared to the lithiated electrolytes (presented in chapter 3) in

terms of thermal and cationic conductive properties. This study will mainly focus on the effect of cation size on the cationic conductive process.

2. Cross-linked ionomer I₁₀₀₀ p-SO₃

The schematics in Fig. 1 illustrates different complexes of the alkali cations in the blend with PEO and in the single-ion matrix. The conductivity of cation in both cases depends on the nature of cation, its size, and the flexibility of polymer chain. However, for the blend of PEO/salt (Fig. 1A), the ionic conductive process is provided by the solvation/desolvation of alkali cations by the PEO ether oxygens (the cation jumps within the cages formed by PEO chain)⁵, and this process is strongly affected by the polarization of free anions, and their mobility. Meanwhile, when the anionic functions are fixed on the polymer chain (Fig. 1B), the SIPEs have the anion mobility approaches to zero, and resulting in a unity cationic transference number. This single-ion structure allows to reach the information of cation transport, and the effect of cation size on the conductivity behavior in polymer.

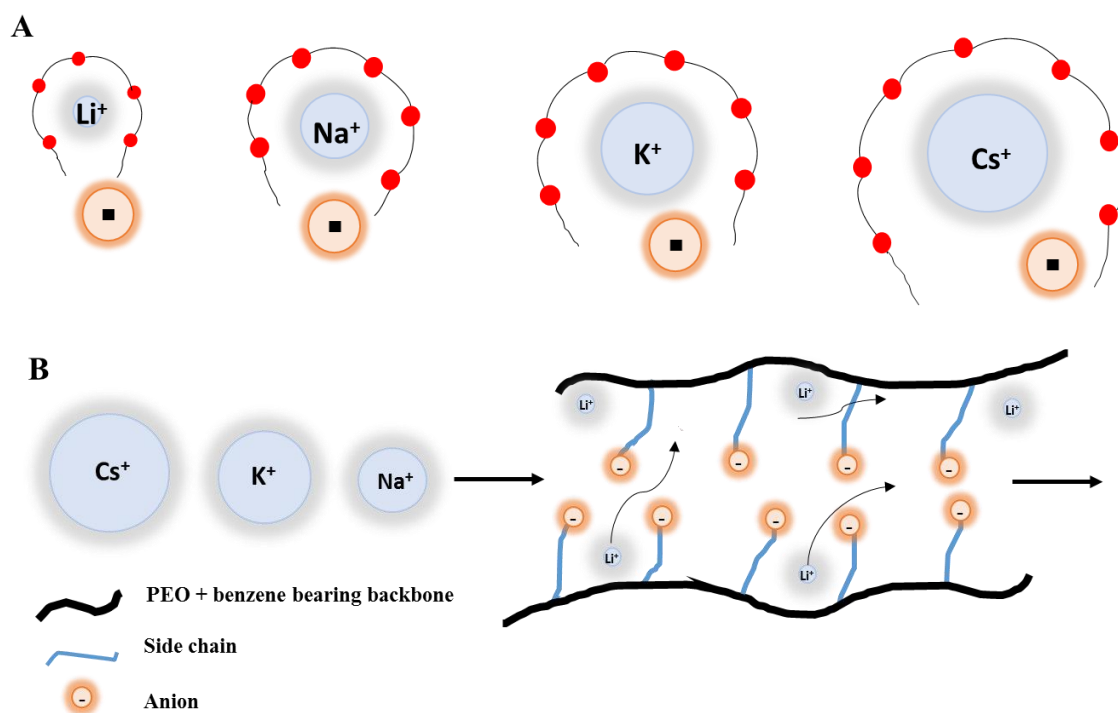


Fig. 1 (A) schema illustrates the solvated alkali cations by the EO units in the PEO/salt blends, and (B) the cation transport mechanism in SIPE.

The ionomer used for this work is the I₁₀₀₀ p-SO₃-db (presented previously in chapter 3) which showed excellent performances in the Li-metal batteries. The alkali-based ionomers were prepared by exchanging the initial cation into a unique form of Na⁺, K⁺, or Cs⁺, following the same experimental process as for the lithiated ionomer. The yield of ion exchange reaction determined by AAS, and the alkali contents in the exchanged ionomers are presented in Table 1. The concentration

of Cs element was not measurable due to the missing of Cs lamp equipment. Meanwhile, the ionomer after synthesis contains only the Na⁺, and (or) K⁺ ions relating to the use of NaH and the initial form of ionic monomers. So that, the negligible concentrations of these ions help to interpret the high yield of Cs⁺ exchange reaction. The results in Table 1 affirm high concentration of the interested cations, with more than 96 % for the exchanged ionomers indicating the successful processes.

Table 1 Alkali contents in the I₁₀₀₀ p-SO₃-db – M form, where M is the alkali metals, determined by AAS.

I ₁₀₀₀ p-SO ₃ -db	% Li	% Na	% K
Li form	96.0	1.6	2.3
Na form	-	99.1	0.8
K form	-	0.6	98.5
Cs form	-	1.8	0.4

These resulting ionomers were reinforced with 6 wt.% of NCC, and casted into membrane. These membranes were then cross-linked in the presence of a photoinitiator (Irgacure 2959). The films are dried under vacuum for 48 h at 80 °C, then moved to a glove box. In the following study, the cross-linked ionomers can be also called Iono-M, where M represents to the alkali ions.

2.1. Thermal properties

The phase transitions of ionomers, and the cross-linked films measured by DSC following two identical heating/cooling cycles, from -100 °C to 150 °C, under N₂ flux, with a scan rate of 10 °C/min, and only the second heating thermograms are presented in this work. The sample was placed in the aluminum crucible for DSC in a glove box to avoid the contamination of humidity. The thermograms in Fig. 2 for the non-crosslinked ionomers show only one T_g at about -40 °C, indicating the completely amorphous state of these materials. This behavior was reported previously for the Li-ionomer in chapter 3. The T_g values are negligible influenced by the cation nature e.g. -40 ± 2 °C for Li, -39 ± 2 °C for Na, -43 ± 2 °C for K, and -45 ± 2 °C for Cs form. Increasing the cation size from Li to Cs inducts a slightly decrease of T_g values.

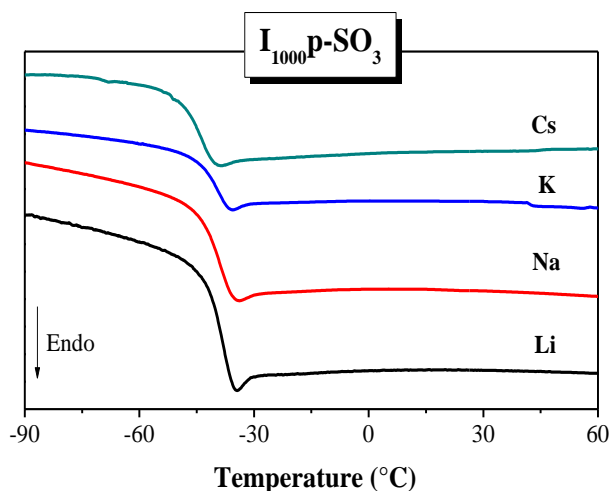


Fig. 2 DSC thermograms of the Iono-M (*M* is the alkali ions) from -90 to 60 °C.

By cross-linking these ionomers, the T_g values exhibit a remarkable change comparing to the non-crosslinked polymer, and as a function of cation size, see Fig. 3. From the first impression, all of the cross-linked ionomers possess higher T_g relating to the decrease of chain mobility. Moreover, the increase of T_g evolves with the cation size form Li to Cs. The cross-linked ionomers exhibit the T_g values of $-37 \pm 2^\circ\text{C}$ for Li, $-33 \pm 2^\circ\text{C}$ for Na, $-34 \pm 2^\circ\text{C}$ for K, and remarkably shifts to $-20 \pm 2^\circ\text{C}$ for the Cs-based ionomer. From small to intermediate alkali cation size (Li, Na, K), the T_g of cross-linked ionomers increases about 3 to 9 °C as compared to the non-crosslinked ones, which mainly relates to the degree of crosslinking, and the effect of cation size on T_g is less announced. This behavior allows to suppose that higher the cation, higher the crosslinking degree of the alkali-based ionomers.

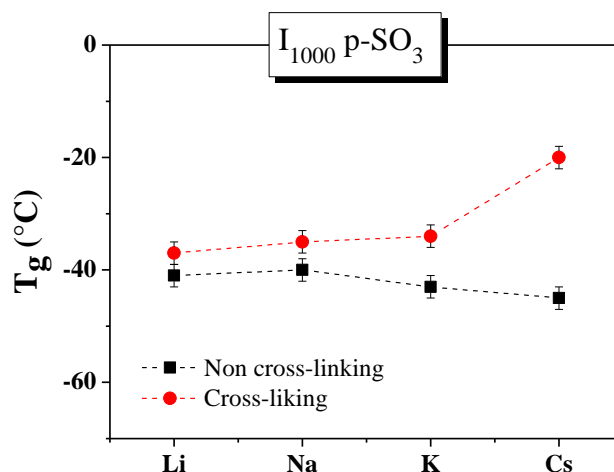


Fig. 3 T_g values of the cross-linked (red) and non cross-linked (black) Iono-M (with *M* is the alkali ions).

Concerning the remarkable change of T_g for Iono-Cs after cross-linking, the hypotheses are suggested, such as (i) the big Cs^+ size favors a high cross-linking degree, hence a strong decrease of

T_g , or (2) the addition of impurities during cation exchange reaction. To further verify these suggestions, the thermal stability of these ionomers were investigated by TGA measurements.

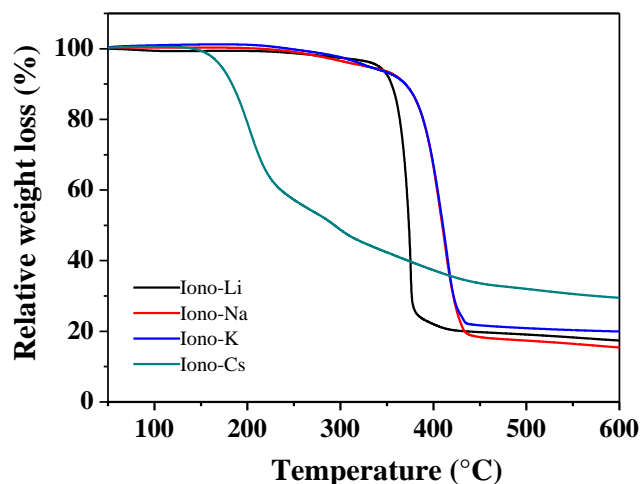


Fig. 4 TGA thermograms from 50 to 600 °C for the Iono-M (M is the alkali ions), under N_2 flux, and 10 °C/min as scan rate.

The TGA thermograms of ionomers possessed the alkali metals performed from 50 to 600 °C, under a N_2 flux, with a scan rate of 10 °C/min, are presented in Fig. 3. All of the samples, except for Iono-Cs, are thermally stable up to 300 °C, and exhibit a shape weight loss corresponding to the relative mass of PEO chain (as discussed in chapter 3). The degradation temperature (T_d) values are: 341 ± 2 °C for Li, and about 328 ± 2 °C for Na and K-based ionomers, which was determined at 5 % of weight loss for all samples.

A suddenly drop of T_d value is observed for the Iono-Cs i.e. 170 ± 2 °C which is about 160 °C lower than other alkali-based ionomers. One of the hypotheses relates to the presence of H^+ in Cs-ionomer. We believe that during the ion exchange, the used Amberlite Cs-form was prepared by mixing the resin H-form with cesium hydroxide in aqueous solution, and the big Cs^+ may inhibit partially this reaction resulting in a remaining H^+ on the surface of Amberlite particles. The cations of ionomer (Na or K form) may exchange to the remaining H^+ on the chromatography column contained the resulted Cs-Amberlite. Although the pH of the output solution (ionomer + solvents) from the column was neutral, we strongly believe that the remaining acid traces can initiate the PEO degradation. Noted that an ether in presence of acid, or a superacid in our case, is not thermally stable. Increasing the temperature higher than 150°C induces the PEO chain breaking, and ionomer weight loss.

In conclusion, these alkali-ionomers are completely amorphous and exhibit only one T_g as observed for the Li-based ionomer in the chapter 3. The cation has certain impacts on the glass transition, and thermal stabilization of ionomer. Increasing the alkali size from Li to K slightly decreases the T_g values relating to higher chain mobility. The alkali-ionomers, except for the Cs one, exhibit high thermal stability over 300 °C which is an advantage of high security electrolytes.

2.2. Conductivity

Conductivities of the cross-linked membranes were investigated as a function of cation. These cross-linked films were sandwiched between two stainless-steel (SS) electrodes of the Swagelok cell, in the glove box, to prevent the contamination of humidity. The measures performed with a heating/cooling cycles from RT to 90 °C, using the EIS method, and only the data from the cooling scan are presented as a function of $1000/T$ in Fig. 4.

The conductivity measured for the cross-linked films represents for the cationic mobility thanks to the single-ion nature of ionomer, as proved in the chapter 3. Conductivity decreases with increasing the cation size from Li to Cs. This behavior cannot be explain only by the increase of T_g due to the negligible changes of T_g values for the small to intermediate alkali cations (Li, Na, and K), and a very high T_g for the Cs-based ionomer. However, a general trend of conductivity data can be assumed such as bigger the cation, lower the measured conductivity.

The difference in conductivity is more considerable at low temperature, and reduces while increasing temperature. At 90 °C, conductivity is $3.4 \times 10^{-5} \text{ S.cm}^{-1}$ for the Li-based ionomer, then decreases to $3.0 \times 10^{-5} \text{ S.cm}^{-1}$ for Na, $2.6 \times 10^{-5} \text{ S.cm}^{-1}$ for K, and end up at $2.0 \times 10^{-5} \text{ S.cm}^{-1}$ for Cs. The representation of conductivity as a function of cation radius give a linear dependency at 90 °C, thus higher the cation radius, lower the ionic conductivity. At low temperature, the sodium and Li-based ionomers have the close conductivities. High cation conductivity (superior to $10^{-5} \text{ S.cm}^{-1}$ at 90 °C) of these materials make them become the interested solid electrolytes for future rechargeable batteries.

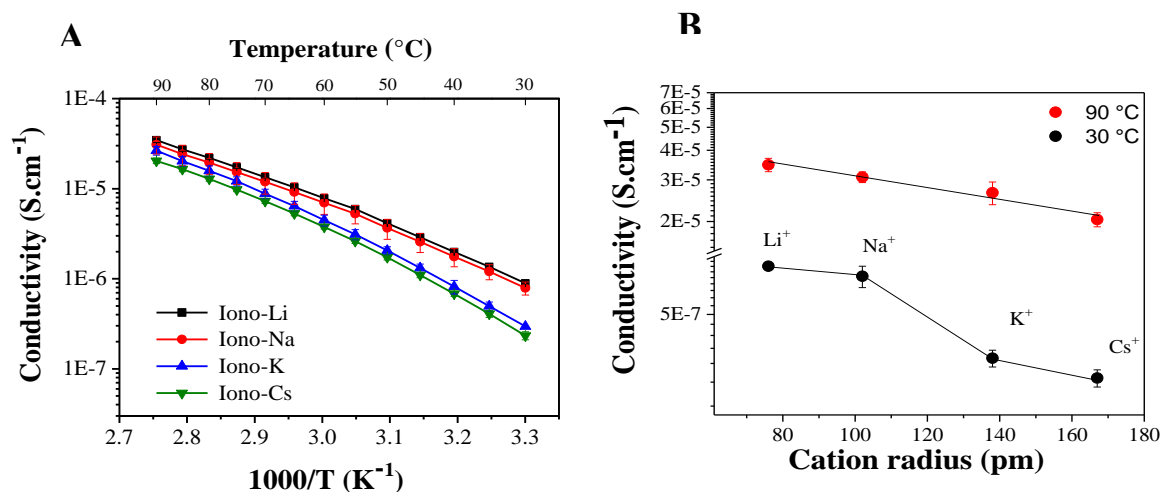


Fig. 5 Conductivity of Iono-M (with M is the alkali ions) (A) as a function of $1000/T$ and (B) at 30 and 90 °C as a function of cation radius.

Moreover, conductivity values increase with increasing the temperature up to 90 °C, following a VTF model for solid polymer electrolyte (equation 1):⁶

$$\sigma = \frac{\sigma_0}{\sqrt{T}} * \exp[-E_a/k(T - T_0)] \quad (1)$$

where σ_0 is a pre-exponential factor, E_a is the pseudo-activation energy and k is the Boltzmann constant. The T_0 is the reference temperature, and is determined as $T_g - 50$, with the T_g determined by DSC measurements. The E_a is an important factor that represents the polymer segmental motion, and links to the ionic mobility⁷. The calculated E_a values for ionomer's conductivity are presented as a function of cation nature in Fig. 6. As seen, all of the cross-linked films show the close energy activation of about 0.11 to 0.13 eV indicating the negligible impact of cation size on the chain mobility activation, hence the difference in conductivity is mostly linked to the effect of cation size.

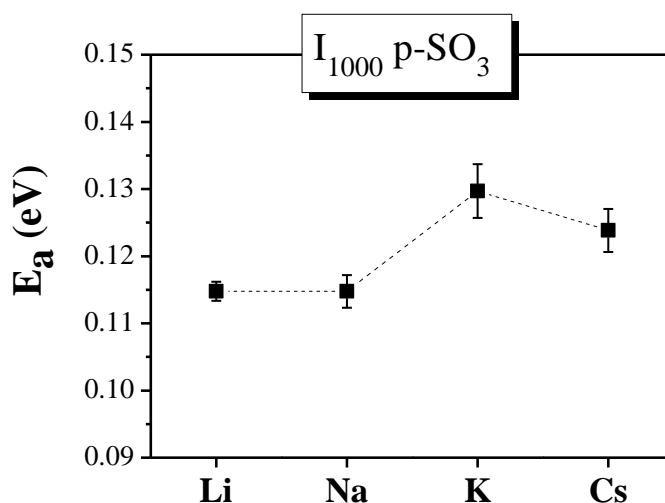


Fig. 6 Energy activation, E_a , values of the Iono-M calculated from the VTF's fitting.

To better understand the ion transport in these ionomers, the blends of high molecular weight PEO (MW 300 kg/mol) and the alkali-based trifluoromethanesulfonate (alkali triflate) salts, denoted as MTf (where M is Li, Na, and K), at the same EO/M of 23 were performed. The CsTf salt is not commercial, and is not easy to synthesize with high purity, so the study was conducted with only three cations. The mixture polymer/salt were dissolved in acetonitrile, and casted into membrane. These obtained films were dried under the reduced vacuum for 48 h, then moved into a glove box. The PTFE gasket with a definite thickness was used to prevent the flowing of polymer at high temperature (above 60 °C). Conductivity of these blends was performed using the same conditions for ionomer, and the data plotted with $1000/T$ are presented in Fig. 7.

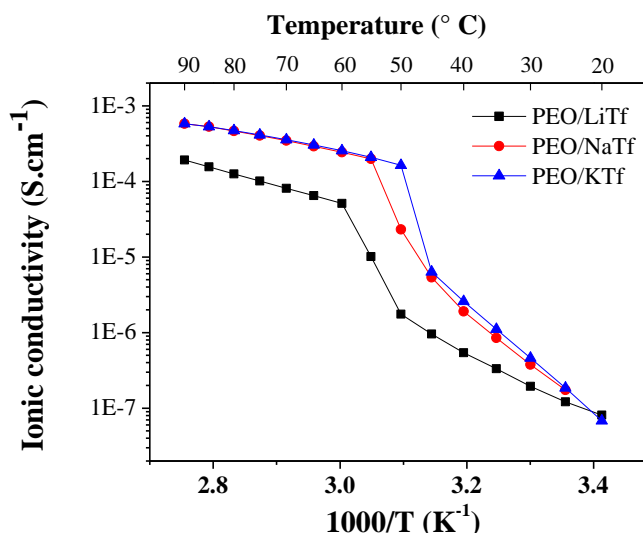


Fig. 7 Conductivity of the blends PEO/MTf (*M* is alkali ion) at EO/*M* of 23 as a function of 1000/*T*.

As seen, conductivity of these blends exhibits two distinct region corresponding to the amorphous (high temperature) and the crystalline phase (low temperature) of polymer. The drop in conductivity at around 60 °C for all curves in Fig.7 relates to the crystallization of polymer, and this temperature shifts with the cation size from Li to K. Conductivity of these blends in the amorphous state (same phase behavior with the ionomer) significantly increases with the increase of cation size form Li to Na, then is constant for Na and K. Similar conductive behavior was observed by Rietman et al.⁶ in 1987. Conductivity of the bigger alkali cations e.g. Rb⁺ and Cs⁺ complexed in PEO matrix was even higher (see Fig. 8). In brief, the study on the blends PEO/ MTf agrees with the study of Rietman et al., and both show an opposite behavior as compared with the ionomers, i.e. the conductivity increase with the size of cation.

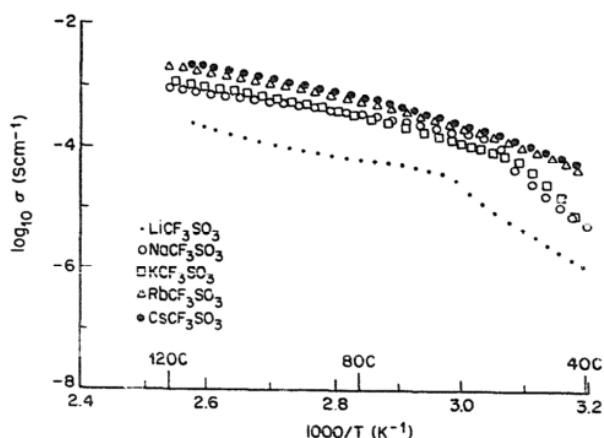


Fig. 8 Arrhenius plots of $\log \sigma$ versus $1000/T$ for the blend PEO/MCF₃SO₃ (or MTf) with *M* is the alkali ions.⁶

The conductive process of the complexes alkali-PEO were also studied by Besner et al.⁴ on two different anions i.e. Tf and SCN⁻. This work proved that, ionic conductivity of the blends polymer/salt was depended on the number of EO units complexed with one cation, and the *T_g* value.

By scaling $\log(\sigma/\text{CN})$ versus $1/(T-T_0)$, where CN is the coordination number corresponded to the cation surface i.e. 1 for Li^+ , 2 for Na^+ , 3 for K^+ , 5 for Rb^+ , 7 for Cs^+ , and T_0 is $T_g - 25$, conductivity of each series, contained a common anion, exhibited the single master curve, see Fig. 9. This behavior inducted that conductive properties of cation in polymer matrix were dominated by the coordination number, chain mobility, anion nature, and the CN value increased proportionally to the cation surface from Li to Cs. The anion polarization may contribute to the correlation of conductivity and cation charge density.

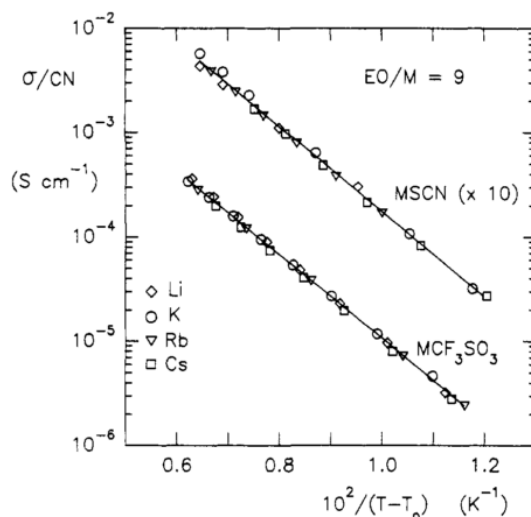


Fig. 9 The $\log(\sigma/\text{CN})$ versus $1/(T-T_0)$ plots for two series of PEO with MCF_3SO_3 and MSCN , where M is the alkali ions. CN is the coordination number corresponds to the cation nature and $T_0 = T_g - 25$.⁴

Based on the obtained results for the blends PEO/MTf (EO/M of 23), and those reported in the literature, the cation transport in high molecular weight PEO has a strong effect of the solvation/desolvation processes of cation by the polymer chain, and the polarization of anion.

Back to the cross-linked ionomers, the single-ion nature allows to reach the cation conductivity without any effect of polymer chain and anion nature. The difference in conductivity obtained for these films reflects only cation mobility inside the amorphous polymer matrix. The evolution of ionomer conductivity, up to 90 °C, proportionally decreases with the alkali size from Li to Cs. However, these membranes require a complicated preparation process, including the reinforcing of nanofillers and the cross-linking reaction under UV irradiation, which may add the uncertainty on the reproducibility of membrane casting. As an effective solution, the alkali-based multi-block copolymers are expected to overcome these issues, and further affirm the conductive process of alkali cations in single-ion polymer matrix.

3. Multi-block copolymer

The multi-block copolymer used for this study is a $Co_{1000}p-SO_3$ which was successfully performed as solid electrolyte for lithium batteries in chapter 3. This structure combines an ionic block $I_{1000}p-SO_3$ and a rigid FPES block to maintain the mechanical properties. A schematic structure of copolymer is presented in Fig. 10. The cations were exchanged into different interested alkali ions i.e. Li^+ , Na^+ , K^+ , Cs^+ by mixing the bulk of polymer in the aqueous solution of MCl (M is the alkali cations), then neutralizing with distilled water. The detailed protocol for ionic exchange is presented in the experimental part.

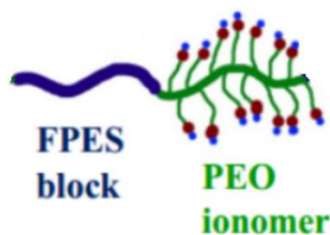


Fig. 10 The network of multi-block copolymer $Co_{1000}p-SO_3$.

To determinate the ion exchange yield, an amount of dried polymer was degraded in the extra-pure acid HNO_3 (65 %) at 60 °C for 24 h. The solution was filtrated to remove the insoluble part including the FPES block. The liquid phase contained the interested cation was diluted with distilled water and the concentration of alkali elements in polymer was measured by ASS. The ration of each element's concentration in the solution contained 5 ppm of cation (an approximate concentration calculated from the molecular weight of copolymer) is presented in Table 2.

Table 2 Ion exchange properties of the $Co_{1000}p-SO_3-M$ (M is the alkali ions) determined by AAS.

$Co_{1000}p-SO_3$	% Li	% Na	% K
Li form	100	-	-
Na form	-	95	5
K form	-	-	100
Cs form	-	2	-

An excellent yield of ion exchange reaction for the alkali-based copolymers (above 95 %) proves an effective ion exchange process. For the Cs-based ionomer, a negligible concentration of Na^+ ion (about 2 wt.% in 5 ppm) indicates the highly cation exchange into the Cs^+ ions. The presence of the hydrophobic block in copolymer limit its solubility, and the ion exchange reaction was performed in the aqueous solution. This advantage helps to eliminate the issue of adding the trace of acid, as supposed for the Cs-based cross-linked ionomer.

The resulted copolymers were dissolved in DMSO as solvent, and casted into membranes to assure a homogenous surface. These films with the thickness ranging from 80 to 100 μm were dried under vacuum at 80 $^{\circ}\text{C}$ for 48 h, and stored in a glove box prior use.

3.1. Thermal properties

The T_g value of these copolymers are measured by DSC. The samples were submitted to two heating/cooling cycles, where in the first cycle, sample is cooled down to -100 $^{\circ}\text{C}$ and heated up to 150 $^{\circ}\text{C}$, then in the second one, after decrease the temperature, the sample is heated up again to 250 $^{\circ}\text{C}$. Experiences run with -30 $^{\circ}\text{C}\cdot\text{min}^{-1}$ as cooling rate and 10 $^{\circ}\text{C}\cdot\text{min}^{-1}$ as heating rate, and only the second cycles are presented in Fig. 11. These DSC thermograms show only the glass transition behavior corresponding to the PEO ionic block where the cation transport process is occurred.

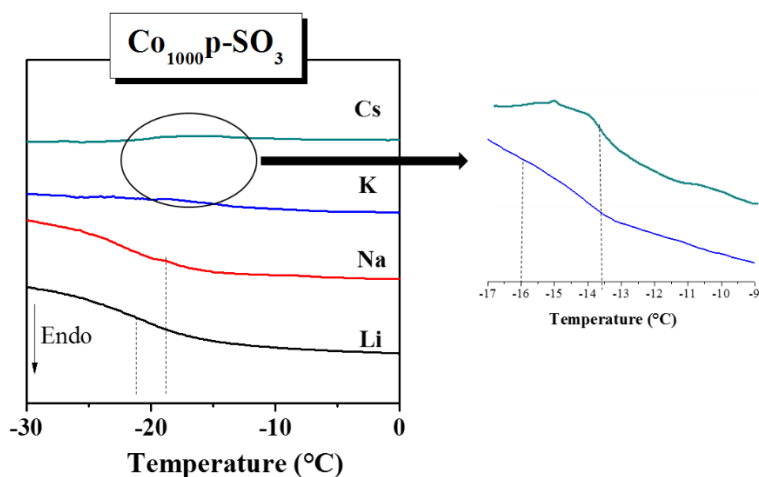


Fig. 11 DSC thermograms for $\text{Co}_{1000}\text{p-SO}_3 - M$, where M is the alkali ions from -60 $^{\circ}\text{C}$ to 60 $^{\circ}\text{C}$.

The alkali-based copolymers are completely amorphous in the large range of studied temperature from -100 $^{\circ}\text{C}$ to 250 $^{\circ}\text{C}$, as reported for the lithiated copolymer in the chapter 3. The evolution of T_g values of the ionic block as a function of cation size is discussed. For the small alkali cations such as Li^+ and Na^+ the shape and clear-cut phase transition are observed (black and red lines in Fig. 11). Meanwhile for the bigger cations, the phase transition is not so clear even at higher scan rate of 20 $^{\circ}\text{C}/\text{min}$. Zoom in the blue and cyan curves, corresponding to the K and Cs-based copolymers, the T_g values increase while increasing the cation size from Li to Cs e.g. -22 \pm 2 $^{\circ}\text{C}$ for Li, -19 \pm 2 $^{\circ}\text{C}$ for Na, -16 \pm 2 $^{\circ}\text{C}$ for K, and about -14 \pm 2 $^{\circ}\text{C}$ for the copolymer Cs form. As compared with the cross-linked ionomers, where T_g was nearly constant for Li, Na, K, and much higher for Cs, for the copolymer a gradual increase of T_g with the size of cation is observed. The increase is linearly proportion to the cation radius, as seen in Fig.12.

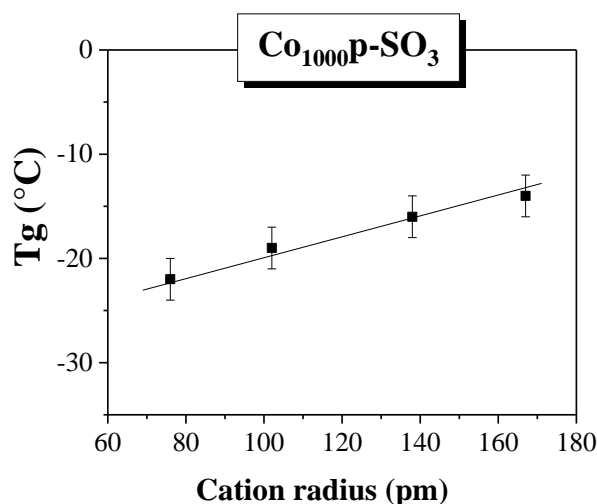


Fig. 12 Evolution of T_g values for $Co_{1000}P-SO_3$ M form, M is the alkali metals, with the cation radius.

All of the alkali-based copolymers exhibit high thermal stabilities above 300 °C as determined by TGA measurements. These analysis of thermal weight loss was performed from 200 to 450 °C, under the N_2 flux with a scan rate of 10 °C/min. The TGA thermograms in Fig. 13 present the relative weight loss of the shape degradation step of copolymer at about 350 °C. This degradation is corresponded to the PEO chain. The degradation of copolymers as a function of cation size varies following the order of Li (343 ± 2 °C), Na (342 ± 2 °C) > K (337 ± 2 °C) > Cs (328 ± 2 °C). The bigger the cation is, the lower the degradation of copolymer observes. But, only about 15 °C different in T_d values are observed for these electrolytes indicating the low cation effect. Moreover, the issues related to the low thermal stability of the Cs-based ionomer (in 2.1.) is non-obvious for the case of $Co_{1000}p-SO_3$ -Cs affirming the hypothesis of having traced of H^+ in ionomer.

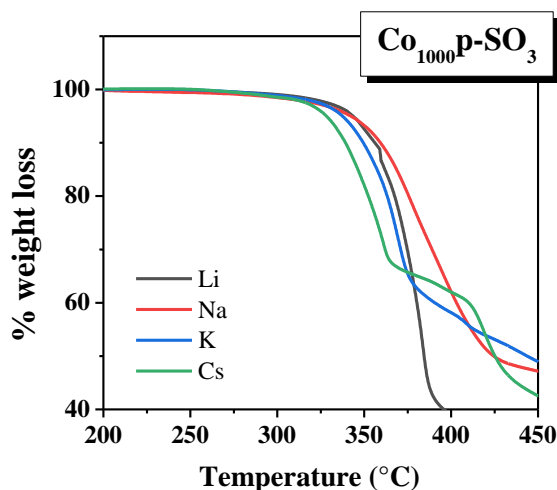


Fig. 13 Thermograms for the $Co_{1000}p-SO_3 - M$, where M is the alkali ions, from 200°C to 450 °C.

In conclusion, the alkali-based $Co_{1000}p-SO_3$ are completely amorphous in the large range of temperature, and the change of their T_g values increase with the cation size. These materials also

possess high thermal stability over 300 °C which is promising for the safe electrolytes. The presence of a hydrophobic block in the copolymer structure prevent the solubility of material in water which helps to overcome the issues relating to the ion exchange process and facilitate the film casting. Thanks to the single-ion nature with a unity transference number, as proved for the Li-based copolymer in the chapter 3, the cation conductivity of these alkali copolymers was investigated in the following part.

3.2. Conductivity

Conductivity data of these alkali-block copolymers plotted with $1000/T$ is presented in Fig. 14. The obtained values are about one order of magnitude lower than those of cross-linked ionomers due to the presence of about 30 wt.% of non-conductive FPES block in copolymer. Obviously, the effect of cation size on the conductivity is clearer for these copolymer relating to the separated data curves in Fig. 13. Conductivity decreases with increasing the cation size from Li to Cs and the difference in conductivity becomes more important at low temperature. The highest conductivity obtained is 3.1×10^{-6} S.cm⁻¹ for Li, 2.5×10^{-6} S.cm⁻¹ for Na, 2.2×10^{-6} S.cm⁻¹ for K, and 1.8×10^{-6} S.cm⁻¹ for Cs-based copolymer, at 90 °C. Clearly, bigger the cation is, lower its mobility in polymer matrix is observed. The electrolytes has an encouraging cationic conductivity, above 10^{-6} S.cm⁻¹ at 90 °C, and can be improved by increasing the ionic chain or adding plasticizers. These materials are promising electrolytes for future rechargeable battery based on the alkali metals.

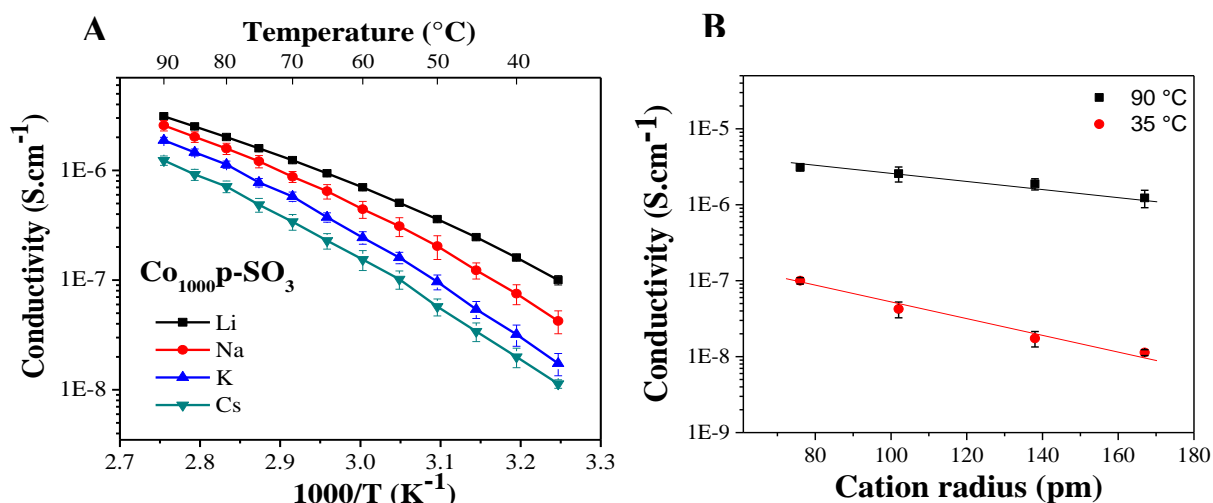


Fig. 14 Conductivity of $Co_{1000}p-SO_3-M$ (with M is the alkali ions) versus $1000/T$.

Conductivity data were also plotted with the scale $T = T_g + X$, where X is the constant, to eliminate the effect of chain mobility, see Fig. 15. The cationic conductivity for these materials is inversely proportional to the cation size e.g. bigger the cation is, lower the conductivity measured. This graph also proves that, although scaling the data with $T_g + X$, the size of cation has an important effect on

its mobility. This phenomenon induces an advantage for further investigating the mechanism of cation conduction using this single-ion copolymer.

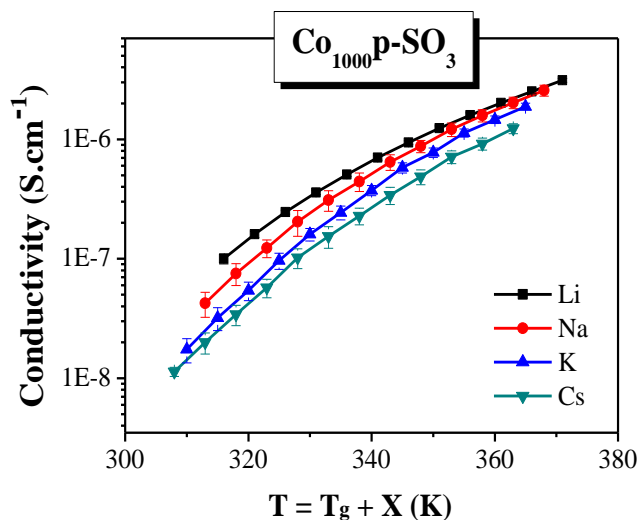


Fig. 15 Conductivity of the $Co_{1000}p-SO_3-M$ (with M is the alkali ions) versus $T_g + X$.

The conductivity data were also fitted with a VTF equation for polymer, and the calculated E_a values are presented with the cation nature in Fig.14. The lowest E_a value is for the Li-based copolymer at 0.093 eV, then increases while increasing the cation size up to Cs. The energy activation associated with the ionic mobility is linked to the alkali radius. Clearly that higher conductivity exhibits the lower E_a value.

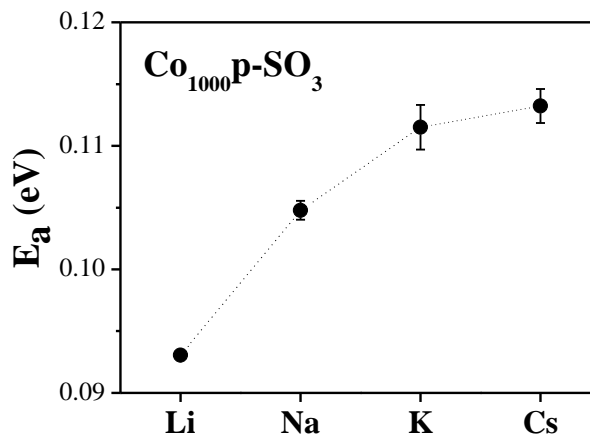


Fig. 16 Energy activation, E_a , values of the $Co_{1000}p-SO_3-M$ calculated from the VTF's fitting.

As compared to the alkali-based ionomers, the effect of cation size on the conductive process is clearer, indicating the significant decrease of ionic mobility with the cation size from Li to Cs. Also from this work, eliminating the impact factors that can influence on the transport properties i.e. anion mobility, anion polarization, cross-linking density, dispersion of nanofillers, etc. helps to get a better understanding of conductivity of cation in the solid state.

4. Conclusion

This chapter presents for the first time the transport properties of alkali cations i.e. Li^+ , Na^+ , K^+ , Cs^+ and the effect of cation size on thermal/conductive properties of polymer-based electrolytes. The study involves two types of single-ion polymers including the cross-linked ionomer I_{1000} p- SO_3 , and the block copolymer Co_{1000} p- SO_3 , which were successfully performed in the lithium metal batteries. These materials are completely amorphous which is favorable for the ion transport, and high thermal stability above 300 °C. Their sufficient cationic conductivity makes them become high interest for future rechargeable devices based on the abundant elements.

Conductive properties of alkali cations in these single-ion polymer matrix was investigated by EIS method in a large range of temperatures up to 90 °C. The advantage of grafting anionic functions on the polymer chain helps to investigate the cation transport properties without the effect of anion, and PEO chain mobility, as observed for the blends PEO/salt. The results inducted the unclear impact of cation size on conductive behavior of ionomers, which is mainly caused by the impact factors i.e. the cross-linking, and the complicated ion exchange process.

The presence of the rigid block in copolymer structure helps to maintain good mechanical properties, and facilitates the ion exchange/ film casting processes that can influence on the transport behavior of cation. The increase of T_g values, which is inversely proportional to the evolution of conductivity with cation size for these alkali-based copolymers, was observed. These results give a better understanding of cation transport in the promising polymer electrolytes.

For the further applications in a battery, these electrolytes require the advancements of electrode materials based on the alkali-metals.

References

1. Fenton D. E., Parker J. M., Wright, P. V., Complexes of alkali metal ions with poly(ethylene oxide), *Polymer*, 14, 589 (1973).
2. Parker J. M., Wright, P. V., Lee C. C., A double helical model for some alkali metal ion-poly(ethylene oxide) complexes, *Polymer*, 22, 1305–1307 (1981).
3. Perrier M., Besner S., Paquette C., Vall A. E., Lascaud S., Mixed-alkali effect and short-range interactions in amorphous poly (ethylene oxide) electrolytes, *Electrochimica acta*, 40, 2123–2129 (1995).
4. Besner S., Vallée A., Bouchard G., Effect of anion polarization on conductivity behavior of poly(ethylene oxide) complexed with alkali salts, *Macromolecules*, 25, 6480–6488 (1992).
5. Do C. *et al.*, Li⁺ transport in poly(ethylene oxide) based electrolytes: Neutron scattering, dielectric spectroscopy, and molecular dynamics simulations, *Phys. Rev. Lett.*, 111, 1–5 (2013).
6. Rietman E. A., Kaplan M. L., Cava R. J., Alkali metal ion-poly (ethylene oxide) complexes. Effect of cation on conductivity, *Solid State Ionics*, 25, 41–44 (1987).
7. Bandara T. M. W. J. *et al.*, Effect of the alkaline cation size on the conductivity in gel polymer electrolytes and their influence on photo electrochemical solar cells, *Phys. Chem. Chem. Phys.*, 18, 10873–10881 (2016).

Conclusions and perspectives

Conclusions

This thesis focused on (i) the advancement of high-security electrolyte materials based on the ionic liquids, and the conducting polymers, for safer and performance lithium battery, and (ii) the development of alkali/alkaline-earth based electrolytes for future technologies beyond lithium. This manuscript contains four chapters dealing with a literature review (chapter 1), the ionic liquid-based electrolytes (chapter 2), new single-ion conducting polymer-based electrolytes for Li-metal batteries (chapter 3), new single-ion conducting alkali-based polymer electrolytes for future rechargeable batteries (chapter 4), and an experimental annex.

The study of the ionic liquid-based electrolytes involves (i) the solubility of different TFSI salts in a common IL i.e. BMIm TFSI; the impact of (ii) cation concentration for two binary systems e.g. IL/LiTFSI and IL/CsTFSI, and (iii) cation nature for the alkali/alkaline-earth based ILs on the physical and ionic transport properties of these blends, by using a multi-technical approach. The TFSI salts exhibit a large solubility in IL, which depends on the choice of cations. The presence of alkali/alkaline-earth cations in IL leads to a significant increase of viscosity, and a consequent decrease of both ionic conductivity and diffusivity. The decrease of self-diffusion coefficients is larger for TFSI than BMIm⁺, and the alkali cations (only measurable for Li⁺ and Cs⁺) are the slowest component despite their smallest sizes, which relates to the strong complexation of alkali cation by the TFSI anions. This behavior is more visible while decreasing the size of coordinated cation, and (or) increasing the salt concentration. The dissociation degree increases with the presence of salt, as compared to the neat IL, and the cationic transference number proportionally increases with the cation concentration. Furthermore, adding the TFSI salt in IL inhibits the crystallization behavior of the neat IL, and T_g value of the blends IL/salt is strongly depended on the concentration, and the nature of coordinated cations e.g. larger effect was observed for the smaller ions, and by increasing the salt content in IL. The relation between viscosity and molar conductivity of the blends IL/salt, whatever is the composition, with temperature leads to (i) a master curve of Walden plots indicating rather similar ionicity, (ii) a master curve of conductivity data with the ratio T_g/T meaning similar fragility. These IL-based electrolytes are promising for advancing the storage devices based on alkali/alkaline-earth metals.

The design and syntheses of the single-ion polymers based on PEO and the highly delocalized charge anions i.e. perfluorosulfonate or perfluorosulfonylimide, were presented in chapter 3. These amorphous polymers are thermally stable over 300 °C, which is promising for high-security devices. By cross-linking and reinforcing with nanofillers, the ionomer membranes exhibit good electrochemical behaviors versus lithium. The tests in a symmetric Li-metal cell confirmed excellent reversibility of

Li plating/stripping and a nearly unity transference number of Li^+ for the cross-linked matrixes. The cycling tests in Li-metal batteries, using $\text{I}_{1000\text{p}}\text{-SO}_3\text{-cr}$ as solid electrolyte, and LFP as cathode, demonstrated the excellent performances, which are comparable and even higher than the reported studies in this field.

To enhance the mechanical strength and simplify the elaboration of ionomer films, the single-ion block copolymers combined an ionic $\text{I}_x\text{p-SO}_3$ block and a hydrophobic FPES block were synthesized and characterized. These materials have the ionic functions attached directly to the PEO chain, contrarily to most of the block copolymers reported in the literature, where anions were fixed on the rigid blocks. The copolymers are amorphous, with good mechanical properties, and high thermal stability over $300\text{ }^\circ\text{C}$. The addition of free DMPEG as plasticizer in $\text{Co}_{400\text{p}}\text{-SO}_3$ decreases the T_g of copolymer while keeping the clear phases separation, and resulting in higher conductivity due to a good percolation and high mobility of ionic domains. The single-ion nature of these materials was determined by both electrochemical and PFG-NMR techniques, and the highest conductor samples i.e. the blend $\text{Co}_{400\text{p}}\text{-SO}_3 + \text{DMPEG}$ were performed as solid electrolyte in a lithium metal battery with LFP cathode. The performances of the blend copolymer are comparable with the cross-linked ionomers at low C-rate, while the cell polarization is higher at high C-rates and this is related to the presence of free plasticizer.

The last chapter studied the transport properties of alkali cations i.e. Li^+ , Na^+ , K^+ , Cs^+ , and the effect of cation size on thermal/conductive properties of polymer-based electrolytes. The single-ion polymers i.e. cross-linked ionomer $\text{I}_{1000\text{p}}\text{-SO}_3$, and block copolymer $\text{Co}_{1000\text{p}}\text{-SO}_3$, which were successfully performed in the lithium metal batteries, were used to characterize the cation conductive behavior. These amorphous alkali-based polymers exhibit high thermal stability over $300\text{ }^\circ\text{C}$, and a sufficient cationic conductivities, which are favorable for electrolyte application. Grafting the anions on the polymer chain eliminates the effect of anion mobility, hence promotes the study of cation conductivity. The cationic conductivity behavior in the cross-linked ionomer matrixes as a function of cation size was unclear and this is supposed to be related to the different cross-linking density, and an inefficient ion exchange at high for the Cs cation. Furthermore, the presence of hydrophobic block in copolymer helps to maintain the ionomer insoluble in water and good mechanical strength and thus facilitates the ion exchange and film casting and thus obtain more reproducible results. The T_g of these alkali-based block copolymers as well as the conductivity are inversely proportional to the evolution cation size. By scaling the conductivity data with T_g+X (to minimize the effect of chain mobility) as a function of cation size, the conductivity decrease with increasing the size of cation. These results proved that the diffusion rate of cation is very dependent of its size. To better understand the conduction mechanism, the complexation by the PEO of cations need to be elucidated.

Perspectives

The dynamic molecular simulations for the alkali/alkaline-earth based IL electrolytes, are still in progress. The results obtained from this calculation may help to consolidate the experimental results obtained in chapter 2. These works are provided by Dr. Patrick Judeinstein and his colleagues.

The mechanical strength of the ionomers and block copolymers, which is an important property of polymer electrolytes was not measurable. Indeed, our materials contained a high fraction of PEO that absorbs very quickly humidity from the environment, and resulting in membranes that are difficult to mount in between the clamps of DMA. The DMA will be equipped with movable glove box that will allow to mount the membrane in dried atmosphere.

To enhance the capacity of the Li-metal batteries using SIPEs as electrolyte, the porosity-free LFP cathode is required. The interface electrode/electrolyte can also be penetrated by hot pressing the assembled cathode/solid electrolyte.

The presence of plasticizer affected the performances at high C-rates of the blend copolymer + PEG. The copolymers with the longer ionic block (higher than 10 kg/mol) are suggested for improving the conductivity, in order to assure a better percolation of the ionic domains. Moreover, the cathode consisted of the same ionic composition to the electrolyte is required to limit the migration of plasticizer from electrolyte to the electrode.

The studies of alkali/alkaline-earth batteries using conducting polymer electrolytes are still in the initial state. Although the promising conductivity and thermal stability of our single-ion polymers, for further application need to be more investigated and improved. The usefulness of these materials as solid electrolytes in the battery requires an evolution of electrode materials.

Annex

A. Synthesis part

1. Synthesis process

1.1. Reagents and solvents preparation

In this thesis, most of solvents were used without any purification, except for the 1-methoxy-2-(2-methoxyethoxy)ethane (DGME) and dimethylacetamide (DMAc). These anhydrous solvents were prepared by distillation over calcium hydride (CaH₂) and stored on molecular sieves (3 Å) in a glove box before use. All of the reagents used for polymer synthesis were dried under vacuum at 80 °C for 48 h and stored in a glove box.

1.2. Synthesis of alkali/alkaline-earth based TFSI salts

The M(TFSI)_x salts with (M is the alkali/alkaline-earth metals) were synthesized via an acid-base reaction between hydroxide of metal M and acid bis(trifluoromethylsulfonyl)imide (HTFSI) with a ration of 1:1.1 in aqueous solution, following the equation:



At first, a 0.1 M alkali hydroxide solution in distilled water was prepared by adding 0.05 mol of alkaline hydroxide in 500 mL of water. Then acid HTFSI was added drop by drop in the beaker containing the base solution using a magnetic stirring. A pH of 5 was required for the final solution to avoid the excess of hydroxide. After freeze-drying, the white powder was recrystallized in a mixture of solvents. The solvents used for recrystallization processes are presented in Table 1. A high reaction yield, over 90 %, obtained for the sodium, potassium, calcium, and magnesium based TFSI salts. The two other alkali-TFSI salts i.e. LiTFSI and CsTFSI, purchased from Sigma Aldrich and Solvionic, were used directly without any purification. These salts were dried carefully under vacuum at 200 °C for 72 h, and were stored in the glove box prior to use.

Table 1 The mixture of solvents used for recrystallization process.

TFSI salts	Solvents
NaTFSI	1,2-dichloroethane, ethanol
KTFSI	1,2-dichloroethane
Ca(TFSI) ₂	1,2-dichloroethane, diethylether, ethyl acetate
Mg(TFSI) ₂	1,2-dichloroethane, anisol

1.3. Synthesis of ionomers

1.3.1. Synthesis process

The monomers used in this work such as sodium-5-(3',5'-difluorophenyl)-3-oxoperfluoropentane sulfonate - (**p-SO₃**), sodium-N-(trifluoromethane)-5-(3',5'-difluorophenyl)-3-oxoperfluoropentane sulfonylimide (**p-TFSI**) are provided by ERAS Labo. The ionomers (with and without the double-bonds) was synthesized via the polycondensation reaction. All the materials and chemicals were dried carefully before use to eliminate the presence of water.

For the linear **I_p-SO₃** and **I-pTFSI** ionomers, an amount of PEG was dissolved in 15 mL of DGME and 20 mL of toluene into a tri-neck round bottom flask, under Argon flux. The flask was heated at 150 °C (temperature of the oil bath) to distill the azeotropic mixture (toluene –water) using a Dean-Stark apparatus. After the whole volume of toluene was recovered, the flask was cooled down at 60 °C, and the calculated amount of NaH was added directly in the reaction. Magnetic stirring was used to mix the reaction with a 500 round/minute rate. A changing color from colorless to dark-brown, after about 2 h of stirring indicated the formation of the alcoholate O⁻Na⁺ group at the end chain of PEG. In the next step, the flask was heated to 140 °C (temperature of oil bath) and the monomer p-SO₃ or p-TFSI dissolved in approximate 1 mL DGME was added. The reaction was followed by NMR spectroscopy every 2 h. The disappearance of the aromatic fluorines signal at -108 ppm, observed in the ¹⁹F-NMR spectrum in acetone-d₆ as deuterated solvent, indicated a successful reaction.

For the ionomers on which the double-bonds grafted on the PEO chain e.g. **I_xp-SO₃-db** and **I₁₀₀₀p-TFSI-db**, after the first step of ionomer's backbone formation described above, the flask was cooled down to 70 °C, and a volume of 1,3-dichloro-2-methyl-propene was added by micro-pipette. The reaction was stirred over-night (about 12 h) at 70°C, and the final product was followed by the ¹H-NMR spectrum in acetone-d₆ (the spectrum at the beginning and the end of reaction was discussed in chapter 3).

The quantities of used chemicals were calculated following the Carother's equation in chapter 3 and the amount of chemicals for ionomer syntheses are presented in Table 2. In detail, since the amount of used PEG corresponds to 1 equivalent (eq.), the others reagents' equivalent were calculated as NaH: ~ 3eq.; monomer sulfonate or sulfonylimide: (1-r)eq.; and 1,3-dichloro-2-methylpropene: r eq.

Table 2 Chemicals for synthesis of ionomers.

Ionomer	M_n theory g.mol⁻¹	M_w POE g.mol⁻¹	EO/M ratio	POE (g)	NaH (g)	Monomer (g)	Dichloropropene (μL)
Ip-SO ₃	10 000	1000	23	4.0	0.3	1.54	-
I ₁₀₀₀ p-SO ₃ -db	5000	1000	23	4.0	0.3	1.35	114
I ₆₀₀ p-SO ₃ -db		600	14	4.0	0.5	2.45	138
I ₄₀₀ p-SO ₃ -db		400	9	2.0	0.3	1.90	86
Ip-TFSI	10 000	1000	23	4.0	0.3	1.98	-
I ₁₀₀₀ p-TFSI-db	5000	1000	23	4.0	0.3	1.65	122

1.3.2. Purification process

At the end of the reaction, the flask was cooled down completely to room temperature (RT), and the ionomer was precipitated in a beaker containing 200 mL of n-pentane, using magnetic stirring. After solvent removal, the ionomer precipitated on the bottom of the beaker was rinsed several times with fresh solvent (n-pentane) to remove the excess of reaction's solvents i.e. DGME. To eliminate most of inorganic salt content such as NaF (or KF) formed during the reaction, the product dissolved in approximate 50 mL of acetonitrile, then centrifuged for 3 times x 5 minutes at 5000 rounds/min. The liquid phase after each time of centrifugation was extracted to repeat the step, and the insoluble part containing inorganic salt was removed.

The ionomer was recovered by evaporation of solvent (rotavapor), then was dissolved in deionized water for the next step of purification. A dilute acetic acid solution (about 0.1 M) was used to neutralize the ionomer (pH ~ 7). The solution was filtrated under low pressure (~ 2 bar) using a plastic ultra-filtration cell, with the Millipore ultrafiltration membrane of 3 kDa to remove residual inorganic salts, and low molecular weight polymer (lower than 3000 g/mol). Distilled water passed through the cell during the filtration and magnetic stirring was used to mix the ionomer's solution. Conductivity of the output water, at the end of the purification process, was close to the conductivity of the input water (~2 μS.cm⁻¹). The neat ionomer obtained by freeze-drying at -117 °C under vacuum, and dried at 80 °C for 48 h. A high yield of purification obtains with about 80 % of weight of ionomer was recovered after the filtration.

1.3.3. Ion exchange process

After synthesis, ionomer contains the mixture of Na⁺ and K⁺ as 'free' cations, and needs to be exchanged to M⁺ form (with M is Li, Na, K, Cs, etc.). The ion-exchange resin i.e. Amberlite® IR120 H-form, purchased from Sigma Aldrich with the exchange capacity of 1.8 meq/mL by wet volume,

was used for ionomer's ionic exchange process. The hydroxide of metal M was used to neutralize the amberlite H-form into M-form in aqueous solution.

At first, an amount of amberlite H-form was exchanged into M-form by mixing with a MOH solution. The quantity of MOH needs to be 10 eq. higher than the exchange capacity of amberlite to be sure that all H^+ ions were replaced by M^+ . After 2h of magnetic stirring, the amberlite was carefully poured into the chromatography column topped with cotton. A mixture of solvents contained acetonitrile: water (1:1) was used as the fresh solvent to neutralize the excess of hydroxide, and also for the ion exchange reaction. When the column was neutralized (pH of solvents passed through the column is ~ 7), ionomer dissolved in fresh solvent was slowly added on the top of the column. The fresh solvent was added frequently while opening slightly the tap. As the solvents flowed down, the ionomer K^+ or Na^+ form exchange to M^+ form. The process was repeated four more times to ensure a complete ion exchange. Before finish, the column was washed several times with fresh solvent to recuperate the whole amount of ionomer. The polymer M-form was then recovered by evaporating the solvent using rotavapor. Almost 100 % of ionomer's quantity was obtained after the ion exchange process.

The neat materials were dried carefully under vacuum at 80 °C for 48 h, and the ionic exchange reaction's yield was checked by Atomic Absorption Spectroscopy (AAS).

1.3. Synthesis of copolymer

1.3.1. Synthesis process

a) *Synthesis of FPES block*

The FPES block with desired molecular weight of 5000 g/mol was synthesized by mixing dihydroxy diphenyl sulfone (DPS) (5.37 mmol, 1.35 g) and K_2CO_3 (18 mmol, 2.5 g) in a three-neck flask, equipped with a mechanical stirring. About 20 mL of a mixture of solvents containing DMAc:cyclohexane (1:1) was added into the reaction at RT. The flask was heated to 100 °C, and the azeotropic mixture cyclohexane-water was distilled using a Dean-Stark apparatus. When the whole volume of cyclohexane (about 10 mL) was recovered, and the flask cooled down at 70 °C, then decafluorobiphenyl (DFB) (5.98 mmol, 2.0 g) dissolved in 3 mL of DMAc was added. After 2 h, a slightly yellowish viscous mixture obtained indicating the end of reaction. The NMR spectrum in chloroform- d_3 was checked to confirm the structure of FPES block (NMR spectrum was presented in the chapter 3). The polymer was precipitated in an HCl 1 M solution, under magnetic stirring, and neutralized with distilled water (until pH of the solution ~ 7). The hydrophobic block was dried under vacuum at 80 °C for 24 h and stored in a glove box.

b) *Synthesis of Co_xp-SO_3*

The SO_3 -based copolymers were synthesized with a desired molecular weight of 10 kg/mol for the ionic function Ip- SO_3 block, and 5 kg/mol for the hydrophobic FPES block. The required ratio of the

two blocks was calculated using the Carother's equation. The quantity of reagents for copolymer's synthesis are presented in Table 3.

Table 3 Chemicals for synthesis of multi-block copolymers.

Ionomer	MW_{PEG} g/mol	EO/M ratio	PEG g	NaH g	monomer p-SO₃ (g)	FPES g	DGME: DMAc (mL)
Co ₁₀₀₀ p-SO ₃	1000	23	2.0	0.2	0.8	1.0	10
Co ₄₀₀ p-SO ₃	400	9	2.0	0.6	4.2	1.2	15

For the multi-block copolymer **Co,p-SO₃**, in the first step, the PEG dissolved in the mixture of DGME: DMAc (3:7), and 20 mL of toluene were added in a tri-neck round bottom flask, equipped the magnetic stirring, under Argon flow. The mixture was boiled at 150 °C to distill the azeotropic mixture toluene – water using a Dean-Stark apparatus. When the whole volume of toluene was distilled, the flask cooled down at 60 °C, and NaH was added. A changing color from colorless to dark-brown, after about 2 h of stirring, indicated the formation of the O-Na⁺ groups at the polymer end chain. Next, the temperature was heated to 140 °C and the monomer p-SO₃ dissolved in 1 mL of DGME was added. The disappearance of aromatic fluorines at -108 ppm was checked by ¹⁹F-NMR spectrum in acetone-d₆. When the structure of the ionic block Ip-SO₃ was defined, temperature of reaction was kept at 50 °C, and the FEPS block was added. The mixture was stirred overnight, and the copolymer structure was determined by ¹⁹F-NMR in DMSO- d₆ corresponding to the disappearance of the fluorines of the end chain.

- *Purification*

The mixture of reaction was precipitated in approximate 500 mL distilled water, under magnetic stirring, to precipitate the polymer while eliminating the excess of inorganic salts formed during the reaction. After 12 h swelling in deionized water (water was changed after every 4 h), the copolymer was recuperated by filtration and washed several times with fresh deionized water. The final product was dried under vacuum at 80 °C for 48 h, and stored in a glove box. A yield of reaction about 55 % obtained after purify.

1.3.2. Ion exchange process

The ion exchange was carried out in aqueous solution. At first, 0.2 g of copolymer dissolved in approximately 3 mL of DMSO was casted in an evaporation PTFE Petri dish. Next, solvent was evaporated in an oven at 60 °C overnight. The thin copolymer films immersed in a solution of M(Cl)_n 1M (where M is Li, Na, K, Cs or Mg) during 48 h, under magnetic stirring. The fresh solution was changed every 12 h. Then, water was used to neutralize the copolymer for more than 48 h to extract

the residual excess of salts. The copolymer M-form obtained after drying under vacuum at 80 °C was casted again into membrane and stored in a glove box.

2. Polymer film casting

2.1. PEO/salt film

The salt concentration in PEO determined by the ratio EO/Mⁿ⁺ corresponding to the number of ether oxygen atoms per the number of Mⁿ⁺ ions. The amount of polymer and salt were calculated according to the ratio EO/Mⁿ⁺ following the relation below:

$$\frac{EO}{M^{n+}} = \frac{n_{EO}}{n_{M^{n+}}} = \frac{m_{POE}}{M_{POE}} * \frac{M_{salt}}{m_{salt}}$$

To obtain the polymer films, about 0.2 g of POE and the required amount of salt dissolved in approximately 5 mL of solvent. After about 3 h of stirring, the resulted homogenous mixture was degassed and poured in the PTFE evaporating bowl of 3.5 mm of diameter. Solvent was slowly evaporated in an oven at 40 °C during 24 h. The films were dried under vacuum for 72 h at 40 °C and stored in the glove box under an Argon flux to eliminate the excess of solvent. These polymer films with a range of thickness between 180 µm and 200 µm were used to characterize.

2.2. Cross-linked ionomer film

In a vial, about 0.2 g of ionomer and 8 mg (4 wt. %) of Irgacure® 2959 (1-[4-(2-Hydroxyethoxy)-phenyl]-2-hydroxy-2-methyl-1-propane-1-one) were dissolved in 5 mL acetonitrile. The solution was degassed under reduced vacuum to remove the air bubbles, and poured into the PTFE evaporating Petri dish (d = 3.5 mm). The solution was kept away from light to avoid any decomposition of photoinitiator. After solvent evaporation in an oven at 60 °C, the film was crosslinked under UV irradiation for 1 minute (2 times of 30 second), in an Argon-filled atmosphere. The cross-linked membranes were dried under vacuum at 80 °C for 48 h and stored in a glove box. These films with thickness ranging from 100 µm to 120 µm were used to further investigate.

➤ *Ionomer cross-linked films filled NCC*

The solution of nano crystals cellulose (NCC) dispersed in water was used to reinforce the cross-linked film. An amount of 6 wt% of NCC was added to enhance the film's mechanical properties. About 0.2 g of ionomer with 8 mg of irgacure and ~ 3 mL of a dispersed NCC 4 % in aqueous solution were mixed in approximately 5 mL of solvent. The similar cross-linked process for ionomer film was used, but acetonitrile was replaced by distilled water.

2.3. Dispersion of NCCs in water

In a beaker, 4 g of NCC were solubilized in 100 mL of distilled water. The mixture was subjected to 2 cycles of 10 min under a mechanical stirrer IKA® Ultra-Turrax, at 13 000 revolutions/minute. After, an ultrasonic treatment was performed by dipping a VCX130 ultrasound probe (Sonics & Materials, Inc.) directly in the solution. The pulse of 20 000 J was applied for 3 cycles with 10 minutes/cycle until homogenous. The flask was placed in a cold bath to prevent heating of the dispersion. Concentration of 4 wt.% of the dispersed NCC in water was verified by evaporating a volume of solution in an oven and checking the mass of remained NCC. The NCC solution was kept in a refrigerator.

2.4. Copolymer film

The copolymer films were casted using DMSO as solvent. About 0.2 g of copolymer dissolved in 5 mL of DMSO until homogeneous, then the solution was filtered using 1 µm Teflon syringe-filter. A reduced pressure was used to remove the air bubble. The copolymer solution was poured into a PTFE evaporation Petri dish (d = 3.5 mm) and solvent was evaporated at 60 °C in an oven. The films with the thickness ranging from 100 to 120 µm were dried under vacuum, at 80 °C for 48 h, and stored in a glove box.

3. Ionic liquid/ salts preparation

The 1-Butyl-3-methylimidazolium bis(trifluoromethylsulfonyl)imide, denoted as BMIm TFSI, purchased from [®]Solvionic was used without any additional purification. All of the organic MTFSI salts (with M is the alkali/alkaline-earth metals) such as LiTFSI, NaTFSI, KTFSI, CsTFSI, Ca(TFSI)₂ and Mg(TFSI)₂ were dried under vacuum at 200 °C for 72 h before use. The blends IL/salt were prepared by mixing a unity of volume of BMIm TFSI with an aiming amount of TFSI salt in the glove box. The mixture was stirred at 80 °C until homogenous and cooled down to RT to verify the complete dissolution of salt. The amount of salts adding in IL was calculated following the relation:

$$m_{\text{salt}} = \frac{f * d_{\text{IL}} * V_{\text{IL}}}{M_{\text{IL}}} * M_{\text{salt}}$$

Where f is the ratio of molar of M^{n+} ion and IL, d_{IL} is the density of used IL (1.43 g/mL at 20 °C), V_{IL} is the volume of used IL (1.0 mL), M_{IL} is the molecular weight of IL (419.36 g/mol), and M_{salt} corresponds to the molecular weight of the MTFSI salts.

B Characterization techniques

1. Spectroscopy

1.1. Nuclear magnetic resonance (NMR)

NMR spectroscopy experiments were performed using a Bruker Avance III HD spectrometer at 400.15 MHz for ^1H and 376.52 MHz for ^{19}F spectroscopies. The spectra were treated with a TopSpin 3.2 software and the chemical shift (δ) was presented by the unit of parts per million (ppm). The deuterated solvents used in this study were DMSO- d_6 ($\delta_H = 2.50$ ppm), acetone- d_6 ($\delta_H = 2.04$ ppm) and acetonitrile- d_3 ($\delta_H = 1.94$ ppm). Multiplicities of the peaks were reported as: s = singlet, d = doublet, t = triplet, m = multiplet.

- Sample preparation for NMR analysis.

The chemicals dissolved in approximate 0.3 mL of deuterated solvent was added in a 5 mm of diameter tube for NMR. In some cases, an insert-tube ($d = 4$ mm) containing the reference solution was used to calibrate the quantities of product in the NMR tube. For each measure, 0.2 mL of sample was filled in the NMR tube and the small tube of reference was inserted. The reference is a solution of tetraethylammonium tetrafluoroborate ($\text{Et}_4\text{N}^+\text{BF}_4$) 0.5 M dissolved in DMSO- d_6 .

- Pulsed-gradient spin-echo (PGSE-NMR)

The self-diffusion coefficients were measured by PGSE-NMR using a Bruker Avance III HD spectrometer equipped with a diffusion probe of 5 mm and a temperature regulation unit (20 - 80°C). The frequencies are 400.13, 376.50, and 155.51 MHz for ^1H , ^{19}F and ^7Li , respectively. For the ^{133}Cs PFG-NMR, experiments were performed using a Bruker 300 spectrometer at the frequency of 39.351 MHz. Stimulated echo sequence was used. The maximum magnitude of the pulsed field gradient was $900 \text{ G}\cdot\text{cm}^{-1}$, the diffusion delay Δ was adjusted between 50 and 100 ms, and the gradient pulse length δ was set between 1ms and 5ms depending on the diffusion coefficient and the nature of the mobile species. For the liquid samples, some measurements were also performed with $\Delta = 200$ ms as well to confirm that no convection artifacts occur. The self-diffusion coefficients were determined from the classical Stejskal-Tanner equation:¹

$$\ln(I/I_0) = -DG^2\gamma^2\delta^2(\Delta-\delta/3)$$

where G is the magnitude of the two gradient pulses applied, γ is the gyromagnetic ratio of the nucleus under study and I and I_0 are the integrated intensities of the signal obtained respectively with and without gradient pulses. Here, we used 16 equally spaced gradient steps for each PGSE-experiment. Data acquisition and treatment were performed with Bruker Topspin software.

- Sample preparation

The ILs and polymers were filled into small diameter tube ($d = 4$ mm) in the glove box, then were sealed to prevent the humidity. The level of sample was ensured at about 1.5 cm along the tube. The tubes were covered with the plastic caps and closed by flame welding. The measurements were carried out from 20 °C to 80 °C.

1.2. Size exclusion chromatography coupled multi-angle laser light scattering (SEC-MALLS)

The SEC measurements were performed with the WATERS 515 HPLC, with a differential refractometer SOPARES RI2000 and a light scattering detector WYATTDawn EOS at 690 nm. The data were treated with ASTRA 6 software. NaNO_3 (0.1 M) in DMF (Alfa aesar-HPLC grade 99.7%) was used as solvent at a flow rate of $1 \text{ mL}\cdot\text{min}^{-1}$ through a 10 AGILENT 2xPLgel-Mixed-D column. The molecular weight was determined by the signals of the light scattering detector and the refractometer assuming that all of the injected product passing through the column was analyzed by the MALLS detector and was also compared with the polystyrene equivalent.

- Sample preparation

An amount of polymer (~20 mg) dissolved in the appropriate solvent (~2 mL) for SEC analysis. Solution of 1 wt % of polymer in solvent was filtered with the PP Millipore filter of $0.45 \mu\text{m}$ before injecting into the machine.

1.3. Atomic absorption spectroscopy (AAS)

The ion exchange efficiency was determined using a Perkin Elmer PinAAcle 900F AAS, and the data were treated with the Syngistix software. The lamps for absorption corresponding to different elements such as Li, Na, K, and Mg were used to detect the presence of these ions in the sample. Unfortunately, we couldn't measure the concentration of Cs due to the lack of Cs lamp. However, all of the ionomers after reaction containing a mixture of Na^+ and K^+ as cations were then transformed to Cs^+ through the ion-exchange process. The fact that the ionomer Cs-form contain tiny (or no measurable) quantities of Na^+ and K^+ can further affirm a successful ion-exchange process. The solution containing a definite concentration, usually about 5 ppm of the interested ion, was injected into the machine. Each sample were tested 3 times with different lamps such as Na, K, and an element of interest, to ensure the reasonable results. The efficiency of ion exchange process was presented by the percentages of concentration of each element contained in 5 ppm of polymer.

- Sample preparation

The ionomers were dissolved in distilled water and the M^{n+} concentration estimated from the mass molar of ionomer was approximately 5 ppm. For the copolymers, an amount of polymer was

degraded in acid nitric extra pure and filtered with a PTFE syringe-filter of 0.45 μm . Distilled water was used to dilute the acid from $\sim 65\%$ to $\sim 2\%$ before inject in the machine.

1.4. Infrared spectroscopy (IR)

FTIR analyses were carried out using an IR spectrometer Spectrum ONE (Perkin Elmer). The samples were analyzed in absorbance in wavenumber range between 4000 and 400 cm^{-1} . The IR spectra were acquired with 16 accumulations and a resolution of 1 cm^{-1} . The ionomers (non-crosslinked and crosslinked) and ionic liquid were placed in a liquid cell with ZnSe window. All of the IR measurements were performed in N_2 atmosphere. Before the treatment, the IR spectra were normalized respectively at 1450 and 654 cm^{-1} for ionomers and ionic liquids.

1.5. Field-Emission Scanning Electron Microscopy (SEM)

SEM analyses were performed with an Ultra 55 (Zeiss) microscope using a voltage of 3 kV, and a SE detector, the obtained image was post-treated and analyzed using ImageJ. In details, the NCC dispersion was analyzed with a binaryzation and a statistic analysis of particles. Then the diameter distribution of particles can be extracted and presented using Histogram from OrginPro.

- Sample preparation

The dispersion of nano crystalline celluloses into the cross-linked ionomer was observed on the fracture surface of membranes. To obtain a net fracture surface, samples were frozen in liquid nitrogen, then fractured and coated with carbon (thickness of coating layer was about 5 – 10 nm). The LFP electrodes were fixed to the SEM support with graphite tape and coated with a layer of carbon.

2. Thermal and physical properties

2.1. Thermogravimetric analysis (TGA)

The thermogravimetric measurements were carried out using a TGA 1 STARe instrument of METTLER TOLEDO. Data were treated by a STARe software version 12.20. The measurements were performed under a N_2 flux at 50 $\text{mL}\cdot\text{min}^{-1}$. The temperature increased from RT up to 800 $^\circ\text{C}$ with a heating rate of 10 $^\circ\text{C}$ per minute. The dry samples of average weight 10-15 mg were placed into the open crucibles of aluminum oxide for TGA.

2.2. Differential scanning calorimetry (DSC)

The DSC were carried out using a DSC 1 STARe instrument of METTLER TOLEDO. The data were treated by STARe software version 12.20. The different analysis programs were applied for each type of sample with the heating/cooling rate of 10 $^\circ\text{C}/\text{min}$, or 20 $^\circ\text{C}/\text{min}$ depending on the nature of sample. The rate of nitrogen flux around the DSC chamber was controlled at 150 $\text{mL}\cdot\text{min}^{-1}$ and 50

mL.min⁻¹ inside the chamber. Liquid nitrogen was used to cool the samples. The phase transition behaviors were measured during the second heating cycle. The following programs were used to perform the DSC analysis:

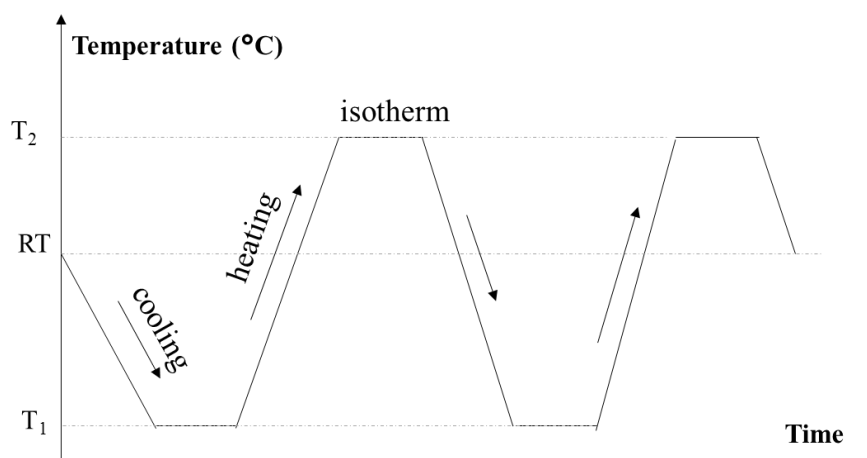


Fig. 1 DSC thermograms for two identical heating/cooling processes

- Ionic liquid performed two identical heating/cooling cycles. The samples were cooled down to $T_1 = -150\text{ }^{\circ}\text{C}$ following 3 minutes of isotherm, then heated up to $T_2 = 100\text{ }^{\circ}\text{C}$ following also an isotherm of 5 minutes.
- Polymer performed two identical heating/cooling cycles. The samples were cooled down to $T_1 = -60\text{ }^{\circ}\text{C}$ following 3 minutes of isotherm, then heated up to $T_2 = 100\text{ }^{\circ}\text{C}$ following also an isotherm of 5 minutes.
- Ionomers performed two heating/cooling cycles. The samples were cooled down to $T_1 = -100\text{ }^{\circ}\text{C}$ following 3 minutes of isotherm, then heated to $T_2 = 150\text{ }^{\circ}\text{C}$ following also an isotherm of 5 minutes.
- Copolymer performed two heating/cooling cycles. The program of ionomer was applied for the first cycle. In the second one, the sample was heated to $T_2 = 250\text{ }^{\circ}\text{C}$ to reach the T_g of the hydrophobic block polymer. To observe the glass transition of the hydrophobic block for $\text{Co}_{1000}\text{P-SO}_3$, a scan rate of $20\text{ }^{\circ}\text{C}/\text{minute}$ was applied for both heating/cooling cycles.
 - Sample preparation.

The dry samples of average weight 5-10 mg encapsulated in the aluminum crucibles for DSC, in a glove box. The samples were placed in the apparatus next to an empty reference capsules.

2.3. Viscosity

Viscosity measurements were carried out by using an AR-G2 Rheometer, with a geometry cone and plate of 40 mm diameter. The body of the rheometer is a rigid, single metal casting comprising a base and a column. The head contains a motor that form a rotating spindle of the column. The machine was covered by a glove bag in plastic, filled with dried air, to avoid the humidity. The

temperature was controlled by a peltier plate with a circulation of water, and could vary from -10 to 90 °C. The data were treated by a TRIOS software.

- Sample preparation.

Approximately 0.6 mL of sample was placed between a horizontal plate and a shallow cone, which attached on the instrument rotating spindle. The angle between the surface of the cone and the plate was around 1-2 degrees. The viscosity of IL was measured every 5 °C from -10 to 90 °C.

2.4. Density

Density of the blends IL/salts were measured in an Argon-filled glove box. In a volumetric flask of 1 mL, 1 ± 0.05 mL of IL taken by micropipette with a plastic tip, was filled. The level of liquid inside need to reach the etched ring of the flask. The whole flask contained IL was weight with a precision balances, readability of 0.001 g. The measure was repeated 5 times for each sample, in order to obtain the average density values at RT.

2.5. Karl Fischer titration

This technique was used to measure the amount of water in the sample. It was invented by the chemist Karl Fischer in 1935. The principle is based on an oxidation of sulfur dioxide in the presence of water:



- Sample preparation

An amount approximately 0.3 mL of sample i.e. IL or anhydrous solvents were weighted, then injects in the Karl Fischer cell. The water content was given in μg of water per g of sample, denoted as ppm. For the reproducibility of measure, each sample was injected at least three times.

3. Electrochemical properties

3.1. Impedance spectroscopy

In this thesis, Electrochemical Impedance Spectroscopy (EIS) was used to study the interfaces, i.e. electrode-electrolyte and the ionic conductivity of the electrolytes. A wide range of frequencies from 1 MHz to 10 mHz was carried out using an impedance meter Hewlett Packard 4192A, for the ionic conductivity measurement, and a VMP3 potentiostat from Biologic for the observation of electrolyte-electrode interface. The results were fitted by Zview software.

- Sample preparation and EIS program

For the ionic conductivity measurement of solid membrane electrolytes, the coin cells (Fig. 2), and Swagelok cells (Fig. 3) were prepared in a glove box. The membrane of 10 mm of diameter were

sandwiched between two stainless steel electrodes ($d = 9 \text{ mm}$). The cells were submitted to two heating/cooling cycles, from $20 \text{ }^\circ\text{C}$ to $90 \text{ }^\circ\text{C}$, with a scan rate of $5 \text{ }^\circ\text{C/ hour}$. An EIS was measured every hour during the heating/cooling processes. For the PEO/salt membranes, a PTFE ring with a definite thickness was placed around the membranes to maintain the shape of the sample even above the melting point.

The conductivity of ILs were carried out with the micro conductivity cells (Fig. 4). The sample were prepared in a glove box and PTFE tap was used to ensure an anhydrous environment. The temperature was performed from 90 to $-10 \text{ }^\circ\text{C}$. The cell constant (κ) determined by the value of the conductance for 0.1 M KCl ($\kappa_{\text{KCl}} = 12.85 \text{ mS.cm}^{-1}$, at $25 \text{ }^\circ\text{C}$) and its resistance, following the equation below:

$$\sigma = \frac{l}{R * S} = \frac{\kappa}{R}$$

Where σ : Ionic conductivity (S.cm^{-1})

l : distance between two electrodes (cm)

R : electrolyte resistance (Ω)

S : electrode surface (cm^2)

And $\kappa = \frac{l}{R}$: constant of the cell

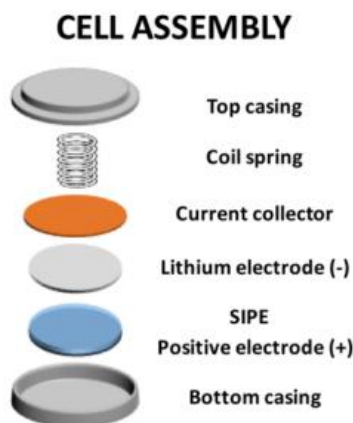


Fig. 2 Coin cell structure for electrochemical measurements

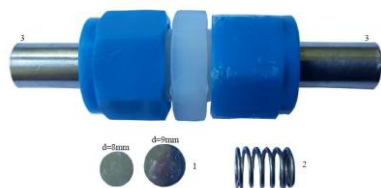


Fig. 3 The picture of Swagelok cell, two stainless steel electrodes, and spring.



Fig. 4 Cell 2-Pole Stainless steel Suit Micro-Samples for ionic conductivity measurement of ionic liquids

3.2. Cyclic voltammetry (CV)

CV is a popular electrochemical technique, in which the oxidation and reduction processes of a system can be investigated. The current density was recorded during the applying of a potential sweep as a function of time. In this work, CV method was used to determine the electrochemical stability, the presence of the intermediates or impurities in oxidation-reduction reactions and the reversibility of a reaction. The trace in Fig. 5 describes an example of a cyclic voltammogram where the horizontal axis represents the applied potential (E), and the vertical axis records the response of the current density (i). The arrows indicate the direction of applied potential.² The CV technique was carried out using a VMP3 potentiostat from Biologic. Data were treated using an EC-lab version 10.40 software.

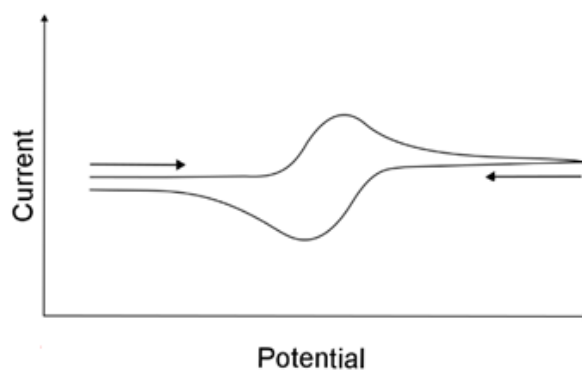


Fig. 5 An example of a cyclic voltammogram

- Sample preparation and CV program

The membrane was sandwiched between a stainless steel electrode and a lithium metal, in a coin cell. These cells were prepared in an anhydrous glove box and the performed temperature was controlled in an oven. An applied potential range starts from OCV up to 4.1 V vs Li⁺/Li in the anodic sweep and reverses to -0.1 V vs Li⁺/Li in the cathodic scan, at a scan rate of 0.1 mV.s⁻¹.

3.3. Chronopotentiometry (CP)

In this thesis, CP technique was used to study the plating/stripping processes of Li^+ in a symmetric Li-metal cell. The method was carried out using a VMP3 potentiostat from Biologic. Data were treated with an EC-lab version 10.40 software. A constant current was applied across the symmetric cell while the potential was recorded as a function of time. The cell was prepared in a glove box following the same concept with the conductivity cell, but the two disks of lithium metal were used in place of stainless steel electrodes.

- CP program

An EIS was applied from 1 MHz to 10 mHz across the cell during 24 h, following a rest of 2 h between each scan. The cell stability was checked by obtaining identical Nyquist plots after 1 day operation at 80 °C. Then 10 pre-conditioning cycles at $10 \mu\text{A}\cdot\text{cm}^{-2}$ were submitted to the cell. The current was imposed for 4 h in each direction, followed by 45 minutes of rest between each side. The strong and constant currents density increasing from 50, 100, 120, 150, up to $200 \mu\text{A}\cdot\text{cm}^{-2}$ were further applied across the cell and the evolution of over-potential as a function of current were recorded.

3.4. Chronoamperometry (CA)

This method was used to measure the transference number of Li^+ ions between the two Li-metal electrodes. In CA technique, a constant potential was applied across the cell and the current response was recorded versus time. The cell using for this test was a symmetric lithium metal coin cell. At first, an EIS was performed to obtain the initial resistance interface (R_i), then a 40 mV polarization (ΔV) was applied to the cell in order to reach the initial current (I_i) value. Next, the EIS was performed by applying a 40 mV perturbation from 1 MHz to 1 Hz in every 10 minutes, at open circuit conditions to observe the cell's resistance until the polarized current reached constant. The resistance and current after polarization were noted as R_s and I_s , respectively.

3.5. Batteries cycling

The batteries cycling was investigated using the Galvanostatic Cycling with Potential Limitation (GCPL) technique, with a VMP3 potentiostat from Biologic. The performance of batteries was presented as a function of their charge/discharge conditions. The galvanostatic rate expresses as C/h, which means the time that the charged species passed through the two electrodes. The galvanostatic rate can be calculated by the specific capacity of electrode material ($\text{mA}\cdot\text{h}\cdot\text{g}^{-1}$) i.e. LiFePO_4 ($170 \text{ mA}\cdot\text{h}\cdot\text{g}^{-1}$). The cells were cycled at 80 °C at different current regimes from low to fast constant current charge/discharge between 2.5 and 3.8 V vs Li^+/Li . The cell for this test was an asymmetric coin cell combined a solid electrolyte sandwiched between a cathode LiFePO_4 and a disk of lithium

metal. The cells were performed at 80 °C in a controlled temperature oven under various power rates from low to high.

References

1. E. O. Stejskal, J. E. Tanner, Spin diffusion measurements: spin echoes in the presence of a time-dependent field gradient. *J. Chem. Phys.* 42, 288–292 (1965).
2. Elgrishi N. et al. A practical beginner's guide to cyclic voltammetry. *J. Chem. Educ.* 95, 197–206 (2018).

Abstract

Safety issues related to chemical leakage, external heating, or explosion restrain the advancement of renewable storage devices based on classical liquid electrolytes. The urgent need for safer batteries requires new technologies such as the replacement of carbonate solvents by green ionic liquid-based electrolytes or the use of conducting polymer membranes. Moreover, facing a future shortage of raw materials such as lithium, trends are to promote the development of rechargeable batteries based on abundant elements i.e. alkali/alkaline-earth metals. A better understanding of cation conductive behavior in these electrolytes become the mainstream for developing high-security lithium and post-lithium batteries.

In this work, the first goal was to focus on the physical and ionic transport properties of several binary systems based on the solution of different alkali/alkaline-earth TFSI salts in a common ionic liquid BMIm TFSI. These ionic liquid electrolytes possess unique characteristics that are promising for electrolyte applications e.g. low vapor pressure, non-inflammable, high thermal stability, with sufficient ionic conductivity. These mixtures are studied with the multi-technique approach to reach thermodynamics (thermal properties), dynamics (viscosity, ionic conductivity self-diffusion coefficients) and structural (IR and Raman spectroscopy) description of these systems. The cationic transport behavior in these ionic liquid electrolytes is strongly influenced by the nature of the cation and its concentration. These viscosity dependent phenomena are related to the alkali/alkaline-earth coordination shell.

Another goal of this work is the development of new single-ion conducting polymers based on PEO as solid electrolytes for safer lithium and post-lithium rechargeable batteries. These materials exhibit a cation transference number which nearly reaches unity for the cross-linked ionomers and multi-block copolymers. The cycling tests in symmetric lithium-metal cell affirmed the reversibility of electrolyte with stable lithium plating/stripping between two electrodes. High performances in lithium metal batteries using 'home-made' LiFePO_4 cathodes demonstrate the potential of these materials as solid electrolytes. An ultimate aim showed the conductivity behavior of the alkali cations in the different polymer matrix. Thanks to the grafting anionic function distributed along the polymer chain, the effect of cation size on its mobility were clearly observed.

Résumé

Les problèmes de sécurité liés aux fuites de produits chimiques, au chauffage externe ou aux explosions sont un frein au développement de dispositifs de stockage renouvelables à base d'électrolytes liquides. La sécurité des batteries nécessite le développement de nouvelles technologies telles que les électrolytes à base de liquide ionique ou de membranes polymères conductrices. Simultanément, et face à l'épuisement des ressources en lithium, la tendance énergétique cherche à privilégier le développement de piles rechargeables à base d'éléments abondants, tels que les métaux alcalins / alcalino-terreux. Une meilleure compréhension du comportement conducteur cationique de ces électrolytes est nécessaire pour développer des batteries au lithium et post-lithium de haute sécurité.

Le premier objectif de ce travail était axé sur les propriétés de transport dans des électrolytes liquides ioniques obtenus en dissolvant des sels alcalin/alcalino-terreux dans un liquide ionique, le BMIm TFSI. Ces mélanges possèdent des caractéristiques prometteuses telles qu'une faible tension de vapeur, une ininflammabilité, une stabilité thermique élevée et une bonne conductivité ionique. Ces électrolytes ont été étudiés par une approche multitechnique pour une description thermodynamique (propriétés thermiques), dynamique (viscosité, conductivité ionique, coefficients d'autodiffusion des différentes espèces) et structurale (spectroscopies IR et Raman). Ces travaux ont permis de montrer que le comportement du transport cationique dans ces électrolytes liquide-ionique est fortement influencé par la nature et la concentration des cations. Ces variations dépendent de la viscosité, qui sont reliés à la sphère de coordination des ions alcalins/alcalino-terreux dissous.

Une autre partie de ce travail présente le développement de nouveaux ionomères à base de POE comme électrolytes solides pour des batteries rechargeables au lithium ou de génération post-lithium. Ces matériaux, ionomères réticulés et copolymères, présentent un nombre de transport ionique pratiquement égal à 1. L'excellent comportement en cyclage dans une batterie symétrique au lithium-métallique ont confirmé le bon comportement de l'électrolyte et une réversibilité parfaite de l'intercalation/désintercalation du lithium dans les deux électrodes. Les hautes performances des batteries au lithium métallique utilisant des cathodes LiFePO_4 , ont confirmé l'adéquation de ces matériaux pour une utilisation en tant qu'électrolytes solides. Un dernier objectif de ce travail a été l'étude du comportement de conductivité des cations alcalins dans différentes matrices de polymère. Grâce au greffage des fonctions anionique, une conductivité cationique unitaire a pu être atteinte, ce qui a permis de mesurer l'effet de la taille du cation sur sa mobilité.